Julius-Maximilians-
UNIVERSITÄT
WÜRZBURG

UNIVERSITÄT WÜRZBURG
PHYSIKALISCHES INSTITUT
epVI

# Electrothermal Investigation on Charge and Heat Transport in the Low-Dimensional Organic Conductor $(DCNQI)_2Cu$

Dissertation zur Erlangung des
naturwissenschaftlichen Doktorgrades
der Julius-Maximilians-Universität Würzburg

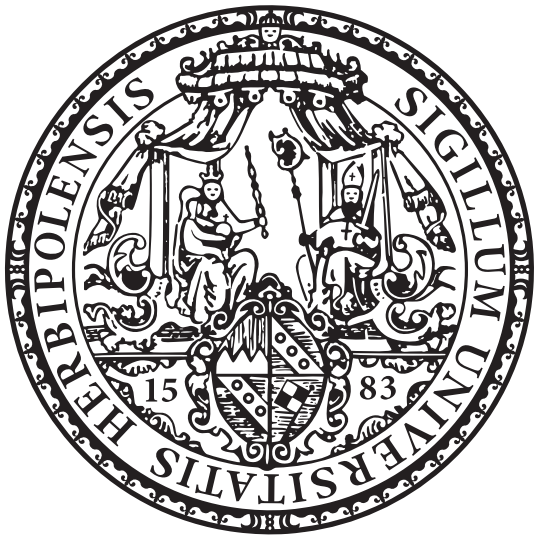


vorgelegt von

**Florian Hüwe**
aus Münster

Würzburg, 2017

Eingereicht am: 2. Februar 2017
bei der Fakultät für Physik und Astronomie

1. Gutachter: Prof. Dr. Jens Pflaum
2. Gutachter: Prof. Dr. Hartmut Buhmann
3. Gutachter: .....
der Dissertation.

Vorsitzende(r): Prof. Dr. Jean Geurts

1. Prüfer: Prof. Dr. Jens Pflaum
2. Prüfer: Prof. Dr. Hartmut Buhmann
3. Prüfer: Prof. Dr. Giorgio Sangiovanni
im Promotionskolloquium.

Tag des Promotionskolloqiums: 26.07.2017

Doktorurkunde ausgehändigt am .....

# Contents

# Chapter 1

# Introduction

The BCS theory, named after its founders Bardeen, Cooper & Schrieffer, explains conventional superconductivity by the phonon-assisted coupling of electrons to a bosonic ground state [1]. Because the coupling depends on the lattice dynamics, the critical temperature for superconductivity to occur was found to be inversely related to the ion mass of the lattice via $T_c \propto \sqrt{\frac{1}{m_{ion}}}$. In 1964, Little suggested that charge carriers may form a bosonic ground state via an exchange interaction mediated by the electronic polarization of functional side groups in a one-dimensional organic conductor. In this case, the coupling dynamics were governed by the electron mass rather than by the ion mass and accordingly, a rise in the superconducting transition temperatures would be expected [2].

Much effort was spent in the following years on the synthesis of one-dimensional organic conductors, e.g. the prominent charge transfer salt Tetrathiafulvalene-Tetracyanoquinodimethane (TTF-TCNQ) with an electrical conductivity of up to $700\,\mathrm{S\,cm^{-1}}$ at room temperature [3, 4]. Instead of a superconducting state, a phase transition from a metallic into a semiconducting or insulating state was observed upon cooling which has already been predicted for a one-dimensional conductor by Rudolf Peierls in the 1950s [5]. It originates from a spatially modulated electron density, called charge-density-wave (CDW), accompanied by a periodic distortion of the crystal lattice. This transition is often called Peierls transition and is one of many intriguing examples of how physical properties change in case of reduced dimensionalities. Further research led to the synthesis of many more low-dimensional organic conductors with a variety of ground states, among them Peierls insulators, Mott insulators and also superconductors based on two-dimensional electronic structures [6]. However, none of these materials realized the superconducting ground state via the coupling mechanism proposed by Little since the one-dimensional systems are prone to undergoing a metal-insulator phase transition upon cooling [7].

A prominent class of organic metals is constituted by radical anion salts based on the Dimethyl-Dicyanoquinonediimine (DMe-DCNQI) acceptor molecule synthesized by the group of Siegfried Huenig for the first time in 1984 at the University of Würzburg [8]. In combination with copper the molecule forms $(\mathrm{DMe\text{-}DCNQI})_2\mathrm{Cu}$ single crystals which

admit even higher electrical conductivities than TTF-TCNQ. Moreover, the material is stable against the formation of a CDW and retains its metallic character down to cryogenic temperatures by virtue of the pronounced 3d-$\pi$-hybridization of copper orbitals and the lowest unoccupied molecular orbital (LUMO) of DCNQI. The crystals reach an electrical conductivity of up to $5 \times 10^5\,\mathrm{S\,cm^{-1}}$ at 1.5 K being on the order of pure copper's conductivity at room temperature [9]. In addition, the ground state of DCNQI radical ion salts may be adjusted by chemical manipulation of the DCNQI molecule and by variation of the counter ion. For example, even a partial deuteration of the molecule is sufficient to induce a steep first-order CDW transition with tunable critical temperature [10]. Although no one-dimensional superconductor emerged from the above research efforts, organic conductors have been proposed for a variety of technological applications by virtue of their rich phase diagrams and unconventional properties [11]. For example, the CDW transition in deuterated $(DCNQI)_2Cu$ may be driven by short laser pulses demonstrating the material as potential candidate for ultra-fast optical switches [12]. Furthermore, nonlinear conductivity phenomena have been observed in a variety of low-dimensional molecular metals with distinctively different ground states [13, 14, 15, 16, 17], including the CDW state of $(DCNQI)_2Cu$ [18]. These effects might yield new devices based on organic materials, such as organic thyristors converting a DC to an AC current [19, 20]. Other proposals include the utilization of thin films and nanocrystals based on organic charge transfer salts to create resistive memories [21, 22].

More recently, the potential of low-dimensional molecular metals for thermoelectric applications has been discussed [23, 24, 25]. Thermoelectric generators (TEGs) have been claimed as key technology to make use of the tremendous amount of available waste heat constituting about 70 % of the primary energy consumed world-wide [26, 27]. To-date, the efficiency of thermoelectric generators is rather limited, particularly in the temperature regime below 100 °C where most of the heat is dissipated. Furthermore, the high production costs as well as the energy intensity of conventional inorganic thermoelectric materials limit a large scale application so far [28]. Chemically tunable organic thermoelectric materials may resolve some of the challenges and have been on the rise in the recent years [29, 30, 31, 32]. Prerequisites for an efficient thermoelectric material are a high electrical conductivity, a large Seebeck coefficient as well as a low thermal conductivity. Improvements on the electrical conductivity of organic polymers rendered a thermoelectric performance possible advancing that of conventional inorganic thermoelectrics [33]. These materials exhibit a low thermal conductivity by virtue of their complex structure in combination with their weak dispersive binding forces. Yet, their inherent disorder also places restrictions on the charge carrier mobility. Low-dimensional molecular metals rep-

resent an alternative organic material class for thermoelectric applications. Their ordered crystal structure allows for a high charge carrier mobility and a high electrical conductivity over macroscopic distances necessary for thermoelectric generators. Their Seebeck coefficients surpass values of ordinary metals by one order of magnitude. $(DCNQI)_2Cu$ is a material system of special interest because it marks one of the best n-type organic conductors which are still lacking for all-organic thermoelectric devices. Furthermore, owing to their reduced electronic dimensionality, fundamental restrictions on a material's thermoelectric performance, like the Wiedemann-Franz law, may be lifted in these solids. Yet, a coherent investigation of the thermal conductivity in organic conductors is lacking so far to evaluate their thermoelectric potential. Therefore, a consistent and thorough characterization of the thermoelectric key parameters is of technological as well as of fundamental interest. As the transport quantities are interrelated and depend sensitively on the purity and the perfection of single crystals, one aim of this thesis was to develop a setup to measure the Seebeck coefficient as well as the electrical and thermal conductivity on a single specimen of $(DCNQI)_2M$ (M=Cu,Li) radical anion salts in order to study their correlation.

This thesis is divided into three parts. In the first chapter, the theoretical basics for the work are laid out. Thermoelectric transport properties are discussed in general as well as with focus on organic metals. The material class of organic conductors together with their electrical and thermal properties are introduced using the archetypical example of $(DCNQI)_2Cu$. A short overview on the electronic ground states occurring in DCNQI radical anion salts is given. The second part of the work mainly outlines the experimental measurement setup designed and implemented in the course of my PhD work along with its characterization and calibration. It also briefly describes the electrocrystallization procedure to grow high-quality single crystals. In the final chapter, the results obtained for the $(DCNQI)_2M$ material system are presented. The novel setup allowed for a coherent study of the electrical and the thermal transport quantities together with their relation to the low-dimensional electronic structure. Especially the thermal conductivity data is of unprecedented quality and enabled a detailed analysis of the Wiedemann-Franz law and of the lattice thermal conductivity in molecular metals. Nonlinear conductivity effects in $(DCNQI)_2Cu$ have been explained in terms of the charge carriers' interaction with optical phonons and an explanation for their universal occurrence in organic conductors is provided. A study of latent heat across the CDW transition of chemically varied $(R_1,R_2$-$DCNQI)_2Cu$ ($R_i$=$CH_3$, $CD_3$, Br) crystals facilitated a verification of the thermodynamic model of the phase diagram based on charge, spin and lattice degrees of freedom [34]. Finally, the thermoelectric performance of the $(DCNQI)_2Cu$ material system was evaluated

to be of similar potential as compared to conducting polymers at room temperature. In the temperature regime below 40 K a figure-of-merit outperforming even the best inorganic thermoelectric materials was attained. Finally, a first prototypical TEG was built in combination with the p-type organic conductor $TTT_2I_3$ (TTT: Tetrathiotetracene) achieving specific power outputs unrivaled in organic thermoelectrics.

# Chapter 2

# Theory

## 2.1 Introduction to Thermoelectricity

In 1821, Thomas Johann Seebeck discovered that heating the junction of two metals in an electrical circuit deflects a compass needle [35]. Initially, he explained this effect by a thermally induced magnetism. Subsequently, it was realized that a *thermoelectric effect*, or *Seebeck effect*, describing an electric field $\vec{E}$ generated under a temperature gradient $\vec{\nabla}T$ in a material

$$\vec{E} = S \cdot \vec{\nabla}T \tag{2.1}$$

was responsible for the observed phenomenon and affected the magnetic needle due to the associated current and Ampere's law. The *Seebeck coefficient* $S$ is a material property in units of $\mathrm{V\,K^{-1}}$, i.e. it is an intensive quantity independent of the sample dimensions. It may take positive (p-type) and negative values (n-type) in the range of $\mu\mathrm{V\,K^{-1}}$ to $\mathrm{mV\,K^{-1}}$. Later on, Jean-Charles Peltier found a heating or cooling effect in the presence of an electrical current flow through a similar junction [36]. The *Peltier effect* relates the heat flow $\vec{J}_Q$ to a charge flow $\vec{J}_e$ [37]

$$\vec{J}_Q = \Pi \cdot \vec{J}_e \tag{2.2}$$

with the *Peltier coefficient* $\Pi$ quantified in V. It was William Thomson (Lord Kelvin) recognizing that the two effects are based on the same physical phenomenon and thus are connected with each other by the so-called *Kelvin relation* [38]:

$$S = \frac{\Pi}{T} \quad . \tag{2.3}$$

### 2.1.1 Basic Equations

The thermoelectric phenomena discovered by Seebeck, Peltier and Thomson are more rigorously described by the following set of equations [39]:

$$\vec{J_e} = \sigma\vec{E} - \alpha_P\vec{\nabla}T \tag{2.4a}$$

$$\vec{J_Q} = \beta\vec{E} - \kappa'\vec{\nabla}T \quad . \tag{2.4b}$$

The first equation states that an electric current density $\vec{J_e}$ can either flow upon application of electric fields and thermal gradients to a material. Its response to the external stimuli is characterized by the *electrical conductivity* $\sigma$ and the *Peltier conductivity* $\alpha_P$. Setting $J_e = 0$ in Eq. 2.4a, the Seebeck coefficient $S$ is obtained with the help of Eq. 2.1:

$$S = \frac{\alpha_P}{\sigma} \quad . \tag{2.5}$$

According to Eq. 2.4b, the same external perturbations further cause a heat flow $\vec{J_Q}$ with the corresponding thermoelectric coefficient $\beta = \alpha_P \cdot T$ and thermal conductivity $\kappa'$. The above-mentioned thermoelectric effects are not only of technological importance for temperature sensing, generating electricity or cooling applications. They also enable a deeper understanding of charge carrier transport in solids because they are related to a diffusion of electrons along a temperature gradient. However, a thermodynamic treatment already gives a basic understanding of its origin without the inclusion of charge carrier transport theory, as will be shown in the following.

### 2.1.2 Thermodynamic View on Thermoelectricity

In 1948, Herbert Callen published a thermodynamic treatment of thermoelectric phenomena [40]. The starting point is a system of $N$ particles with chemical potential $\mu$ at temperature $T$ and pressure $p$ in a box of volume $V$. An infinitesimal change of the system's free energy $U$ is described by [39]

$$\delta U = T\delta\Sigma + \mu\delta N + p\delta V \quad . \tag{2.6}$$

For a system of constant volume the last term may be neglected. The free energy may be enhanced by introducing new particles or by increasing the entropy $\Sigma$. The chemical potential $\mu$ as well as the temperature $T$ constitute the respective measures of the energy gain. In a similar manner, the energy flux $\vec{J_U}$ in the system

$$\vec{J}_U = T\vec{J}_\Sigma + \mu\vec{J}_N \tag{2.7}$$

is connected to the entropy ($\vec{J}_\Sigma$) and particle flow ($\vec{J}_N$) densities per unit area and time. This means that energy can be transported in the system by displacing particles being at chemical potential $\mu$ or by changing the entropy at a given temperature $T$. The divergence of Eq. 2.7 defines the response of the system to any spatial variation in temperature or chemical potential:

$$\vec{\nabla}\cdot\vec{J}_U = (\vec{\nabla}T)\cdot\vec{J}_\Sigma + T(\vec{\nabla}\cdot\vec{J}_\Sigma) + (\vec{\nabla}\mu)\cdot\vec{J}_N + \mu(\vec{\nabla}\cdot\vec{J}_N) \quad . \tag{2.8}$$

To obey the energy conservation law, the flow of energy into and out of each region of the box should be equal, i.e. $\vec{\nabla}\cdot\vec{J}_U = 0$. Without the local generation of particles ($\vec{\nabla}\cdot\vec{J}_N = 0$) Eq. 2.8 then reads

$$0 = \vec{J}_\Sigma\cdot(\vec{\nabla}T) + T\dot{\vec{s}} + \vec{J}_N\cdot\vec{\nabla}\mu \quad , \tag{2.9}$$

$\dot{\vec{s}} = \vec{\nabla}\cdot\vec{J}_\Sigma$ defining the rate of change in entropy per volume. If no entropy is produced ($\dot{\vec{s}} = 0$), Eq. 2.9 indicates that particles moving along a gradient in chemical potential cause a temperature difference by virtue of an entropy flow. It is due to the particle's energy change which has to be balanced by the entropy flow. The direction and magnitude of the temperature gradient are set by the energy gain of the particles upon moving along the chemical potential. The effect occurs in any system with constant energy and particle number and as such, does not depend on the particles obeying Fermi-Dirac statistics or not. Furthermore, no particle scattering mechanism producing local entropy ($\dot{\vec{s}} \neq 0$) is required. The thermoelectric effect simply follows from the first law of thermodynamics for a system with fixed particle number. Inserting an electrical current density $\vec{J}_e = -e\cdot\vec{J}_N$ for the particle flow and introducing the heat flow $\vec{J}_Q = T\cdot\vec{J}_\Sigma$, the well-known Peltier effect emanates from Eq. 2.9, again for $\dot{\vec{s}} = 0$:

$$\vec{J}_Q = T\cdot\vec{J}_\Sigma = \underbrace{\frac{T}{e}\cdot\frac{\nabla\mu}{\nabla T}}_{\Pi}\vec{J}_e \quad . \tag{2.10}$$

With the Peltier coefficient $\Pi = S\cdot T$, the thermodynamic derivation provides two

alternative definitions of the Seebeck coefficient [41]:

$$S = \frac{J_\Sigma}{J_e} = \frac{\text{entropy per carrier}}{\text{charge per carrier}} \tag{2.11a}$$

$$S = \frac{J_Q}{J_e \cdot T} = \frac{\text{heat per carrier}}{\text{charge per carrier}} \cdot \frac{1}{T} = \frac{c_{el}}{e} \quad . \tag{2.11b}$$

The first definition explains the Seebeck coefficient as *entropy per charge carrier* and was first pointed out by Callen [40]. The second definition relates the Seebeck coefficient to the specific heat $c_{el}$ carried by each charge carrier. Hence, the thermopower provides experimental access to one of the thermodynamic state functions and may be used to understand the electronic phase diagram of solids.

### 2.1.3 The Thermoelectric Generator

The Seebeck effect can be utilized to convert heat into electrical energy by means of a thermoelectric generator. The corresponding layout is shown in Fig. 2.1a. It consists of many p- and n-type thermoelectric legs which are electrically connected in series but thermally parallelized. The principle of a single thermocouple in the generator is illustrated in Fig. 2.1b. The electrical junction of the two materials is kept at a temperature $T_2 > T_1$. In the p-type material holes will diffuse from the hot to the cold side while in the n-type leg electrons will move along the same direction.

The electric fields generated by the effective gradient in carrier density accumulate to a voltage of [37]

$$V_{TC} = (S_p - S_n)(T_2 - T_1) \tag{2.12}$$

with positive p-type Seebeck coefficient $S_p$ and negative n-type thermopower $S_n$. The voltages of many thermocouples connected in series will add up to the total open circuit voltage of the thermoelectric generator [37]:

$$V_{OC} = \sum_i V_{TC,i} \quad . \tag{2.13}$$

Connecting a load resistor $R_L$ to a single thermocouple with perfect contacts, the generated current will be [37]

$$I = \frac{(S_p - S_n)(T_2 - T_1)}{R_L + R_p + R_n} \tag{2.14}$$

where $R_n$ and $R_p$ are the resistances of the individual thermoelectric legs supplying

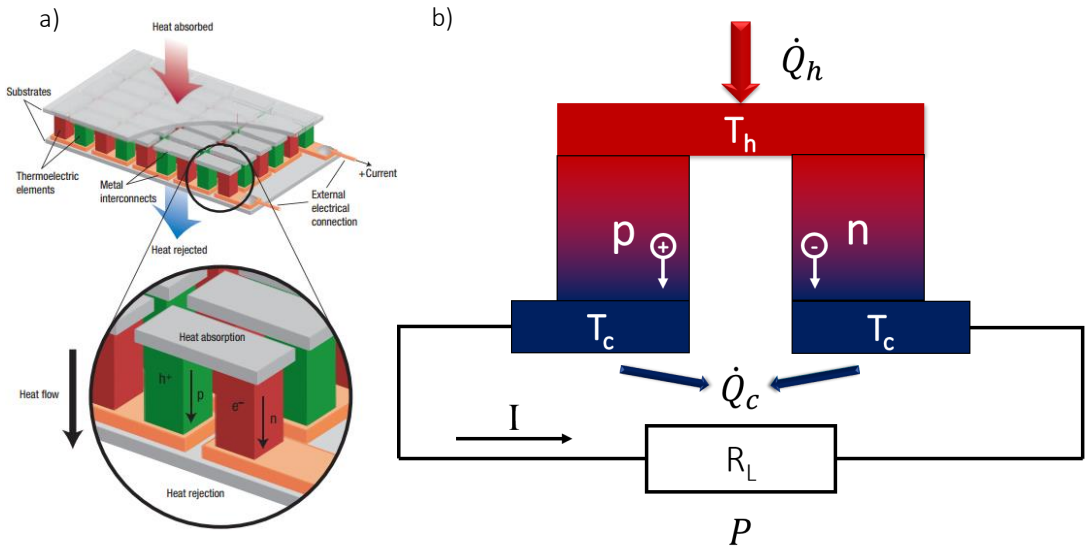


Figure 2.1: Concept and working principle of a thermoelectric generator. (a) A number of p- and n-type thermocouples are connected electrically in series and thermally in parallel to transform the absorbed heat into electrical energy. From: [42] (b) In a single thermocouple electrons (holes) drift from the hot to the cold side in the n-type (p-type) thermocouple leg adding up to an electric potential and supplying power $P$ to a load $R_L$.

the overall power output of [37]

$$w = \left( \frac{(S_p - S_n)(T_2 - T_1)}{R_L + R_p + R_n} \right)^2 R_L \quad . \tag{2.15}$$

The heat $q$ supplied at the hot contact will on the one hand flow across the sample via thermal conduction and on the other hand balance Peltier heating effects due to the current flow [37]:

$$q = (S_p - S_N)T_1 I + (K_p + K_n)(T_2 - T_1) \quad . \tag{2.16}$$

$K_i$ are the thermal conduction coefficients along the legs. The maximum efficiency of the generator $\eta = w/q$ amounts to [37]

$$\eta = \underbrace{\frac{(T_2 - T_1)}{T_1}}_{\eta_{Carnot}} \frac{\sqrt{1 + zT} - 1}{\sqrt{1 + zT} + T_2/T_1} \tag{2.17}$$

where $\eta_{Carnot}$ is the *Carnot efficiency* and $zT$ is the so-called *dimensionless thermoelectric figure of merit*. For a single material of resistance $R$ and thermal conductance $K$ it is defined as [37]:

$$zT = \frac{S^2}{R \cdot K} \cdot T = \frac{\sigma \cdot S^2}{\kappa'} \cdot T = \frac{PF}{\kappa'} \cdot T \quad . \tag{2.18}$$

$S$, $\sigma$ and $\kappa$ denote the thermopower as well as the electrical and thermal conductivity of the material, respectively. $PF = \sigma \cdot S^2$ defines the power factor. For a thermoelectric generator made from a series of p- and n-type legs the maximum combined thermoelectric figure of merit for optimized leg geometries reads [37]:

$$zT = \frac{(S_p - S_n)^2 T}{\sqrt{(\rho_p \kappa'_p + \rho_n \kappa'_n)}} \quad . \tag{2.19}$$

### 2.1.4 Waste Heat Recovery by Thermoelectric Generators

More than 70 % of the primary energy consumed world-wide is wasted, mostly in the form of heat at temperatures below 100 °C [27]. Thermoelectric energy converters have been proposed as technological solution to recover a substantial amount of this energy into electrical power [26]. However, high production costs and the lack of efficient thermoelectric materials operating in this temperature regime have limited large-scale applications to date. Fig. 2.2a illustrates the maximum conversion efficiency of a thermoelectric generator calculated by Eq. 2.17 for different values of $zT$. At high $zT$ values it approaches the Carnot limit while state-of-the-art devices only reach values of $zT \approx 0.5$ providing rather inefficient energy conversion compared to other thermodynamic heat engines [43]. The Curzon-Ahlborn limit represents a more realistic efficiency limit for thermodynamic heat cycles taking into account irreversible processes. While conventional energy harvesting systems are already close to this limit, there is plenty of room for the improvement of thermoelectric generators. Much of the present research focuses on exploring new materials with high $zT$ values.

Some characteristic figures of merit for conventional inorganic thermoelectric materials are depicted in Fig. 2.2b. At ambient temperature, $Bi_2Te_3$ and $Sb_2Te_3$ are among the most prominent p- and n-type materials, respectively. However, these materials contain toxic elements and can only be efficiently used in a small and besides, rather high temperature regime [42]. The need for new, sustainable materials providing high $zT$ values in the mid-temperature range of about 400 K prompted a tremendous, ongoing growth in scientific research activities in the last two decades. To maximize $zT$, and hence the thermoelectric conversion efficiency, a material with high electrical conductivity and large Seebeck coefficient but low thermal conductivity is desirable in order to achieve $zT \geq 1$. The interdependence of these quantities places severe restrictions on the optimization strategies of $zT$. The power factor may be maximized by optimum doping of semiconductors [42]. A further reduction of the phononic contribution to the thermal conduction by means of superlattice engineering on nanometer lengths scales facilitated enhanced $zT$ values on the order of one [44, 45]. For $Bi_2Te_3$, the best RT thermoelectric material to

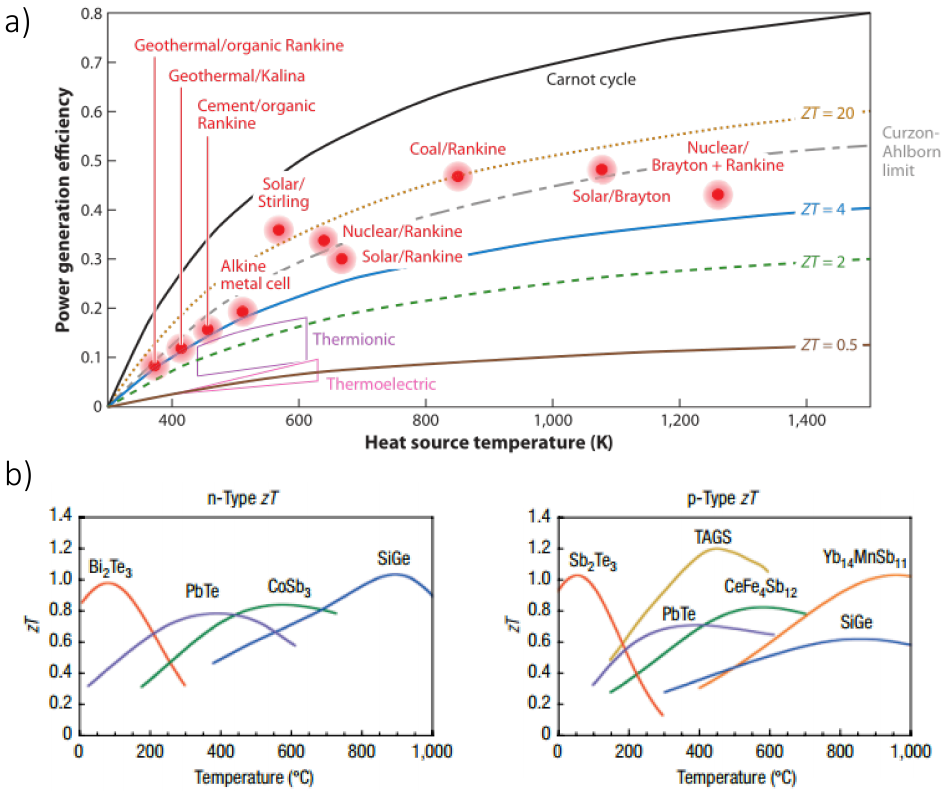


Figure 2.2: Current state of research on thermoelectrics. (a) Power generation efficiencies of a thermoelectric generator for different values of $zT$ compared to other thermodynamic power generation cycles. For high values of $zT$ the efficiency approaches the Carnot limit. However, state-of-the-art commercial thermoelectric generators only reach values of $zT \approx 0.5$ making them rather inefficient compared to other energy converters. From: [43] (b) Inorganic thermoelectric n- and p-type materials with $zT \approx 1$ have been found. Yet, most high-$zT$ materials are only efficient in a small and besides, high temperature regime. From: [42]

date, a value of $zT = 2.4$ has been obtained in this way [44]. However, this result has not been reproduced by other research groups yet.

To overcome the inherent limitation of three-dimensional materials on $zT$, a reduction of the electronic dimensionality has been discussed [46]. This may not only favor a violation of the Wiedemann-Franz law [47, 48, 49] but could also enhance the thermoelectric power factor due to attendant exotic properties observed in low-dimensional solids, such as phonon drag contributions to the thermopower [50]. Zintl compounds [51] and skutterudites [52] were also evaluated as good thermoelectric candidates by virtue of their complex crystal structure facilitating low lattice thermal conductivity and tunability of the electronic band structure. Yet, a tremendous amount of materials are unexplored with respect to their thermoelectric properties, especially synthetic ones.

In recent years, the field of organic thermoelectrics based on conducting polymers has been on the rise with high potential to tackle many of the challenges raised above [29, 30, 33, 31, 32]. In addition to their low-cost production and processability, they offer

an intrinsic low thermal conduction while appreciable electrical conductivity and Seebeck coefficients can be obtained by tuning the oxidation state of polymers. Values of $PF = 469\,\mu\mathrm{W\,K^{-2}\,m^{-1}}$ and $zT = 0.42$ have been reported for the polymer PEDOT:PSS (poly(3,4-ethylenedioxythiophene):polystyrene-sulfonate) as an example [33], advancing values obtained for $Bi_2Te_3$. Some authors question the above results because the transport quantities have been measured along different sample directions, neglecting the anisotropy due to different intra- and interchain charge carrier conduction in polymers [53, 54]. Their measurements on PEDOT:PSS only yield $zT = 0.01$ but reliable values of $zT = 0.1$ are obtained for the polymer PEDOT:Tos (poly(3,4-ethylenedioxythiophene):tosylate) [54]. In this thesis, the alternative material class of crystalline low-dimensional organic conductors is addressed and the foundation for the implementation in thermoelectrics is laid. Theoretical basics to understand their electrical and thermal properties are outlined in the following, starting with possible electronic ground states established in this material class.

## 2.2 Metal-Insulator Transitions

Before introducing the transport theory to understand thermoelectric material properties, the ground states of low-dimensional conductors will be reviewed. For many crystalline materials, the treatment of valence electrons as free quasiparticles moving in the effective periodic potential of the ions and other electrons is a good approximation. The ground state with respect to the conduction properties is then based on the structure and filling of the energy bands formed by the valence states of the constituting atoms. Materials with partially filled bands are expected to reveal metallic behavior while an energy gap at the Fermi level yields insulating or semiconducting properties, depending on the size of the gap. This generalization does not necessarily hold for low-dimensional conductors. The instability of 1D Fermi gases against the formation of a charge-density-wave as well as the influence of larger electronic correlations in lower dimensions are therefore discussed in this section.

### 2.2.1 1D Electron Gas Coupled to the Lattice

In organic crystals, electrons interact rather efficient with phonons due to the low energy of the latter compared to inorganic crystal structures. While the details of the phonon dynamics will be discussed in Sec. 2.4, the peculiar ground states emerging from the efficient coupling of a low-dimensional electronic system to the lattice will already be presented here.

#### Charge-Density-Wave Transition

Quasi-one-dimensional organic conductors are prone to undergo a metal-insulator transition called *Peierls* or *Charge-Density-Wave (CDW)* transition. The transition is caused by a modulation of the charge density in space, triggering a periodic static lattice distortion in the case of sufficiently strong electron-phonon coupling [55]. In the following, a short, theoretical introduction into the phase transition predicted by Rudolph Peierls shall be given [56]. A one-dimensional metallic system of electrons coupled to the lattice can be described by the Fröhlich Hamiltonian in second quantization [57]:

$$\mathcal{H} = \sum_k \epsilon_k a_k^\dagger a_k + \sum_q \hbar\omega_q b_q^\dagger b_q + \sum_{k,q} g_q a_{k+q}^\dagger a_k (b_{-q}^\dagger + b_q) \quad . \tag{2.20}$$

The first term corresponds to an electron gas in one dimension, $\epsilon_k$ symbolizing the electronic band dispersion in $k$-space, $a_k^\dagger(a_k)$ being creation (annihilation) operators. The second term describes the lattice vibrations with the phonon dispersion $\omega_q$ in the reciprocal

$q$-space, with the phonon creation and annihilation operators $b_q^\dagger$ and $b_q$. The third term accounts for electron-phonon interactions with the coupling constant $g_q$. For small phonon amplitudes as well as $g$ independent of $q$, the electron-phonon coupling term leads to a renormalized phonon dispersion [55]

$$\omega_{ren,q}^2 = \omega_q^2 + \frac{2g^2\omega_q}{\hbar}\chi(q,T) \tag{2.21}$$

where $\chi(q,T)$ is the *Lindhard response function*. It characterizes the rearrangement of charge $\rho_{ind}$ in the presence of a time-independent potential $\Phi(\vec{q})$:

$$\rho_{ind}(\vec{q}) = \chi(\vec{q},T)\Phi(\vec{q}) \quad . \tag{2.22}$$

By approximating a linear electronic dispersion close to the Fermi energy $\epsilon_F$, $\chi(\vec{q})$ can be evaluated in one dimension [55]

$$\chi(q) = -\int \frac{d\vec{k}}{(2\pi)^d}\frac{f_{\vec{k}} - f_{\vec{k}+\vec{q}}}{\epsilon_{\vec{k}} - \epsilon_{\vec{k}+\vec{q}}} \overset{d=1}{=} -g(\epsilon_F)\ln\left|\frac{q+2k_F}{q-2k_F}\right| \quad , \tag{2.23}$$

with the dimensionality $d$ and the density of states per spin at the Fermi-level $g(\epsilon_F)$. Eq. 2.23 diverges for $|\vec{q}| = 2k_F$ in one dimension making the electron gas at $T = 0$ unstable against the formation of a modulated charge density of period $\lambda = 2\pi/q = \pi/k_F$. The Lindhard response function, compared for different dimensionalities in Fig. 2.3a, reveals a divergence at $q = 2k_F$ only for the one-dimensional case. The major contribution to the integral in Eq. 2.23 originates from electron-hole states that are degenerate in energy and connected by a wave vector $|\vec{q}| = 2k_F$ which is commonly called *nesting vector*.

For higher dimensionalities the number of nested states is reduced as illustrated in Figure 2.3b. Whereas in one dimension the whole Fermi sheet at $q = \pm k_F$ can be projected onto each other by just one nesting vector (arrow), in two dimensions only the states along the red line can be connected to the opposite of the Fermi cylinder, reducing the divergent contribution to the integral in Eq. 2.23. In 3D only two points can be connected by a single nesting vector. Hence, perfect nesting only occurs for a one-dimensional system. However, also slightly corrugated quasi-one-dimensional Fermi surfaces, as frequently observed in organic conductors, may exhibit good nesting qualities as illustrated in Figure 2.3c. Evaluating the integral in Eq. 2.23 at finite temperature and $|\vec{q}| = 2k_F$ up to a cutoff energy $\epsilon_0$, the renormalized phonon frequency in Eq. 2.21 yields [55]:

$$\omega_{ren,2k_F}^2 = \omega_{2k_F}^2 - \frac{2g^2 n(\epsilon_F)\omega_{2k_F}}{\hbar}\ln\left(\frac{1.14\epsilon_0}{k_B T}\right) \quad . \tag{2.24}$$

The reduction of the phonon frequency by electron-phonon interaction is called phonon

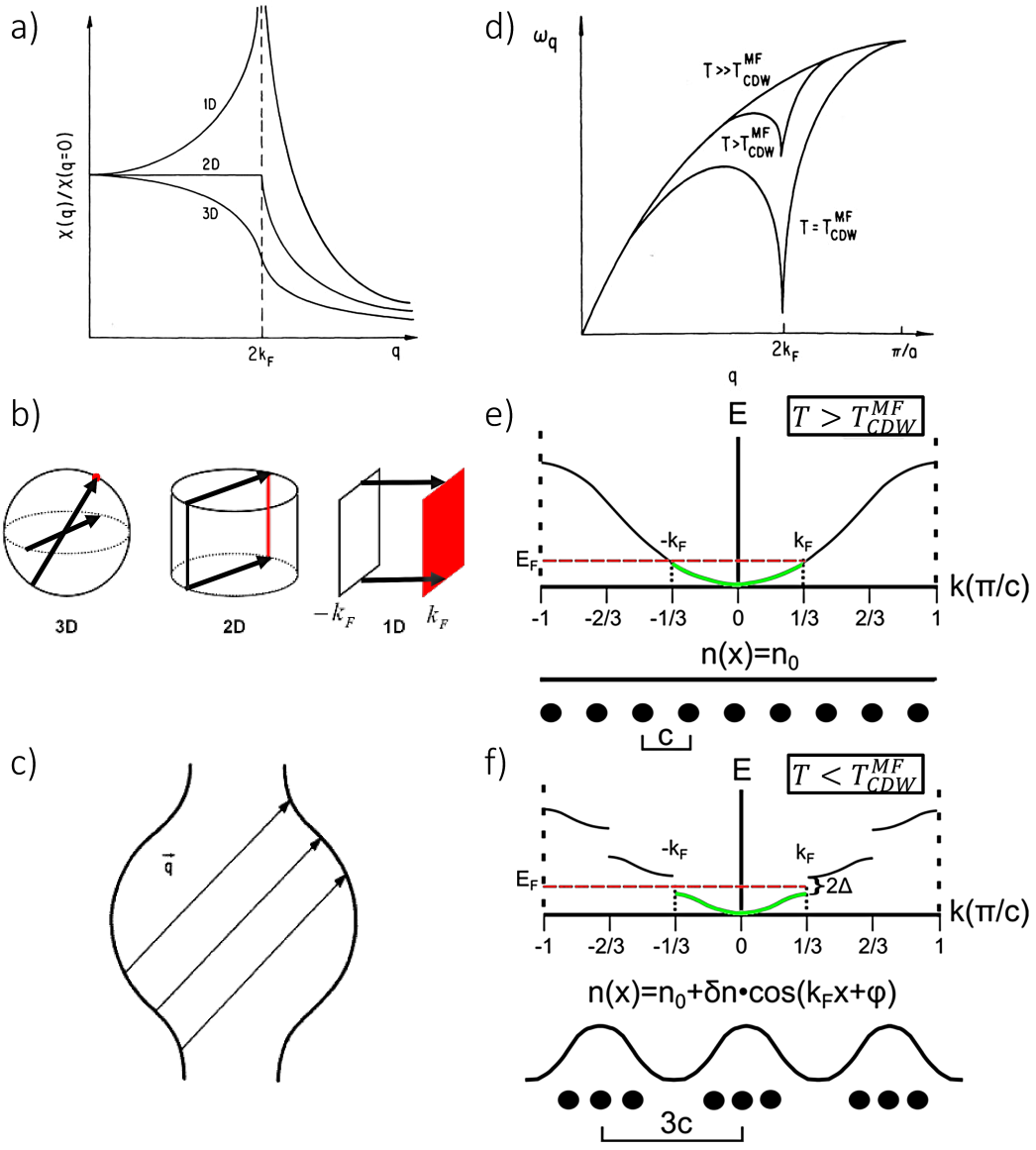


Figure 2.3: Fermi surface instability in low dimensions. (a) Comparison of the Lindhard response functions for different dimensionalities: only in 1D a divergence at $q = 2k_F$ occurs. (b) Nesting qualities in 1D, 2D and 3D: The number of electron and hole states (indicated red) on the Fermi surface that can be connected by just one nesting vector $\vec{q} = 2\vec{k}_F$ is much higher in 1D compared to 2D. Only two states can be connected on a Fermi sphere in 3D by a single nesting vector. (c) A quasi-one-dimensional warped Fermi surface may still connect a significant number of electron-hole-states with one distinct nesting vector yielding good nesting quality. (d) Phonon softening upon approaching the transition temperature $T_{CDW}^{MF}$. (e) One-dimensional crystal lattice of metallic ground state with the charge being equally distributed over the entire lattice leading to a thirdly-filled band. (f) In the charge-density-wave ground state an energy gap opens at the Fermi energy due to the trimerization of the lattice sites and the reduction of the Brillouin zone. The system becomes semiconducting and the charge density varies periodically in space. (a)-(d) Adapted from: [55]

softening. At $|\vec{q}| = 2k_F$, it vanishes on condition that [55]:

$$k_B T_{CDW}^{MF} = 1.14\epsilon_0 e^{-\frac{1}{\lambda}} \tag{2.25a}$$

$$\text{with} \qquad \lambda = \frac{g^2 n(\epsilon_F)}{\hbar\omega_{2k_F}} = g' n(\epsilon_F) \quad . \tag{2.25b}$$

$T_{CDW}^{MF}$ defines the transition temperature according to *Mean Field Theory* for which a frozen-in distortion occurs. $\lambda$ denotes the dimensionless electron-phonon coupling constant. The phonon softening at different temperatures is shown in Figure 2.3d. For $T \gg T_{CDW}^{MF}$ the logarithmic divergence of the Lindhard response function is smeared-out and the ordinary acoustic phonon dispersion is obtained. When T approaches $T_{CDW}^{MF}$, a dip in the acoustic phonon spectrum occurs at $|\vec{q}| = 2k_F$ with vanishing phonon frequency at $T = T_{CDW}^{MF}$. A frozen-in distortion at $|\vec{q}| = 2k_F$ corresponds to a macroscopically occupied phonon mode since no energy is required for an excitation. The new periodicity of the charge density and the lattice also has significant impact on the electronic ground state of the crystal.

Figure 2.3e illustrates the band structure of a linear chain of atoms with lattice constant $c$ each contributing 2/3 of an electron to the conduction band, resulting in occupation of states up to the Fermi wave vector $k_F = \pi/3c$ at one third of the bandwidth. This represents the situation for the investigated $(DCNQI)_2Cu$ compound at RT. The charge density is equally distributed over the lattice and the system exhibits a metallic ground state. A static distortion of the lattice by the wave vector $|\vec{q}| = 2k_F$, as indicated in Figure 2.3f, corresponds to a modulation of atomic positions with periodicity $\lambda = 2\pi/2k_F = 3c$, meaning that a trimerization of the lattice takes place. The new lattice constant $3c$ results in a back-folding of the Brillouin zone. The new Brillouin zone edge is now located directly at the Fermi wave vector $k_F$, giving rise to an energy gap $2\Delta$ at the Fermi energy, thereby causing an insulating or semiconducting ground state. The lattice distortion is accompanied by a periodic modulation of the charge density. In the case of similar periodicity to the underlying lattice it is denoted a *commensurate Charge-Density-Wave* [58].

### Spin-Peierls Transition

Similar to the electronic degrees of freedom in a CDW, the coupling of spin excitations to the lattice may result in a ground state of lower total energy. The Hamiltonian of a 1D magnetic Heisenberg chain with alternating exchange interaction $J$ reads [59]

$$\mathcal{H} = -J \sum_{i}^{N/2} \left( \vec{S}_{2i} \vec{S}_{2i-1} + \alpha_J \vec{S}_{2i} \vec{S}_{2i+1} \right) \quad , \tag{2.26}$$

with the spin vector $\vec{S}_i$ at site $i$ and the parameter $\alpha_J = J_2/J_1$ defining the relative strength of the exchange interaction between alternating lattice sites. Negative $J$ portray an antiferromagnetic behavior which will be exemplary assumed in the following.

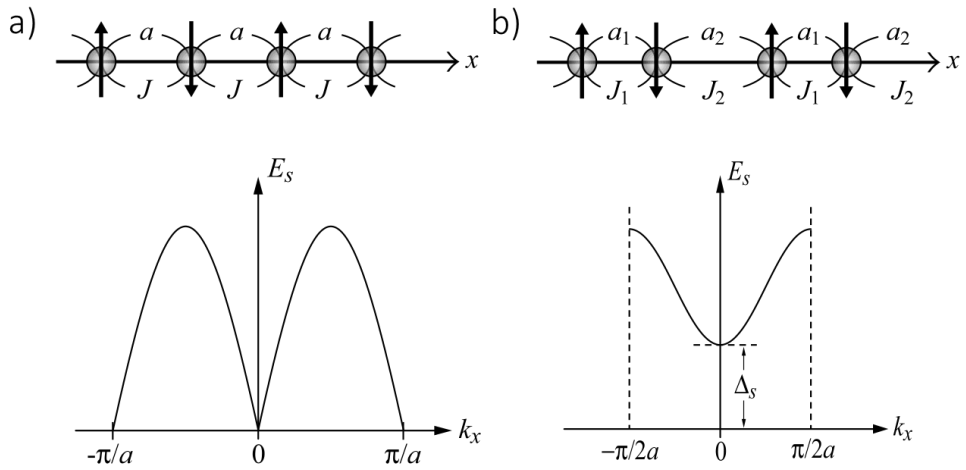


Figure 2.4: Mechanism of the spin-Peierls transition. (a) For a uniform antiferromagnetic Heisenberg chain the spin excitation spectrum appears to be gapless. (b) A dimerization of the lattice alternates the exchange interaction strength $J_i$ between adjacent lattice sites leading to a gap $\Delta_S$ in the magnetic excitation spectrum which compensates for the elastic energy cost of the lattice distortion. From: [7]

For a uniform antiferromagnetic Heisenberg chain the exchange energy is homogeneous ($J_1 = J_2 \rightarrow \alpha = 1$). It is illustrated in Fig. 2.4a together with its magnetic excitation spectrum. The spin is alternating between equally spaced lattice sites and the excitation spectrum is gapless at zero energy. Even in the zero temperature limit, this gives rise to non-vanishing susceptibility by virtue of low-energy spin excitations with $S = 1/2$, so-called spinons [7]. A dimerization of the lattice will alternate the exchange interaction along the chain ($\alpha < 1$) as clarified in Fig. 2.4b. The resulting excitation spectrum reveals a gap $\Delta_S$ at zero energy hindering spin excitations to take place. The gain in magnetic energy can compensate for the elastic energy cost of the $2k_F$ lattice distortion resulting in a ground state of lowered total energy. In analogy to the electron-hole paring of the CDW transition, the pairing of spins together with the $2k_F$ lattice distortion is called *spin-Peierls (sP) transition*. The spin gap $\Delta_S$ separates the non-magnetic singlet ground state ($S = 0$) from the triplet excited state with $S = 1$. Hence, the transition is accompanied by a decrease in the magnetic susceptibility of the chain.

### 2.2.2 Ground States in Correlated Metals

In three-dimensional electron gases, charge carriers are often treated as free quasiparticles and their Coulomb correlation is neglected compared to the interaction with the lattice ions and phonons. Upon reducing the dimensionality, their mutual interaction may however not only increase the scattering of electrons but also may unfold new electronic ground states. This part illuminates possible metal-insulator transitions emanating from electronic correlation in low-dimensional conductors.

#### Mott Transition

Already in the 1930s, the semiconducting behavior of metal oxides with partially filled 3d bands was discussed in terms of electronic correlations by Mott [60, 61]. In 1963, Hubbard developed a simple model to incorporate these effects into the traditional band theory [62]:

$$\mathcal{H} = -t \sum_{<ij>,\sigma} \left( a_{i\sigma}^{\dagger} a_{j\sigma} + h.c. \right) + U \sum_{i} n_{i\uparrow} n_{i\downarrow} \quad . \tag{2.27}$$

Here, $<ij>$ denotes the summation over all nearest neighbor pairs $i$ and $j$, $\sigma$ is the spin index and $n_i = a_i^{\dagger} a_i$ the number operator. The first term accounts for the kinetic energy similar to Eq. 2.20 with the hopping integral $t$ determined by the orbital overlap between lattice sites. The on-site energy $U$, sometimes referred to as *Hubbard* $U$, quantifies the energy cost for two electrons to occupy the same lattice site due to the Coulomb repulsion of charge carriers. The meaning of $t$ and $U$ is exemplified in Fig. 2.5a.

The relevance of electronic correlation manifests in the relative strength of $U$ and $t$. It is intuitive to take a look at the two limiting cases for a half-filled energy band: First of all, for $U/t \ll 1$, the Hubbard term may be neglected and Eq. 2.27 corresponds to a simple band model resulting in a band of width $W = 4t$ being half-filled. In this limit, a metallic ground state will be established. In the opposite limit, i.e. for $U/t \gg 1$, the energy cost for an electron to hop onto an occupied lattice site is large and electrons tend to equally distribute and localize on the lattice sites. The band splits up into an upper and lower Hubbard band (see Fig. 2.5b) and no spectral weight is left at the Fermi energy. Hence, such a material exhibits an insulating ground state, often called Mott-Hubbard insulator. The bandgap equals the Hubbard $U$ being the energy required to add an additional electron to the chain of singly occupied lattice sites. A typical phase diagram of Mott insulators, exhibiting $U/t \approx 1$, is depicted in Fig. 2.5c. The ground state can be tuned by the relative interaction strength as well as by the band filling, both of which may be functions of temperature, pressure and chemical or field-induced doping. A band filling of 1/2, featuring the smallest critical $U/t$ value, most easily enables a Mott

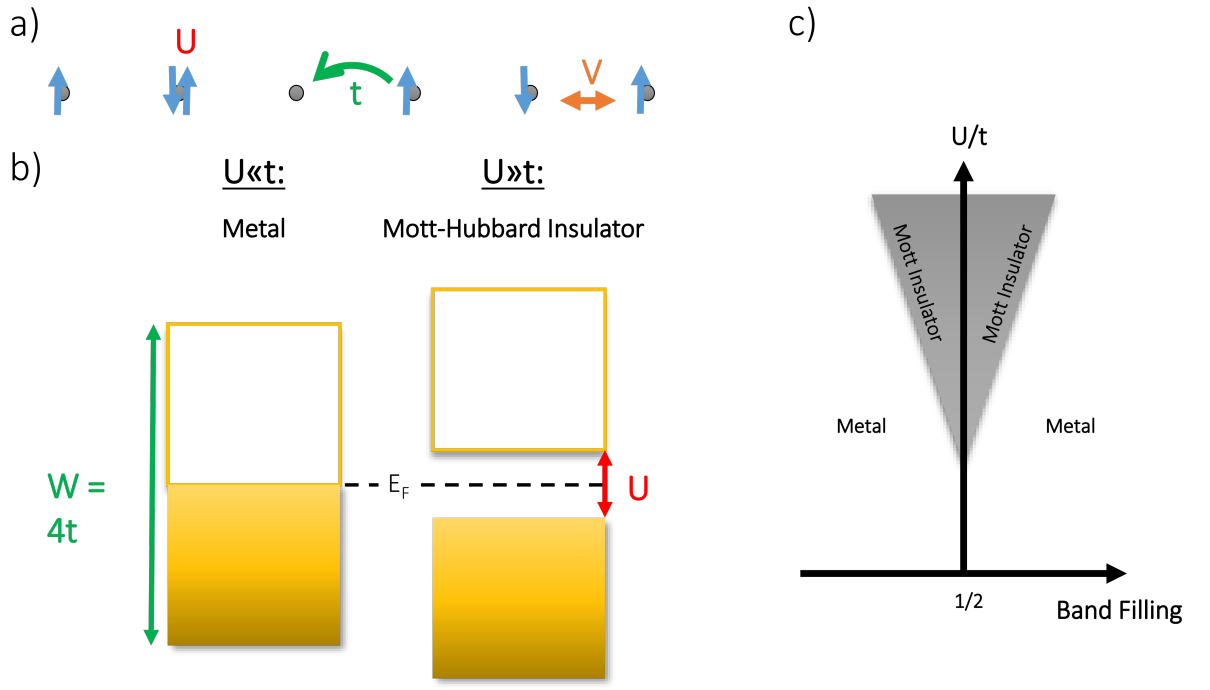


Figure 2.5: Theory of the Mott insulator. (a) 1D Hubbard chain: The Hubbard model is characterized by the hopping integral $t$ as well as the on-site Coulomb repulsion $U$. The extended Hubbard model also includes the nearest-neighbor intersite interaction $V$. (b) Two extreme limits of the Hubbard model for a half-filled band: Negligible on-site Coulomb repulsion establishes an ordinary metallic ground state while in the opposite limit, a bandgap of magnitude $U$ is formed removing the spectral density at the Fermi energy, i.e. the material becomes insulating. (c) Typical phase diagram of a Mott-Hubbard insulator: A transition between metallic and insulating states may be tuned by band filling and relative interaction strength.

insulating ground state. In the following, the influence of additional nearest neighbor Coulomb interactions on quarter-filled band systems will be discussed.

### $4k_F$-Charge-Density-Wave Transition

The Mott insulating state is established for materials with half-filled bands in the strong $U$-limit. In contrast, a quarter-filled band, corresponding to one charge-carrier per two lattice sites, should reveal metallic behavior even in the case of a considerably large Hubbard $U$, because charge carriers are able to hop onto the available free lattice sites. However, in some cases not only the short-range Coulomb repulsion of electrons on the same lattice site has to be taken into account, but even neighboring electrons repel each other to a sufficient amount. The extended-Hubbard model accounts for the nearest-neighbor interaction $V$ as well as the degree of lattice dimerization $\Delta_d$ by [7]:

$$\mathcal{H} = \sum_{<ij>,\sigma} \left( -t[1 + (-1)^i \Delta_d] a^\dagger_{i\sigma} a_{j\sigma} + h.c. \right) + U \sum_i n_{i\uparrow} n_{i\downarrow} + V \sum_i n_i n_{i+1} \quad . \tag{2.28}$$

Fig. 2.6a illustrates the effect of $V$ for a quarter-filled 1D-chain. Neglecting dimerization, for $V/t \geq 1$ the nearest-neighbor interaction inhibits a hopping of charge-carriers to free lattice sites. The electrons will stay apart from each other and distribute equidistantly among the available lattice sites. The charge density will be modulated with the periodicity $\lambda = 2a$ relative to the lattice constant $a$. With the Fermi wave vector $k_F = \pi/(4a)$ of a quarter-filled band, this corresponds to a periodicity of $q = 2\pi/\lambda = \pi/a = 4k_F$ in terms of the Fermi wave vector [59]. Accordingly, the ground state is a $4k_F$-CDW but it is also often denoted *Wigner crystal* as well as *charge-disproportionate (CP)* or *charge-ordered (CO) state* [63].

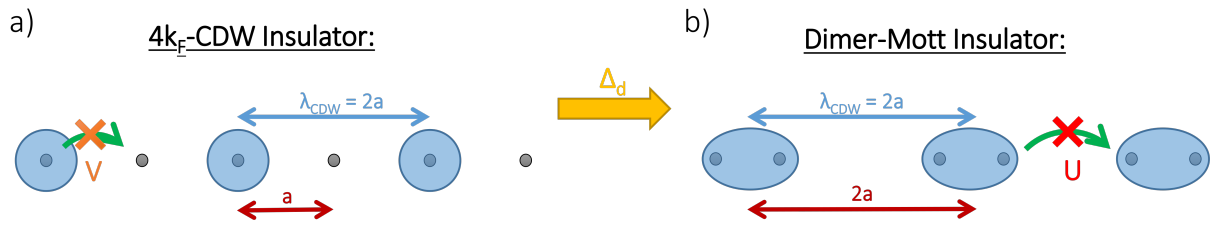


Figure 2.6: $4k_F$-Charge-Density-Wave transition. (a) Charge-ordered state formed due to nearest-neighbor Coulomb interactions inhibiting the hopping of charge carriers. The blue-shaded area corresponds to electrons occupying a lattice site (gray dots). (b) Upon dimerization charges are localized in between two dimerized atoms. For the effectively half-filled band, a Mott insulator is formed due to the on-site Coulomb interaction $U$.

For some lattices it is energetically favorable to dimerize at quarter-filling. The effect of dimerization on the ground state is captured in Fig. 2.6b. The dimerization doubles the unit cell of the crystal which back-folds the Brillouin zone similarly to the Peierls transition discussed above, i.e. the resulting sub-bands are now effectively half-filled instead of quarter-filled. Charges localize in the bound state of the dimerized atoms but their ability to move to the next dimer is limited by the on-site Coulomb repulsion, as discussed for the Mott-Hubbard insulator in the case of half band filling. Hence, this type of ground state is called dimer-Mott insulator [63]. Although going along with a lattice distortion as well, the insulating behavior is caused by the on-site electron repulsion at one dimer site in contrast to the electron-phonon coupling leading to the Peierls transition described above.

## 2.3 Organic Metals Exemplified by $(DCNQI)_2M$ Radical Anion Salts

*Organic charge transfer salts* are composed of two organic compounds which exchange charges when forming a crystal. If only one of the building blocks is organic one refers to *radical ion salts*. Together, both systems constitute the class of *organic metals* or *organic conductors* by virtue of their extraordinary high electrical conductivity of up to $10^4\,\mathrm{S\,cm^{-1}}$ at RT [64]. Below, distinct properties of these materials are presented with special emphasis on $(DCNQI)_2M$ (M=Cu, Li) radical anion salts following the theory section of my diploma thesis [65].

### 2.3.1 Structural Properties

#### Crystal Binding

Molecular crystals usually consist of organic building blocks weakly bound by van-der-Waals or static dipole interactions [58]. A different class of organic crystals, providing much higher electrical conductivities, are charge transfer (CT) salts. In these crystals, molecules often arrange in parallel, spatially adjacent stacks by reason of ionic interactions and the mutual charge transfer may create mobile, delocalized charge carriers facilitating high electrical conductivity. A charge transfer salt consists of an electron donor $D_m$ with a low ionization energy $I_0$ and an acceptor molecule $X_n$ with a high electron affinity $A$, energetically favoring a fractional or even integer charge transfer from the donor to the acceptor [7]:

$$[D_m] + [X_n] \rightarrow [D_m]^{\delta} + [X_n]^{-\delta} \quad . \tag{2.29}$$

Here $m$ and $n$ are integers and $\delta$ denotes the charge transfer ratio. This charge transfer results in a potential energy gain of

$$\Delta E = I_0 - A - C < 0 \tag{2.30}$$

where $C$ accounts for Coulomb, polarization and exchange energy contributions. The mean number of mobile charges is governed by the charge transfer from the donor to the acceptor and hence, is almost temperature-independent. Figure 2.7a shows the disubstituted 2,5-Dicyanoquinonediimine ($R_1$,$R_2$-DCNQI) molecule. This compound is very similar to the electron acceptor Tetracyanoquinondimethane (TCNQ) and also consists of a quinone ring but with only two instead of four cyano groups attached to it. In addition, two functional groups $R_i$ may be linked to the ring. In this work three variations of

the DCNQI molecule have been utilized. The molecule containing two functional methyl groups ($CH_3$), from now on referred to as DCNQI-$h_8$ or DMe-DCNQI, and its deuterated analogue ($CD_3$) from now being referred to as DCNQI-$d_6$. Both molecules have similar electronic properties but the deuterated methyl groups are slightly less bulky compared to $CH_3$ [10]. Substituting one of the methyl groups by a bromine atom withdraws electron density from the $\pi$-system of the molecule. Thereby, MeBr-DCNQI changes its alignment and charge transfer in a crystal by a small amount compared to DMe-DCNQI [66].

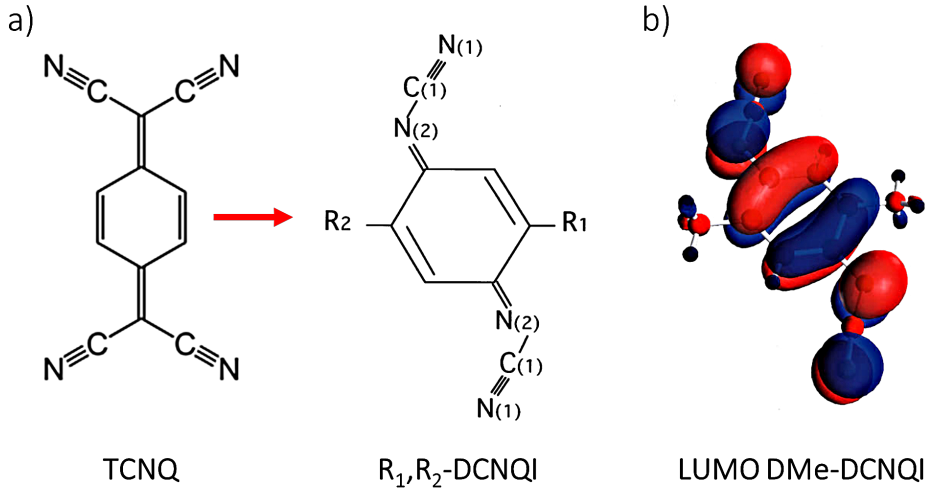


Figure 2.7: Chemical structure and LUMO of the DCNQI molecule. (a) The DCNQI molecule consists of one quinone ring with two cyano groups attached. The two functional groups $R_i$ are directly conjugated to the ring. (b) Calculated LUMO of the DMe-DCNQI molecule: The cyano groups show a high density of unoccupied states making the molecule a good electron acceptor. Adapted from: [67]

Figure 2.7b illustrates that the LUMO of the DMe-DCNQI molecule is $\pi$-conjugated. The high density of unoccupied states located on the cyano groups yields good acceptor qualities. Charges transferred to the molecule are weakly bound and thus, delocalize over the whole molecule. In combination with copper, DCNQI forms a radical anion salt $(DCNQI)_2Cu$ of 1:2 stoichiometry [9]. The copper atoms in the crystal have a valency of $\delta = +4/3$ resulting in an average DCNQI valence of $-2/3$ per DCNQI molecule [68]. The ionization energy of elementary copper amounts to $I_0 = 7.73\,\mathrm{eV}$ [69] and the LUMO energy level of DMe-DCNQI is located at $E_{LUMO} = 2.42\,\mathrm{eV}$ [70]. The relevant Coulomb energy contribution $C$ is rather difficult to calculate due to the extension of the molecule and the delocalization of transferred charges, i.e. its metallic character. Hence, the point charge model employed to estimate the Madelung energy of simple ionic salts, such as NaCl, is not applicable anymore. The DCNQI molecule also forms the radical anion salt $(DCNQI)_2Li$ where the valence electron of lithium is transferred to two DCNQI molecules, each charged by $-1/2\,\mathrm{e}$.

### Crystal Structure

In order to create highly conducting molecular solids, not only a sufficient number of mobile charge carriers on the molecule is necessary, but also a delocalization along certain crystallographic directions is inevitable. Figure 2.8 shows the crystal structure of $(DCNQI)_2Cu$. The material crystallizes in space group $I4_1/a$ (space group No. 88) [68] which constitutes a tetragonal dipyramidal crystal system with a basal squared unit cell ($|\vec{a}| = |\vec{b}|$) of height $|\vec{c}|$. The copper atoms and the DCNQI molecules arrange in spatially separated, parallel stacks giving rise to highly anisotropic electronic properties. Lined up on a chain, the copper atoms are nearly tetrahedrally coordinated by one of the cyano groups belonging to the respective four adjacent DCNQI molecules. The almost planar DCNQI molecules are packed face-to-face with an intermolecular distance of $d_{\pi-\pi} = 3.213\,\text{Å}$ [66] allowing for a substantial overlap of the $\pi^*$-LUMO orbitals.

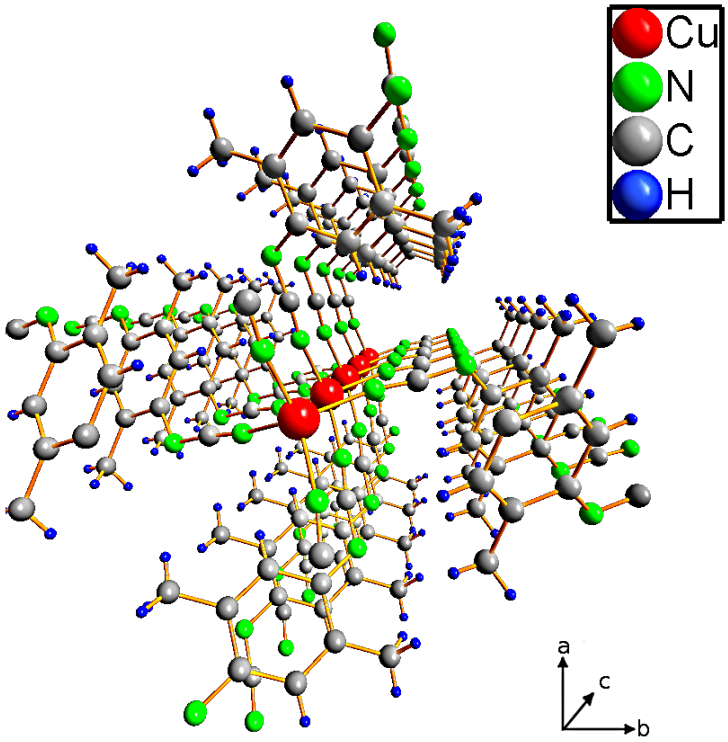


Figure 2.8: Crystal structure of $(DCNQI)_2Cu$ perspectively viewed along the direction of high conductivity, *viz.* the crystallographic $\vec{c}$-axis. With data from: [66]

Table 2.1 specifies the structural properties of several $(DCNQI)_2M$ crystals at different temperatures. All of the systems crystallize in the same space group with slightly different lattice constants and coordination angles $\alpha_{co}$ of the DCNQI molecule around the metal ion. As will be outlined below, $\alpha_{co}$ is an important parameter with respect to the dimensionality and the electronic ground state of the $(DCNQI)_2Cu$ system. Upon cooling

it increases more significantly for the deuterated (DCNQI-$d_6$)$_2$Cu crystal compared to the undeuterated compound. Even more drastic is the change in $\alpha_{co}$ when just one methyl group is replaced by bromine. In (DCNQI)$_2$Li, lithium atoms replace the copper atoms in the lattice yielding similar lattice constants. This enables the synthesis of a miscible, crystalline (DCNQI)$_2$Cu$_x$Li$_{1-x}$ alloy where copper and lithium atoms occupy equivalent lattice sites and only a minimum distortion of the unit cell is introduced.

| radical anion salt | T [K] | $\|\vec{a}\|$[Å] | $\|\vec{c}\|$[Å] | $V_{unit}$ [Å$^3$] | coord. angle $\alpha_{co}$[°] | Ref. |
|---|---|---|---|---|---|---|
| (DCNQI-$h_8$)$_2$Cu | 300 | 21.606 | 3.8811 | 1811.7 | 124.8 | [66] |
| (DCNQI-$h_8$)$_2$Cu | 20 | 21.654 | 3.792 | 1778.0 | 126.3 | [66] |
| (DCNQI-$d_6$)$_2$Cu | 300 | 21.619 | 3.8744 | 1810.8 | 124.8 | [66] |
| (DCNQI-$d_6$)$_2$Cu | 20 | 21.693 | 3.776 | 1776.7 | 128.5 | [66] |
| (MeBr-DCNQI)$_2$Cu | 300 | 21.606 | 3.856 | 1799.2 | 125.5 | [71] |
| (MeBr-DCNQI)$_2$Cu | 100 | 21.627 | 3.780 | 1768.0 | 128.2 | [71] |
| (DCNQI-$h_8$)$_2$Li | 300 | 21.830 | 3.832 | 1826.1 | | [72] |

Table 2.1: Structural data of (DCNQI)$_2$M crystals at different temperatures: The coordination angle $\alpha_{co}$ (see Figure 2.9e) increases more in (MeBr-DCNQI)$_2$Cu and (DCNQI-$d_6$)$_2$Cu than in (DCNQI-$h_8$)$_2$Cu upon cooling. (DCNQI)$_2$Li has a crystal structure similar to that of (DCNQI)$_2$Cu.

According to the volume of the unit cell $V_{unit}$ (see Table 2.1), the transferred charge of $\delta/2 = -2/3\,\mathrm{e}$ residing on each DCNQI molecule, the density of $Z = 8$ DCNQI molecules per unit cell and by assuming transport only along the molecular stacks, the mobile charge carrier density in the conduction band can be estimated to

$$n = \frac{Z \cdot \frac{\delta}{2}}{V_{unit}} = \frac{8 \cdot \frac{2}{3}}{1811.7\mathring{A}^3} = 2.94 \times 10^{21}\,\mathrm{cm}^{-3} \tag{2.31}$$

which is about one order of magnitude lower than for copper ($n_{Cu} = 8.5 \times 10^{22}\,\mathrm{cm}^{-3}$ [73]) but still very high compared to e.g. neat polyaromatic hydrocarbons. For comparison, the theoretical intrinsic charge carrier density for an organic semiconductor with a typical bandgap of 2.5 eV amounts about $n_{int} = N_0 \cdot e^{-E_g/(2k_BT)} = 1\,\mathrm{cm}^{-3}$ at RT, taking $N_0 = 10^{21}\,\mathrm{cm}^{-3}$. It is about ten orders of magnitude smaller than in Silicon [74]. Such ultra-low values are not achieved in real molecular crystals where the charge carrier density is limited by impurities [58]. As already pointed out, in addition to free charge carriers a large orbital overlap is required to obtain a highly conducting solid. Hence, the electronic band structure of (DCNQI)$_2$M crystals will be discussed next.

### 2.3.2 Electronic Properties

#### Band Structure

Since $(DCNQI)_2M$ radical anion salts form densely packed crystals, the mobility of the charge carriers is determined by the overlap of adjacent molecular orbitals rather than by intramolecular delocalization like in polyacetylen [75] and thus, a band structure is formed [7]. To understand the electronic properties and therewith the charge carrier transport, it is necessary to calculate the band structure of the CT salts. Similar results have been obtained for the $(DCNQI)_2M$ system by *tight binding* methods [10] as well as *ab-initio* calculations [67], the latter are being presented here.

The band structure of $(DMe\text{-}DCNQI)_2Cu$ is depicted in Fig. 2.9a and shows its anisotropic character caused by the larger overlap of $\pi$-orbitals along the stacking direction compared to the perpendicular axes. The bandwidth along the $\Gamma$-Z direction, corresponding to the stacking direction $\vec{c}$ of the crystal structure, amounts to $W_{ab} \approx 1\,\mathrm{eV}$. The bandwidth calculated by a tight-binding model yielded slightly smaller values of $W_{tb} = 792\,\mathrm{meV}$ [10]. The band structure also reveals a significant dispersion along the transverse $\Gamma$-X/Y directions of about 250 meV characterizing $(DMe\text{-}DCNQI)_2Cu$ as an anisotropic organic metal with pronounced three-dimensionality (quasi-3D). As a consequence, the material is resistant to metal-insulator transitions - as typical for low-dimensional conductors - down to lowest temperatures of 50 mK [76]. The three-dimensionality can be understood from the 3d copper orbitals energetically located between the HOMO and the LUMO bands of the DCNQI molecule. These orbitals hybridize with the DCNQI p$\pi$-bands and contribute significantly to the density of states at the Fermi level. Two of the LUMO bands are almost degenerate and can be regarded as purely one-dimensional. They are also obtained in the tight binding model and result in a flat Fermi surface FS1 as illustrated in Fig. 2.9c. For the other bands the degeneracy is lifted and the hybridized bands disperse along the transverse crystallographic direction. While Fermi surface FS2 still has a dominating one-dimensional character but is slightly corrugated, FS3 is of three-dimensional, hole-like character. Due to the charge transfer of $\delta/2 = -2/3\,\mathrm{e}$ onto each DCNQI molecule, the conduction band is filled-up to one-third since two degenerate spin states are available. Accordingly, a metallic ground state is established. The position of the wave vector corresponding to a thirdly filled LUMO band is indicated by the arrows in Fig. 2.9a.

The $3d_{xy}$-orbitals exhibit the smallest energy difference to the LUMO and accordingly, they supply the largest spectral density of all copper orbitals at the Fermi energy. Their share to the density of states is depicted in Fig. 2.9b. Of major importance for the details

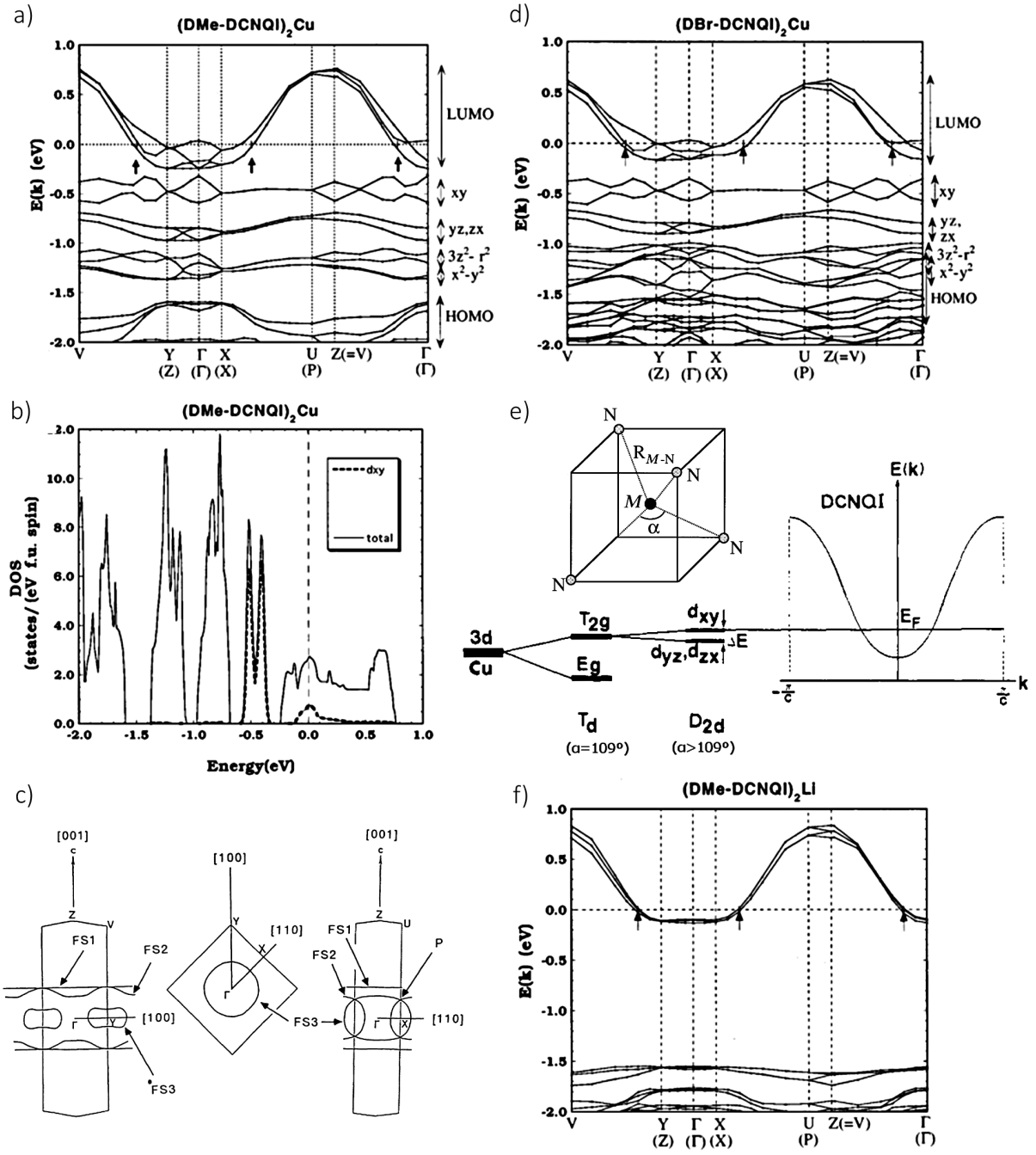


Figure 2.9: Band structure and Fermi surfaces of $(DCNQI)_2M$. (a) Energy bands of $(DMe\text{-}DCNQI)_2Cu$ calculated by *ab-initio* methods together with the (b) projected density of states clarifying the contribution of Cu $3d_{xy}$ orbitals to the density of states at the Fermi level. (c) Corresponding Fermi surfaces (FS): While FS1 is completely flat and thus 1D, FS2 is slightly corrugated due to the LUMO-$3d_{xy}$-interaction and FS3 possesses 3D topology. (d) In the band structure of $(DBr\text{-}DCNQI)_2Cu$ the $3d_{xy}$ orbitals are located at slightly lower energies due to the (e) larger tetrahedral distortion of the coordination angle $\alpha_{co}$ and the resulting smaller $\pi$d-hydridization. (f) Accordingly, the band structure of $(DCNQI)_2Li$ lacking 3d states between HOMO and LUMO is accordingly far more one-dimensional. From: [67, 77, 78].

of the 3d-$\pi$-hybridization in the $(DCNQI)_2Cu$ system is the coordination angle $\alpha_{co}$ of the molecules around the copper atom, as depicted in Fig. 2.9e. In a tetrahedrally coordinated crystal field ($\alpha_{co} = 109°$) the $3d_{xy}$, $3d_{yz}$ and $3d_{zx}$ orbitals are energetically degenerate and contribute the same amount to the density of states at the Fermi energy and also to the charge transfer. A distortion of the tetrahedral coordination angle ($\alpha_{co} > 109°$) lifts this degeneracy and shifts the $3d_{xy}$ energy closer to the LUMO compared to the other two. In $(DMe\text{-}DCNQI)_2Cu$ the value of $\alpha_{co} = 124.8°$ deviates from the ordinary tetrahedral coordination angle, enabling an efficient $3d_{xy}$-$\pi$-hybridization of orbitals. Yet, tight binding calculations pointed out that the hybridization of the other 3d orbitals still plays a key role in the dimensionality of $(DCNQI)_2Cu$ [68].

Upon further increase of $\alpha_{co}$ the $3d_{xy}$-$\pi$-hybridization increases leading to a larger charge transfer. In contrast, the contribution from $3d_{yz}$ and $3d_{zx}$ orbitals may subsequently be neglected and the band structure becomes more one-dimensional and as such, prone to Fermi surface instabilities. It also stabilizes a formal charge of $Cu^{+4/3}$ ($Cu^{+}$-$Cu^{+}$-$Cu^{2+}$) on the copper chain. In $(DBr\text{-}DCNQI)_2Cu$ both methyl groups are replaced by bromine atoms and the coordination angle amounts to $\alpha_{co} = 125.3°$ at room temperature [71]. The band structure at room temperature, as delineated in Fig. 2.9d, is very similar to that of $(DMe\text{-}DCNQI)_2Cu$ but with slightly smaller dispersion along the transverse direction by virtue of the smaller $3d_{zx/yz}$-$\pi$-hybridization. Upon cooling below a temperature of $T_P = 160\,K$, the coordination angle increases and exceeds a critical angle of $\alpha_{co,crit} \approx 126.4°$ above which the hybridization is lifted. Thereby, the system's dimensionality is changed from quasi-3D to quasi-1D [66]. The quasi-1D $(DCNQI)_2Cu$ system has a Peierls insulating ground state due to the thirdly filled band and hence, the material instantly undergoes a Peierls metal-insulator transition. In contrast to the second order metal-insulator transition as predicted by Peierl's theory outlined in Sec. 2.2.1, this transition is of first order due to the discrete modification of dimensionality. The same distortion is obtained by replacing only one of the methyl groups with bromine. $(MeBr\text{-}DCNQI)_2Cu$ crystals investigated in this work undergo a Peierls transition at the critical temperature $T_P = 155\,K$.

Even more subtle, the change in dimensionality can be reached by deuteration of the methyl groups in the DMe-DCNQI molecule. The deuterated DCNQI-$d_6$ molecule is isoelectrical with respect to its undeuterated equivalent. While the crystal lattice parameters of $(DCNQI\text{-}d_6)_2Cu$ at RT are quite similar to those of $(DCNQI\text{-}h_8)_2Cu$, the replacement of methyl groups ($CH_3$) by the deuterated ones ($CD_3$) of higher mass creates an internal pressure which leads to larger changes of $\alpha_{co}$ upon cooling. At 20 K, $\alpha_{co}$ amounts to 128.5° for $(DCNQI\text{-}d_6)_2Cu$ while it only increases to $\alpha_{co} = 126.3°$ for $(DCNQI\text{-}h_8)_2Cu$ [66].

Whereas (DCNQI-$h_8$)$_2$Cu remains metallic down to cryogenic temperatures because of its quasi-three-dimensionality, in (DCNQI-$d_6$)$_2$Cu the overlap between the $3d_{yz/zx}$-orbitals and the LUMO is reduced and the system undergoes a Peierls transition at $T_P \approx 73\,\mathrm{K}$ by virtue of the reduced dimensionality, similar to the case for (DBr-DCNQI)$_2$Cu [66].

It is also interesting to compare the band structure of (DCNQI)$_2$Cu with that of (DCNQI)$_2$Li illustrated in Fig. 2.9f. This material crystallizes in a similar structure as its copper equivalent and as a consequence, the resulting LUMO bands along the Γ-Z direction reveal a similar width and shape as the ones in Fig. 2.9a. However, the lack of 3d valence states at the lithium counterion prohibits a hybridization of Li orbitals with the LUMO of the DCNQI molecule and accordingly, a flat dispersion in the transverse direction is obtained. Due to the smaller charge transfer in (DCNQI)$_2$Li, the LUMO band is only quarterly filled and as a result, the ground state of the system is a $4k_F$ Wigner crystal undergoing a spin-Peierls transition at about $T_{sP} = 60\,\mathrm{K}$ [79] (compare Sec. 2.2.2). The pronounced one-dimensional character of the material manifests itself in stronger electronic correlation effects as well as a higher anisotropy of the conductivity.

### 2.3.3 Phase Diagrams of (DCNQI)$_2$M salts

#### Phase Diagram of (DCNQI)$_2$Cu

In the previous sections the influence of different substituents at the quinone ring of the DCNQI entity on the electronic and crystallographic structure of (DCNQI)$_2$Cu has been discussed. Based on these findings, the phase diagram of (DCNQI)$_2$Cu as illustrated in Fig. 2.10d can be understood. In principle, three different ground states are known for the variety of ($R_1$-$R_2$-DCNQI)$_2$Cu compounds: a metallic, a Peierls (CDW) insulating and an antiferromagnetic ground state. The latter only plays a role below 8 K and will not be discussed in detail here [80]. At RT and ambient pressure, (DCNQI)$_2$Cu salts are metallic with decreasing electrical resistivity upon cooling. Depending on the change of the coordination angle $\alpha_{co}$ upon cooling (see Fig. 2.10e), they can be categorized into three groups [78]:

- Group I salts stay metallic down to at least 50 mK with a coordination angle $\alpha_{co} \leq 126.3°$ over the whole temperature regime, i.e. they keep their quasi-3D electronic structure. One representative of this group is the undeuterated (DMe-DCNQI)$_2$Cu (also often denominated (DCNQI-$h_8$)$_2$Cu) for which the resistivity is depicted in Fig. 2.10a-b.

- Group II salts exhibit a Peierls metal-insulator transition as the coordination angle approaches a critical value of $\alpha_{co,crit} = 126.3°$. Due to accompanying lattice distor-

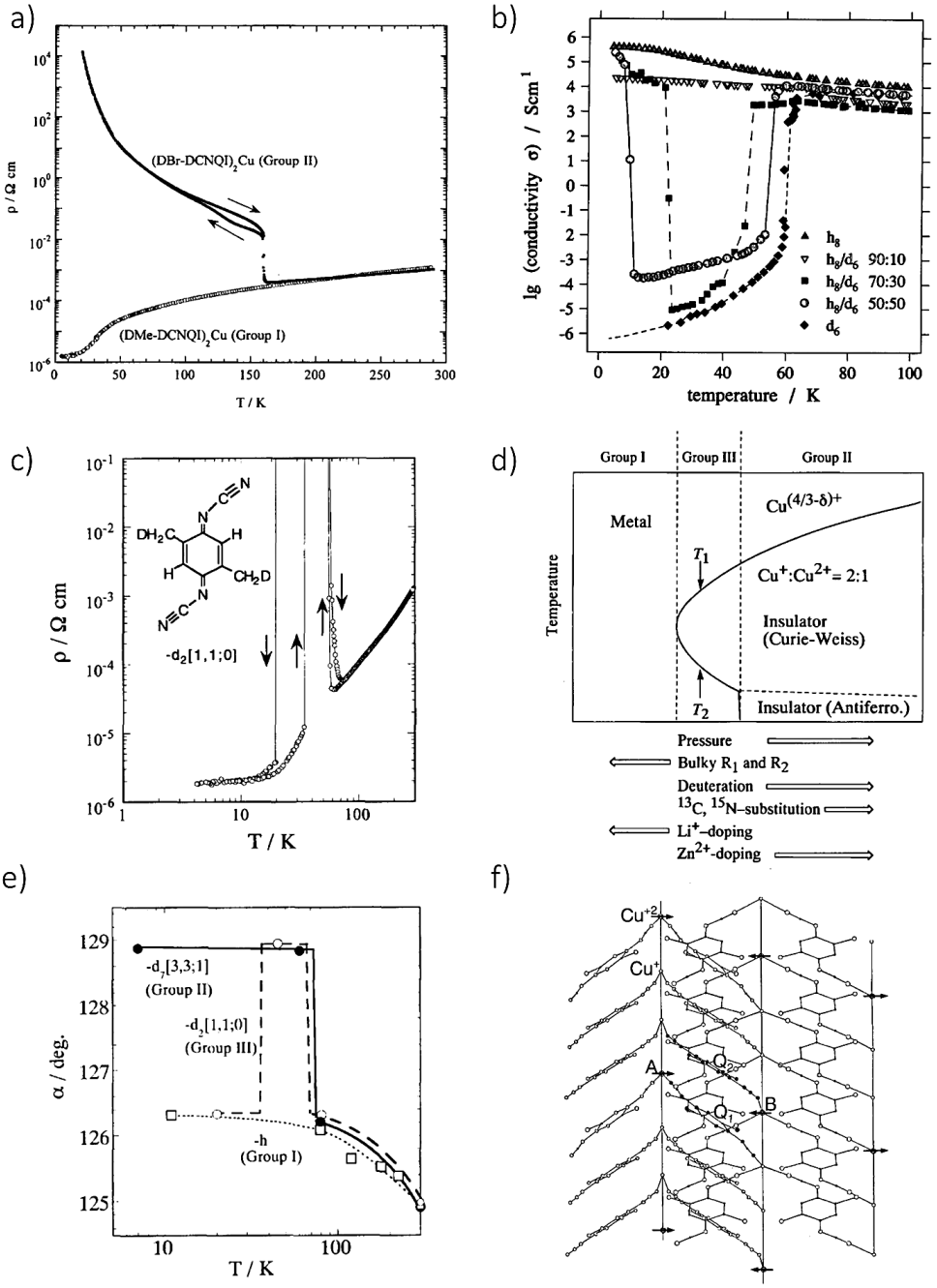


Figure 2.10: Phase diagram of the $(DCNQI)_2Cu$ system. (a) Representative resistivity curves for the $(DCNQI)_2Cu$ salts of group I and group II, resembling a metallic and a CDW ground state, respectively. The (b) conductivity of group I salt $(DCNQI\text{-}h_8)_2Cu$ reveals a metallic behavior down to lowest temperature but a metal-insulator transition can be induced by deuteration of the methyl group, as in $(DCNQI\text{-}d_6)_2Cu$ which belongs to group II. The alloy $(DCNQI\text{-}h_8/d_6)_2Cu$ [70:30] undergoes a Peierls transition but recovers its metallic state by a low-temperature re-entry transition typical for group III salts. (c) A similar re-entry transition is also observed for $(DMe\text{-}DCNQI)_2Cu$ crystals with smaller degree of deuteration, e.g. $(DCNQI\text{-}d_2)_2Cu$. The transition occurs with hysteresis upon heating. (d) Phase diagram of the $(DCNQI)_2Cu$ compounds: the position in the phase diagram can be tuned by the choice of the substituents, isotopes, pressure and counter ion doping. This mainly influences the (e) coordination angle $\alpha_{co}$ being crucial for the respective ground state. In the insulating Peierls state, not only a trimerization along the DCNQI stack occurs but also a (f) charge ordering on the copper chain takes place leading to localized $Cu^{2+}$ spins. From: [78, 81]

tion, the coordination angle shows a sudden increase by almost three degree at the phase transition. By virtue of the drastic dimensionality change, the transition is of first order revealing a jump in the resistivity curve, as depicted for (DBr-DCNQI)$_2$Cu and (DCNQI-d$_6$)$_2$Cu in Fig. 2.10a-b which both belong to the group II salts.

- Group III salts are peculiar in a sense that they undergo a phase transition similar to group II salts but recover their metallic behavior at even lower temperatures. Their coordination angle $\alpha_{co}$ jumps back to the initial value below a critical temperature. The so-called re-entry transition has been observed for crystalline (DCNQI-h$_8$/d$_6$)$_2$Cu alloys, shown in Fig. 2.10b, as well as for partially deuterated crystals, such as (DCNQI-d$_2$)$_2$Cu, depicted in Fig. 2.10c. For the latter compound, the hysteresis of the phase transition occurring between the cooling and the heating cycle is shown in the figure, too. This hysteresis is characteristic for a first-order phase transition.

As illustrated by Fig. 2.10d, the phase transition can be induced by the choice of substituents as well as by external pressure. Tab. 2.2 lists the phase transition temperatures for certain (DCNQI)$_2$Cu salts. The deuteration denoted for the (DCNQI-d$_x$)$_2$Cu salts refers to the methyl groups. The influence of the deuteration has been discussed in terms of an effective chemical pressure deduced from crystal structure data which are also listed [10]. The drastic influence of the coordination angle $\alpha_{co}$ on the system's dimensionality can be understood by X-ray photoemission spectroscopy (XPS) experiments on the respective crystals [82]. The average valence of the copper atom was found to slightly deviate from the expected value of $\delta = +1.33$ at RT, i.e. the charge transfer is reduced according to the order of MeBr- ($\delta = +1.32$) $>$ DMe- ($\delta = +1.28$) $>$ DI-salts ($\delta = +1.22$) and depends on $\alpha_{co}$. At a critical angle of $\alpha_{co,crit} \approx 126.3°$, the charge transfer is expected to lock into the value of $\delta = +1.33$ inducing a $Cu^{2+}$-$Cu^{+}$-$Cu^{+}$ Mott transition on the copper chains and an accompanying CDW transition on the DCNQI stacks stabilized by its commensurability with the underlying lattice. The larger the deviation from the commensurate charge transfer of $\delta = 4/3\,e$, the harder it is to induce the phase transition by applying a pressure or reducing the temperature. For example, the critical pressure required to switch (DI-DCNQI)$_2$Cu into the Peierls ground state is more than two orders of magnitude larger than for (DCNQI-h$_8$)$_2$Cu. The trimerization of the lattice is reflected by the discontinuity of the coordination angle $\alpha_{co}$, as depicted in Fig. 2.10e.

Because the conduction of charge takes place on the DCNQI chains, the CDW transition mainly manifests itself in the resistivity jump. In addition, the $Cu^{2+}$ spins align in the (ab)-plane, as illustrated in Fig. 2.10f. The $Cu^{2+}$ spins can be probed by AC susceptibility measurements and by determining the anisotropic g-factor of the Zeeman splitting

| $(DCNQI)_2Cu$ salt | $T_{M-I}$ | $T_{I-M}$ | $P_{crit}$ | $P_{eff}$ (bar) |
|---|---|---|---|---|
| $(DCNQI\text{-}h_8)_2Cu$ | - | - | 100 bar | 0 |
| $(DCNQI\text{-}d_2)_2Cu$ | 55 K | 21 K | | 160 |
| $(DCNQI\text{-}d_4)_2Cu$ | 61 K | 13 K | | 192 |
| $(DCNQI\text{-}d_6)_2Cu$ | 75 K | - | | 480 |
| $(DCNQI\text{-}d_8)_2Cu$ | 80 K | - | | 512 |
| $(MeBr\text{-}DCNQI)_2Cu$ | 155 K | - | | |
| $(DBr\text{-}DCNQI)_2Cu$ | 160 K | - | | |
| $(DI\text{-}DCNQI)_2Cu$ | - | - | $\approx 15$ kbar | |

Table 2.2: Critical temperatures for the Peierls metal-insulator (M-I) and the re-entry insulator-metal (I-M) transition in different $(DCNQI)_2Cu$ compounds. The critical pressures to induce a phase transition in $(DCNQI\text{-}h_8)_2Cu$ and $(DI\text{-}DCNQI)_2Cu$ as well as the effective chemical pressures induced by deuteration are also cited [78].

by means of electron spin resonance experiments (ESR) [80, 83]. The simultaneous occurrence of two distinct phase transitions on the copper and the DCNQI chains, respectively, has been incorporated into a phenomenological thermodynamic model of the phase diagram by Nishio *et al.*, taking into account the charge, spin and lattice degrees of freedom [34]. By virtue of latent heat ($Q_L$) measurements on selected deuterated $(DCNQI\text{-}d_x)_2Cu$ single crystals with varying Peierls transition temperatures $T_P$, they determined the entropy difference $\Delta\Sigma$ between the metallic and the insulating ground state, revealing a linear relation [34]

$$\Delta\Sigma = \frac{Q_L}{T_P} = \gamma^* T_P - S_I \tag{2.32}$$

where $\gamma^* = 40\,\mathrm{mJ\,mol^{-1}\,K^{-2}}$ and $S_I = (k_B N_A/3)\ln 2 = 1.9\,\mathrm{J\,mol^{-1}\,K^{-1}}$. $S_I$ corresponds to the $Cu^{2+}$ spin degrees of freedom implying a threefold-periodicity of $Cu^{2+}$-$Cu^{+}$-$Cu^{+}$ along the copper chains, i.e. one third of the copper atoms carry an electron spin of $1/2$, in agreement with magnetic susceptibility and ESR results [80, 83]. A similar value was found in the latent heat analysis of the antiferromagnetic transition observed in fully deuterated $(DCNQI\text{-}d_8)_2Cu$ at 6.8 K, clearly identifying it as the spin contribution to the entropy [34]. The value of $\gamma^* = 40\,\mathrm{mJ\,mol^{-1}\,K^{-2}}$ significantly differs from the expected and experimentally determined Sommerfeld coefficient $\gamma_{el} = 25\,\mathrm{mJ\,mol^{-1}\,K^{-2}}$ deduced from low-temperature measurements on the specific heat of $(DMe\text{-}DCNQI)_2Cu$ [34]. It has been argued that an additional contribution $\gamma_{lat}$ by the lattice increases the effective $\gamma^* = \gamma_{el} + \gamma_{lat}$. In general, the lattice entropy is expected to split into a configurational and a vibrational part. The configurational entropy accounts for the change in the lattice symmetry while vibrational contribution quantifies the repopulation of phonons across the insulator-to-metal transition [84].

For a system at constant pressure, the ground state of minimized Gibbs free energy $G = U - T\Sigma + PV$ is established. Considering only the energy difference $\Delta G$ between metallic and insulating state, its total differential is given by [34]:

$$d(\Delta G) = -\Delta\Sigma dT + \Delta V dP \quad . \tag{2.33}$$

At constant pressure the second term is neglected. With the entropy difference $\Delta\Sigma$ given by Eq. 2.32, upon integration one obtains [34]:

$$\Delta G = -\frac{1}{2}\gamma^* T^2 + S_I T + \Delta G_0(P_{eff}) \quad . \tag{2.34}$$

Here, the integration constant $\Delta G_0(P_{eff})$ comprises the external and chemical pressure dependence of the model. A phase transition will occur at temperatures fulfilling the condition $\Delta G(T_p) = 0$, i.e. at a critical temperature of [34]

$$T_p = \left( S_I \pm \sqrt{S_I^2 + 2\gamma^* \Delta G_0} \right) / \gamma^* \quad . \tag{2.35}$$

Depending on the value of the integration constant $\Delta G_0$, three different regimes may be distinguished. For $\Delta G_0 < -S_I^2/2\gamma^*$, Eq. 2.35 has no real solution and $\Delta G$ is negative for all temperatures. This models the case of group I salts remaining metallic over the entire temperature regime. For intermediate negative values of $-S_I^2/2\gamma^* \leq \Delta G_0 \leq 0$, two real solutions are obtained with $T_{P,1} > T_{P,2}$, corresponding to the group III salt behavior where two phase transitions are observed. Two critical temperatures also result from positive $\Delta G_0$ values. However, one of them is negative and hence, without physical relevance. This situation represents the group II salts with one metal-insulator transition. The effect of deuteration is considered by the integration constant $\Delta G_0$ [34]

$$\Delta G_0 = -G_0 + P_{eff}\Delta V \tag{2.36}$$

where $P_{eff}$ characterizes an external or chemical (substituent-induced) pressure. $P_{eff} = 0$ corresponds to the (DCNQI-$h_8$)$_2$Cu crystal at ambient pressure. $\Delta V = 3.2\,\text{Å}^3$ is the volume difference of the unit cell between the metallic and the insulating state [66]. Under these conditions, $G_0$ remains the only free parameter for fitting. To explain the phase diagram qualitatively (see dashed black curve in Fig. 2.11), a value of $G_0 = 59\,\text{J mol}^{-1}$ had to be chosen. The figure also illustrates the phase diagram experimentally determined from the phase transition temperatures of the selected deuterated (DCNQI-$d_x$)$_2$Cu crystals [78]. Releasing the other fit parameters as well, the phase diagram can be reproduced very well with $\gamma^* = 95\,\text{mJ mol}^{-1}\,\text{K}^{-2}$ and $S_I = -3.5\,\text{J mol}^{-1}\,\text{K}^{-1}$. Both values are even larger than the experimentally determined ones. Still, due to the

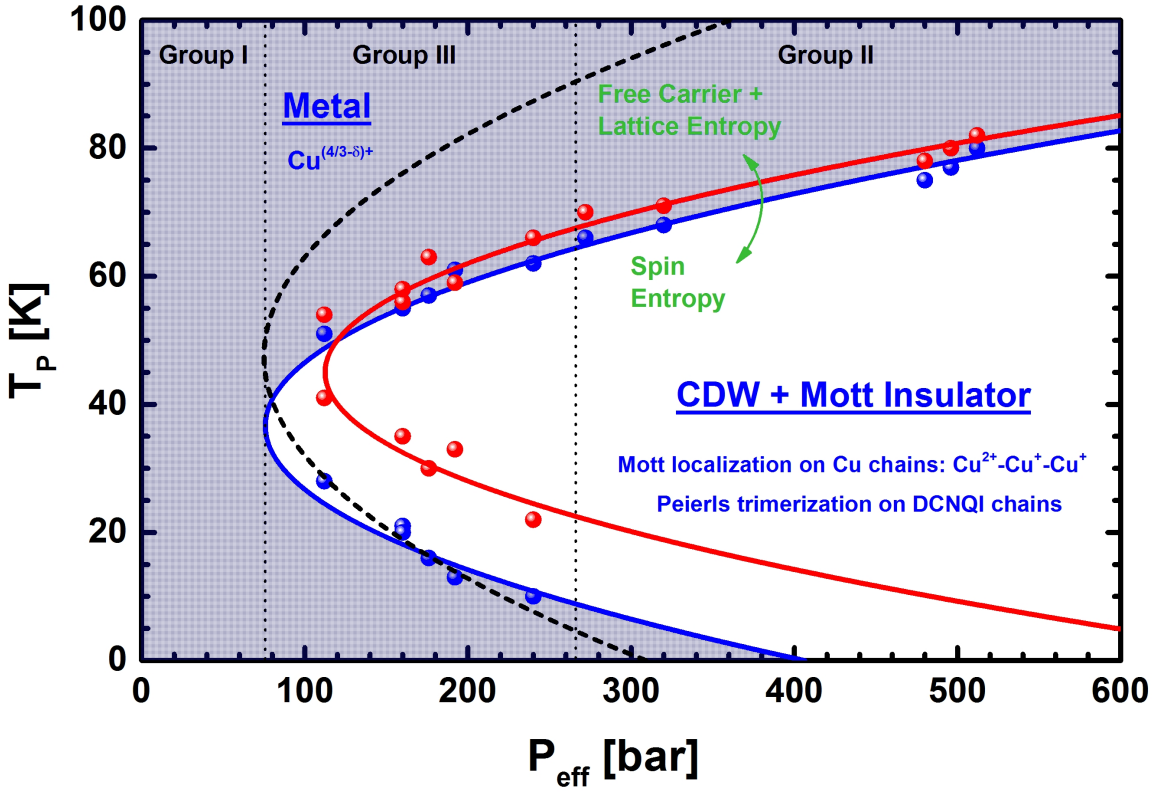


Figure 2.11: Phenomenological phase diagram calculated by the thermodynamic model described in the text [34]. Dotted vertical lines separate the three groups of $(DCNQI)_2Cu$ salts. The diagram was determined from the phase transition temperatures of selected deuterated $(DCNQI\text{-}d_x)_2Cu$ upon cooling (blue) and heating (red) together with the one calculated by combining Eqs. 2.36 and 2.35 (dashed black curve). Taking $G_0$ as the only free fit parameter, the phase diagram can be reproduced qualitatively. A better agreement between calculation and experimental data can be obtained from polynomial fits (blue and red curves) according to Eq. 2.35, revealing a slightly larger $\gamma^*$. The model explains the phase diagram on the basis of the competion between the spin entropy of localized $Cu^{2+}$ spins and the entropy of free charge carriers while large $\gamma^*$ values point to other degrees of freedom playing a certain role as well. These might be the configurational and vibrational entropy of the lattice.

ambiguity in the determination of the effective pressure values, it is not possible to directly draw conclusions from these quantitative $\gamma^*$- and $S_I$-values.

To sum up, the phase diagram of $(DCNQI)_2Cu$ can be well explained by the dependence of the Cu valency on the coordination angle $\alpha_{co}$. A transition between metallic and insulating state, characterized by a CDW on the DCNQI chains accompanied by a Mott charge ordering on the Cu sites, occurs upon reaching a critical $\alpha_{co,crit}$, enabling commensurate conditions for the CDW transition. Thermodynamically, the phase transition is mainly driven by the competition between spin and charge degrees of freedom while contributions by the lattice are expected to be relevant as well [34].

### Phase Diagram of $(DCNQI)_2Li$

In spite of the similar crystal structure as compared to $(DCNQI)_2Cu$, the charge transfer in $(DCNQI)_2Li$ only amounts to $\delta/2 = 0.5\,e$ due to the lack of 3d valence states leaving the one-dimensional band quarter-filled [85]. Mazumdar and Bloch showed that the effective short range Coulomb interaction in organic conductors strongly depends on the band filling [86]. While being negligible at a charge transfer of $\delta/2 = 0.66\,e$, as observed in $(DCNQI)_2Cu$, it gains importance below $\delta/2 = 0.55\,e$. This is corroborated by the occurrence of a $4k_F$-CDW at $T_{4k_F} \approx 100\,K$ in the isostructural organic conductor $(DCNQI)_2Ag$ which also reveals a charge transfer of $\delta/2 = 0.5\,e$, giving rise to a quarter-filled one-dimensional band structure [87]. At an even lower temperature of $T_{sP} = 83\,K$ the occurrence of a $2k_F$ spin-Peierls transition was observed. As discussed in Ch. 2.2.2, both ground states are driven by the Coulomb repulsion of charge carriers. The spin-Peierls transition was also observed in $(DCNQI)_2Li$ at $T_{sP} = 52\,K - 63\,K$ [88, 89] and accordingly, electronic correlation effects are expected to be of importance in this material as well. Raman spectroscopy and the linewidth analysis of ESR signals furthermore support the existence of a $4k_F$-CDW even far above $T_{sP}$ in $(DCNQI)_2Li$ [90, 91]. In the crystalline $(DMe\text{-}DCNQI)_2Cu_xLi_{1-x}$ alloys, a spin-Peierls transition appears for samples with $x \leq 0.3$ and $T_{sP}$ decreases with increasing copper content [79, 89]. For any copper content above $x > 0.5$ the material remains metallic down to 4 K.

## 2.4 Lattice Dynamics in Crystals

Phonons play an important role in organic crystals due to their lower excitation energies, the large number of atoms per unit cell and the lower Debye temperatures compared to inorganic solids. The low energy relative to the electronic bandwidths along with the strong electron-phonon coupling enables an efficient interaction of charge carriers with phonons. Furthermore, the complex phonon spectra cause distinctively different thermal properties in organic solids. Here, the general theory on phonons will be outlined based on the atomic chain model which is consecutively extended to molecular solids.

### 2.4.1 Phonon Dispersion

Phonons are quantized coupled vibrations of the solid state lattice [92]. They do not occur as isolated, local excitations but represent a collective motion propagating like waves through the solid, transporting energy and interacting with one another as well as other excitations. The vibrational energy of a crystal is defined by its anharmonic interatomic potential as shown in Fig. 2.12a in which atoms can be displaced around their equilibrium position at distance $R_0$ from each other. For small displacements the potential is well approximated by a parabola. This *harmonic approximation* represents the model of atoms joined by springs in a crystal as visualized in Fig. 2.12b for a one-dimensional chain of a diatomic lattice with unit length $2a$.

The displacement of atoms propagates as a linear combination of plane waves through the lattice, each of the form $A\exp[\vec{q}\cdot\vec{r}-\omega(\vec{q})t]$, $\vec{q}$ denoting the wave vector of propagation, $A$ the amplitude and $\omega(\vec{q})$ the angular frequency of the vibration. In the harmonic approximation phonons are treated as non-interacting quasiparticles. Although the propagating wave does not carry a net mass and hence, no momentum, a quasi-momentum $\hbar\vec{q}$ is associated with each phonon of quantized energy $\hbar\omega(\vec{q})$. The lattice dynamics are described by the phonon dispersion $\omega(\vec{q})$ relating energy and quasi-momentum of a phonon. A lattice comprised of $N$ atoms contains $3N$ normal modes of vibration. Similar to the quantum mechanic harmonic oscillator, the energy of the $\vec{q}_{th}$ mode is given by [92]

$$E_{\vec{q}} = \left(n_{\vec{q}} + \frac{1}{2}\right)\hbar\omega_{\vec{q}} \tag{2.37}$$

where the average number of phonons in mode $\vec{q}$ at temperature $T$ is given by the Bose-Einstein distribution in thermal equilibrium [92]:

$$n_{\vec{q}} = \frac{1}{\exp[\hbar\omega(\vec{q})/(k_B T)]-1} \quad . \tag{2.38}$$

The population of phonon modes vanishes at $T=0$, then rises exponentially in the

low-temperature regime $k_B T \ll \hbar\omega$ and approaches a high temperature limit of $n_{\vec{q}} \propto T$ for $k_B T \gg \hbar\omega$.

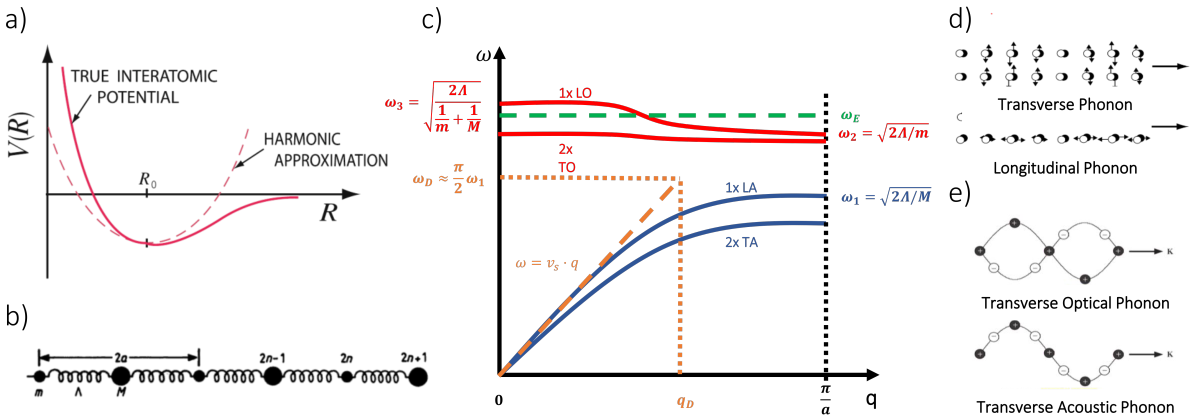


Figure 2.12: Phonons in crystals. (a) Interatomic potential together with its harmonic approximation. (b) The harmonic model of a one-dimensional diatomic lattice chain with its constituents coupled by springs results in a (c) phonon dispersion containing acoustic (blue) and optical (red) phonon branches. Each branch contains one longitudinal phonon mode and two degenerate transverse phonon modes. (d) Transverse phonon modes are characterized by atomic displacements perpendicular to the wave propagation while for longitudinal modes atoms oscillate in the same direction. (e) Acoustic phonon modes are characterized by neighboring atoms moving in-phase in contrast to the out-of-phase displacement of optical phonon modes. Adapted from: [93, 92, 94, 95]

For a characterization of the lattice dynamics the phonon dispersion relationship $\omega(\vec{q})$ needs to be calculated. The dispersion relation of a one-dimensional diatomic chain, as illustrated in Fig. 2.12b with atoms of mass $M > m$ connected by springs of force constant $\Lambda$, reads [92]

$$\omega^2 = \Lambda\left(\frac{1}{m}+\frac{1}{M}\right) \pm \Lambda\sqrt{\left(\frac{1}{m}+\frac{1}{M}\right)^2 - \frac{4}{mM}\sin^2\vec{q}\cdot\vec{a}} \quad . \tag{2.39}$$

It is schematically depicted in Fig. 2.12c for the first Brillouin zone. The phonon dispersion consists of two types of phonon branches, that of the acoustic and of the optical phonons. The longitudinal acoustic (LA) branch starts at zero frequency in the mid of the Brillouin zone and rises proportional to the velocity of sound $\vec{v}_S = \partial\omega/\partial\vec{q}$ at small $\vec{q}$. Its dispersion saturates at a frequency $\omega_1 = \sqrt{2\Lambda/M}$. In contrast, the longitudinal optical (LO) phonon branch starts at non-zero frequency $\omega_3 = \sqrt{2\Lambda/(1/m+1/M)}$ in the mid of the Brillouin zone reducing to $\omega_2 = \sqrt{2\Lambda/m}$ at the boundary $q = \pi/a$. In addition to the longitudinal displacement along the propagation direction, the oscillation of atoms in the other two perpendicular directions are also possible as clarified in Fig. 2.12d. These additional polarizations result in two separate transverse acoustic (TA) and optic (TO) branches which are doubly degenerate each. They are lower in energy due to the smaller force constant $\Lambda' < \Lambda$ for transverse displacements as compared to longitudinal modes.

The difference between acoustic and optical phonon modes is illustrated in Fig. 2.12e. Acoustic modes of propagation displace neighboring atoms along the same direction while in optical phonon modes adjacent atoms oscillate anti-phase-wise. Accordingly, the latter are expected to be higher in energy. In case of ionic crystals, the dynamic dipole moment of optical phonon modes allows for an excitation by electromagnetic waves, from which the classification as *optical* phonon modes originates. In general, for a three-dimensional lattice containing $N$ atoms per unit cell 3 acoustic and $3N-3$ optical phonon branches are obtained in the phonon dispersion spectrum.

### 2.4.2 Lattice Heat Capacity

The heat capacity relates the increase of a solid's internal energy $U$ by a temperature rise of one Kelvin at constant volume [96]:

$$C_V = \left(\frac{\partial U}{\partial T}\right)_V \quad . \tag{2.40}$$

A solid's internal energy $U$ mainly constitutes of the thermal energy $E$ stored in lattice vibrations of quantized energy, as outlined above. Neglecting the zero point energy, the total energy accumulated in the phonon system follows from Eq. 2.37 [96]:

$$E = \sum_{\vec{q}} \sum_{s=1}^{3} n_{\vec{q},s} \hbar \omega_{s,\vec{q}} \quad . \tag{2.41}$$

Here, the sum runs over all phonon branches in the first Brillouin zone, each indexed by its polarization $s$ and wave vector $\vec{q}$. To obtain analytical expressions for the heat capacity of solids, some approximations on the phonon dispersion need to be made.

#### Einstein Model

Einstein assumed all atoms to oscillate independently of each other at a frequency $\omega(\vec{q}) = \omega_E$ [97]. The resulting phonon energy is independent of the wave vector $\vec{q}$, as shown in Fig. 2.12c by the dashed green line. Thus, it appears to be a rather good approximation for optical phonon modes of flat dispersion. The total thermal energy of a crystal containing $N$ atoms including three polarization modes reads

$$E = 3N\hbar\omega_E n_E = \frac{3N\hbar\omega_E}{\exp[\hbar\omega_E/(k_B T)] - 1} \tag{2.42}$$

and yields, with the help of Eq. 2.40, a molar lattice heat capacity of

$$C_V = 3N_A k_B \left(\frac{\hbar\omega_E}{k_B T}\right)^2 n_E(n_E+1) = 3N_A k_B \left(\frac{\theta_E}{T}\right)^2 \frac{e^{\theta_E/T}}{(e^{\theta_E/T}-1)^2} \quad . \tag{2.43}$$

Here, $N_A$ denotes the Avogadro constant and $\theta_E = \hbar\omega_E/k_B$ the *Einstein temperature*. For $T \gg \theta_E$, Eq. 2.43 reaches a constant limit of $C_V = 3N_A k_B$, also known as *Dulong-Petit law*. In contrast, at low temperatures the Einstein model predicts $C_V \propto T^{-2}\exp[-\theta_E/T]$ which does not accurately explain the experimentally observed heat capacities of most solids. This is due to the large dispersion of acoustic phonon modes being not accurately captured by the constant dispersion.

### Debye Model

An improved model to better account for the dispersion of low-frequency acoustic phonon modes was formulated by Peter Debye in 1912 [98]. For large $N$, the sum over $\vec{q}$ in Eq. 2.41 can be replaced by an integral yielding

$$E = \sum_s \int d^3q \frac{N_0\Omega}{8\pi^3}\hbar\omega_s(\vec{q})n_s(\vec{q}) = \sum_s \int_0^\infty d\omega_s g_s(\omega_s)\hbar\omega_s(\vec{q})n_s(\vec{q}) \tag{2.44}$$

which can be transformed into an integral over surfaces of constant energy $S_\omega$ by introducing the phonon density of states $g(\omega)$, defined as

$$g(\omega) = \frac{N_0\Omega}{8\pi^3}\int \frac{dS_\omega}{\nabla_{\vec{q}}\omega(\vec{q})} \tag{2.45}$$

for a three-dimensional crystal. Here, $\Omega$ is the size of the unit cell and $N_0$ the denotes number of unit cells. Debye approximated the three acoustic phonon modes by a linear dispersion $\omega = v_S \cdot q$, $v_S$ denoting the velocity of sound. The relation is depicted by the orange line in Fig. 2.12c. The linear phonon branch contains all 3N states of the acoustic phonon branches up to a cut-off frequency $\omega_D$, i.e.

$$\int_0^{\omega_D} d\omega g(\omega) = \frac{N_0\Omega\omega_D^3}{2\pi^2 v_S^3} = 3N \tag{2.46}$$

which defines the Debye frequency

$$\omega_D = v_S\left(\frac{6\pi^2 N}{N_0\Omega}\right)^{1/3} \quad . \tag{2.47}$$

With Debye's approximation the heat capacity evaluates to

$$C_V = 9Nk_B\left(\frac{T}{\theta_D}\right)^3 \int_0^{\theta_D/T} dz \frac{z^4 e^z}{(e^z-1)^2} \tag{2.48}$$

where $\theta_D = \hbar\omega_D/k_B$ is the so-called *Debye temperature*. It constitutes an upper limit for the energy of acoustic phonons in a crystal. Eq. 2.48 reproduces the experimentally observed $C_V \propto T^3$ behavior at low temperatures and merges into the constant value of $3Nk_B$ at high temperatures as predicted by the Einstein model as well by the *Dulong-Petit law* for an ideal gas. Consequently, it is expected to provide a better approximation to describe the lattice specific heat of acoustic phonons.

### 2.4.3 Lattice Properties of Organic Crystals

The phonon dispersion of organic crystals is quite complex [58]. This is on the one hand due to the weak intermolecular potential of the van-der-Waals bound crystals together with the rather large mass of the molecules constituting the unit cell, resulting in low phonon frequencies, Debye temperatures and sound velocities. Moreover, a molecule contains additional rotational degrees of freedom compared to an atom and the large number of atoms per unit cell further increases the number of optical phonon modes. Not all of these modes are energetically as widely separated from the acoustic phonon modes as in most inorganic solids of less complex unit cell. Tab. 2.3 compares some electronic and thermal properties of the organic semiconductor naphthalene to silicon and the organic metal TTF-TCNQ.

The complex phonon structure is reflected in larger molar specific heat values of organic materials. The large anharmonicity of the intermolecular potentials, characterized by the Grüneisen constant, results in thermal expansion coefficients being two orders of magnitude larger than in inorganic solids. Weak binding forces may be inferred from the low melting point of naphthalene, too. The crystal binding forces in TTF-TCNQ are larger and under ambient conditions the compound decomposes at 492 K prior to the melting of the crystal structure [109]. The distinct phonon structure of organic solids also manifests itself in the electronic properties, such as the charge carrier mobility being two to three orders of magnitude smaller than in silicon by reason of the more efficient interaction with the numerous low-frequency phonon modes available in organic materials. The electron-phonon interaction potential is often of similar magnitude to the narrow electronic bandwidth in organic crystals.

The total number of phonon branches amounts to $3N$, $N$ denoting the number of atoms per unit cell. Furthermore, in molecular crystals *external* and *internal* phonon modes have to be distinguished [58]. *Internal modes* refer to the atoms oscillating within the molecule against each other. For a molecule of $N_m$ atoms, there exist $3N_m - 6$ intramolecular normal modes of vibration. In organic molecules composed of covalently bound elements of small atomic number, the internal mode frequencies are rather high compared to the

| | Naphthalene | Silicon | TTF-TCNQ |
|---|---|---|---|
| Density $[\frac{\mathrm{g}}{\mathrm{cm}^3}]$ | 1.14 | 2.328 | 1.62 |
| Atomic Mass [amu] | 128 | 28 | 408 |
| $\theta_D$ [K] | 130[99] | 465[100] | 90[101] |
| Sound Velocity $[10^3 \frac{\mathrm{m}}{\mathrm{s}}]$ | 1-3 | 8.4[102] | 1.8-3[103, 104] |
| RT Specific Heat $[\frac{\mathrm{J}}{\mathrm{g\,K}}]$ | 1.3 | 0.7 | 1.5[105] |
| Thermal Expansion Coefficient $[10^{-6} \frac{1}{\mathrm{K}}]$ | 127[106] | 2.6 | 150[107] |
| Grüneisen Constant | 3-4[108] | 0.5[92] | 2.56[103] |
| Melting Temperature [K] | 353 | 1688 | 492 (dec.)[109] |
| RT Mobility $\mu$ ($e^-/h^+$) $[\frac{\mathrm{cm}^2}{\mathrm{V\,s}}]$ | 0.44/0.39 | 1500/450 | 4 |
| Electronic Bandgap [eV] | 5 | 1.1 | |
| Dielectric Constant $\epsilon$ | 3[110] | 11.9 | |

Table 2.3: Electrical and thermal properties of organic and inorganic materials. The archetypical organic semiconductor naphthalene is compared to silicon and the organic conductor TTF-TCNQ. Unless otherwise declared, silicon properties are cited from [111] and values for naphthalene and TTF-TCNQ are taken from [112].

oscillation of complete van-der-Waals bound molecules in a crystal. Nonetheless, similar low frequencies to external modes may also be attained for internal modes, e.g. for some bending and breathing modes of the molecule involving more than two atoms. The energy spectrum of internal phonon modes in a molecular crystal is very similar to the vibrational spectrum of the single molecule. For example, naphthalene only contains carbon and hydrogen atoms from the two upper rows of the periodic system. The vibrational frequency of the antisymmetric C-C stretching mode at a wave number of $\nu = 1595\,\mathrm{cm}^{-1}$ is retained when going from the vapor phase to the crystal [113]. Yet, the vibrational spectrum also contains an internal ring mode at a frequency of only $\nu = 176\,\mathrm{cm}^{-1}$ [114].

*External modes* characterize the thermal movement of rigid molecules around their equilibrium position in the lattice. Every molecule possesses three translational and three rotational degrees of freedom. A crystal containing $Z$ molecules per unit cell will accordingly exhibit $6Z$ external phonon branches, 3 acoustic and $6Z - 3$ optical ones [58]. Sometimes, the external phonons derived from translational and rotational motions are named *translons* and *librons*, respectively [115].

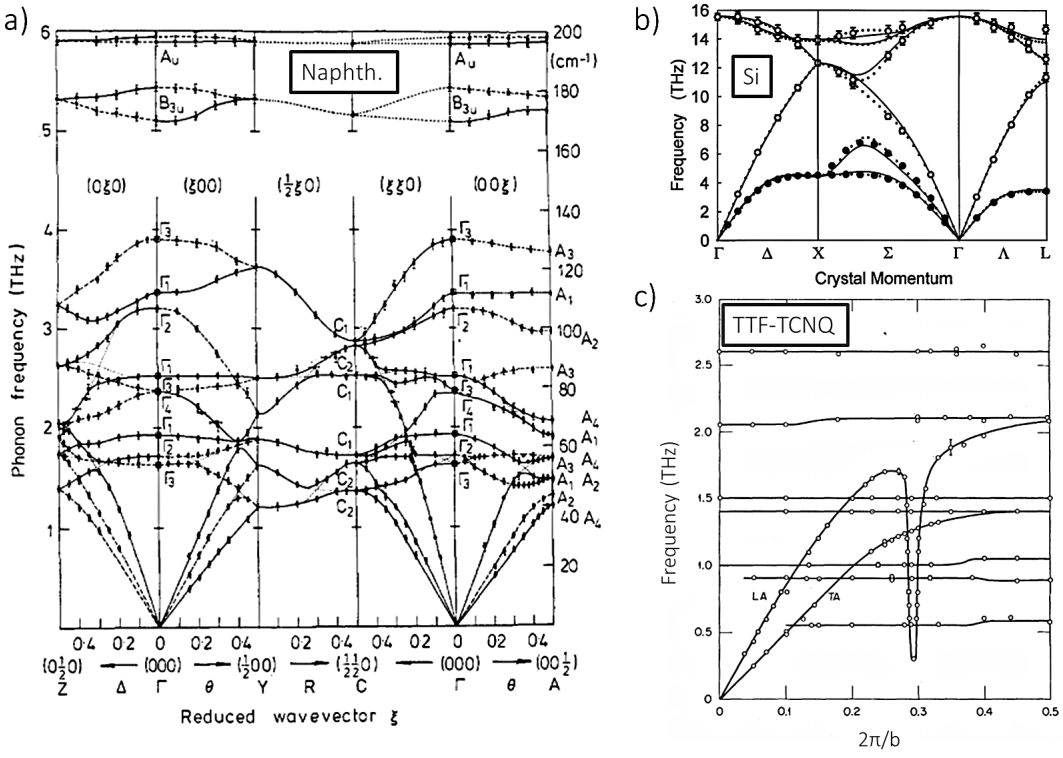


Figure 2.13: Phonon dispersion in crystals. (a) Measured phonon dispersion of perdeuterated naphthalene, (b) silicon and (c) the organic conductor TTF-TCNQ along the $\vec{b}$-axis, i.e. the direction of high conductivity. Adapted from: [116, 117, 104].

In Fig. 2.13a the phonon dispersion measured for the organic semiconductor $d_8$-naphthalene, crystallizing in a structure with $Z = 2$ molecules per unit cell, is shown [58]. As

expected, it consists of 3 acoustic and 9 optical external phonon branches. Optical phonon modes already arise in a low frequency regime of about 2 THz. Above 5 THz internal vibrational modes begin to appear. The frequencies of the phonon modes are significantly lower than in silicon, the dispersion of which is depicted in Fig. 2.13b for comparison [117]. It nicely demonstrates the lower sound velocity and Debye temperature in naphthalene. The phonon dispersion of the organic metal TTF-TCNQ, which is delineated in Fig. 2.13c, exhibits optical phonon modes to intersect with acoustic phonon branches at frequencies as low as 0.5 THz. Furthermore, the LA phonon mode exhibits a Kohn anomaly at around $|\vec{q}_b| \approx 0.3$ Å$^{-1}$ indicating the Peierls state discussed in Sec. 2.2.1. The velocity of sound in TTF-TCNQ takes values of $v_{LA} \approx 3000\,\mathrm{m\,s^{-1}}$ and $v_{TA} \approx 1800\,\mathrm{m\,s^{-1}}$ for the longitudinal and transverse mode, respectively [104].

### Specific Heat in Organic Crystals

Specific heat measurements on naphthalene and silicon are illustrated in Fig. 2.14. The data on silicon roughly agrees with the Debye model described by Eq. 2.48 but the Debye temperature is a function of temperature and takes values in the range of $\theta_D = 465-631\,\mathrm{K}$ [118]. The curve seems to approach a value close to $C_V = 3N_Ak_B = 25\,\mathrm{J\,mol^{-1}\,K^{-1}}$ in agreement with the Dulong-Petit law at high temperatures. In contrast, the specific heat of naphthalene exceeds the limit of Dulong-Petit by far due to additional thermal energy stored in low-frequency optical phonon modes. Instead of a saturating behavior an upward curvature is observed at high temperatures due to the increasing number of optical phonon modes contributing. To model the specific heat per mole at constant pressure in organic crystals, Sallamie and Shaw proposed a combined Debye-Einstein model of the form [119]:

$$\begin{aligned} C_P = \quad & 18R\left(\frac{T}{\theta_D}\right)^3 \int_0^{\theta_D/T} \frac{x^4 e^x}{(e^x-1)^2}dx && \text{3 translational + 3 rotational modes} \\ & + R\sum_{i=1}^{3N_m-6}\left(\frac{\theta_{E,i}}{T}\right)^2 \frac{e^{\theta_{E,i}/T}}{[e^{\theta_{E,i}/T}-1]^2} && \text{internal + external optical phonons} \\ & + \frac{3RA_0C_PT}{T_m} && \text{volume correction} \quad . \end{aligned} \tag{2.49}$$

The model consists of three terms: The first term accounts for three translational and three rotational degrees of freedom which are approximated by Debye's theory of lattice heat capacity as described by Eq. 2.48. $R = N_Ak_B$ represents the universal gas constant. The six phonon branches are approximated by an averaged sound velocity $\vec{v}_S$ and Debye temperature $\theta_D$.

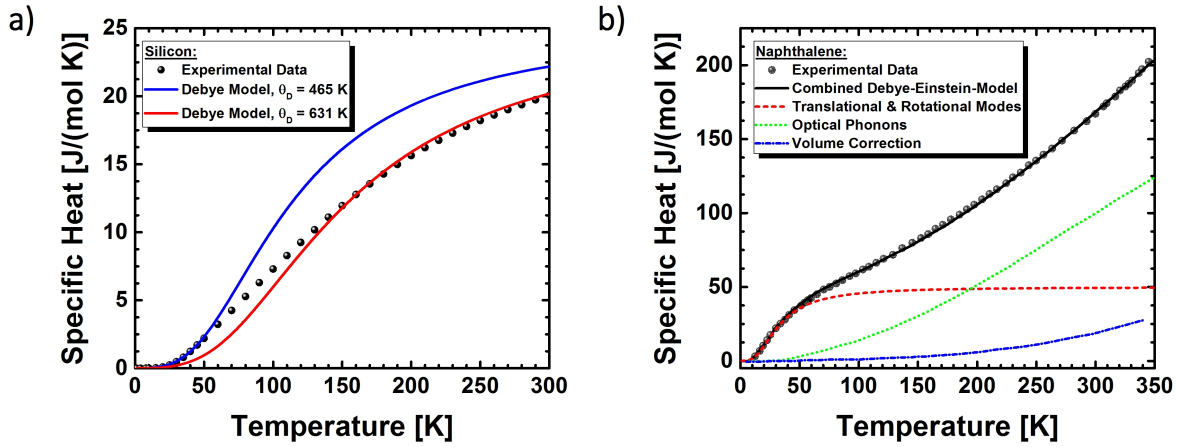


Figure 2.14: Specific heat measured and modeled for (a) silicon as well as (b) naphthalene. Adapted from: [119, 100]

The red dashed line in Fig. 2.14b delineates the portion of heat contained in these modes for naphthalene. It saturates at $50\,\mathrm{J\,mol^{-1}\,K^{-1}}$, i.e. at twice the value obtained by the rule of Dulong-Petit according to the additional rotational degrees taken into account. The second term accounts for all other internal and external optical phonon modes being more appropriately represented by the flat dispersion of the Einstein model, as outlined above. Approximating each optical phonon branch by an Einstein temperature $\theta_{E,i} = \hbar\omega_{E,i}/k_B$, the sum of Einstein oscillators represented by Eq. 2.43 runs over all optical phonon frequencies. This term gives rise to the non-saturating, monotonously rising contribution to the molar specific heat of organic solids because the number of participating optical phonon modes increases with temperature, as shown by the green dotted curve in Fig. 2.14b. The third term accounts for the large thermal expansion in organic crystals. The specific heat is usually measured at constant pressure while the Einstein and Debye model both assume constant volume conditions. The functional form was derived from the Nernst-Lindemann equation by Pan *et al.* for linear macromolecules [120]. $T_m$ is the melting temperature of the solid and the constant $A_0$ may be calculated from the thermal expansion, compressibility and specific heat data, but a quite universal approximation of $A_0 = 3.9 \times 10^{-3}\,\mathrm{K\,mol\,J^{-1}}$ was found from the analysis of 22 polymers. The magnitude of the correction term is illustrated by the blue dot-dashed curve in Fig. 2.14b. The correction term obviously gains importance at rather high temperatures, explaining the upward curvature of naphthalene's specific heat.

The combined Debye and Einstein model allows for an accurate description of the experimental specific heat data for naphthalene as well as for other $\pi$-conjugated organic molecules, such as coronene or perylene [119]. While it has not been employed for low-dimensional organic metals so far, it should be equally valid for this material class by virtue of the similar phonon spectra compared to the above organic semiconductors.

## 2.5 Charge Carrier Transport

The thermoelectric properties of solids are usually treated semiclassically by the Boltzmann transport theory which will be outlined following Refs. [39, 121]. Including several charge carrier scattering mechanisms, the electrical conductivity of ordinary metals in comparison to quasi-1D organic conductors is discussed. A brief introduction to the one-dimensional Tommonaga-Luttinger liquid theory is given at the end of this section.

### 2.5.1 Boltzmann Transport Theory

Fermi-Dirac statistics quantify the number of occupied electronic states in a system of non-interacting fermions in a solid. In equilibrium the average occupation number of a single-particle state of energy $\epsilon$ at temperature $T$ is given by the Fermi-Dirac function [121]

$$f^0_{\vec{k}}(\epsilon(\vec{r},\vec{k}),T) = \frac{1}{e^{[\epsilon(\vec{r},\vec{k})-\mu]/k_BT}+1} \tag{2.50}$$

with the chemical potential $\mu$ being the energy necessary to add one electron to the system. At $T = 0$ the chemical potential is equal to the Fermi energy $\epsilon_F$ separating the occupied states below from the empty states above this energy, i.e. the Fermi function is a step function at $f_0 = 1$ for $\epsilon < \mu$ and $f_0 = 0$ for $\epsilon > \mu$. The energy of an electron $\epsilon(\vec{r},\vec{k},T)$ depends on its wave vector $\vec{k}$, its spatial coordinate $\vec{r}$ and temperature $T$. Upon increasing temperature the distribution smears out in an energy range of about $4k_BT$ around the chemical potential. External perturbations of the electronic system cause a deviation from the equilibrium distribution function which can be described by the semi-classical *Boltzmann theory*. In the presence of an external electric field $\vec{E}$ and a temperature gradient $\vec{\nabla}T$, the steady-state linearized Boltzmann differential equation reads [121]:

$$\frac{f_{\vec{k}} - f^0_{\vec{k}}}{\tau_{\vec{k}}} = -\vec{v}_{\vec{k}} \cdot \left( \frac{\partial f^0_{\vec{k}}}{\partial T}\vec{\nabla}T + e\frac{\partial f^0_{\vec{k}}}{\partial \epsilon_{\vec{k}}}\vec{E} \right) \quad . \tag{2.51}$$

Here, $f^0_{\vec{k}}$ and $f_{\vec{k}}$ are the equilibrium and non-equilibrium Fermi distribution functions and $\vec{v}_{\vec{k}}$ and $e$ denote the electron velocity and electron charge. The employed *relaxation time approximation* assumes that scattering processes can be described by a parameter $\tau_{\vec{k}}$ specifying the time to equilibrate the electronic system after perturbation. In order to calculate the charge current $\vec{J}_e = \frac{2e}{8\pi^3}\int \vec{v}_{\vec{k}} f_{\vec{k}} d\vec{k}$ as well as the heat current $\vec{J}_Q = \frac{2}{8\pi^3}\int \vec{v}_{\vec{k}} f_{\vec{k}} \cdot [\epsilon - \mu] d\vec{k}$ in response to external fields, the k-space integration can be performed over surfaces of constant energy $d\vec{k} = dSd\vec{k}_\perp = 8\pi^3\hbar g(\epsilon)d\epsilon$ leading to the

respective energy representations by [121]:

$$\vec{J}_e = 2e^2 \int \left[\vec{v}(\epsilon) \otimes \vec{v}(\epsilon)\right] \tau(\epsilon) \left(\frac{\partial f^0}{\partial \epsilon}\right) \left[\vec{E} - \frac{1}{e}\vec{\nabla}\mu\right] g(\epsilon) d\epsilon$$
$$+ 2e \int \left[\vec{v}(\epsilon) \otimes \vec{v}(\epsilon)\right] \tau(\epsilon) \left(\frac{\partial f^0}{\partial \epsilon}\right) \left[\frac{\epsilon - \mu}{T}\right] (-\vec{\nabla}T) g(\epsilon) d\epsilon \tag{2.52a}$$

$$\vec{J}_Q = e \int \left[\vec{v}(\epsilon) \otimes \vec{v}(\epsilon)\right] \tau(\epsilon) \left(\frac{\partial f^0}{\partial \epsilon}\right) [\epsilon - \mu] \left[\vec{E} - \frac{1}{e}\vec{\nabla}\mu\right] g(\epsilon) d\epsilon$$
$$+ T \int \left[\vec{v}(\epsilon) \otimes \vec{v}(\epsilon)\right] \tau(\epsilon) \left(\frac{\partial f^0}{\partial \epsilon}\right) \left[\frac{\epsilon - \mu}{T}\right]^2 (-\vec{\nabla}T) g(\epsilon) d\epsilon \quad . \tag{2.52b}$$

Here, $g(\epsilon)d\epsilon = \frac{1}{(2\pi)^3\hbar} \int \frac{dS}{|\vec{v}|} d\epsilon$ defines the electronic density of states. By introducing the generalized transport integral with a separated material-dependent part $I_{Mat}$ of the integrand [39]

$$K_s = -2 \int \underbrace{g(\epsilon) \left[\vec{v}(\epsilon) \otimes \vec{v}(\epsilon)\right] \tau(\epsilon)}_{I_{Mat}} \left[\epsilon_{\vec{k}} - \mu\right]^s \frac{\partial f^0}{\partial \epsilon} d\epsilon \quad , s = 0, 1, 2, \tag{2.53}$$

Eqs. 2.52a and 2.52b may be further simplified to [39]

$$\vec{J}_e = e^2 K_0 \vec{E}_{eff} - \frac{e}{T} K_1 \vec{\nabla} T \tag{2.54a}$$

$$\vec{J}_Q = e K_1 \vec{E}_{eff} - \frac{1}{T} K_2 \vec{\nabla} T \quad , \tag{2.54b}$$

with the effective field $\vec{E}_{eff} = \vec{E} - \vec{\nabla}\mu/e$ acting on the charge carriers. The equation system is similar to Eqs. 2.4a-b and describes the thermoelectric transport phenomena in a solid, allowing for a calculation of the material's *Seebeck coefficient* $S$ as well as its *electrical conductivity* $\sigma$ and *electronic thermal conductivity* $\kappa'$ [121]:

$$\sigma = e^2 K_0 \tag{2.55a}$$

$$S = \mp \frac{1}{eT} \frac{K_1}{K_0} \tag{2.55b}$$

$$\kappa' = \frac{1}{T} \left[K_2 - \frac{K_1^2}{K_0}\right] \quad . \tag{2.55c}$$

Obviously, the parameters interdepend and thus, cannot be optimized individually. A large electrical conductivity, for instance, necessitates a high density of states close to the Fermi energy in contrast to the Seebeck coefficient which scales with the energy difference of the transport level to the chemical potential. For this reason, high electrical

conductivities as well as small Seebeck coefficients are observed in metals and, vice versa, in semiconductors. The material-dependent part of the transport properties is represented by the kernel $I_{Mat}$ of the integrand in Eq. 2.53. It depends on the material's band structure as well as the details of the electron scattering mechanisms.

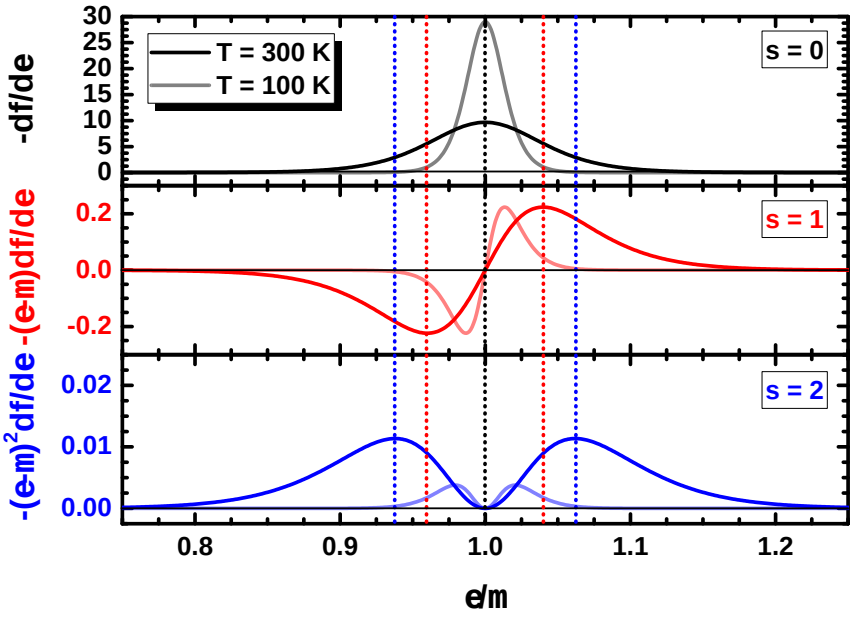


Figure 2.15: Material-independent part $(\epsilon - \mu)^s \frac{\partial f_0}{\partial \epsilon}$ of the transport integrand in Eq. 2.53 for s=0,1,2 at two distinct temperatures.

The remainder of the integrand only depends on the energy dependence of the Fermi function and is illustrated for s=0,1,2 in Fig. 2.15 at two distinct temperatures. While the conductivity probes energetic states at the chemical potential, the thermopower and the thermal conductivity are related to states slightly above and below. Only the Seebeck coefficient can obtain negative values due to the integrand's symmetry with respect to the chemical potential. On decreasing temperature all three integrands become narrower and probe states closer to the chemical potential. To analytically evaluate the transport integrals in Eq. 2.53 several assumptions have to be made. Two distinct cases, namely the approximations of a *degenerate* and a *non-degenerate electron gas* are being considered in the following sections. The degenerate case treats the Fermi energy being large compared to the thermal energy, i.e. $\epsilon_F \gg k_B T$. The assumption is valid for metals, semimetals and heavily doped semiconductors where the Fermi energy lies in the conduction or valence band. The opposite, non-degenerate limit ($\epsilon_F \ll k_B T$) generally applies for lightly doped semiconductors [37].

### 2.5.2 Electrical Conductivity

#### Mobility and Scattering Rates

The electrical conductivity $\sigma$ (resistivity $\rho$) of a material can in principle be calculated from Eqs. 2.55a and 2.53. However, the calculation can become quite elaborate depending on the complexity of the band structure and the scattering mechanism contributing to the transport integral. Approximating the electronic band structure by a parabolic band, that is for quasi-free electrons with effective mass $m^*$, and assuming an energy-independent relaxation time $\tau(\epsilon) \approx \tau(\epsilon_F)$, it can be evaluated to

$$\sigma = e^2 K_0 = \frac{ne^2\tau(\epsilon_F)}{m^*} = en\mu = \rho^{-1} \tag{2.56}$$

where $n$ is the number of mobile charge carriers and $\mu = e\tau/m^*$ is the *charge carrier mobility* depending on the *relaxation time* $\tau$ due to all present scattering mechanisms. The renormalized, effective mass $m^*$ accounts for the motion in the periodic potential of the lattice as well as for electron-electron correlation. By virtue of the charge transfer process governing the band filling in the metallic state of organic conductors, the charge carrier density is assumed to be independent of temperature. Therefore, the temperature dependence of the conductivity is governed by the sum of the individual scattering rates $1/\tau_i$ [39]

$$\frac{1}{\tau} = \sum_i \frac{1}{\tau_i} \quad . \tag{2.57}$$

#### Scattering Mechanisms

The calculation of distinct electron scattering rates is a difficult task and several different theories and approaches have been presented in literature [121]. Since detailed calculation procedures are beyond the scope of this thesis, only some results being relevant for organic conductors and low-dimensional electron gases are briefly presented in the following. The scattering time depends on the transfer integral and thus, is an anisotropic tensorial quantity. In principle it depends on the energy of the charge carrier and it is often simplified by assuming the form [39]

$$\tau(\epsilon) = c_0 \epsilon^r \quad , \tag{2.58}$$

$r$ being the scattering parameter. For example, $r = 1/2$ is obtained for the interaction of an electron with a single acoustic phonon mode in one dimension [122]. More elaborate theoretical scattering rates with relevance for organic conductors are listed in

Tab. 2.4. Two given scattering entities inside a crystal are impurities and defects. Their temperature-independent scattering of electrons was found to scale with the degree of alloying in metals [123]. According to Eqs. 2.56 and 2.57, this leads to the idea of a temperature-independent impurity resistivity $\rho_{imp}$ and a temperature-dependent scattering term $\rho_{sc}(T)$ [121]

$$\rho(T) = \rho_{imp} + \rho_{sc}(T) \tag{2.59}$$

which is also known as *Matthiessen's rule*. $\rho_{sc}$ depends on the distinct electron scattering processes which will be briefly discussed below.

| Scattering Process | Abbrev. | Scattering Rate [$s^{-1}$] |
|---|---|---|
| Charged Impurities [39] | $\tau_{e-imp}^{-1}$ | $\frac{2n_i E_F Z^2}{3\hbar} F\left[\frac{4k_F^2}{k_{TF}^2}\right]$ |
| 3D Normal-Phonon | $\tau_{e-N}^{-1}$ | $\frac{ne}{m^*} A \left(\frac{T}{\theta_D}\right)^5 J_5\left(\frac{\theta_R}{T}\right)$ |
| 1D Umklapp-Phonon [122] | $\tau_{e-U}^{-1}$ | $\left(\frac{\partial W}{\partial u}\right)^2 \frac{k_B T}{\hbar M \omega_0^2 \sqrt{\epsilon(W-\epsilon)}}$ |
| 2 Phonons [124] | $\tau_{e-2Ph}^{-1}$ | $\left(\frac{\partial^2 W}{\partial u^2/\theta^2}\right)^2 \frac{\pi g(\epsilon)}{32} \left(\frac{k_B T}{M/J}\right)^2 \int_{-\pi/a_0}^{-2k+\pi/a_0} \frac{f_2^2}{\omega_q^2 \omega_{q'}^2} dq$ |
| Optical Phonon [125] | $\tau_{e-opt}^{-1}$ | $g(\epsilon)\frac{4\pi a_0 C2}{M\omega_i} e^{-\hbar\omega_i/k_B T}$ |
| Mutual Acoustic Phonons [126] | $\tau_{map}^{-1}$ | $\frac{2a_0^2 k_B T(\partial t/\partial x)^2}{\hbar M v_k^2 t^2} \frac{\gamma^2(\epsilon-\Delta_0^{s,p})^2+4t^2D^2}{\sqrt{\epsilon(W-\epsilon)}}$ |
| Electron (3D) [127] | $\tau_{e-e,3D}^{-1}$ | $B_{ee,3D} \cdot T^2$ |
| Electron (1D) [127] | $\tau_{e-e,1D}^{-1}$ | $B_{ee,1D} \cdot T^1$ |

Table 2.4: Several theoretical electron scattering rates. (Quantities and functions: $n_i$ - impurity concentration; Z: charge of impurity; $F[x] = 2[ln(1+x) - x/(1+x)]/x^2$; $k_{TF}$ - Thomas Fermi wavelength; $A = 9\pi h^2 C^2 \sqrt{m^*}/(8\sqrt{2} n e^2 a_0^3 M k_B \theta_D \epsilon_F^{3/2})$; $C$ - coupling constant; $J_n(z) = \int_0^z x^n e^x/(e^x-1)^2 dx$; $\theta_R$ - Bloch-Grüneisen temperature; $W$ - bandwidth; $\epsilon$ - electron energy; $u/\theta$ - translational/rotational molecular displacement; $M/J$ - mass/inertia of molecule; $\omega_i$ - phonon frequency; $a_0$ - lattice constant; $f_2(k,q,q') = 2[\cos k a_0 - \cos(k+q)a_0]$; $t$ - transfer integral; $\Delta_0^{s,p} = 2t(\gamma \pm 1)/\gamma$; $\gamma = 2e^2\alpha_0/(a_0^5 \partial t/\partial x)$; $\alpha_0$ - polarizability; $v_k$ - carrier velocity; $D$ - impurity scattering parameter.)

The scattering of electrons by phonons is one of the most important interaction mechanisms limiting the charge carrier mobility in single crystals. While the influence of the periodic potential caused by the lattice ions is captured by means of the effective electron mass, the oscillation of the ions represents an additional perturbation to charge carriers due to the fluctuation of the transfer integral (deformation potential scattering). In organic crystals there exists a large number of thermally excited phonons due to the low

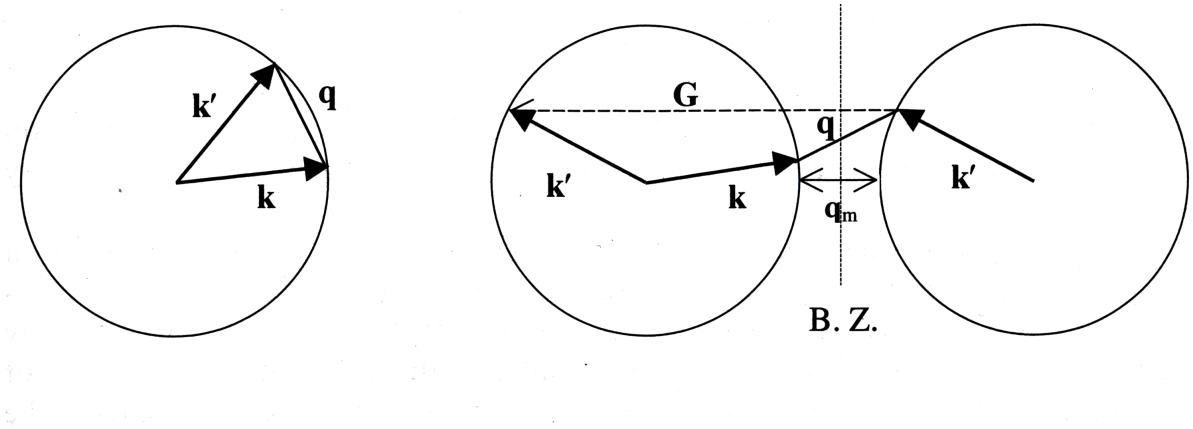


Figure 2.16: Normal vs. Umklapp scattering events. While Normal scattering processes only slighty change the momentum of the charge carrier, Umklapp processes are very efficient in generating resistance due to the large momentum transfer by scattering the electron out of the first Brillouin zone. From: [121]

energy and dispersion of the phonon spectrum (compare Sec. 2.4). In combination with the strong electron-phonon coupling, scattering of electrons by phonons is generally very efficient in these materials [128]. The momentum conservation law for scattering of an electron from the state $\vec{k}$ into the state $\vec{k}'$ by one phonon $\vec{q}$ requires [121]:

$$\vec{k} \pm \vec{q} = \vec{k}' + \vec{G} \quad . \tag{2.60}$$

Fig. 2.16 distinguishes two possible scattering processes in a crystal: For *Normal processes* (N-processes) the involved reciprocal lattice vector $\vec{G}$ vanishes, i.e. $\vec{k}'$ lies in the same Brillouin zone as $\vec{k}$. This process is ineffective in generating resistance due to its small change in momentum. Contrarily, by *Umklapp processes* (U-processes) the electron is scattered into the next Brillouin zone and can be mapped back into the first zone by a reciprocal lattice vector $\vec{G}$. This leads to a large momentum transfer now that the scattered wave vector essentially points into the opposite direction than the incoming one. Umklapp processes therefore are very effective in contributing to the electrical and thermal resistance. To scatter electrons out of the first Brillouin zone, phonon states with wave vectors $\vec{q}$ of sufficient magnitude have to be excited, weakening this effect upon decreasing temperature. Hence, at low temperature normal processes may still dominate the conduction in ordinary metals, leading to the established *Bloch-Grüneisen formula* [121]:

$$\rho(T) = A \left(\frac{T}{\theta_R}\right)^5 J_5\left(\frac{\theta_R}{T}\right) = \begin{cases} 124.4 \cdot A \left(\frac{T}{\theta_R}\right)^5 & , T \ll \theta_R \\ \frac{A}{4}\left(\frac{T}{\theta_R}\right) & , T \geq \theta_R \end{cases} \tag{2.61}$$

which has been validated for most ordinary metals. The Bloch-Grüneisen temperature

$\theta_R$ commonly takes values between the Debye temperature $\theta_D$ and the longitudinal sound velocity temperature $\theta_S = v_s\hbar k_F/k_B$. Eq. 2.61 predicts a linear temperature dependence of the resistivity at $T \geq \theta_R$. Similar linear high temperature dependences have also been predicted by scattering theories for one-dimensional organic conductors including Umklapp processes (see Tab. 2.4) due to the number of excited acoustic phonons increasing with temperature.

A scattering process involving two translons or librons of wave vectors $\vec{q}$ and $\vec{q}'$ has been proposed in literature to account for the $\rho \propto T^2$ dependence frequently observed in organic conductors [124]. Being a second order process, it also explains the strong pressure-dependence of the resistivity. In another theory, Casian *et al.* incorporated the mutual cancellation of two interfering interaction mechanisms between electrons and longitudinal acoustic phonons into their calculation of the scattering time for a strictly one-dimensional model [126]. In addition to the deformation potential scattering (i.e. the effective fluctuation of the transfer integral $t$) described above, a polaronic interaction taking into account the polarization and the accompanied shift of surrounding molecules by the excess electrons is considered in their theory. A high relative strength $\gamma$ of the latter to the former scattering mechanism predicts high mobility states inside the conduction band of the quasi-1D organic conductor tetrathiotetracene-iodine ($TTT_2I_3$), as depicted in Fig. 2.17. When the polaronic interaction becomes comparable to the deformation potential scattering ($\gamma$>1), a small band of electronic states attains very high conductivity values due to the divergent relaxation time. Whether a preferred polaronic interaction is achievable is doubted by other authors because the theory neglects the rather high screening effects limiting the polaronic interaction in organic conductors compared to semiconductors [122]. In addition to acoustic phonons, the interaction of optical phonons with charge carriers may need to be considered. In Tab. 2.4 a scattering rate for nonpolar optical phonons is therefore included, too.

The simple band description of charge transport in solids neglects the electrons' mutual interaction due to their Fermi character and the Pauli exclusion principle. At first glance, this may seem contradictory in view of the quite strong Coulomb interaction between charged particles. The influence of electron-electron interactions was incorporated into the theory by Lew Landau's approach on Fermi liquids introducing the concept of the quasiparticle [129]. The idea is the following: In a gas of non-interacting fermions the particles will behave free and independent of each other. Slowly turning on the interaction between them is similar to increasing the density of the gas, mimicking the change from a gas to a liquid. Landau showed that fermions in an interacting liquid can be treated similar to the particles in an ideal gas but with renormalized effective mass $m^*$ and momentum $p$. They are called quasiparticles. This concept has spread into other theories as well,

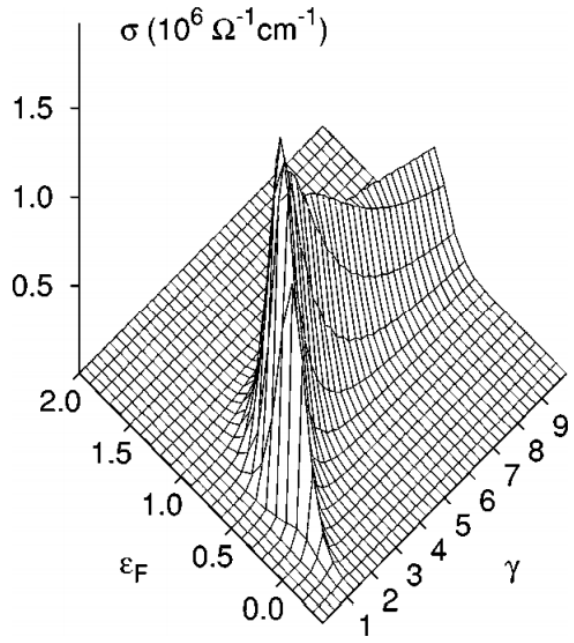


Figure 2.17: Theoretically calculated electrical conductivity of the organic conductor $TTT_2I_3$. When the polarization scattering becomes comparable to the deformation potential interaction ($\gamma$>1), a band of electronic states attains very large relaxation times leading to high conductivity states. From: [126]

e.g. in the description of lattice vibrations by phonons or of holes in semiconductors. In a metal, a free charge carrier with energy $\epsilon_1$ will only be able to interact with states close to the Fermi energy. As the interaction includes two particles, the scattering rate $\tau^{-1}_{e-e,3D}(\epsilon_1) \propto (\epsilon_1 - \epsilon_F)^2 \propto (T/T_F)^2$ results in a temperature-dependent resistivity of the form [127]:

$$\rho = A_{ee} \cdot T^2 \quad . \tag{2.62}$$

This temperature dependence is found in ordinary metals at low temperatures validating their Fermi liquid behavior. On the other hand, a linear temperature dependence is predicted for one-dimensional electron gases with strong electron-electron interaction [127].

### Electrical Conductivity in Organic Metals

For $(DCNQI\text{-}h_8)_2Cu$ the resistivity between 1.5 K and 300 K was determined to follow a power law [85]

$$\rho(T) = \rho_0 + A \cdot T^{\alpha} \quad , \tag{2.63}$$

with $\alpha = 2.3$ supporting the idea of an increased electron-electron scattering determining the charge carrier mobility. Yet, the assignment to a distinct scattering mech-

anism is not straightforward [7]. There has been an intense discussion with regard to the temperature-dependent conductivity of the related charge transfer salt TTF-TCNQ, also revealing $\alpha = 2.3$, and whether this exponent originates from strong electron correlations or anomalous electron-phonon scattering [122]. Mazumdar and Bloch calculated short-range electron correlations as a function of band filling and concluded that, when long-range electrostatic effects are included, a screening of the charge carrier's Coulomb repulsion becomes efficient at intermediate band fillings between 1/4 and 1/2. In these cases electronic correlation effects are negligible [86]. Contrarily, for quarter- or semi-filled bands the correlations are strong, resulting in a gap at the Fermi energy and therewith, to a Mott-Hubbard transition, as outlined in Sec. 2.2. TTF-TCNQ as well as $(DCNQI)_2Cu$, with charge fractions of $\delta_{TCNQ} = 0.59$ [130] and $\delta_{DCNQI}/2 = 0.67$ [68] residing on the respective molecule, both give rise to band fillings of about 1/3. Therefore electronic correlations should be of minor importance in these material systems. In contrast, the conduction band of $(DMe\text{-}DCNQI)_2Li$ is only filled to 1/4. The resulting stronger electronic correlations are reflected in the semi-metallic transport properties above 60 K, corresponding to a $4k_F$ Wigner crystal (compare Sec. 2.2).

The generally quite large electron-phonon interaction with respect to the electronic bandwidth in organic semiconductors intuitively marks charge carrier scattering by phonons to govern the relaxation time in organic conductors as well. The two-libron scattering processes discussed above scale the resistivity at high temperatures proportional to $T^2$ because the distribution functions of two phonons are involved. It compares well to the temperature dependence of many organic conductors. Yet, a preferred interaction with two librons instead of one phonon is controversial. For example, inserting the calculated scattering time of $\tau_{2l} = 3 \times 10^{15}\,\mathrm{s}^{-1}$ for TTF-TCNQ into Heisenberg's uncertainty principle unfolds a bandwidth of 2 eV being several times larger than the observed one [122]. On the other hand it may explain the huge pressure dependence observed for the electrical resistivity of organic metals due to the higher-order process involved. In contrast, a scattering rate following electron-electron interactions is supposed to be independent of pressure [127]. Optical phonon scattering in TTF-TCNQ may also account for a temperature dependence of $\rho \propto T^{2.3}$, as calculations by Conwell have shown, taking into the account the details of the phonon spectrum [131].

An important point when comparing scattering theories to experimental data is that all of them have been derived for constant-volume conditions. As the resistivity is generally measured under constant pressure, the large contraction of organic conductors needs to be considered when comparing to any theoretical prediction [132]. For instance, the electrical resistivity of TTF-TCNQ changes from a $\rho \propto T^{2.3}$ to a $\rho \propto T^1$ behavior when going from constant pressure to constant volume conditions [133], in agreement with a mobility

limited by acoustic phonon scattering. Even more, the electron-electron scattering rate in one-dimensional electron gases also predicts a linear temperature dependence of the resistivity [127]. Hence, it is important to not only analyze the electrical resistivity of organic conductors but to holistically investigate all electrical transport quantities which is the aim of this thesis.

### Tomonaga-Luttinger Liquid

The *Tomonaga-Luttinger-liquid model* (or often just called *Luttinger liquid*) describes the properties of perfectly one-dimensional metals. In the strict one-dimensional limit, some of the previous assumptions on the Fermi liquid, e.g. the negligible electron-electron interaction and its transfer into renormalized parameters like the effective mass, do not hold as a result of the reduced dimensionality. A Luttinger liquid is a *paramagnetic one-dimensional metal without Landau quasiparticle excitations* [134].

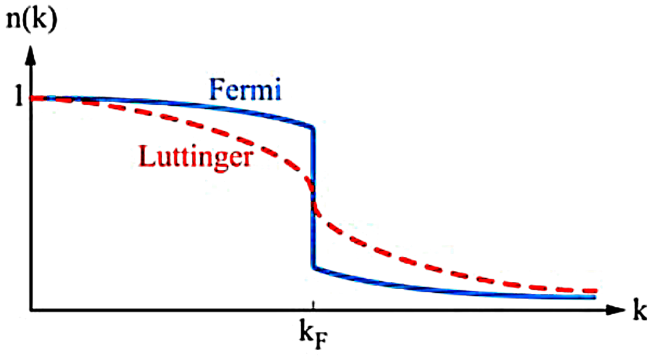


Figure 2.18: Comparison of the momentum distribution predicted by Fermi and Luttinger liquid theory. Whereas the Fermi liquid shows a sharp drop at $k_F$ at $T = 0$ even for finite interactions, the Luttinger liquid follows a power-law behavior. From: [135]

Basic assumptions of the Luttinger liquid are the gapless spin and charge excitations and their linear dispersion ($\omega_\nu \approx v_\nu \, |\vec{q}|$) for low-energy excitations close to the Fermi wave vector $k_F$. In the absence of electron-electron interactions the velocity $v_\nu$ is equal to the Fermi velocity $v_F$ for electron-hole excitations. When interactions are switched on, they may cause a gap in the spin or charge excitation spectrum, indicated by a Mott insulator or spin-density-wave. An energy gap in the charge carrier excitation spectrum will shift the system to a band insulator. It is also possible that excitations of charges and spins remain gapless but decouple from each other, with different velocities $v_\nu$ for spins and charges [135]. Compared to the Fermi liquid, the momentum distribution function of the Luttinger liquid does not show a discrete step at $k_F$ for $T = 0$ but varies continuously following a power-law $n(k) \propto |k - k_f|^\phi$, as indicated in Figure 2.18. The exponent $\phi$ is connected to the Luttinger interaction parameter $K_\rho$ by [134]:

$$\phi = \frac{1}{4}\left(K_\rho + \frac{1}{K_\rho} - 2\right) \quad . \tag{2.64}$$

$K_\rho$ characterizes the strength of electron-electron interactions with $K_\rho < 1$ ($K_\rho > 1$) referring to repulsive (attractive) electron-electron interactions and $K_\rho = 1$ representing the case of negligible mutual interactions. The temperature dependence of the conductivity can be derived to [134]

$$\sigma \propto T^{3-n^2 K_\rho} \quad , \tag{2.65}$$

with $1/n$ being the band filling. The Luttinger liquid theory only holds true for strictly one-dimensional conductors but nearly all real sample systems do not exhibit perfectly one-dimensional Fermi surfaces. This is especially the case for organic crystals in which conduction occurs on spatially separated chains with finite coupling. Therefore, the Luttinger liquid theory should only be of limited significance for this material class. However, it was demonstrated that some quasi-1D organic conductors show rather Luttinger liquid-like behavior at high temperatures [136]. It was suggested that the corrugated Fermi surfaces, originating from interchain coupling, smooth out for $k_B T > t_\perp$, with $t_\perp$ being the interchain transfer integral characterizing the orbital overlap perpendicular to the direction of preferred charge transport [137]. As a result, a crossover from a Fermi liquid to a Luttinger liquid is likely to occur.

### Conduction in Semiconductors

In intrinsic semiconductors, the temperature dependence of the electrical conductivity will not only depend on the mobility $\mu(T)$ of charge carriers, but also on the number of charge carriers $n(T)$ excited across the energy gap $\epsilon_g$, i.e. [39]

$$\sigma(T) = n(T) \cdot \mu(T) \cdot e \propto T^{-\alpha} e^{-\epsilon_g/(2k_B T)} \quad . \tag{2.66}$$

An extrinsic semiconductor provides additional charge carriers from dopants at an energy level of $\epsilon_d$ with respect to the transport band. In this case, the conductivity scales according to:

$$\sigma(T) = n(T) \cdot \mu(T) \cdot e \propto T^{-\alpha} e^{-\epsilon_d/(k_B T)} \quad . \tag{2.67}$$

In some cases, even conducting states inside the energy gap may be formed. For instance, disorder may create tails of localized energy states reaching into the bandgap and contributing via hopping processes to conduction. The *variable range hopping model* predicts a conductivity of [41]

$$\sigma(T) \propto e^{-(T_0/T)^{\frac{1}{1+d}}} \tag{2.68}$$

where $d$ denotes the dimension of the crystal volume and $\Delta\epsilon = k_B T_0 (T/T_0)^{\frac{1}{1+d}}$ is the energy spread of the localized states. This contribution may gain importance at low temperatures when the thermal energy to excite charge carriers across the bandgap is small.

### 2.5.3 Nonlinear Conduction in Organic Conductors

In organic CT salts characteristic nonlinear conduction phenomena have first been reported for the quasi-one-dimensional mixed-stack organic conductor Tetrathiafulvalene-p-Chloranil (TTF-CA) [13]. Subsequently, the characteristic nonlinear conduction phenomena have been observed in a variety of organic charge transfer salts characterized by different ground states, such as spin-Peierls systems like K-TCNQ [17] or charge-ordered states as in $\alpha$-(BEDT-TTF)$_2$I$_3$ [138, 139]. The effects have been proposed for application in organic thyristors, i.e. DC/AC converters, as well as resistive memories [19, 21]. Most of the observed nonlinear phenomena seem to have in common, that the current voltage characteristics are S-shaped when current-driven with negative differential resistance (NDR) above electric fields of about $10^2 - 10^4 \frac{V}{cm}$. The nonlinear conduction only seems to occur in a temperature range of strongly temperature-dependent resistivity. In materials exhibiting an insulator-to-metal transition nearby this temperature regime, the effect is further enhanced [20]. Experimentally, Iwasa *et al.* found a phenomenological relationship between the current density $J$ and the electrical conductivity $\sigma$ for organic CT salts [140]

$$\sigma = \sigma_1 \cdot \exp^{-\frac{\Delta\epsilon}{k_B T}} + \sigma_2 \cdot J^n \tag{2.69}$$

in which the first term is the usual low-field conductivity and the second term describes the nonlinearity with $n \approx 1.5 - 1.8$. In spite of the similar phenomenological description by Eq. 2.69, the unambiguous microscopic origins of the nonlinear conduction are still under debate and may vary for the different material systems under study [20, 141, 16, 139, 142, 14].

#### Electrothermal Model

The distinct nonlinear conduction effects observed in a variety of organic conductors with different ground states call for a more uniform theoretical description. Mori *et al.* [143] were the first to emphasize the connection between the steepness of resistivity curves and the electric threshold field for the onset of nonlinear conduction. Employing a phenomenological electrothermal model, nonlinear current-voltage characteristics have been successfully

simulated for a variety of organic conductors [142, 143], including $(DCNQI)_2Cu$ [18]. The model elucidates the temporal increase of a system's temperature $T$ in the presence of the Joule heating power $P$ and thermal losses due to heat conduction, characterized by the thermal conductivity $\kappa$ [143]:

$$nC_{eff}\frac{dT}{dt} = P - \nabla\{\kappa\nabla T\} \quad . \tag{2.70}$$

Here, the effective heat capacity per volume $nC_{eff}$ is distinctive for the subsystem the electrical energy is transferred to. The supplied electrical energy reads $P = \sigma(T)\cdot E^2$ and $P = \frac{J^2}{\sigma(T)}$ for a two-probe voltage-driven and a four-probe current-driven setup, respectively. $E$ and $J$ denote the electric field and current density while $\sigma(T)$ represents the temperature-dependent conductivity of the material. Under the assumption of homogeneous current distribution in the sample and Newtonian cooling, Eq. 2.70 simplifies to [143]

$$nC_{eff}\frac{dT}{dt} = \sigma(T)\cdot E^2 - \alpha^*\cdot\{T - T_0\} \tag{2.71}$$

where the parameter $\alpha^*$ is an energy transfer rate to the environment characterized by the respective dissipation mechanism and sample geometry. Assigning the effective specific heat to distinct microscopic origins of electronic or phononic nature, the energy flow into the individual microscopic subsystems may be uncovered and conclusions on the scattering mechanisms of charge carriers may be drawn. A value close to the specific heat of the material discloses a uniform electrical heating of the sample while smaller values indicate the non-equilibrium excitation of specific quasiparticles being unable to efficiently dissipate the deposited excess energy to the environment or to other excitations.

By numerical integration of Eq. 2.71, the transient conductivity $\sigma(T[t])$ after applying an electric field pulse may be calculated in case of known temperature-dependent conductivity. Adjusting the parameters $\alpha^*$ and $nC_{eff}$ enabled Mori *et al.* to simulate the experimental, nonlinear current-voltage characteristics at fixed pulse widths for a variety of organic conductors. The temperature-independent values derived for $nC_{eff}$ are usually small compared to the total specific heat of the materials and are taken to be indicative of the electronic origin of the nonlinear conduction. In this context, the temperature $T = T_e$ can be interpreted as a parameter for the population of excited electronic states which may decouple from the lattice temperature $T_L$. The energy flow proposed by the electrothermal model is illustrated in Fig. 2.19. At first, the power provided by the electric field increases the electronic energy. When the transfer of energy from the electronic to the lattice system is insufficient, electrons begin to populate excited stated in the band which is phenomenologically described by the electron temperature $T_e$. This non-equilibrium

population of hot electron states implies a small electron-phonon interaction. Only subsequently, the electronic system is able to transfer its energy to the lattice which is usually assumed to be in good thermal contact with the external environment, i.e. $T_L = T_0$.

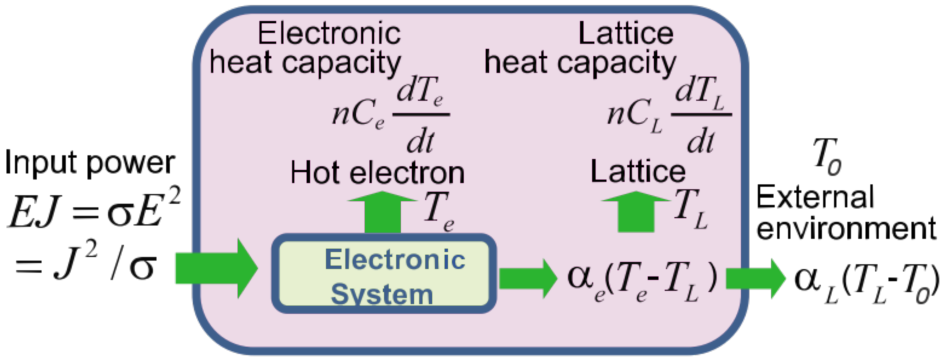


Figure 2.19: Microscopic interpretation of the electrothermal model proposed by Mori *et al.* [143]. The energy provided by the electric field is absorbed by the electronic subsystem. Due to ineffective energy transfer from the electronic system to the lattice, electrons begin to populate excited energy states and only subsequently thermalize. The lattice is in thermal contact with the surrounding heat bath but is usually assumed to be at ambient temperature, i.e. $T_L = T_0$. Adapted from: [143]

### 2.5.4 Electronic Specific Heat

Electrons in metals buffer not only electric but also thermal energy. The specific heat of electrons treated as a free Fermi gas at constant volume reads [144]

$$c_{el} = \frac{\pi^2}{3} g(\epsilon_F) k_B^2 T = \frac{m k_B^2}{\hbar^2} \left(\frac{\pi^2 n}{9}\right)^{1/3} T = \frac{\pi^2}{3} \frac{T}{T_F} \frac{3 n k_B}{2} = \gamma T \tag{2.72}$$

which is reduced compared to the value of $\frac{3}{2} n k_B$ expected for a classical free electron gas by a factor $\frac{\pi^2}{3} \frac{T}{T_F}$, reflecting the quantum-mechanical nature of electrons. The experimental and theoretical Sommerfeld coefficients $\gamma$ of some metals are given in Tab. 2.5.

| | Na | Al | Ag | Cu | $CeCu_2Si_2$[145] | $(DCNQI)_2Cu$ |
|---|---|---|---|---|---|---|
| $\gamma_{exp}$ $[\frac{\mathrm{mJ}}{\mathrm{mol\,K^3}}]$ | 1.38 | 1.38 | 0.65 | 0.7 | 1100 | 25[34] |
| $\frac{\gamma_{exp}}{\gamma_{theo}} = \frac{m^*_{th}}{m_e}$ | 1.26 | 1.48 | 1.38 | 1.00 | 100 | 4 |

Table 2.5: Experimental Sommerfeld coefficient $\gamma$ of some metals compared to their theoretical predictions from Eq. 2.72 [144]. The thermal mass ratio of $(DCNQI)_2Cu$ was calculated from the density of states published by Miyazaki *et al.* [67].

The absolute values of the electronic specific heat are significantly lower than the lattice specific heat contribution outlined in Ch. 2.4.2 and only come into play at cryogenic temperatures. For simple metals, the theoretical prediction by Eq. 2.72 matches the experimental values quite good which are always larger due to the interaction of electrons with the periodic lattice potential, phonons and each other. The deviation can be accounted for by a higher *thermal effective mass* $m^*_{th}$. Some multivalent metals containing f-electrons reveal very high thermal effective masses, an example of which is $CeCu_2Si_2$. These are called *heavy-fermion systems* in which electron-electron interactions govern the relaxation of the electronic distribution [145]. For the organic conductor (DCNQI-$h_8$)$_2$Cu, an enhanced effective thermal mass was found due to a high density of d-electron states at the Fermi-level rather than electronic correlations [146]. For electron-correlated materials, $\gamma$ is related to the resistivity coefficient $A_{ee}$ in Eq. 2.62 by the unified Kadowaki-Woods-Relation [147]

$$A_{ee} = \frac{81}{4\pi\hbar k_B^2 e} \frac{1}{n g^2(\epsilon_F) \langle v_{0x} \rangle^2 \xi^2} \cdot \gamma^2 \propto m^{*2} \tag{2.73}$$

for which the parameter $\xi$ takes values close to unity and the electron velocity $\langle v_{0x} \rangle$ is averaged over the Fermi surface.

## 2.6 Seebeck Coefficient

In Eq. 2.1 the Seebeck coefficient was defined to scale the electric field caused by a temperature gradient applied to a material. Employing the Boltzmann theory outlined in the previous section, analytical representations of the thermopower for metals and semiconductors will be given here. It will be shown that electronic correlation gives rise to distinct thermoelectric effects. Finally, non-diffusive thermopower contributions gaining importance in solids of strongly coupled electron and phonon systems are discussed, too.

### 2.6.1 Diffusive Thermopower

The electronic contribution to the Seebeck coefficient can be calculated in the framework of the Boltzmann theory as outlined in Sec. 2.5. From Eq. 2.55b, the Seebeck coefficient of an isotropic 3D solid evaluates to [39]

$$S = \mp\frac{1}{eT}\frac{K_1}{K_0} = \mp\frac{1}{eT}\frac{\int g(\epsilon)\left[\vec{v}(\epsilon)\otimes\vec{v}(\epsilon)\right]\tau(\epsilon-\mu)\frac{\partial f^0}{\partial\epsilon}d\epsilon}{\int \underbrace{g(\epsilon)\left[\vec{v}(\epsilon)\otimes\vec{v}(\epsilon)\right]\tau\frac{\partial f^0}{\partial\epsilon}}_{\sigma'(\epsilon)}d\epsilon} = \mp\frac{1}{eT}\frac{\int(\epsilon-\mu)\sigma'(\epsilon)d\epsilon}{\int\sigma'(\epsilon)d\epsilon} \quad , \tag{2.74}$$

introducing the differential conductivity $\sigma'(\epsilon)$. Eq. 2.74 reveals the thermopower to be determined in first approximation by the energy of the states contributing to the charge carrier transport relative to the chemical potential. In metals the Fermi energy lies within the band, i.e. the transport levels are close to the Fermi energy and the Seebeck coefficient takes small values of about $\mu\mathrm{V\,K^{-1}}$. In contrast, the Fermi energy of non-degenerate semiconductors is located in the bandgap of forbidden energy states causing a large energy difference to the charge-carrying states, yielding large Seebeck coefficients on the order of $\mathrm{mV\,K^{-1}}$. The two cases of the degenerate and non-degenerate approximation for metals and semiconductors are treated separately in more detail below. In addition, further implications from the correlated interaction of charge carriers and spins will be presented.

#### Metals

For a degenerate conductor ($k_BT \ll \epsilon_F$) with isotropic energy bands, the Seebeck coefficient can be worked out employing the relation $K_1 = \pi^2/3(k_BT)^2[\partial K_0(\epsilon)/\partial\epsilon]_{\epsilon=\epsilon_F}$, giving rise to a linear temperature dependence of the form [121]:

$$S = \frac{\pi^2 e k_B^2 T}{3\sigma} \left[\frac{\partial K_0(\epsilon)}{\partial \epsilon}\right]_{\epsilon=\epsilon_F} = \frac{\pi^2 k_B^2 T}{3e} \left[\frac{\partial \ln \sigma(\epsilon)}{\partial \epsilon}\right]_{\epsilon=\epsilon_F} \quad . \tag{2.75}$$

If a single band dominates the charge carrier transport, the thermopower can be expressed by [148]

$$S = -\frac{\pi^2 k_B^2 T}{3|e|} \cdot \left[\frac{\cos \delta\pi/2}{2|t|(1-\cos^2 \delta\pi/2)} + \frac{\tau'(\epsilon)}{\tau(\epsilon)}\bigg|_{\epsilon=\epsilon_F}\right] \tag{2.76}$$

with the transport integral $t = W/4$, the bandwidth $W$, the charge transfer ratio $\delta$ and the energy-depedent relaxation time $\tau(\epsilon)$ and its respective derivative $\tau'(\epsilon)$. A relaxation time of the form $\tau = c_0 \epsilon^r$ together with a Fermi energy of $E_F = W\delta/2$ yields:

$$S = -\frac{2\pi^2 k_B^2 T}{3|e|W} \cdot \left[\frac{\cos \delta\pi/2}{(1-\cos^2 \delta\pi/2)} + \frac{r}{\delta}\right] \quad . \tag{2.77}$$

Deviations from a linear dependence can occur if the relaxation time strongly depends on energy and temperature or if more than a single band contributes to the electrical conductivity. In general, the Seebeck coefficient can be written as the sum of the individual band thermopowers $S_i$ weighted by their respective conductivities $\sigma_i$ [149]:

$$S = \frac{\sum_i \sigma_i S_i}{\sum_i \sigma_i} \quad . \tag{2.78}$$

Eq. 2.78 again emphasizes that only transport states of high conductivity contribute to the Seebeck coefficient.

### Semiconductors

Assuming a similar energy-dependent relaxation time as above, the Seebeck coefficient for the isotropic, non-degenerate approximation ($k_B T \gg E_F$) reads [37]

$$S = \mp \frac{k}{e} \left[\frac{\epsilon_{c/v} - \epsilon_F}{k_B T} - \left(r + \frac{5}{2}\right)\right] \tag{2.79}$$

where $\epsilon_{c/v}$ denotes the position of the conduction or valence band relative to the Fermi energy. For both, electrons and holes being present in the system, Eq. 2.78 applies and the measurement of the Seebeck coefficient allows for the determination of the majority carriers in semiconductors. Also, information on the Fermi energy in doped semiconductors and the charge carrier scattering mechanisms may be obtained. In the case of incoherent transport via variable range hopping processes as described by Eq. 2.68, the finite density of states $g(\epsilon_F)$ at the Fermi level determines the thermopower [41]:

$$S = \frac{g(\epsilon_F)\Delta\epsilon^2}{eT} = \frac{g(\epsilon_F)k_B^2 T_0^2}{e}\left(\frac{T}{T_0}\right)^{\frac{d-1}{d+1}} \propto \begin{cases} T^{1/2} & , d = 3 \\ T^{1/3} & , d = 2 \\ \text{const} & , d = 1 \end{cases} . \tag{2.80}$$

Similar to the conductivity it depends on the dimensionality $d$ of the system.

#### Interacting Spins and Charges

The mutual interaction of charges as well as the coupling of spins to the magnetic moment of ions can have significant effects on the Seebeck coefficient [41]. In Sec. 2.2.2, a one-dimensional conductor close to half band filling was predicted to be an insulator in the presence of strong electron-electron correlations. This is caused by the electrons repelling each other and distributing almost equidistant among the respective lattice sites. In Eq. 2.11a, the thermopower was defined as the entropy per charge carrier. The entropy $\Sigma$ of a system of $N$ electrons distributing among $N_L$ lattice sites is [41]

$$\Sigma = k_B \ln\left[\frac{N_L!}{N!(N_L - N)!}\right] . \tag{2.81}$$

Taking the derivative with respect to N results in *Heikes' formula* for hopping thermopower [41]:

$$S = \frac{\partial\Sigma}{\partial N} = -\frac{k_B}{|e|}\ln\left[\frac{1-\delta/2}{\delta/2}\right] . \tag{2.82}$$

Here, $\delta$ again denotes the charge transfer ratio determining the band filling in organic conductors. This historic formula does not take into account the Pauli exclusion principle but only allows for one charge carrier per site due to the strong on-site Coulomb interaction. In the strong U-limit, the spin degeneracy is often lifted and the additional spin entropy of $k_B \ln 2$ has to be added to Eq. 2.82, resulting in the Seebeck coefficient of a Mott-Hubbard metal exhibiting strong Coulomb repulsion [41]:

$$S = \frac{\partial\Sigma}{\partial N} = -\frac{k_B}{|e|}\left[\ln\left(\frac{1-\delta/2}{\delta/2}\right) + \ln 2\right] . \tag{2.83}$$

### 2.6.2 Nondiffusive Phonon Drag Thermopower

In addition to the purely electronic contribution, the so-called *phonon drag* can further enhance the thermopower of a given material [41]. It is caused by the phonon heat flow forcing charge carriers along a temperature gradient due to electron-phonon coupling. It can be deduced from the following picture. The charge carrier conduction is limited by the interaction with impurities, defects as well as scattering by other quasiparticles such

as phonons. If electrons and phonons were only interacting with each other, both would eventually move at the same velocity because momentum is only transferred in between them. In this situation the electrical conductivity of the sample would be infinite due to momentum conservation. When receiving momentum from the electrons, the phonons need to redistribute the momentum to other entities in order to give rise to resistivity. These can be impurities, boundaries or other phonons via non-momentum conserving scattering events (U-processes). The velocities of phonons $\vec{u}_{ph}$ and electrons $\vec{v}_{el}$ are then related by [41]

$$\vec{u}_{ph} = \vec{v}_{el} \frac{\tau_{ph-e}^{-1}}{\tau_{ph-e}^{-1} + \tau_{other}^{-1}} \tag{2.84}$$

with the phonon-electron relaxation rate $\tau_{ph-e}^{-1}$, the rate of phonon relaxation via other channels $\tau_{other}^{-1}$. Eq. 2.84 relates the resulting phonon heat flow $\vec{U}_{ph} = C_{ph} T \vec{u}_{ph}$ to the electron velocity $\vec{v}_{el} = \vec{J}/ne$ giving rise to a Peltier heat flow proportional to the current density. With the help of Eqs. 2.2 and 2.3 the corresponding Seebeck coefficient then reads [41]

$$S_{drag} = \frac{C_{ph}}{ne} \underbrace{\frac{\tau_{ph-e}^{-1}}{\tau_{ph-e}^{-1} + \tau_{other}^{-1}}}_{\beta} \quad , \tag{2.85}$$

$C_{ph}$ characterizing the specific heat per volume of the involved phonon modes and $n$ being the charge carrier density. Assuming a Debye-like specific heat as elaborated in Eq. 2.48 and relative scattering rates of the form $\beta = \left(\frac{T_0}{T}\right)^{\upsilon}$, one obtains an analytical expression for the phonon drag thermopower:

$$S_{drag} = \frac{9 N k_B \rho_{dens}}{n e m_{mol}} \left(\frac{T_0}{T}\right)^{\upsilon} \left(\frac{T}{\theta_D}\right)^3 \int_0^{\theta_D/T} dz \frac{z^4 e^z}{(e^z - 1)^2} \quad . \tag{2.86}$$

Here, $\rho_{dens}$ and $m_{mol}$ denote the volumetric mass density and the molar mass, respectively. The phonon drag thermopower rises cubically in temperature for $T \ll \theta_D$, goes through a maximum around $T \approx \theta_D/5$ and falls with $T^{-\upsilon}$ for high temperatures due to the limiting non-momentum conserving scattering process. In case of Umklapp scattering, $\upsilon = 1$ is to be expected. Moreover, the phonon drag effect is responsible for a reduction of the phonon scattering part in the resistivity [41]:

$$\rho = \rho_0 + \rho_{e-ph} \left(1 - \frac{\tau_{e-ph}^{-1}}{\tau_{e-ph}^{-1} + \tau_{other}^{-1}}\right) \quad . \tag{2.87}$$

## 2.7 Heat Transport

A solid's capability to transfer heat is not only of technological relevance in applications such as heat sinking, thermal insulation or thermoelectric energy generation, but also enables a fundamental investigation of solid state transport properties. Heat can be transmitted via charge carriers, phonons, spins, electromagnetic waves and various other excitations. The total thermal conductivity $\kappa$ can be written as the sum of all these contributions [121]

$$\kappa = \sum_i \kappa_i \approx \frac{1}{3} \sum_i C_i v_i l_i \tag{2.88}$$

where $C_i$ is the heat capacity and $l_i = v_i \cdot \tau_i$ is the mean free path of excitation $i$ with relaxation time $\tau_i$ and velocity $v_i$. Therefore, a detailed analysis of the thermal conductivity provides insight into the fundamental excitations and their interaction in a solid. Based on a combination of perturbation theory and Boltzmann equation, in the following the contributions by charge carriers and phonons will be discussed, representing the main contributors to heat transport in the investigated material class.

### 2.7.1 Electronic Thermal Conductivity

Electrons moving in an electric field do not only carry charge but also transport heat. The electronic contribution to thermal conduction can be expressed with the help of Eqs. 2.55c and 2.53 by [121]:

$$\kappa_e' = \frac{1}{T}\left[K_2 - \frac{K_1^2}{K_0}\right] = \kappa_e \left(1 - \frac{S^2 \sigma T}{\kappa_e}\right) = \kappa_e \left(1 - zT\right) \quad . \tag{2.89}$$

The thermal conductivity $\kappa_e'$ relates the heat flow to a thermal gradient in the absence of an electric field. It has to be distinguished from the thermal conductivity $\kappa_e$ in the absence of a charge current ($J_e = 0$) and thus, the obtained thermal conductivity depends on the measurement configuration used. However, for small values of $zT$ both thermal conductivities can be assumed to be identical. In the following, specific approximations to evaluate the transport integrals will be discussed and in particular, the case of the degenerate and the non-degenerate electron gas as well as a delta function in the density of states.

#### Electronic Thermal Conductivity in Metals

The transport integrals $K_s$ can be expanded around the Fermi energy leading to an approximation of $K_2$ for the degenerate electron gas where the Fermi energy lies within the

conduction band [39]:

$$K_2 = \frac{\pi^2}{3}\frac{k_B^2 T^2}{e^2}\sigma(\epsilon_F) + \mathcal{O}(k_B T/\epsilon_F)^2 \quad . \tag{2.90}$$

Neglecting $K_1^2/K_0 \approx \mathcal{O}(k_B T/\epsilon_F)^2$, Eq. 2.89 reads

$$\kappa_e' = \kappa_e = \frac{\pi^2}{3}\frac{k_B^2 T}{e^2}\sigma(\epsilon_F) = L_0 \cdot \sigma(\epsilon_F) \cdot T \tag{2.91}$$

which is the well-known *Wiedemann-Franz law* (WF law) relating the electronic thermal conductivity to the electrical conductivity $\sigma$. It basically states that each charge carrier not only transports charge in an electric field but also energy. The proportionality factor $L_0 = 2.4453 \times 10^{-8}\,\mathrm{W\,\Omega\,K^{-2}}$ is called the *standard Lorenz number*. The Wiedemann-Franz law is well obeyed in metals above the Debye temperature when scattering events are elastic. At lower and intermediate temperatures it breaks down due to inelastic charge carrier scattering [121]. For the specific case of an isotropic, degenerate electron gas it also does not depend on the specific band structure. Similar to the derivation of the Bloch-Grüneisen formula for the electrical conductivity as given in Eq. 2.61, the relaxation rate for thermal perturbations taking into account scattering of electrons by acoustic phonons is given by [121]

$$\frac{1}{\tau_{th}} = \frac{9\pi h^2 C^2}{\sqrt{8m^*}a^3 M k_B \theta_D \epsilon_F^3}\left(\frac{T}{\theta_D}\right)^5 J_5\left(\frac{\theta_D}{T}\right) \times \left[1 + \frac{3}{2\pi^2}\left(\frac{k_F\theta_D}{q_D T}\right)^2 - \frac{1}{2\pi^2}\frac{J_7(\frac{\theta_D}{T})}{J_5(\frac{\theta_D}{T})}\right] \ , \tag{2.92}$$

extending the previously discussed Bloch-Grüneisen formula by two summands originating from differences in the relaxation times. The second term in the squared brackets arises due to small angle scattering events being able to relax the thermally perturbed Fermi distribution back into equilibrium. In contrast, small angle scattering processes do not permit to equilibrate the field perturbation as illustrated in Fig. 2.20. The third term corrects for large angle scattering events which reverse the electron direction but leave the thermal distribution unchanged, corresponding to a scattering event from + (-) region of the thermally perturbed Fermi surface to the + (-) region on its opposite site in Fig. 2.20. The Lorenz number for a degenerate conductor reads with the help of Eqs. 2.92, 2.61 and 2.89 [121]:

$$L = \frac{\kappa}{\sigma T} = L_0 \frac{A\left(\frac{T}{\theta_D}\right)^5 J_5\left(\frac{T}{\theta_D}\right)}{A\left(\frac{T}{\theta_D}\right)^5 J_5\left(\frac{T}{\theta_D}\right) \times \left[1 + \frac{3}{2\pi^2}(\frac{k_F\theta_D}{q_D T})^2 - \frac{1}{2\pi^2}\frac{J_7(\frac{T}{\theta_D})}{J_5(\frac{T}{\theta_D})}\right]} \quad . \tag{2.93}$$

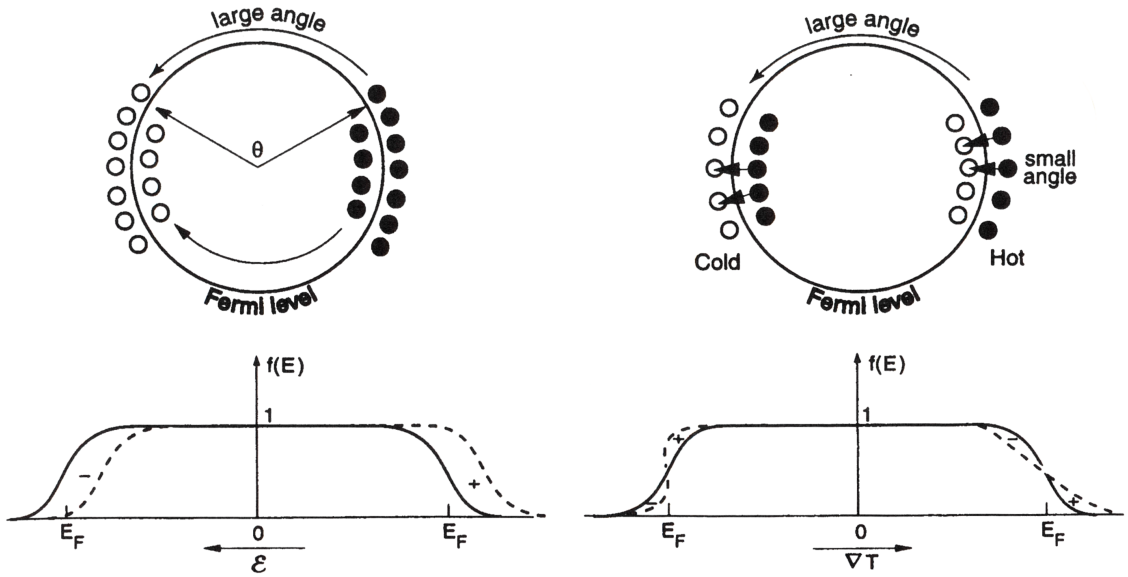


Figure 2.20: Perturbation of the Fermi distribution by an electric field (left) or thermal gradient (right). The electric field shifts the complete Fermi surface while the temperature gradient only smears out the step function. To relax back to equilibrium, large scattering angles are needed for electric fields while small angle scattering events may be sufficient to relax the distribution function in response to thermal gradients. Thus the two relaxation times can differ. From: [121]

In the high and low temperature limits of Eq. 2.93, the Lorenz ratio evaluates to [121]

$$\frac{L}{L_0} \approx \begin{cases} 1, & T \geq \theta_D \\ \frac{\pi^2}{3}(\frac{q_D T}{k_F \theta_D})^2, & T \ll \theta_D \end{cases} . \tag{2.94}$$

At high temperatures, the Wiedemann-Franz law is obeyed due to the dominance of large angle scattering events determining both, the thermal and the electric field relaxation time. Below the Debye temperature, the number of phonons with high wave vectors necessary for large scattering angles is limited and small angle scattering processes gain importance. These only provide a channel for the relaxation of thermal but not of electric field perturbations. As the corresponding relaxation times begin to differ, the Wiedemann-Franz law is violated due to the breakdown of the common relaxation time assumption.

In order to take several scattering mechanisms into account, the thermal resistivities emerging from the individual scattering mechanisms need to be added up [121]:

$$\frac{1}{\kappa_{tot}} = W_{tot} = \sum_i W_i = \sum_i \frac{1}{\kappa_i} \quad . \tag{2.95}$$

Including impurity and acoustic phonon scattering, Eq. 2.93 modifies to [121]

$$L = \frac{\kappa_{tot}}{\sigma T} = L_0 \frac{\rho_{imp}/A + \left(\frac{T}{\theta_D}\right)^5 J_5\left(\frac{T}{\theta_D}\right)}{\rho_{imp}/A + \left(\frac{T}{\theta_D}\right)^5 J_5\left(\frac{T}{\theta_D}\right) \times \left[1 + \frac{3}{2\pi^2}\left(\frac{k_F \theta_D}{q_D T}\right)^2 - \frac{1}{2\pi^2}\frac{J_7(\frac{T}{\theta_D})}{J_5(\frac{T}{\theta_D})}\right]} \quad , \tag{2.96}$$

$\rho_{imp}$ being the electrical impurity resistivity. The normalized temperature dependence of Eq. 2.96 is depicted in Fig. 2.21a for different impurity levels $\rho_{imp}/A$. It clearly shows the reduction of the Lorenz number when going below the Debye temperature in an impurity free sample. Upon increasing the impurity level, a common relaxation time for electric field and thermal perturbations of the Fermi function is restored at low temperatures and the Lorenz ratio approaches one again. The degree of purity is proportional to the residual resistance ratio $RRR = \rho(0\,\mathrm{K})/\rho(300\,\mathrm{K})$ in real samples. In pure copper wires, the impurity parameter on the order of $\rho_{imp}/A = 10^{-2}$ has been improved by one order of magnitude through sample annealing which is reflected in the temperature dependence of the Lorenz number, as illustrated in Fig. 2.21b [150].

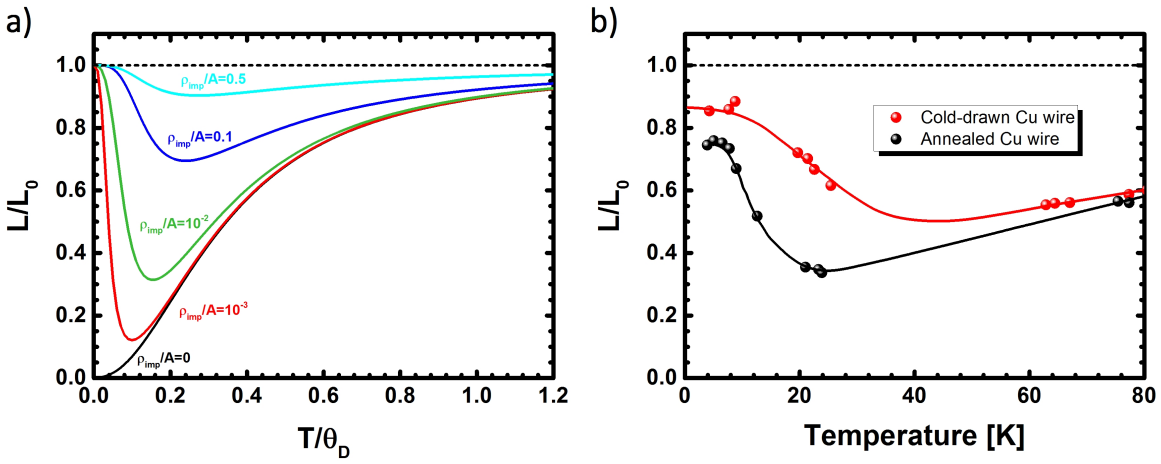


Figure 2.21: Temperature-dependent Lorenz ratio. (a) The temperature dependence of the Lorenz ratio as given by Eq. 2.96 normalized to the Debye temperature $\theta_D$ for different impurity concentrations $\rho_{imp}/A$. The Wiedemann-Franz law is strongly violated below the Debye temperature but on increasing impurity level a common relaxation time for thermal and electric field perturbations is restored at low temperatures due to impurity scattering. (b) An impurity-dependent, low-temperature Lorenz number has been qualitatively verified by increasing the perfection of a copper wire via annealing. Adapted from: [150]

### Electronic Thermal Conductivity in Semiconductors

In semiconductors the electronic part of the thermal conductivity may still have a significant share in the total thermal conductivity. In the nondegenerate approximation, assuming an energy-dependent relaxation time $\tau \propto \epsilon^r$ as expressed in Eq. 2.58, the Lorenz number according to Eq. 2.89 reads [37]:

$$L = \left(\frac{k_B}{e}\right)^2 \left(r + \frac{5}{2}\right) \quad . \tag{2.97}$$

The contribution from minority carriers is neglected in this approximation. When two types of carriers contribute to the electrical conductivity, e.g. electrons and holes in an intrinsic semiconductor, the total electronic thermal conductivity is given by the sum of the carrier's thermal conductivities $\kappa_i$ and an additional bipolar diffusion term [121]:

$$\kappa = \kappa_e + \kappa_h + \frac{\sigma_e \sigma_h (S_e + S_h)^2}{\sigma_e + \sigma_h} T \tag{2.98}$$

$S_i$ and $\sigma_i$ representing the partial Seebeck coefficients and conductivities of the respective charge carrier. The additional term arises from the Peltier heat flow occurring in case of more than just one type of charge carrier. It is most easily observed in small bandgap intrinsic semiconductors where the partial conductivities of electrons and holes are high enough for the effect not to be masked by other contributions, such as phonon thermal conductivity.

### Influence of Density of States

In general, the transport integrals and hence the Lorenz number depend on the material's density of states $g(\epsilon)$. An interesting situation unfolds when the density of states takes the form of a delta function at the Fermi energy, i.e. $g(\epsilon) \propto \delta(\epsilon - \epsilon_F)$. In this case no electronic contribution to the thermal conductivity may be observed due to a vanishing Lorenz number. While the realization in a solid is difficult, theories predict a huge enhancement in $zT$ for a material with delta-functional density of states [151, 152]. The energy-dependent scattering time takes an equivalent position in the transport integral of Eq. 2.53 like the density of states. A narrow Lorentzian shape of the scattering time's energy dependence, as predicted in Sec. 2.5.2 for the organic conductor $TTT_2I_3$, comes very close to the proposed delta-functional form and similarly should lead to a violation of the Wiedemann-Franz law [49].

### 2.7.2 Lattice Thermal Conductivity

The lattice thermal conductivity describes the heat carried by phonons in a solid. It is also sometimes called phonon thermal conductivity. Similarly to Eq. 2.88, the phonon thermal conductivity may be expressed as a sum over the contributions from all phonon branches $i$ [121, 39]

$$\kappa_{ph} = \frac{1}{3}\sum_i c_i v_i l_i \approx \frac{1}{3} c_a v_s l_{ph} \tag{2.99}$$

with the mode-specific heat capacity per unit volume $c_i$, the group velocity $v_i$ and the phonon mean free path $l_i$. More generally, the phonon thermal conductivity may also be anisotropic and the exact phonon dispersion along the different crystallographic directions needs to be considered. The majority of heat is carried by acoustic phonons due to the small group velocity of optical phonon modes. It leads to the approximation given in Eq. 2.99 with the acoustic lattice specific heat per unit volume $c_a$, the speed of sound $v_s$ and the phonon mean free path $l_{ph} = v_s \tau_{ph}$, $\tau_{ph}$ denoting the relaxation time of the acoustic phonons. In the approximation above $\tau_{ph}$ was assumed to be independent of energy. Employing the Debye approximation for the lattice specific heat and taking the speed of sound to be independent of frequency, Callaway applied the Boltzmann theory to the perturbation of the phonon distribution function in order to calculate the lattice thermal conductivity more rigorously [153]

$$\begin{aligned}
\kappa_{ph} =& \kappa_1 + \kappa_2 \\
\kappa_1 =& \frac{k_B}{2\pi^2 v_s}\left(\frac{2\pi k_B T}{h}\right)^3 \int_0^{\theta_D/T} \tau_{tot} \frac{x^4 e^x}{(e^x-1)^2} dx \\
\kappa_2 =& \frac{k_B}{2\pi^2 v_s}\left(\frac{2\pi k_B T}{h}\right)^3 \frac{\left(\int_0^{\theta_D/T} \frac{\tau_{tot}}{\tau_N} x^4 e^x (e^x-1)^{-2} dx\right)^2}{\int_0^{\theta_D/T} \frac{\tau_{tot}}{\tau_N} x^4 e^x (e^x-1)^{-2} dx}
\end{aligned} \tag{2.100}$$

with the Debye temperature $\theta_D$ and the total scattering rate [39]

$$\frac{1}{\tau_{tot}} = \frac{1}{\tau_s} + \frac{1}{\tau_N} + \frac{1}{\tau_U} \tag{2.101}$$

characterizing the phonon relaxation in the solid. A crystal with solely harmonic interaction potentials does not provide any phonon-phonon interaction mechanism and would exhibit infinite thermal conductivity [121]. In real crystals the anharmonicity in the interaction potential between the atoms and molecules allows for phonon-phonon scattering. Three interaction mechanisms are included in Eq. 2.101. In addition to elastic scattering

events described by the relaxation time $\tau_S$, normal processes ($\tau_N$) and Umklapp processes ($\tau_U$) are distinguished. Similarly to the electron scattering theory, Umklapp processes involve a reciprocal wave vector as the scattered phonon wave vector points out of the first Brillouin zone of the crystal, in contrast to normal processes. Hence, the momentum change is significantly larger for Umklapp scattering and results in higher thermal resistivity. Normal processes only play a role at very low temperatures where the number of phonons with sufficiently high wave vectors permitting Umklapp scattering is negligibly small. In case of prevailing Umklapp processes, i.e. for $\tau_N \gg \tau_U$, $\kappa_1$ in Eq. 2.100 dominates the overall thermal conductivity while for N-processes $\kappa_2$ gives the major contribution. Several theories have been developed to calculate the phonon-phonon relaxation rate for Umklapp scattering, the most widely applied one yielding [121]:

$$\frac{1}{\tau_U} = A_U \omega^2 T e^{-B_U \frac{\theta_D}{T}} \quad . \tag{2.102}$$

Here, $\omega$ denotes the phonon frequency while $A_U$ and $B_U$ are material-dependent constants. In addition to the interaction with other phonons, the lattice vibrations can also be scattered by impurities and at the boundary of the crystal. Boundary scattering becomes important at very low temperatures when the phonon mean free path is comparable to the crystal dimensions. It can be described by [121]

$$\frac{1}{\tau_b} = \frac{1.12 v_g}{d} \tag{2.103}$$

with the group velocity $v_g$ of the phonon mode and the dimension $d$ of the crystal. In addition, the interaction with impurities can be expressed as [121]

$$\frac{1}{\tau_{imp}} = \frac{V_0}{4\pi v_g^3} \left( \frac{\Delta M}{M} \right)^3 \omega^4 \quad , \tag{2.104}$$

$V_0$ denoting the effective volume of the impurity, $M$ being the mass of all atoms in a unit cell of the crystal and $\Delta M$ the mass difference between the substance and the impurity. Depending on the relative concentration of impurities, boundary or impurity scattering limits the phonon mean free path at low temperatures. Rarely, the effect of N-processes is observed at very low temperatures as well [121]. At high temperatures ($T > \theta_D$), the lattice heat capacity remains almost constant and the Umklapp-dominated phonon scattering, as described by Eq. 2.102, together with Eq. 2.100 yields a $\kappa_{ph} \propto T^{-1}$ dependence.

So far, the phonon thermal conductivity was discussed in terms of acoustic phonons carrying the majority of heat. Yet, the phonon spectra in molecular crystals are significantly more complex due to the large number of molecules per unit cell and the low

symmetry of the latter, leading to an increased number of optical phonon modes. Some of these modes have frequencies of similar magnitude to the acoustic phonon branches allowing for optical-acoustic phonon coupling. An expression for the resonant scattering rate of acoustic phonon by localized optical phonon modes has been phenomenologically derived from expressions for resonant defect scattering [154]

$$\frac{1}{\tau_R} = N_0 D \frac{\omega_0^2 \omega^2}{(\omega_0^2 - \omega^2)^2} \tag{2.105}$$

with the optical phonon frequency $\omega_0$, the acoustic phonon frequency $\omega$, the coupling strength $D$ and density of scatterers $N_0$. These resonant phonon modes are often due to disorder of molecular units.

### 2.7.3 Minimum Thermal Conductivity in Solids

In glasses, representing amorphous insulators without long-range order, phonons are still the major carrier of heat but with a significantly reduced phonon mean free path [121]. The thermal conductivity of glasses rises for very low temperature ($<$1 K) with $\kappa \propto T^n$ where the observed $n \approx 2$ has been attributed to the scattering of low-energy phonons. Following the steep rise, a plateau is often observed which has been interpreted in terms of several scattering mechanisms, such as structural disorder, tunneling interaction or resonant optical-acoustic phonon coupling as described by Eq. 2.105. Above about 20 K the thermal conductivity of glasses rises again. At sufficiently high temperatures, Kittel argued that the phonon picture of plane waves propagating through a crystal breaks down for glasses by virtue of a phonon mean free path being on the scale of the disorder in the material [155]. It may be compared to charge carrier transport in organic crystals often revealing a crossover from coherent band to incoherent hopping transport. When the mean free path is set by the disorder, the thermal conductivity follows the heat capacity which rises with temperature to a constant value, explaining the characteristic thermal conductivity of glasses. The characteristic temperature-dependent thermal conductivity of a glass is compared to the phonon thermal conductivity of a crystal in Fig. 2.22.

The model of strongly-damped localized Einstein oscillators which transfer their energy within half of an oscillation period $2/\tau_E$ in a random walk can theoretically capture the physics. Implementing the Einstein specific heat of optical phonons, a mean free path corresponding to the interatomic spacing $l = n^{-1/3}$ and a thermal velocity of $v_{th} = 2l/\tau_E$, the Einstein thermal conductivity yields [157]

$$\kappa_{Ein} = \frac{n^{-1/3} k_B^2 \theta_E x^2 e^x}{\pi h (e^x - 1)^2} \tag{2.106}$$

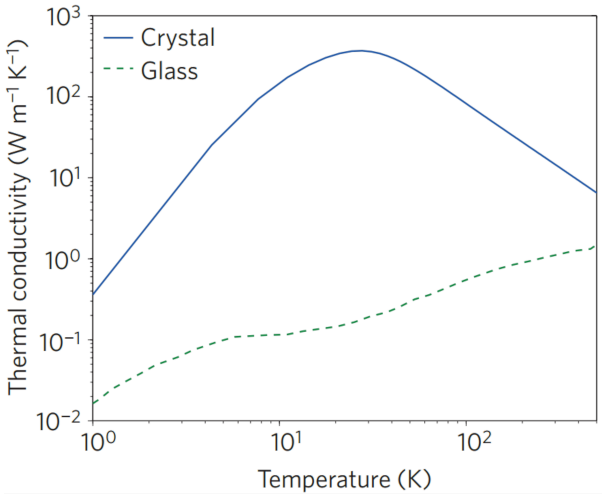


Figure 2.22: Schematic lattice thermal conductivity of a crystal and a glass. For a crystal the thermal conductivity is limited by the phonon mean free path above the Debye temperature and by the heat capacity at cryogenic temperatures, resulting in a pronounced maximum in between these limits. The phonon mean free path of glasses is less temperature-dependent and the thermal conductivity increases with temperature following the heat capacity. Adapted from: [156]

with the Einstein temperature $\theta_E$ and the reduced temperature $x = \theta_E/T$. A similar result can be obtained by applying the Debye instead of the Einstein model. The general approach is to consider different phonon modes contributing to the thermal conductivity by [121]

$$\kappa_{Min} = \int_0^\infty \frac{dC}{d\omega} v(\omega) l(\omega) d\omega \quad . \tag{2.107}$$

Here, $\frac{dC}{d\omega}$ denotes the specific heat per frequency. By applying the Debye model for the specific heat and assuming the scattering length to be half of the phonon wavelength, a minimum thermal conductivity per mode can be deduced from this approach [157]

$$\kappa_{Min} = \frac{2}{2.48} n^{2/3} k_B v \left(\frac{T}{\theta_c}\right)^2 \int_0^{\theta_c} \frac{x^2 e^x}{(e^x - 1)^2} dx, \tag{2.108}$$

with the mode specific cut-off temperature $\theta_c = \frac{\hbar}{k_B v_i (6\pi^2 n)^{1/3}}$. For the total thermal conductivity the two transverse and one longitudinal modes are summed up, resulting in a high temperature limit ($T \gg \theta_D$) of Eq. 2.108 [157]

$$\kappa_{Min} = \frac{1}{2.48} n^{2/3} k_B (2v_t + v_l) \quad , \tag{2.109}$$

with the transverse and longitudinal speed of sound $v_t$ and $v_l$.

Compared to other thermal properties, such as the heat capacity, theories on the thermal conductivity do quantitatively not compare as good to the experimental data. On the one hand this is due to the many simultaneous excitations giving rise to thermal conduc-

tivity in solids which can be hard to distinguish. On the other hand the lack of coherent data sets on high-purity samples of different material classes hinders a comprehensive general understanding. For this reason, the presented theories are expected to predict a certain behavior, trend and magnitude rather than agreeing in absolute values.

# Chapter 3

# Experimental Methods

This chapter is intended to outline all relevant experimental methods employed in this thesis. Firstly, the details of the electrolytic crystal growth to obtain high-purity $(DCNQI)_2M$ single crystals are presented. It follows the more detailed depiction in my diploma thesis [65] and was updated with respect to the latest advances of this procedure. In the second part, the thermoelectric characterization setup is introduced. It was newly designed, implemented and characterized in the course of my PhD work and allows for an unprecedented, comprehensive characterization of all relevant thermoelectric quantities in organic conductors. As such, it constitutes an integral part of the scientific achievement accomplished by this thesis.

## 3.1 Electrolytic Crystal Growth

### Experimental Setup

The investigated $(DCNQI)_2M$ (M=Cu, Li) radical anion salts were grown by electrocrystallization representing a well-established method to grow high-purity single crystals of organic conductors. A typical electrolysis cell used in this thesis is shown in Fig. 3.1a.

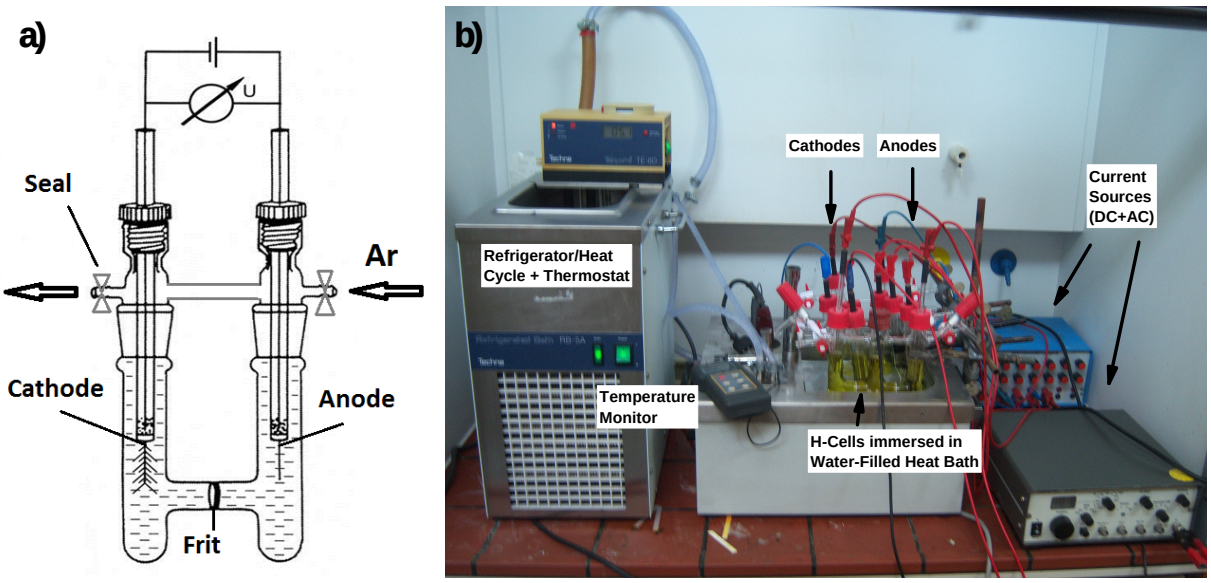


Figure 3.1: Experimental setup for electrocrystallization. (a) Scheme of the electrolysis cell used (adapted from: [58]) and (b) photograph of the electrolytic growth apparatus.

The H-cell (or sometimes U-cell), made of glass with an additional tube connecting the anode and the cathode region at the top, contains a glass filter (frit) at the bottom to prevent diffusion of anode products to the cathode. The two rod-like platinum electrodes have dimensions of 10 mm x 1 mm (length x diameter). The electrical feedthroughs are molded into glass and the whole electrode is fixed onto the H-cell by a Quickfit screw plug with a silicone-PTFE seal. Two inlets with valves allow to flush the filled cell with Argon via the top bridge. As their positions slightly differ in height, filling Argon into the lower inlet will push out the air in the cell due to its higher density, ensuring inert conditions during crystal growth. Because of the sensitivity to impurities, the electrocrystallization process needs to be preceded by a thorough cleaning procedure of all glassware used.

### Cleaning & Preparation of the Cell

In a first step, all glassware was cleaned in an automated laboratory dish washer in an alkaline cleaning detergent. Afterward, the glassware was filled with 0.02 M $KMnO_4$ and was allowed to stand for one week. $KMnO_4$ oxidizes most organic impurities leaving behind

manganese dioxide. After removing the $KMnO_4$ and washing the cell with distilled water, the residual manganese dioxide was dissolved by filling the glassware with concentrated hydrochloric acid (37%) for one day. Next day, the glassware is rinsed again with distilled water at least 5 times before it is baked-out in an oven at 420 K to remove water condensed on the surface. Finally, the last step is repeated with dry acetonitrile which is used as solvent in the crystallization process.

The electrolyte was prepared in a glovebox under nitrogen atmosphere. For this, a screw top jar is taken out of the oven and transferred to the glovebox via a load-lock system while still hot. DCNQI and a proper cation salt are dissolved in 50 ml of acetonitrile at a concentration of 7 mmol/l and 5.5 mmol/l, respectively. $Cu(CH_3CN)_4ClO_4$ or $LiClO_4$ were employed as conducting salts, depending on the desired metallic counterion in the final $(DCNQI)_2M$ (M = Cu, Li) product. The weigh-in and solvation procedure is directly conducted in the purged jar to avoid any contamination from the usage of multiple glass wares. The high-purity acetonitrile (99.9%, Sigma Aldrich) was additionally dried by a molecular sieve of 3 Å pore size before use. The resulting solution was retrieved from the glovebox and outgassed in an ultrasonic bath for 20 minutes. In the mean time, the H-cell is taken out of the oven, sealed and flushed with Argon while still hot. The platinum electrodes are etched with *aqua regia* and washed with acetonitrile. In a last step, the electrolytic solution is immersed into the H-cell in a counter flow of Argon and the electrodes are inserted into the cell. The complete arrangement is finally flushed with Argon after which the cell is sealed and immersed into a thermostat-controlled bath at 305 K. Lastly, a constant current between 5 µA and 20 µA was supplied to the cell for several days by means of an electrolysis cell controller (Elab 18/96). The full working setup is illustrated in Fig. 3.1b.

### Crystal Growth

The redox reaction occurring during the crystal growth are exemplary outlined for the $(DCNQI)_2Cu$ crystals. DCNQI molecules are reduced to $DCNQI^-$ at the cathode and subsequently, they form $(DCNQI)_2Cu$ single crystals by the reaction with the $Cu^+$ ions of the copper perchlorate. Upon crystallization, an additional charge transfer process between $DCNQI^-$ and $Cu^+$ takes place resulting in the formation of the final product:

$$DCNQI + DCNQI^- + Cu^+ \rightleftharpoons (DCNQI^{-2/3})_2Cu^{+4/3} \quad . \tag{3.1}$$

Figure 3.2a illustrates the crystal growth of radical anion salts at the cathode. As one can see, the crystals preferably grow at the edges of the cathode as they will offer a higher local electric field as well as more structural inhomogeneities at the surface serving as

nucleation sites. When the electrolysis is stopped too late, the crystals branch out due to the diffusion-limited aggregation and do not show defined crystalline shape anymore.

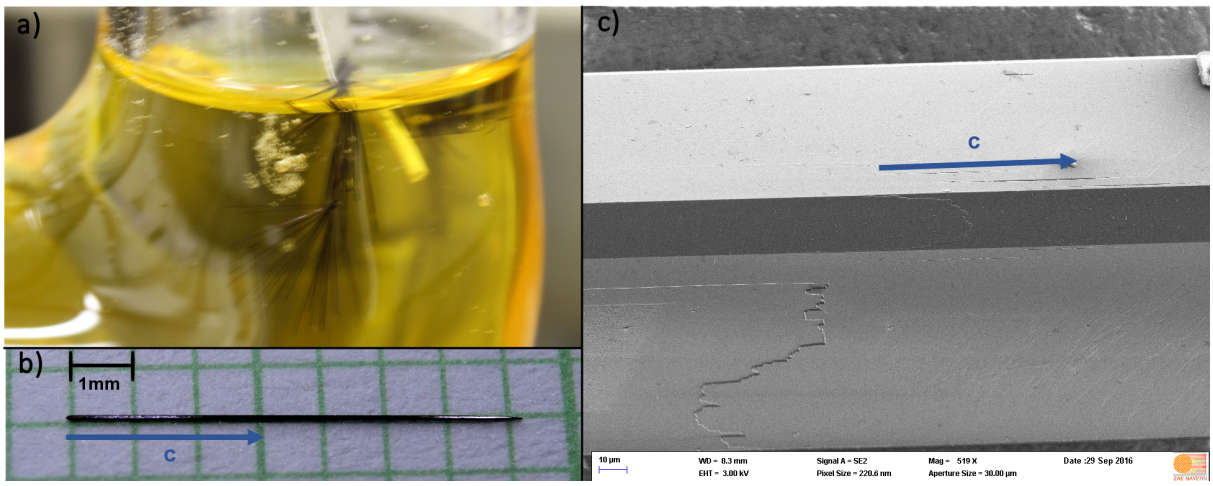


Figure 3.2: Crystals grown by electrolysis. (a) Growth of needle-like crystals at the cathode of an electrolysis cell. (b) $(DCNQI)_2Cu$ single crystal of several mm length and about 0.1 mm in diameter. (c) The SEM image of a crystal was kindly taken by Stephan Braxmeier at the ZAE Bayern.

At the end of the electrocrystallization the cathode is pulled out of the electrolysis cell and the crystals are swept off the electrode by ethanol onto filter paper. Thereafter, the crystals are washed with diethylether, separated with an ultra-fine tweezer and stored under inert conditions.

The dark-colored needle-like crystals attain thicknesses between 15 µm and 200 µm and lengths of up to 3 cm. Their reflective surface indicates the metallic character of the samples. Figure 3.2b depicts a photograph of a $(DCNQI)_2Cu$ crystal. The crystalline morphology with well-defined side faces and edges may also be inferred from the scanning electron microscope (SEM) image in Fig. 3.2c. The crystal structure has been determined by X-ray diffraction and was found to agree with the structures published previously [71, 66]. The weak binding forces in organic crystals generally classify them as soft matter and accordingly, the fragile samples tend to break easily when grabbed with the tweezer. In order to minimize the defects induced by sample handling, they were transferred with the help of a biopunch stamp to which the crystals adhere electrostatically.

## 3.2 Electrothermal Characterization of Charge and Heat Transport

The electronic and lattice properties of organic materials are very sensitive to the degree of purity and crystal perfection [158, 128, 159]. Moreover, the physical properties are most often highly anisotropic due to the strong spatial variation of the electronic overlap. These difficulties complicate a thorough thermoelectric characterization of new organic materials since the relevant transport coefficients are interrelated [53]. An optimum thermoelectric characterization of new materials is therefore conducted by measuring all three relevant quantities - the electrical conductivity $\sigma$, the thermopower $S$ and the thermal conductivity $\kappa$ - on the same specimen and in the same spatial direction. In addition, contacting the sample to wires or substrates easily imposes stress and effective pressures on the soft materials, in particular upon cooling to cryogenic temperatures. The transport properties in organic conductors are known to be highly pressure sensitive [160, 161, 162]. Hence, not only a measurement on the same specimen but also in the same contact configuration and experimental environment is desirable. Here, the novel measurement setup created in the course of this thesis is presented enabling a detailed temperature-dependent characterization of all three thermoelectric quantities on a single organic crystal, on the same sample holder in solely one experimental setup.

### 3.2.1 Measurement Setup

#### Cryostat

The transport measurements have been carried out in an Oxford Instruments He-flow cryostat in a temperature range from 4 K to 300 K. The cryostat was rebuilt and in its final version contains 16 electrical feedthroughs (4x Rigid BNC, 12x LEMO). An Oxford ITC-4 temperature controller finely regulates a resistive heater at the heat exchanger. The liquid helium flow through the heat exchanger is roughly adjusted for different temperature regimes. The samples are cooled down to 4 K at a rate smaller than $0.3\,\mathrm{K\,min^{-1}}$. Inside, a rhodium-iron temperature sensor close to the heater monitors the base temperature of the cryostat but for a more reliable temperature measurement, a silicon diode (Cryocon S900-BB) additionally records the sample temperature. The diode is thermally coupled to the sample holder base plate and is read out by a LakeShore 321 temperature controller. For cooling, the sample chamber is filled with helium gas at a pressure of 1 atm being in thermal contact with the heat exchanger through which liquid helium is pumped. Before cool-down, the sample chamber was flushed three times with pure helium gas to minimize condensing vapors at low temperatures.

For the thermopower and thermal conductivity measurements, heat losses to the environment via convection need to be minimized. These measurements are consequently performed in vacuum and therefore, the sample chamber has been evacuated to $10^{-6}$ mbar utilizing a turbomolecular pump backed by a membrane pump (Pfeiffer HighCube Eco 80). The measurements are performed while heating the sample from 4 K to room temperature (RT) in vacuum. As both, the thermopower and thermal conductivity measurements cannot be performed directly just after another, the sample needs to be cooled down twice to 4 K and the measurements are performed during subsequent temperature cycles.

### Sample Holder & Preparation

As outlined in Ch. 2.4.3, organic crystals show a large thermal expansion coefficient on the order of $10^{-4}\,\mathrm{K}^{-1}$ compared to inorganic materials ($10^{-6}\,\mathrm{K}^{-1}$-$10^{-5}\,\mathrm{K}^{-1}$). Thus, temperature-dependent measurements should be performed on suspended samples of these needle-like, fragile crystals in order to minimize the induced mechanical stress. Fig. 3.3 schematically illustrates the sample holder following Chaikin *et al.* [163]. It consists of a copper base plate onto which the silicon diode is mounted to measure the base temperature $T_0$. Onto the base plate two alumina blocks are glued with epoxy. Around each of the alumina blocks a NiCr heater wire is wound eight times and embedded into Stycast epoxy in order to establish a good thermal contact between the wire and the blocks. This allows for a separate heating of each block by feeding a current on the order of $10-100$ mA through the NiCr wire. The temperature difference between the two blocks is measured by a differential copper-constantan-copper (type-T) thermocouple glued on the top surface with silver paint.

Next, four gold or copper wires with diameters between $20-100$ µm are aligned parallel to each other across the blocks and glued to a respective block on opposite sides. Furthermore, the ends of these wires are glued by silver paint to electrical contact posts thermally grounded to the copper base plate in order to prevent the generation of parasitic thermoelectric voltages by contacts at different temperatures. Afterward, a drop of graphite paint (Dotite XC-12) is applied to the middle of each wire in between the two blocks and the needle-like crystal is placed onto the drops while being still wet. Under a microscope it is checked that the graphite paint creeps around the crystal and establishes electrical contact from all four crystal sides. In this way, contact resistances on the order of $1-10\,\Omega$ at 4 K have been achieved. The contact wires are cut at the end opposite to the contact post leaving behind an organic crystal electrically contacted to free-standing wires allowing for unhindered contraction and expansion. At its both ends, the sample is thermally connected to individual alumina heating blocks to impose a temperature gradient across the sample. As a last step, a radiative shield made of copper is screwed

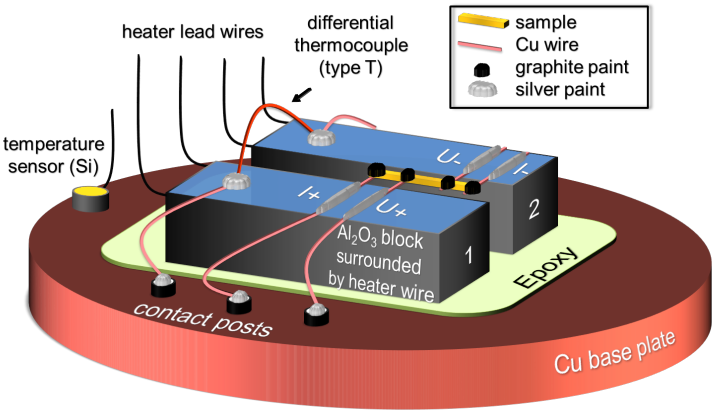


Figure 3.3: Scheme of the sample holder used for all transport measurements. To a copper base plate with electrical contact posts and a temperature sensor, two alumina blocks are glued. By graphite paint the sample is attached to four copper or gold wires which are thermally connected to the two different alumina blocks on opposite ends of the crystal. These can be heated independently by NiCr resistive heater wires wrapped around and glued on each block by thermally conductive Stycast epoxy. The temperature difference between the blocks is monitored by a type-T differential thermocouple (Cu-CuNi-Cu). The electrical contact posts are thermally grounded to the copper base plate to hinder spurious thermoelectric voltages to occur.

onto the copper base plate (not shown). Its surrounding of the sample ensures stable and reliable thermal conditions throughout each measurement. All subsequent measurements were performed on the same sample mounted onto the sample holder described above.

### 3.2.2 Electrical Conductivity

The most straightforward measurement is that of the electrical conductivity by means of a four-probe current-voltage measurement. With a Keithley 236 source measurement unit (SMU), a current $I$ is passed through the outer ones of four electrical contacts and the voltage drop $U$ at the inner two contacts is measured by an Agilent 34420A nanovoltmeter. Under the assumption that the size of the graphite paint contacts is small compared to the length of the crystal, no significant current flows through the voltage contacts facilitating the determination of the electrical conductivity $\sigma$ without the influence of contact resistances and lead wires by

$$\sigma = \frac{1}{R}\frac{2l}{A_{cs}} = \frac{I}{U}\frac{2l}{A_{cs}} \tag{3.2}$$

where $2l$ is the distance of the voltage contacts and $A_{cs}$ is the cross section of the crystal. The voltage can be measured to an accuracy better than 1 µV and the current is applied with an error of less than 1 pA. The overall accuracy of the resistance measurement has been determined to be better than about 1 mΩ. Hence, for sample resistances on the order of $1 - 10\,\Omega$ the main uncertainty of $\sigma$ stems from the error of the cross section $A_{cs}$

which is determined optically under the microscope.

### 3.2.3 Seebeck Coefficient

The Seebeck coefficient was measured following the method introduced by Chaikin and Kwak where a differential temperature gradient is imposed on a sample thermally connected to two heater blocks made of alumina [163]. The temperature difference between the two blocks is monitored by the Seebeck voltage of the differential thermocouple connected to the blocks while simultaneously the thermoelectric voltage of the sample is measured. Both voltages are recorded with an Agilent 34420A nanovoltmeter.

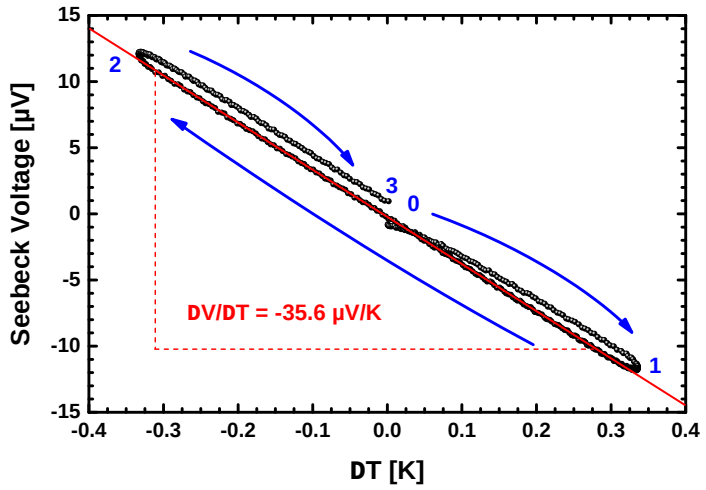


Figure 3.4: Typical curve obtained in the thermopower measurements. At first, block one is heated until a temperature gradient of about 0.3 K is established (0→1). Afterward, the heater is switched off and the second block is heated until a similar temperature gradient of −0.3 K, i.e., into the other direction is obtained (1→2). Finally, the first block is heated again until the temperature gradient is compensated (2→3). This data was recorded on a (DMe-DCNQI)$_2$Cu crystal at RT and the sample was connected to copper wires.

A representative measurement curve is depicted in Fig. 3.4. By slowly heating one of the blocks (0→1) a temperature gradient is imposed on the sample. When the temperature difference amounts to about 0.3 K, the heater of the first block is switched off and block two is heated until a temperature gradient of −0.3 K into the other direction is established (1→2). Then, the heater of the second block is switched off and block one is heated again until the temperature gradient vanishes (2→3). Slow heating rates of about 0.5 K min$^{-1}$ are used to ensure sufficient heat transfer from the alumina blocks to the sample. Away from the starting and turning points the slope of the measurement curve should be equal into both heating directions. From the linear part of the slope $\Delta V/\Delta T$ the thermopower $S$ can be determined by

$$S = \frac{\Delta V}{\Delta T} + S_{cw} \tag{3.3}$$

where $S_{cw}$ is the thermopower of the contact wires (Cu or Au) for which the measurement has to be corrected. It is one to two orders of magnitude smaller than the thermopower of the crystal and well-documented in literature [164]. At RT it amounts to about $1.6\,\mu V\,K^{-1}$. From Fig. 3.4, the Seebeck coefficient of $(DCNQI)_2Cu$ at RT can be determined to

$$S = -35.6\,\mu V\,K^{-1} + 1.6\,\mu V\,K^{-1} = -34.0\,\mu V\,K^{-1} \tag{3.4}$$

being in good agreement with literature data [85]. The measured temperature difference refers to the surface of the two alumina blocks and any heat losses along the length of the contact wires need to be minimized. Thus, measurements are performed in vacuum. After the sample was cooled down to 4 K in helium atmosphere, the sample chamber in the cryostat was evacuated to $10^{-6}$ mbar. While heating the temperature of the sample holder slowly to RT, measurement curves are recorded at temperature steps of $5-10$ K to ensure thermal equilibration in between each measurement cycle. Because cryogenic temperature measurements in vacuum are prone to error, the sample temperature was evaluated independently from the sample resistance determined after each Seebeck measurement and compared to reference measurements under helium atmosphere upon heating.

### 3.2.4 Thermal Conductivity

Compared to electrical transport measurements, determining the thermal conductivity $\kappa$ of a material is a challenging task since heat flow pathways are difficult to control. This problem becomes even more dramatic when performing measurements on small specimen of low thermal conductivity materials as the flow of heat through the sample is easily disturbed by, e.g., sensors. Furthermore, the high surface-to-volume ratio in small samples may lead to an overestimation of the thermal conductivity due to radiative heat losses, especially at high temperatures. To circumvent these issues, a variation of the $3\omega$ method has been applied to organic conductors for the first time in this thesis. It not only facilitates an accurate determination of $\kappa$ but moreover, yields a comprehensive investigation of the thermoelectric performance.

#### The $3\omega$ Method

The $3\omega$ method was developed by Cahill to measure the thermal conductivity of solid bulk samples and thin films [165]. The idea is straightforward: A periodic current of amplitude

$I_0$ and frequency $\omega$ is applied to a Joule heater of resistance $R_0$ causing a periodic heating at frequency $2\omega$:

$$P(t) = R_0 I_0^2 \sin^2(\omega t) = \frac{1}{2} R_0 I_0^2 \left(1 - \cos(2\omega t)\right) \quad . \tag{3.5}$$

In general, the resulting temperature oscillation $\Delta T$ caused by the periodic heating power $P(t)$ inside the heater is expressed by a thermal transfer function $Z(\omega)$ [166, 167]

$$\Delta T(t) = P(t) \otimes F^{-1}[Z(\omega)] \quad , \tag{3.6}$$

i.e. by a convolution of $P(t)$ with the inverse Fourier transform of the complex transfer function $Z(\omega)$ characterizing the thermal response of the system. Employing the convolution theorem, Eqs. 3.5 and 3.6 lead to [167]:

$$\Delta T(t) = \frac{R_0 I_0^2}{2} \left\{ Z(0) - Re[Z(2\omega)] \cos(2\omega t) + Im[Z(2\omega)] \sin(2\omega t) \right\} \quad . \tag{3.7}$$

Without including any boundary conditions, Eq. 3.7 describes the stationary heating as well as the temperature oscillation at frequency $2\omega$ in a resistor driven by a sinusoidal current of frequency $\omega$. The temperature amplitude is complex, meaning the respective real and imaginary part to oscillate *in-phase* and *out-of-phase* with respect to the heating power. If the resistance of the heater is temperature-dependent, the oscillating temperature driven by the periodic current inside the heater will lead to a voltage drop of the form [167]

$$\begin{aligned} U = & \quad R(t) \cdot I(t) \\ = & \quad \left\{ R_0 + R_0 \chi \Delta T(t) \right\} I_0 \sin(\omega t) \quad , \end{aligned} \tag{3.8}$$

$\chi = \partial \ln R / \partial T$ being the temperature coefficient of the heater's resistance. With the help of Eq. 3.7 it follows that [167]:

$$\begin{aligned} U(t) = & \quad R_0 I_0 \sin(\omega t) \\ & + \chi R_0^2 I_0^3 \left\{ \left( \tfrac{Z(0)}{2} + \tfrac{Re[Z(2\omega)]}{4} \right) \sin(\omega t) + \tfrac{Im[Z(2\omega)]}{4} \cos(\omega t) \right\} \\ & - \chi R_0^2 I_0^3 \left\{ \tfrac{Re[Z(2\omega)}{4} \sin(3\omega t) + \tfrac{Im[Z(\omega)]}{4} \cos(3\omega t) \right\} \quad . \end{aligned} \tag{3.9}$$

The voltage drop contains two frequency components, one at the excitation frequency $\omega$ and a second phase-shifted one at $3\omega$. Since the $3\omega$ voltage signal depends on the system's thermal response $Z(\omega)$ and is related to the thermal losses from the heater to

the environment, it enables a determination of thermal properties, such as the thermal conductivity or the specific heat. Depending on the measurement geometry and boundary conditions, the thermal properties of the environment or the heater itself can be measured if a suited model of the thermal transfer function is applied. In the following, the thermal transfer functions of two distinct measurement geometries are discussed.

### Line Heater on Semi-Infinite Solid

The classical $3\omega$ method was developed for a metal strip heater of thickness t, width $2b$ and length $2l \gg t, b$ deposited onto a bulk material or film of thickness $d \gg \lambda_S$, with the thermal penetration depth [168]

$$\lambda_S = \sqrt{\frac{D_S}{2\omega}} \tag{3.10}$$

of a material revealing the thermal diffusivity $D_S = \kappa_S/(\rho_{dens} c_p)$. Here, $\kappa_S$ denotes the thermal conductivity, $c_p$ the specific heat per volume and $\rho_{dens}$ the density of the bulk or substrate material underlying the metal strip heater. In the frequency regime where $b \ll \lambda_S \ll d$, the thermal transfer function $Z_S$ of such a system is approximated by [165]

$$Z_S(\omega) = \frac{1}{\pi 2 l \kappa_S}\left[-\frac{1}{2}\ln(2\omega) + \eta - \frac{1}{2}\ln\left(\frac{ib^2}{D_S}\right)\right] \quad , \tag{3.11}$$

$\eta = 0.923$ being a material-independent constant. Eq. 3.11 relates the complex $3\omega$ voltage to the thermal conductivity of the bulk material. By measuring the frequency dependence of the *in-phase* $3\omega$ voltage, the thermal conductivity can be determined by linearly fitting $Re[U_{3\omega}]$ against $\ln(2\omega)$.

### Suspended Wire

In the recent two decades, the $3\omega$ method was further developed to measure the thermal conductivity of small rod-like samples, e.g. carbon nanotubes or inorganic nanowires [169, 170]. In this situation, the sample itself is used a Joule heater and its thermal losses are assumed to be governed by heat conduction to the electrical contacts. For a wire of diameter $d$ suspended between its voltage contacts at distance $2l \gg d$, the thermal transfer function has been evaluated to [166]

$$Z_{SW}(\omega) = \frac{(\sinh\beta - \sin\beta) + i\{\sinh\beta + \sin\beta - \beta(\cosh\beta + \cos\beta)\}}{2\beta c\omega(\cos\beta + \cosh\beta)}, \tag{3.12}$$

with $\beta = \sqrt{\omega\tau}$ and the characteristic thermal response time $\tau = (2l)^2/D$ being related to the thermal diffusivity $D$ of the wire. The frequency dependence of $Z_{SW}$ is similar to

the response function of a lumped first-order RC system, i.e. Eq. 3.12 is well-approximated by the transfer function [166]:

$$Z_{SW,lump}(\omega) = \frac{R_{th}}{12}\frac{1 - i\omega\tau/5}{1 + (\omega\tau/5)^2} \tag{3.13}$$

The thermal resistance $R_{th} = 2l/(\kappa A_{cs})$ relates $Z$ to the thermal conductivity $\kappa$ of the wire of cross section $A_{cs}$ and length $2l$. Fig. 3.5a compares the frequency-dependence of the real and imaginary part of $Z_{SW,lump}$ and $Z_{SW}$, indicating the good agreement between the lumped approximation and the entire solution described by Eq. 3.12.

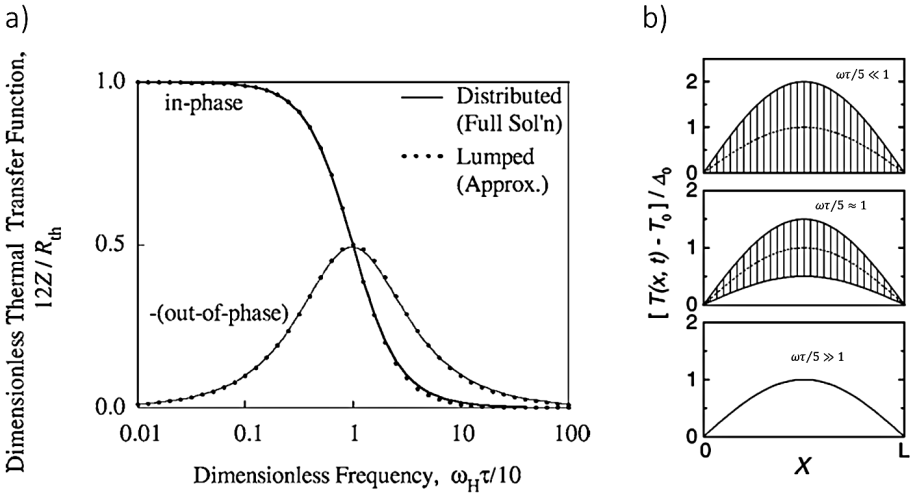


Figure 3.5: Thermal transfer function of a suspended wire. (a) Real and imaginary part of the thermal transfer function given by Eq. 3.12 and compared to the approximation in Eq. 3.13. The abscissa is normalized to a dimensionless frequency $\omega_H\tau/10$, $\omega_H = 2\omega$ being the frequency of the heating power P(t). (b) The temperature distribution along the wire oscillates between zero and finite value for low frequencies (indicated by the striped area). As the excitation frequency approaches $5/\tau$, the temperature difference does not fully relax back to zero anymore but alternates between finite, non-zero values. In the large frequency limit, the temperature profile corresponds to a DC heating of the crystal as the thermal response of the sample can no longer follow the dynamics of the excitation. Adapted from: [166, 169]

The characteristic behavior can be understood in the following way: At small excitation frequencies, the thermal response is fast compared to the periodic heating current. Hence, the temperature oscillation follows the excitation power and oscillates *in-phase* while the (imaginary) *out-of-phase* thermal response function vanishes. At zero frequency the real part extrapolates to a constant value of

$$Re\left[Z_{SW,lump}(\omega)\right] \xrightarrow{\omega\tau \ll 1} \frac{R_{th}}{12} = \frac{2l}{12\kappa A_{cs}}, \tag{3.14}$$

being inversely proportional to the thermal conductivity $\kappa$. In this limit, the thermal response function is independent of the material's specific heat $c$ and allows for a characterization of $\kappa$ without knowledge of the former. This is highly advantageous over other

transient thermal conductivity measurements, such as laser flash [121]. The specific heat comes into play via the thermal response time $\tau$.
With increasing excitation frequencies, the thermal response will no longer be able to follow the dynamic external stimulus and the thermal response occurs phase-shifted with respect to the excitation power. This phase shift yields to an imaginary part contributing to $Z_{SW}$ and peaking at a frequency

$$\omega = 5/\tau \quad . \tag{3.15}$$

At this frequency, real and imaginary part of $Z_{SW}$ are equal in amplitude being exactly half of the low-frequency limit given by Eq. 3.14. The position of the peak in the imaginary part allows for an experimental determination of the specific heat if the value of $\kappa$, as evaluated from the low-frequency *in-phase* signal, is known:

$$c_{mol} = \frac{m_{mol} \cdot \tau \cdot \kappa}{\rho_{dens} \cdot (2l)^2} \quad . \tag{3.16}$$

Here, $m_{mol}$ denotes the molar mass of the material.
At even higher frequencies $\omega > 5/\tau$ both, the imaginary and the real part of the temperature oscillation decrease leading to a DC heating of the crystal. The temperature distributions along the wire for the three frequency limits are schematically illustrated in Fig. 3.5b. At low frequencies ($\omega\tau \ll 1$) the temperature profile completely follows the dynamic variation of the heating power, i.e. the temperature rise $\Delta T$ oscillates between its maximum value and 0. With increasing excitation frequency the temperature amplitude becomes smaller and does not completely vanish after each cycle. For the extreme limit of $\omega\tau \to \infty$, the temperature cannot follow the excitation anymore but remains stationary increased without generating a $3\omega$ voltage component. The absolute complex amplitude of $Z_{SW,lump}$

$$|Z_{SW,lump}(\omega)| = \frac{R_{th}}{12} \frac{1}{\sqrt{1 + (\omega\tau/5)^2}} \xrightarrow{\omega\tau \gg 1} \frac{10}{24 A_{cs} (2l) \rho_{dens} c_p} \cdot \frac{1}{\omega} \tag{3.17}$$

follows an $\omega^{-1}$-behavior in the high-frequency limit and is independent of $\kappa$. The asymptotic limits indicate that the low frequency thermal response of the system is sensitive to the thermal conductivity $\kappa$ while the high frequency part is conditioned by the heat capacity $c$. Hence, measuring the low-frequency part $\omega\tau \ll 1$ with high accuracy is crucial to extract the thermal conductivity from the experimental data.

### 3$\omega$ Measurement Setup

The setup to measure the frequency dependence of the $3\omega$ voltage $U_{3\omega}$ is depicted in Fig. 3.6. The analog output of a simultaneously sampled 24-bit data acquisition card (NI PXI-4461) is used to apply a sinusoidal voltage to the measurement circuit. A load resistor $R_L$, about two orders of magnitude larger than the sum of sample and contact resistance $(R_S + 2R_C)$, is used to establish constant current conditions. The voltage drop at the inner contacts of the organic crystal is connected to a Thomson bridge consisting of four precision 10 kΩ ($\pm 0.01\%$) resistors. For sample resistances above 1 kΩ a home-built subtractor circuit consisting of a dual INA 2128 instrumentation amplifier is used instead of the Thomson bridge. Prior to each measurement, the bridge is automatically balanced by a computer controllable resistance decade (Orbit Controls 642) which is connected in series to the sample $(R_P)$. The output of the balanced bridge reads $U = U_{3\omega}/2 + U_{noise}$ because the bridge circuit evens out the $1\omega$ part of Eq. 3.9, typically being three to four orders of magnitude larger than $U_{3\omega}$ [171].

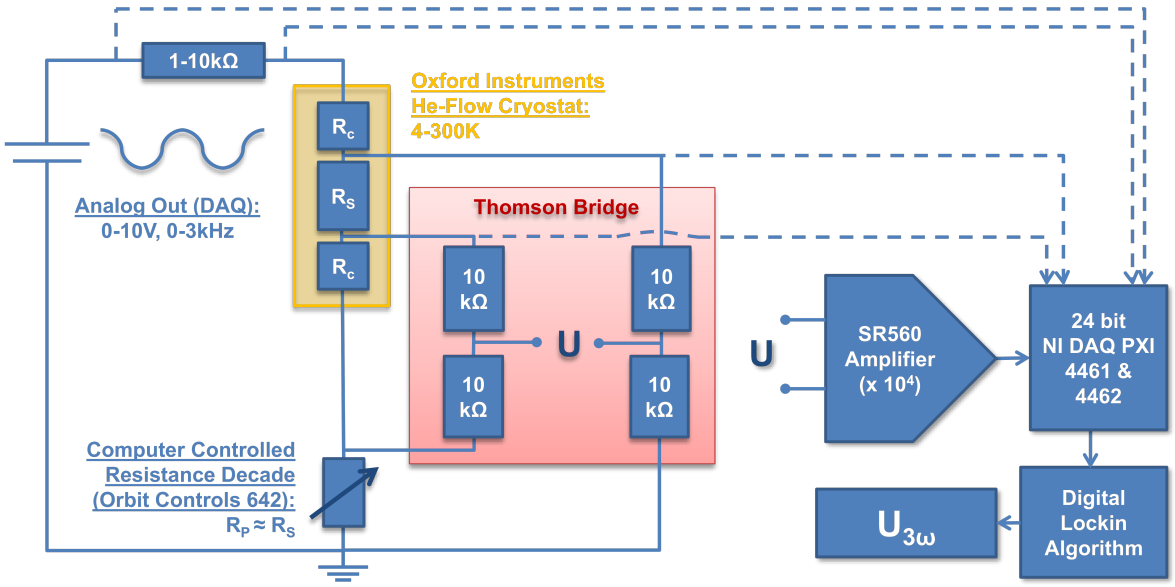


Figure 3.6: Scheme of the $U_{3\omega}$ measurement setup. A sinusoidal voltage from a 24-bit data acquisition card (NI PXI-4461 DAQ) is applied to a series of load resistor $R_L$, sample resistance $R_S$ and resistance decade $R_P$. The load resistor is large compared to the sample resistance. The voltage drop at the sample is fed into a Thomson bridge which is equilibrated by the resistance decade and subtracts the $U_{1\omega}$ voltage from the signal. The output of the bridge is amplified by a voltage preamplifier and digitized with the same 24-bit DAQ card the AC driving voltage was provided by. Finally, $U_{3\omega}$ is extracted by a self-programmed digital LockIn algorithm developed in Labview.

The bridge voltage is amplified with the help of a Stanford Research SR560 voltage preamplifier by a factor of $10^3 - 10^4$ and afterward digitized with the same data acquisition card the AC voltage is supplied by. The $3\omega$ voltage $U_{3\omega}$ is extracted by a self-programmed

digital LockIn algorithm in Labview. The $1\omega$ voltages at the sample and load resistor are also digitized by an additional DAQ card (NI PXI-4461) in order to determine the current and the sample resistance. To accurately determine $\kappa$, these quantities should always be measured together with $U_{3\omega}$ as Eq. 3.9 crucially depends on the relevant parameters. The simultaneous measurement of the sample resistance additionally allows to balance the Thomson bridge for each frequency step, ensuring the rated accuracy also for regimes with a pronounced temperature-dependent resistivity. The self-programming approach was chosen over an experimental setup employing two commercial LockIn amplifiers in order to attain higher flexibility and automation in the measurement setup. Measurements on the thermal conductivity are also performed as described for the thermopower measurements, i.e. while heating up the sample from 4 K to RT in vacuum. The measurements are not performed in the same cycle as the thermopower measurements to avoid any temperature gradient from previous Seebeck measurements within the sample holder. Thus, the sample needs to be cooled to 4 K for a second time.

**Data Evaluation**

Combining Eqs. 3.9 and 3.13, the real and imaginary part of the third harmonic voltage evaluate to:

$$Im[U_{3\omega}(f)] = \frac{\chi \cdot R^2 \cdot (2l) \cdot I_0^3}{48 \cdot \kappa \cdot A_{cs}} \cdot \frac{\frac{2\pi\tau}{5} \cdot f}{1 + (\frac{2\pi\tau}{5} \cdot f)^2} \tag{3.18a}$$

$$Re[U_{3\omega}(f)] = \underbrace{\frac{\chi \cdot R^2 \cdot (2l) \cdot I_0^3}{48 \cdot \kappa \cdot A_{cs}}}_{U_{3\omega}(f=0)} \cdot \frac{1}{1 + (\frac{2\pi\tau}{5} \cdot f)^2} \quad . \tag{3.18b}$$

Here, the frequency representation with $f = \omega/(2\pi)$ allowing for a straightforward data evaluation is given. All voltage and current values in the thesis are amplitude and not rms-values, as sometimes employed in literature and displayed by commercial LockIn amplifiers. To extract the thermal conductivity and specific heat, the real and imaginary part of the $3\omega$ signal were plotted against frequency. The imaginary part was fitted to Eq. 3.18a in order to determine the thermal response time $\tau$ from the position of the peak. Afterward, the real part was fitted by Eq. 3.18b with fixed $\tau$ to obtain the amplitude $U_{3\omega}(f = 0)$ and hence $\kappa$. The resistance $R$ and current $I_0$ are determined from the average over all frequency points. The measured resistance also enables a more accurate determination of the sample temperature from the previously measured temperature-dependent resistivity. The measured temperature at the silicon diode was found to deviate up to 5 K from the actual sample temperature when measuring in vacuum at cryogenic temperatures

which might be due to temperature-gradients across the sample holder. The temperature coefficient $\chi$ was determined from the resistivity measurement at each ambient temperature. The thermal conductivity $\kappa$ as well as the specific heat at constant volume $c_p$ and per mole $c_{mol}$ may then be evaluated by:

$$\kappa = \frac{\chi \cdot R_0^2 \cdot (2l) \cdot I_0^3}{48 \cdot U_{3\omega}(f=0) \cdot A_{cs}} \tag{3.19a}$$

$$c_p = \frac{\tau\kappa}{(2l)^2 \rho_{dens}} \tag{3.19b}$$

$$c_{mol} = c_p \cdot m_{mol} \quad . \tag{3.19c}$$

### Setup Calibration

In order to validate the measurement principle, the designed setup was calibrated by determining the thermal conductivity and specific heat of a stainless steel wire of 21 µm diameter and several mm in length which was mounted to the sample holder as described in Sec. 3.2.1 with an overall contact distance of $2l = 3.75\,\text{mm}$. These wire dimensions are similar to typical sizes of the investigated organic single crystals. Moreover, the availability of high-quality literature data on the thermal properties of stainless steel enables a sound and appropriate setup calibration [172].

| | $R_0$ [Ω] | $I_0$ [mA] | $\chi$ [$10^{-3}$ K$^{-1}$] | $2l$ [mm] | $d$ [µm] | $\tau$ [s] | $U_{3\omega}(f=0)$ [µV] |
|---|---|---|---|---|---|---|---|
| Value | 8.43 | 1.465 | 1.22 | 3.75 | 21 | 3.40 | 4.00 |
| Abs. Err. | 0.07 | 0.007 | 0.01 | 0.1 | 1 | 0.03 | 0.02 |
| Rel. Err. [%] | 0.8 | 0.5 | 0.8 | 2.6 | 4.7 | 0.9 | 0.5 |

Table 3.1: Experimental parameters to evaluate the thermal conductivity and specific heat of a stainless steel wire with the help of Eqs. 3.19a and 3.19b. The circular sample cross section is obtained from the diameter $d$ by $A_{cs} = \pi(d/2)^2$ and the density $\rho_{dens} = 7.9\,\text{g cm}^{-1}$ was taken without error from the literature [172].

In Fig. 3.7a the measured frequency dependence of the real and the imaginary amplitude of $U_{3\omega}$ is shown together with the two fits of Eqs. 3.18a and 3.18b which agree very well with the experimental data. The anticipated cubic current dependence of the total $3\omega$ voltage has also been verified (see Fig. 3.7b). It demonstrates the measurement accuracy of the $3\omega$ voltage to be better than 100 nV below which the signal becomes comparable

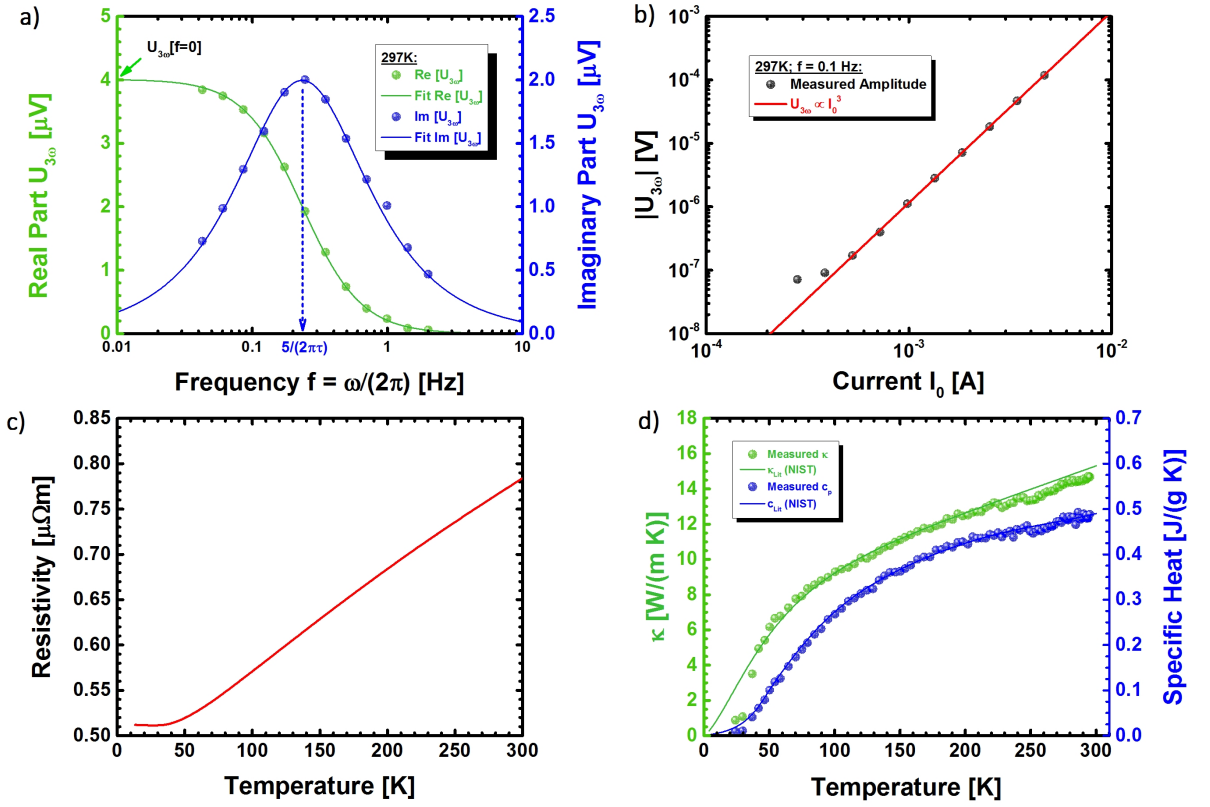


Figure 3.7: Self-heating $3\omega$ method applied to a stainless steel wire as reference. (a) The frequency dependence of the complex $3\omega$ voltage for a current of 1.46 mA at RT fits well to Eqs. 3.18a and 3.18b. (b) The cubic current dependence of $|U_{3\omega}|$ at 0.1 Hz is also well established. (c) From the temperature-dependent resistivity the temperature coefficient $\chi$ can be extracted, enabling the determination of (d) the thermal conductivity $\kappa$ and specific heat $c_p$. The measured values agree extraordinary well with literature data over a broad temperature regime between $40 - 300$ K [172]. The deviation below 40 K can be attributed to the flatness of the resistivity curve in this temperature range limiting the sensitivity and accuracy of the $3\omega$ method.

to the flicker noise of the amplifiers causing a deviation from the $I_0^3$-law. From the fit of the frequency dependences, $\tau$ as well as $U_{3\omega}(f = 0)$ can be determined which are cited together with the other experimental values in Tab. 3.1. They permit to determine the thermal conductivity and the specific heat of the stainless steel sample:

$$\kappa_{meas} = (14.7 \pm 2.6)\,\mathrm{W\,m^{-1}\,K^{-1}} \tag{3.20a}$$

$$c_p = (0.49 \pm 0.08)\,\mathrm{J\,g^{-1}\,K^{-1}} \quad . \tag{3.20b}$$

These values reproduce the literature measurements of $\kappa_{Lit} = 15.3\,\mathrm{W\,m^{-1}\,K^{-1}}$ and $c_p = 0.49\,\mathrm{J\,g^{-1}\,K^{-1}}$ [172] within their errors. From Tab. 3.1 the origin of the significant error instantly becomes clear. The ambiguity in the sample diameter as determined optically under the microscope limits the absolute accuracy of the thermal properties. This

problem constitutes a major challenge when measuring thin samples over macroscopic transport distances. However, when evaluating the thermoelectric figure of merit $zT$ or comparing the electrical to the thermal conductivity, the sample dimensions do not play an important role as they both enter the calculation formula of the conductivities in the same way and thus, cancel out each other. Hence, it is intuitive to look at the effective errors not including uncertainties in the sample dimensions

$$\kappa_{meas} = (14.70 \pm 0.62)\,\mathrm{W\,m^{-1}\,K^{-1}} \tag{3.21a}$$

$$c_p = (0.488 \pm 0.025)\,\mathrm{J\,g^{-1}\,K^{-1}} \quad , \tag{3.21b}$$

for which we obtain relative standard errors of 4.2 % and 5.1 % for $\kappa$ and $c_p$, respectively. This underlines the accuracy of the chosen experimental approach. The temperature-dependent electrical resistivity $\rho$, thermal conductivity $\kappa$ and specific heat $c_p$ are illustrated in Fig. 3.7c-d. The measured values of $\kappa$ and $c_p$ very well reflect the literature data as provided by the National Institute of Standards and Technology (NIST) [172]. The deviation below 40 K is caused by the flatness of the resistivity curve in this temperature regime. The resulting small temperature coefficient limits the sensitivity of the $3\omega$ approach.

### Accuracy of the $3\omega$ Method

In the previous section, the validity of the measurement approach as well as the accuracy of the setup were verified by means of a stainless steel sample. In the following, the applicability of the suspended wire's thermal transfer function $Z_{SW}$ is evaluated with special focus on the previously described sample holder and the material class of organic conductors. One major assumption is that the contacts are at ambient temperature $T_0$. $Z_{SW}$ was originally derived for nanowires with electrical contacts on a substrate of large thermal mass compared to the sample. In this case, the condition on temperature is easily met. In the sample geometry applied here, the crystals are only connected via thin free-standing copper wires of cross section $A_{cs,C}$ and length $l_C$ to the two alumina blocks serving as heat reservoirs. The heat flux from the sample of cross section $A_{cs,S}$ and length $2l_S$ needs to be dissipated through the two contact wires, i.e.

$$Q_S = A_{cs,S} \cdot \kappa_S \frac{T_{mid} - T_C}{(2l_S)} = 2Q_C = 2A_{cs,C} \cdot \kappa_C \frac{T_C - T_0}{l_C} \tag{3.22}$$

needs to be fulfilled. $T_{mid}$ corresponds to the temperature in the middle of the sample wire and $T_C$ represents the temperature of the contact. This yields the condition for negligible contact heating:

$$\frac{T_{mid} - T_C}{T_C - T_0} = \frac{2\kappa_C d_C^2 (2l_S)}{\kappa_S d_S^2 l_C} \gg 1 \tag{3.23}$$

for a sample (contact wires) of diameter $d_S$ ($d_C$) and thermal conductivity $\kappa_S$ ($\kappa_C$). From Eq. 3.23 it is obvious that contact wires should be kept as short and as thick as possible. On the other hand, the thicker the wires, the more stress they induce on the fragile organic samples. For the measurement on the stainless steel samples the relevant parameters $2l_S = 3.6\,\mathrm{mm}$, $l_C = 2\,\mathrm{mm}$, $d_S = 21\,\mu\mathrm{m}$, $d_C = 50\,\mu\mathrm{m}$, $\kappa_S = 15\,\mathrm{W\,m^{-1}\,K^{-1}}$ and $\kappa_C = 380\,\mathrm{W\,m^{-1}\,K^{-1}}$ yield a $\frac{T_{mid}-T_C}{T_C-T_0} = 422 \gg 1$ satisfying Eq. 3.23 by far. For organic samples with thermal conductivity values on the order of $1\,\mathrm{W\,m^{-1}\,K^{-1}}$ the condition is even more easily met. Thus, it can be concluded that the Ansatz of using the suspended wire model to describe rod-like organic conductors with thermal conductivities smaller than $15\,\mathrm{W\,m^{-1}\,K^{-1}}$ attached to free-standing wires is valid.

Secondly, the high surface to volume ratio facilitates radiation losses from the surface imposing uncertainties on the measured $\kappa$. The radiation losses can be approximated by the Stefan-Boltzmann law. To be neglected, the total radiation loss $P_{rad}$ needs to be much smaller than the heat flux $Q_S$ conducted through the sample, necessitating the boundary condition:

$$\frac{P_{rad}}{Q_S} = \frac{\epsilon\sigma_{SB} A_{surf} (2l_S) T_0^3 (T_{mid} - T_C)}{\kappa_S \pi (d_S/2)^2 (T_{mid} - T_C)} = \frac{4\epsilon\sigma_{SB}(2l_S)^2 T_0^3}{\kappa_S d_S} \ll 1 \quad . \tag{3.24}$$

Here, $A_{surf} = \pi d_S \cdot (2l_S)$ is the surface area of the crystal, $\epsilon$ the emissivity of the material and $\sigma_{SB}$ the Stefan-Boltzmann constant. In the worst case, at an ambient temperature of $T_0 = 300\,\mathrm{K}$ and an emissivity of $\epsilon = 1$, the error for the stainless steel sample amounts to $\frac{P_{rad}}{Q_S} = 0.1 \ll 1$. Taking into account a smaller emissivity and that most data has been recorded at smaller temperatures, the condition in Eq. 3.24 is considered to be satisfied. However, for the organic samples this condition imposes a bigger challenge: A sample of same geometry with $\kappa_S \approx 1\,\mathrm{W\,m^{-1}\,K^{-1}}$ yields $P_{rad}/Q_S = 1.5$ and the radiation error dominates the measurement accuracy. Hence, the contact distance $2l_S$ should be kept as short as possible and the diameter $d_S$ of the rod-like sample may not be too small. For a typical sample of $50\,\mu\mathrm{m}$ diameter and $2\,\mathrm{mm}$ length, even with $\kappa_S = 1\,\mathrm{W\,m^{-1}\,K^{-1}}$ an error of only $\frac{P_{rad}}{Q_S} = 0.2$ is obtained, again assuming the worst case of $\epsilon = 1$ and $T_0 = 300\,\mathrm{K}$. Hence, the condition is generally also satisfied for the organic samples. Yet, the condition should be checked for each sample under investigation.

### Finite-Element Simulations

To indepedently prove whether the assumptions made hold true or not, the temperature and voltage response to sinusoidal current excitations have been simulated with the help of the software *Comsol Multiphysics* by finite-element methods (FEM) for the organic conductor $(DCNQI)_2Cu$ at RT. The applied measurement geometry was transferred to the discrete model, as depicted in Figs. 3.8a&c with and without mesh. It consists of a rodlike organic crystal attached to four copper wires by graphite paint. The literature properties, as given in the Comsol material database, were used for copper and graphite while the values for $(DCNQI)_2Cu$ were experimentally determined (see Tab. 3.2) by measurements on a sample of same geometry. The simulated thermal response to an AC current is illustrated in Fig. 3.8c for three excitation frequencies.

The temperature profiles between the current contacts along the needle axis (right projection) are quasi-parabolic and, indeed, the voltage contacts at $\pm l_{el}$ almost remain at ambient temperature, confirming a good thermal connection to the alumina blocks. In the upper projection, the temporal evolution of the temperature in the middle of the crystal is shown and compared to the oscillating current. At the excitation frequency $f = 0.01\,\mathrm{Hz} \ll 5/(2\pi\tau)$, the temperature oscillates *in-phase* with the current as anticipated by the thermal transfer function in Eq. 3.17. With increasing frequency, the maximum amplitude of the temperature oscillation not only decreases but also phase-shifts with respect to the current. The temperature difference does not fully relax back to zero for vanishing current amplitude because the thermal response is too slow to follow the excitation. At high frequencies, the temperature oscillation amplitude decreases with $\omega^{-1}$ leading to constant cw-heating effects. This behavior qualitatively agrees with the theoretical predictions outlined above.

| $\sigma$ [$\mathrm{S\,cm^{-1}}$] | $I_0$ [mA] | $\chi$ [$10^{-3}\,\mathrm{K}$] | $2l_{el}$ [mm] | $d$ [µm] | $\tau$ [s] | $\kappa$ [$\frac{\mathrm{W}}{\mathrm{m\,K}}$] | $c_m$ [$\frac{\mathrm{J}}{\mathrm{mol\,K}}$] |
|---|---|---|---|---|---|---|---|
| 1070 | 1.41 | 8.9 | 2.175 | 55.5 | 4.2 | 1.73 | 527 |

Table 3.2: Experimental values determined and used for the FEM simulations of a $(DCNQI\text{-}h_8)_2Cu$ crystal.

To check on the quantitative agreement, the $3\omega$-voltage was extracted from the simulation, as depicted in Fig. 3.9b. The real part amplitude at small frequencies compares well with the measured curve validating the chosen approach to accurately determine $\kappa$. The position of the peak in the imaginary part - corresponding to the frequency at which the real part divides in half - slightly shifts toward smaller frequencies as compared to the measurement. This effect can be attributed to the $l^2$-dependence of $\tau$. The thermal

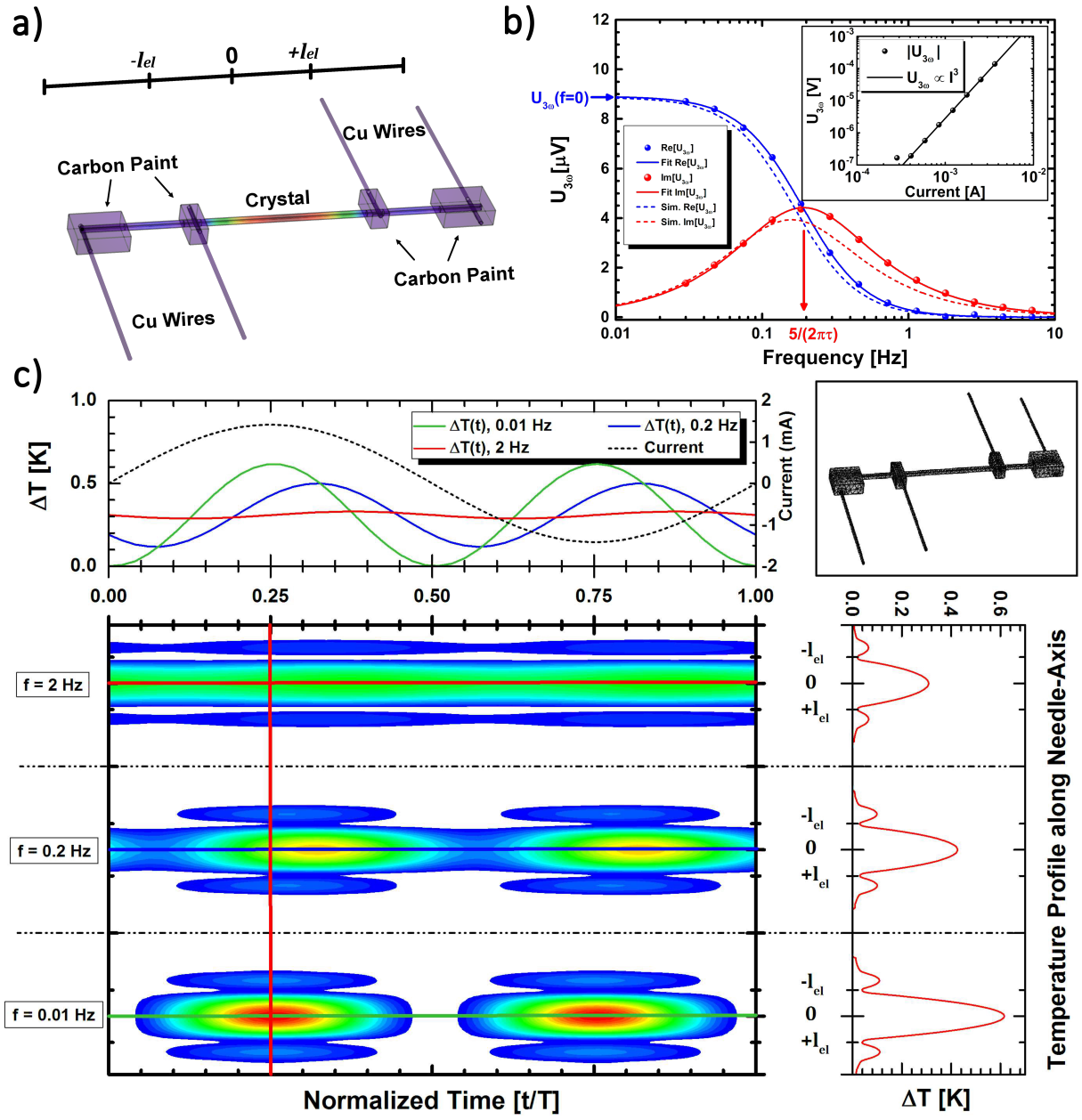


Figure 3.8: Finite-element simulations on the $3\omega$ method. (a) Geometry used for the finite-element modelling. It comprises the crystal, four cuboid graphite paint contacts and four copper wires of 50 µm diameter each. The temperature at the end of the copper wires was set to the ambient temperature of the alumina blocks. (b) The measured and calculated $3\omega$-voltages for $(DCNQI)_2Cu$ at RT agree very well, especially at low frequencies. This facilitates an accurate determination of $\kappa$ because the thermal conductivity is determined from the amplitude of the real part extrapolated to zero frequency while $\tau$ is characterized by the position of the peak in the imaginary part. The cubic current dependence of the total, experimental $3\omega$-voltage as anticipated by Eq. 3.18b is depicted in the inset for $f = 0.1$ Hz. (c) Simulated temporal evolution of the temperature distribution along the crystal profile in response to an AC current of amplitude $I_0 = 1.41$ mA at three different frequencies. The dynamic evolutions were normalized to the period $T = f^{-1}$ of the excitation current. From the upper projection, a shift and decrease in amplitude of the temperature oscillation with respect to the current is observed toward higher frequencies. In the right projection, the quasi-parabolic temperature profiles as anticipated by Eq. 3.12 in between the voltage contacts are demonstrated. The finely-meshed model is also shown in the upper right.

length involves some error due to the extension of the voltage contacts and their crude approximation by cuboid boxes.

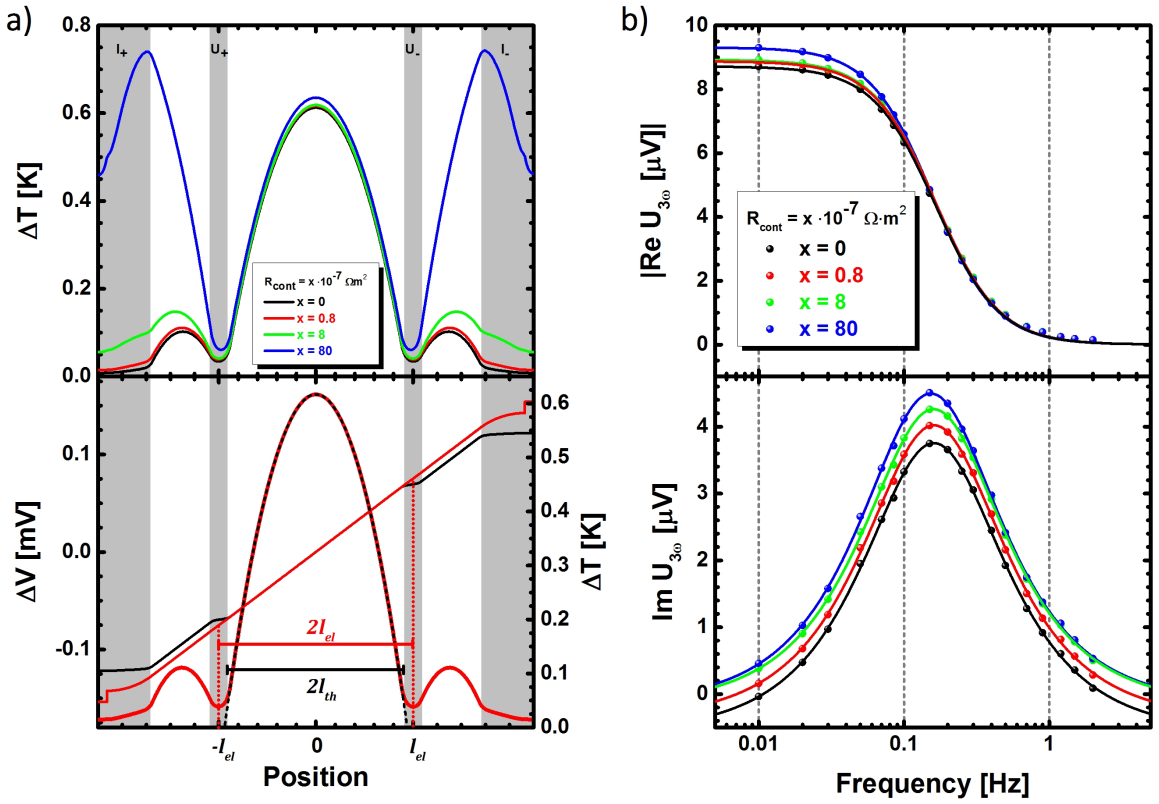


Figure 3.9: FEM-simulations of contact resistance effects. Contact resistivities of magnitude $R_{cont} = x \cdot 10^{-7}\,\Omega\,\mathrm{m}^2$ disturb the (a) low-frequency temperature profiles mostly at the current-injecting contacts. The shaded gray areas mark the extended graphite contacts. The temperature profiles for $x = 0$ and $x = 0.8$ are also compared to the voltage profiles along the crystal. The ideal temperature profile is given by the parabola intersecting $\Delta T = 0$ at the boundary of the graphite contacts, the latter being separated by a distance $2l_{th}$. Contrarily, in the presence of contact resistances the voltage drops across a distance of $2l_{el}$, quantifying the distance between the copper wires in the middle of each graphite paint contact. It is the characteristic length scale to calculate the electric field and hence, the electrical conductivity. The small effect of contact resistances on the temperature profile in between the voltage contacts is also evidenced by (b) the simulated $3\omega$-signals deviating only slightly from each other. The constant offset in the imaginary part is accounted for in the fits. The frequency position of the peak remains fixed.

The model incorporates a small electrical contact resistivity of $0.8 \times 10^{-7}\,\Omega\,\mathrm{m}^2$ at the interface between crystal and graphite paint, corresponding to a contact resistance of about $0.7\,\Omega$ for each current injecting and of $1.8\,\Omega$ for each voltage contact. To elucidate the influence of the contact resistances, the temperature profiles and $3\omega$-voltages were simulated for different values of the contact resistivity. The simulated temperature profiles illustrated in Fig. 3.9a become highly disturbed for large contact resistances due to the Joule heat generated upon current injection. However, the temperature profile in between the voltage contacts remains quasi-parabolic and almost undistorted. The temperature at the graphite paint voltage contact at $\pm l_{el}$ as well as the temperature oscillation in between

the voltage contacts slightly increase with $R_{cont}$, as also evidenced by the rising values of $U_{3\omega}$ (compare Fig. 3.9b). Taken as a whole, this may lead to an underestimation $\kappa$.

Typical experimental contact resistivity lies in the range between $0.8 \times 10^{-7}\,\Omega\,\mathrm{m}^2$ and $8 \times 10^{-7}\,\Omega\,\mathrm{m}^2$ for which the resulting error was found to be smaller than 2% at room temperature. Even for the very high value of $80 \times 10^{-7}\,\Omega\,\mathrm{m}^2$ the relative error amounts to only 6.8%. Hence, if contact resistances are kept small, the induced error in $\kappa$ is negligible but the effect should be kept in mind for samples of very low resistivity.

As another observation, the characteristic length of thermal and electric field modulation deviate from each other for samples with extended voltage contacts of finite resistance. Again, the lower graph in Fig. 3.9a illustrates the temperature profile for the sample with contact resistivity of $0.8 \times 10^{-7}\,\Omega\,\mathrm{m}^2$. The parabolic fit marks the temperature profile assumed in the suspended wire model. Clearly, the parabola does not intersect $\Delta T = 0$ at $\pm l_{el}$ but rather at the boundaries of the graphite paint contacts at distance $2l_{th}$ because the temperature profile under the contacts appears to be rather flat. Accordingly, sample length determining the thermal conductivity is assumed to be $2l_{th}$.

The graph also depicts the voltage profiles along the crystal with and without contact resistance. For zero contact resistance, the current will flow out of the needle-like crystal via the graphite paint contact, i.e. the potential under the voltage contact is flat due to the high conductivity of the graphite paint. To accurately determine the sample's resistivity, the length $2l_{th}$ as obtained from the thermal profile is utilized. In contrast, already a small contact resistance hinders the current to flow out of the crystal at the voltage contacts, leading to a constant gradient of the electric field under the voltage contacts. In order to evaluate the electric field and the electrical conductivity, the voltage reading is divided by the characteristic length of $2l_{el}$, being the distance between the copper wires positioned in the middle of each graphite paint contact, as marked in the graph. Due to the contact resistance being always present, thermal and electrical lengths were always separately determined. Nevertheless, care was taken to prepare small contacts of $(l_{th} - l_{el})/l_{el} < 0.1$. Taking a closer look at the simulated imaginary part in Fig. 3.9b, an offset seems to be induced by the contact resistivity which can be accounted for in the fit. Yet, the peak position seems to remain at the same frequency. Therefore, the imaginary part was only utilized to determine $\tau$. The extrapolation $U_{3\omega}(f \to 0)$ was taken from the fit of the real part which seems to be more robust and less prone to errors. The susceptibility of the imaginary part to the contact resistance is due to time-delayed heat flows from the outer areas into the center of the crystal.

Another important aspect of thermal conductivity measurements is the error due to neglected radiation losses. This influence was simulated by varying the surface emissivity $\epsilon$ of the crystal. The temperature profile in Fig. 3.10a delineates a significant reduction of

the temperature oscillation due to the additional radiative heat loss channel. Unlike the contact resistance, the radiative heat loss causes an overestimation of $\kappa$, as demonstrated by the lowered imaginary and real part of $U_{3\omega}$ in Figs. 3.10b-c. In this case, the error amounts up to 10% for the worst case of an ambient temperature of 295 K and $\epsilon = 1$ but will loose importance upon lowering the temperature as explained above. Considering the smaller emissivity of real samples and that most data points are recorded at reduced temperatures, radiation effects can be neglected in first approximation. Care has to be taken for single crystal with small cross section for which the radiative heat loss might dominate. Furthermore, in the imaginary part the peak position drifts to higher frequencies on increasing radiative losses, resulting in specific heats underestimated by up to 10%.

Further simulations were conducted with more dense meshes to investigate the influence of spatially anisotropic electrical and thermal conductivities. However, no significant effect was found on the measured quantities proving the method to be applicable for materials of reduced electronic dimensionality.

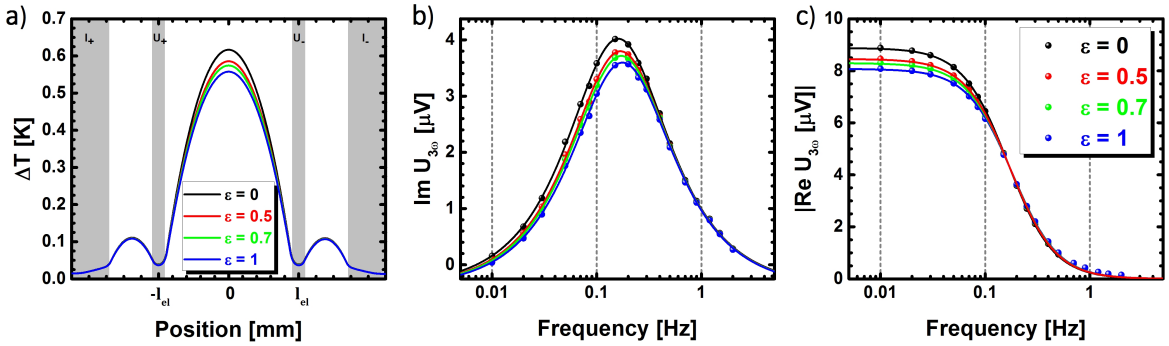


Figure 3.10: FEM-simulations on radiative losses. The simulated (a) temperature profiles along the crystal axis as well as the (b) *out-of-phase* and (c) *in-phase* $3\omega$ signals reveal a diminished temperature swing upon increasing radiation losses which are characterized by the respective surface emissivity $\epsilon$.

To sum up, the self-heating $3\omega$ method for a suspended, needle-like sample proves to be a powerful tool to accurately measure the thermal conductivity and specific heat of fragile, single-crystalline, quasi-1D organic conductors. The largest uncertainties may arise from radiative heat losses at high temperatures and contact resistance effects at cryogenic temperatures. In temperature regimes of almost constant electrical resistivity the method is expected to reveal some ambiguities. In the determination of absolute values for $\kappa$ the largest uncertainty stems from the determination of the crystal cross section. Influencing the electrical conductivity in the same manner, the described method allows to investigate the correlation between $\sigma$ and $\kappa$ with an accuracy of better than 10%, a precision unrivaled in all previous studies on the thermal conductivity of organic metals [173, 174, 175]. This will be highly-advantageous for an accurate determination of the thermoelectric figure of merit in this material class.

### Data Analysis

The error analysis described above has proven the $3\omega$ method to be a reliable technique at RT. The radiative losses should furthermore lose importance on lowering the ambient temperature. In contrast, the contact resistance may gain importance for samples of very high conductivity at cryogenic temperatures. The thermally activated behavior of the contact resistance can further lead to high-ohmic contacts in the low-temperature regime.

Fig. 3.11a shows the temperature-dependent behavior of $\kappa$ and of $c_{mol}$ for (DCNQI-$h_8$)$_2$Cu as measured by the $3\omega$ method. In addition, the temperature-dependent literature data on the specific heat of (DCNQI)$_2$Li is illustrated [88]. This is the only data set available for a (DCNQI)$_2$M system that was obtained from a study on single crystals over the entire temperature regime between 4 K and 300 K. It is regarded as the literature data of highest confidence. At least in the temperature regime above 20 K studied here, it should resemble the specific heat's temperature dependence of (DCNQI)$_2$Cu quite accurately due to the similar phonon spectrum of the two materials. The literature values are given in arbitrary units and the curve has to be multiplied by a factor **A** to match the measured specific heat at RT. In this case, a factor of **A=1.354** was employed.

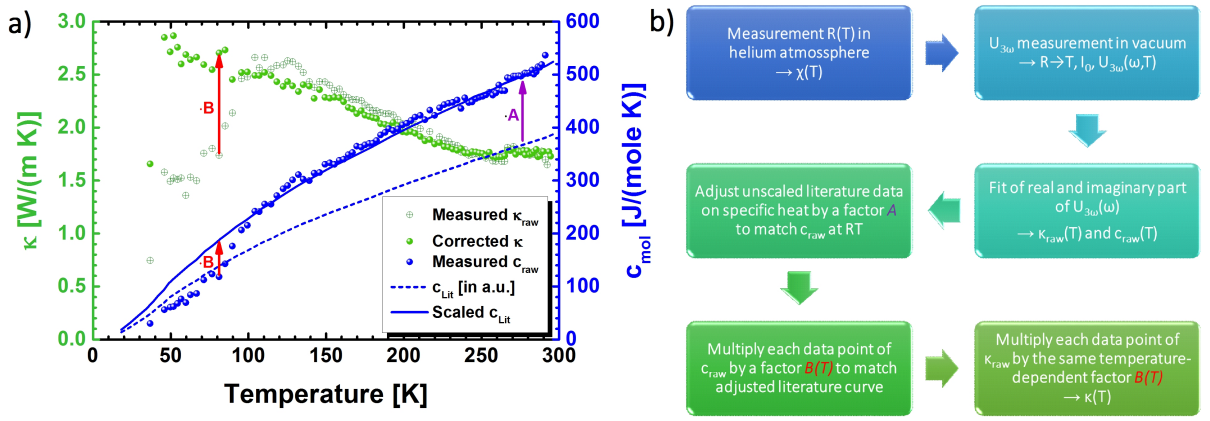


Figure 3.11: Applied data evaluation procedure to account for contact resistance effects. (a) The literature specific heat data [88] measured in arbitrary units on a (DCNQI)$_2$Li single crystal was multiplied by a factor **A** to account for the unit transformation and to match the measured specific heat data of (DCNQI)$_2$Cu at RT. When satisfying agreement between the curves over a wide temperature regime was obtained, all measured specific heat values were multiplied by a temperature-dependent factor **B** to exactly match the literature curve. The measured $\kappa$ values were adjusted by the same factor. While the correction is small at high temperatures, it may be significant in the cryogenic temperature regime. (b) Summary of the whole data evaluation process.

Fig. 3.11 demonstrates the measured molar specific heat to be in good agreement with the adjusted literature curve over a broad temperature range between 100 K and 300 K. It should be noted that the absolute values of the molar specific heat at about 150 K agree well with values measured by Matsui *et al.* on pellet samples of (DCNQI)$_2$Cu, too [176]. Below about 100 K the contact resistance effect gains importance in the high conducting

$(DCNQI)_2Cu$ crystal. This manifests in a sudden decrease of the thermal conductivity as well as in a deviation of the measured $c_{mol}$ from the literature curve. Howbeit, the simulations above demonstrated the measured thermal response time $\tau$ to be unaffected by the high contact resistance and hence, any deviation of $c_{mol} \propto \kappa/\tau$ from the literature curve is caused by erroneous $\kappa$ readings. To account for this error, each data point of the measured specific heat is adjusted to the literature curve by a factor **B**, ranging between 0.95 and 2.2 in this set of data. Multiplying each corresponding, experimental $\kappa$ value by the same factor results in a corrected measurement curve of the thermal conductivity, as delineated in Fig. 3.11a as well.

Effectively, in this temperature regime only the thermal response time $\tau$ has been used to evaluate the thermal conductivity with the help of literature specific heat data. The correction described above adjusts the literature data to the reliable, absolute data at high temperature and only employs the former's temperature dependence. In this way, the advantage of determining the electrical and the thermal conductivity on the same sample volume is maintained and any error related to the probed dimensions is canceled when calculating the temperature-dependent thermoelectric figure of merit or the Lorenz number. Hence, the thermal conductivity data below 100 K is still of high quality. The evaluation procedure has been conducted on all sets of data presented in this thesis unless otherwise stated. It is also viable to correct data in temperature regimes where the temperature coefficient of the resistivity changes drastically or where it is very flat, e.g. near the occurring metal-insulator transitions.

# Chapter 4

# Results

The newly designed electrothermal transport setup was introduced and characterized in the previous section. In the following, the measurement system has been employed to determine the Seebeck coefficient as well as the electrical and thermal conductivity in $(DCNQI)_2M$ (M=Cu, Li) single crystals. It will provide new insight into the transport of charge and heat in this material class (4.1 & 4.3). By application of an advanced electrothermal model to the observed nonlinear conduction phenomena in the Peierls insulating state of $(DCNQI)_2Cu$ crystals, a more detailed analysis of their origin could be achieved (4.2). An entropy analysis of the different ground states confirms the thermodynamic phase diagram based on competing spin, charge and lattice degrees of freedom in $(DCNQI)_2Cu$ and extends its validity to temperatures above the Debye temperature (4.4). Finally, the potential of radical ion salts for thermoelectric applications is evaluated in terms of the power factor and the thermoelectric figure of merit (4.5). The results of Sec. 4.2 have been published in *Physical Review B* **92**, 155107 (2015) [177]. Distinct parts of the other sections have been merged into a Communication in *Advanced Materials* (2017, accepted) together with data on the p-type organic conductor $TTT_2I_3$ provided by Alexander Steeger.

## 4.1 Electronic Properties of ($R_1$,$R_2$-DCNQI)$_2$M

In this section, the electronic transport properties of disubstituted ($R_1$,$R_2$-DCNQI)$_2$M ($R_{1/2}$=$CH_3$, $CD_3$, Br; M=Cu, Li) as determined by the electrothermal characterization setup described in Ch. 3.2 will be analyzed. In the first part, the influence of different functional groups $R_{1/2}$ on the electrical resistivity is discussed. This analysis is combined with thermopower measurements in the second part. Finally, the influence of different counter ions M on both quantities is studied in the alloyed (DMe-DCNQI)$_2$Cu$_x$Li$_{1-x}$ single crystal reference system.

### 4.1.1 Electrical Resistivity of ($R_1$,$R_2$-DCNQI)$_2$Cu

The temperature-dependent electrical resistivity data of four (DCNQI)$_2$Cu salts recorded during cooling is shown in Fig. 4.1a. All $\rho(T)$-curves reveal metallic behavior at room temperature (RT) with decreasing resistivity upon cooling. The undeuterated (DCNQI-h$_8$)$_2$Cu salt achieves electrical resistivities as low as $\rho_{RT} = 9.3 \times 10^{-6}\,\Omega\,\mathrm{m}$ and represents one of the best conducting organic materials [178]. Smaller electrical resistivities have only been attained by few organic compounds. In very pure $TTT_2I_3$ crystals values of $1 \times 10^{-6}\,\Omega\,\mathrm{m}$ have been obtained [64]. In a recent study, a very low electrical resistivity of $1.8 \times 10^{-6}\,\Omega\,\mathrm{m}$ was demonstrated for the polymer PEDOT:Sulf-NMP [179]. Yet, both materials are p-type organic conductors. Therefore, with the filled conduction band emerging from the LUMO of the DCNQI acceptor molecule, (DCNQI-h$_8$)$_2$Cu marks the n-type organic conductor of highest electrical conductivity, at least to my knowledge. With the help of Eq. 2.56 and under the assumption of $n = 2.94 \times 10^{21}\,\mathrm{cm}^{-1}$, a RT mobility of $\mu_{RT} = 2.3\,\mathrm{cm}^2\,\mathrm{V}^{-1}\,\mathrm{s}^{-1}$ is deduced, a value usually only obtained in organic single crystals of highest purity [180]. This underlines the high quality of the single crystals grown and characterized in this thesis.

(DCNQI-h$_8$)$_2$Cu remains metallic down to cryogenic temperatures because it retains its quasi-3D electronic structure retarding any kind of metal-insulator transition frequently observed in low-dimensional conductors. As discussed in Ch. 2.3.3, the metallic ground state may be lifted by alternation of the functional groups attached to the quinone ring in DCNQI. Replacing one of the methyl group by a bromine atom, a first-order Peierls metal-insulator (MI) transition at $T_{P,c} = 156\,\mathrm{K}$ is observed, as evidenced by the step-like increase in the resistivity. Even more remarkable, already a deuteration of the methyl groups is sufficient to induce a phase transition at $T_{P,c} = 82\,\mathrm{K}$. As a typical feature of a first-order phase transition, the resistivity curves reveal hysteretic behavior between the cooling and heating run. This is illustrated in Fig. 4.1b for (DCNQI-d$_6$)$_2$Cu with the phase transition occurring at $T_{P,c} = 82\,\mathrm{K}$ upon cooling and at $T_{P,h} = 90\,\mathrm{K}$ upon

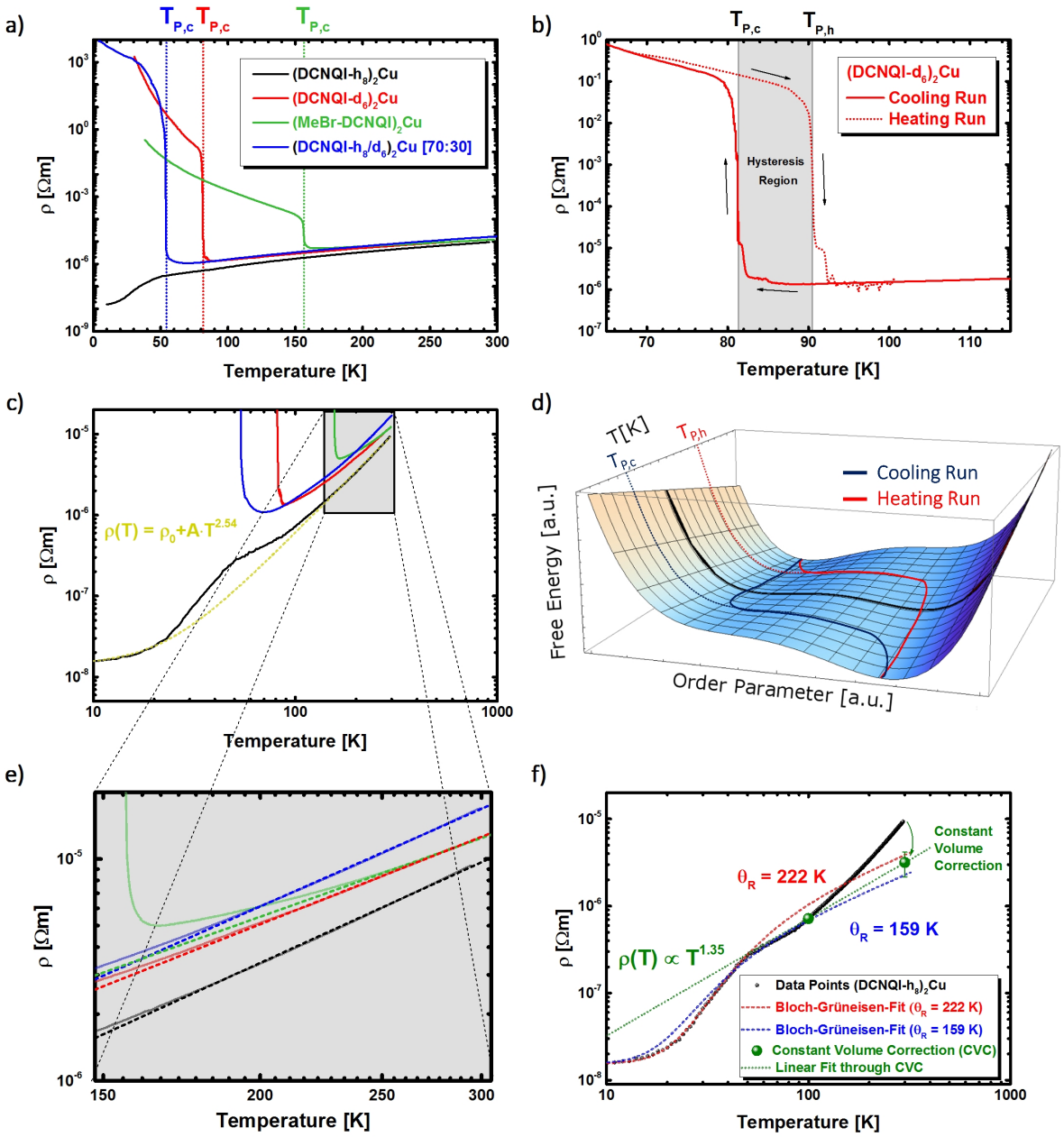


Figure 4.1: Resistivity data of four different $(DCNQI)_2Cu$ salts. (a) While $(DCNQI\text{-}h_8)_2Cu$ stays metallic down to lowest temperatures, the other three materials undergo a first-order Peierls metal-insulator transition at different $T_{P,c}$ which becomes manifest in a step-like increase of the resistivity. (b) Observed hysteresis between cooling and heating run being common for a first-order phase transition, here shown for $(DCNQI\text{-}d_6)_2Cu$. (c) The log-log plot reveals an anomalous hump at about 50 K also in the purely metallic sample which might be indicative of a phase transition occurring in some domains. (d) The free energy has two local minima with respect to the order parameter of the phase transition and the global miminum changes at the black solid line. A small energy barrier needs to be overcome to reach the global minimum, causing the hysteresis in the phase transition between the cooling and the heating run. (e) The temperature exponent $\alpha$ of the resistivity at high temperatures is decreased in materials with higher $T_P$ as evidenced by a reduced slope of the linear fit. (f) When correcting the resistivity data for the thermal expansion, the hump at 50 K transforms into a kink. The resistivity may then be approximated by the Bloch-Grüneisen formula with a characteristic temperature of $\theta_R \approx 159\,\mathrm{K} - 222\,\mathrm{K}$.

heating the sample. The hysteresis may be understood from the free energy landscape close to the transition points, as schematically illustrated in Fig. 4.1d. The coordination angle $\alpha_{CO}$ has been identified as the order parameter for the Peierls phase transition in $(DCNQI)_2Cu$ (compare Ch. 2.3, [66, 71]). The free energy has two local minima and the global minimum changes with respect to the order parameter at the indicated black solid line. Yet, additional energy is required to overcome the energy barrier in order to reach the global minimum. Therefore, the transition occurs at a temperature $T_{P,c}$ below the black line upon cooling and at a higher temperature $T_{P,h}$ upon heating. The excess energy is provided by thermal fluctuations.

The critical temperatures of the other salts are stated in Tab. 4.1. The experimental data agrees with values published in literature [85, 78, 9, 181, 182] and again confirms the excellent crystal quality. Alloying deuterated and undeuterated molecules in a single crystal, as in $(DCNQI\text{-}h_8/d_6)_2Cu$ at a ratio of 70:30, the phase transition may be shifted toward a lower temperature of $T_{P,c} = 54\,K$. In literature, a re-entry behavior from the insulating into the metallic state is observed at even smaller $T$ but the exact transition temperatures vary in literature [81, 182, 183]. The re-entry transition was not observed for the crystals investigated in this thesis, probably due to a deviating ratio of deuterated and undeuterated molecules as compared to the net weights used for crystal growth. However, the slight deviation from the expected activation behavior of the resistivity curve below 40 K presumably marks already the onset of the re-entry phase transition in some domains.

A more detailed comparison of the metallic part of the resistivity curves is shown in the log-log plot of Fig. 4.1c. $(DCNQI\text{-}h_8)_2Cu$'s purely metallic resistivity seems to obey a power law $\rho(T) = \rho_0 + A \cdot T^{\alpha}$ with an additional hump superimposed at around 50 K which has also been observed in literature before [184]. It may be indicative of a hidden phase transition, i.e. that in the presence of time-dependent fluctuations some parts of the sample already undergo a phase transition for the reason that $(DCNQI\text{-}h_8)_2Cu$ is located at the boundary between two phases (see Fig. 2.10d). Not only deuteration, but also the presence of $^{13}C$ carbon isotopes can promote a phase transition via steric distortion causing an effective pressure [78]. The existence of small amounts of $^{13}C$ in the starting material has been verified by mass spectrometry, pointing into this direction.

The temperature exponent of the resistivity amounts to $\alpha = 2.54$ for $(DCNQI\text{-}h_8)_2Cu$ and is reduced in salts undergoing a phase transition. Fig. 4.1e magnifies the log-log-plot of the temperature-dependent resistivity curves between 150 K and 300 K together with the corresponding, linear fits. The temperature coefficients $\alpha$ obtained from the slope of the fits are given in Tab. 4.1. A clear reduction of $\alpha$ with increasing transition temperature $T_P$ was found, suggesting that some domains already undergo a phase transition above

$T_P$. A reduced $\alpha$ may also be inferred from slight changes in the dimensionality of the electronic structure of the different compounds and a resulting gradual change of the dominant scattering mechanism.

In all cases, $\alpha$ is close to the value of two which is commonly considered to be indicative of either electron-electron scattering or electron-phonon scattering involving two librons or optical phonons (compare Ch. 2.5.2). It also complies with the value of $\alpha = 2.3$ obtained by Mori *et al.* [85]. In order to compare $\alpha$ to scattering theories, pressure and thermal expansion effects need to be taken into account. To transfer the resistivity measured at constant pressure to a value at constant volume (for which theories usually apply), the compressibility $\beta_c(T) = -\frac{1}{V}(\frac{\partial V}{\partial p})_T$, the coefficient of thermal expansion $\varsigma(T) = \frac{1}{V}\frac{\partial V}{\partial T}$ and the pressure dependent resistivity $\rho_P(P,T)$ at each measured temperature $T$ need to be known. With respect to the resistivity value at $T_0$, the other temperature-dependent values may then be corrected by [136]:

$$\rho_{corr}(T = T_0 + \Delta T) = \rho_P \left( \frac{\varsigma(T) \cdot \Delta T}{\beta_c(T)} \right) \quad . \tag{4.1}$$

Unfortunately, the data is not available in the whole temperature range for (DCNQI-$h_8$)$_2$Cu, but some estimates of the RT value relative to a base temperature of $T_0 = 100\,\mathrm{K}$ can be made by taking a compressibility of $\beta_c = 1.1 \times 10^{-3}\,\mathrm{kbar}^{-1}$ [185], a pressure-dependent resistivity of about $\rho_P(300\,\mathrm{K}, P) \approx \frac{\rho(300\,\mathrm{K},1\,\mathrm{bar})}{1+0.15\,\mathrm{kbar}^{-1}\cdot P}$ [186] (both at RT) and a thermal expansion coefficient of $\varsigma = 70 \times 10^{-6}\,\mathrm{K}^{-1}$ [187] being almost constant between 100 K and RT. Employing Eq. 4.1, the RT resistivity is reduced by a factor of three compared to its value measured at constant pressure. The volume-corrected resistivity at RT is delineated in Fig. 4.1f together with the reference value at $T_0 = 100\,\mathrm{K}$ as green dot.

The slope of the line connecting these two resistivity points (green) corresponds to an exponent of $\alpha = 1.35$ differing significantly from the $T^2$ behavior expected for the anomalous scattering mechanisms discussed above. Even more surprisingly, the temperature dependence of $\rho$ between 50 K and 100 K is also very well reproduced by this slope. In this temperature regime the thermal expansion slows down [188] and constant volume conditions already might have been established. Hence, the hump at 50 K might rather represent a gradual change in the conduction mechanism of the crystal. For example, an increased low-temperature contribution to the electrical conductivity by holes originating from a 3D Fermi surface at the Γ-point has been suggested from the analysis of Hall, magnetotransport and transient thermoelectric measurements [189]. The origin of the holes at the Γ-point and their influence on electrical transport quantities will be discussed in more detail in the subsequent analysis of the thermopower. A phonon drag effect could also lead to a decreased electrical resistivity at cryogenic temperatures (compare Eq. 2.87).

Applying the Luttinger liquid (LL) theory outlined in Ch. 2.5.2 to the corrected $\alpha = 1.35$, Eq. 2.65 yields a Luttinger interaction parameter of $K_\rho = 0.48 < 1$ suggesting significant electron-electron repulsion in the material above 50 K. Similar values of $K_\rho$ have been obtained in the quasi-1D organic metal $(TMTSF)_2PF_6$ [136]. Due to the quasi-3D character of the band structure in $(DCNQI\text{-}h_8)_2Cu$, the applicability of the LL theory may be challenged and the value of $\alpha$ close to one might rather imply acoustic phonon scattering to be the dominant scattering mechanism (compare Ch. 2.5.2). In this view it should be pointed out that the resistivity data below 100 K, for which constant volume conditions may be assumed, fits fairly to the Bloch-Grüneisen formula (Eq. 2.61) with a characteristic temperature of $\theta_R = 159 - 222$ K. The fits are illustrated in Fig. 4.1f and hint at a rather ordinary scattering mechanism similar to inorganic metals.

The Bloch-Grüneisen temperature $\theta_R$ usually takes values between the Debye temperature $\theta_D$, representing the average upper energy limit of all three acoustic phonon branches, and the temperature $\theta_S = v_S \hbar k_F / k_B$ [121] defining the upper energy limit of longitudinal acoustic phonon branch. Here, the characteristic Bloch-Grüneisen temperature $\theta_R$ takes significantly higher values compared to the Debye temperature of $\theta_D = 82$ K [34] implying efficient interaction with additional high-energy optical phonon modes. To elucidate the electrical conduction mechanisms in more detail, the complementary investigation of additional transport quantities, such as the thermopower or the thermal conductivity, will provide further insight within this thesis.

| | $T_{P,c}$ [K] | $T_{P,h}$ [K] | $\rho_{RT}$ [µΩ m] | $\alpha$ | $\Delta E_{act}$ [meV] | $2\Delta$ [meV] |
|---|---|---|---|---|---|---|
| $(DCNQI\text{-}h_8)_2Cu$ | - | - | 9.5 | 2.54 | - | - |
| $(DCNQI\text{-}h_8/d_6)_2Cu$ [70:30] | 54 | 66 | 16.5 | 2.50 | 31-43 | 77 |
| $(DCNQI\text{-}d_6)_2Cu$ | 82 | 90 | 12.8 | 2.24 | 34-55 | 79 |
| $(MeBr\text{-}DCNQI)_2Cu$ | 156 | 156 | 12 | 2.00 | 21-65 | 45 |

Table 4.1: Material parameters extracted from temperature-dependent resistivity measurements on four chemically different $(DCNQI)_2Cu$ salts.

### Charge Carrier Transport in the Peierls State

In order to investigate the charge-carrier activation energies in the Peierls insulating state, Fig. 4.2a plots the resistivities of the three Peierls insulating $(DCNQI)_2Cu$ compounds

logarithmically against the inverse temperature. It neither follows the behavior of a conventional intrinsic semiconductor, described by Eq. 2.66, nor does it represent the variable range hopping model characterized by Eq. 2.68. In principle, the charge-carrier activation energy $\Delta E_{act}$ may be estimated from the slope of the plots in 4.2a below $T_P$. However, the curves do not strictly but rather piecewise follow a linear behavior below $T_P$. This is illustrated for $(\text{MeBr-DCNQI})_2\text{Cu}$ showing an activation energy of about $\Delta E_{act} = 65\,\text{meV}$ just below $T_P$ which reduces to $\Delta E_{act} = 21\,\text{meV}$ at even lower temperatures. This may indicate a temperature-dependent charge-carrier activation energy. However, a reduction of the Peierls gap upon decreasing temperature seems counter-intuitive. More likely, the relative mobility of electrons and holes changes in this temperature regime, leading to an increased hole conduction at reduced ambient temperature. More evidence for this interpretation will be provided by the analysis of the Seebeck coefficient in the oncoming part.

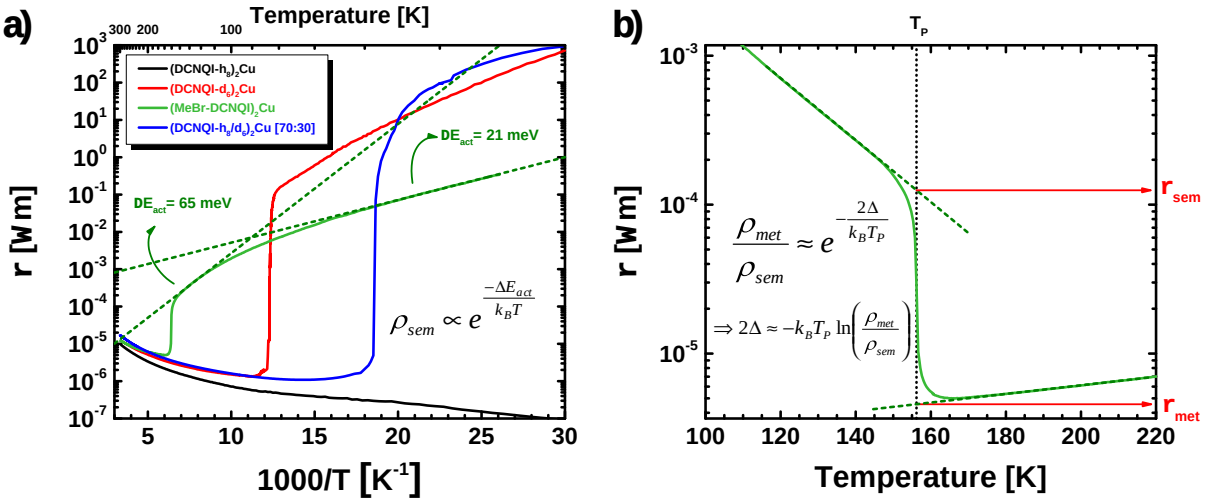


Figure 4.2: Electrical resistivity in the Peierls insulating state. (a) Plotting the resistivity data against inverse temperature indicates a piecewise linear behavior with a related temperature-dependent activation energy $\Delta E_{act}$ in the Peierls state. (b) The energy gap $2\Delta$ obtained from the jump in resistivity exceeds the values obtained from the slopes in (a).

Alternatively, the energy gap may also be estimated from the jump of the resistivity at the first-order Peierls transition. Extrapolating the resistivity data from just above and below the transition temperature, exemplary depicted in Figure 4.2b for $(\text{MeBr-DCNQI})_2\text{Cu}$, the energy gap $2\Delta$ opening at the Peierls transition can be estimated to

$$\frac{\rho_{met}}{\rho_{sem}} = e^{-\frac{2\Delta}{k_B T_P}} \tag{4.2a}$$

$$\rightarrow 2\Delta = -k_B T_P \ln \frac{\rho_{metallic}}{\rho_{sem}} \quad . \tag{4.2b}$$

The estimation neglects the differing mobilities in the metallic and in the insulating regime and assumes only one type of charge carrier to be responsible for electrical conduction in the semiconducting regime. By virtue of the higher band curvature and the smaller electron-electron interaction at a reduced charge carrier density, the mobility is expected to be larger in the semiconducting regime, i.e. Eq. 4.2b represents a lower estimate of the energy gap [122].

In Tab. 4.1 the energy gaps estimated for the three $(DCNQI)_2Cu$ salts undergoing a phase transition are compared to the activation energies obtained from the temperature-dependent resistivity in the semiconducting regime. Except for temperatures just below the phase transition, the activation energy $\Delta E_{act}$ is significantly smaller than the energy gap $2\Delta$, i.e. the transport is governed by activation of charge carriers from shallow states in the bandgap [182]. At sufficiently low temperatures, the activation energy is roughly smaller by a factor of two as compared to the energy gap at the phase transition. This might be indicative of solitons or polarons forming as charge-carrying entity [75]. In this context, the soliton is an elementary domain wall pair excitation separating two degenerate lattice ground states in space. The domain wall usually extends over several lattice constants and its activation energy is about half the Peierls gap [190, 191]. A polaron describes a quasiparticle formed by a slow-moving charge carrier together with its polarization of nearby lattice ions. The effective mass of a polaron is increased compared to the free electron value and the effect is more pronounced in polar semiconductors. Due to the ionic character of organic charge transfer salts, it may thus be of importance in the semiconducting regime of these materials. The polaron energy amounts to $E_p = \Delta/2^{1/2}$ [75], i.e. the polaron forms states in the electronic energy gap of a polar semiconductor. Yet, the accuracy of the gap determination does not permit to directly assign the dominant quasiparticle carrying the current in the semiconducting regime.

### 4.1.2 Thermopower of $(R_1,R_2\text{-DCNQI})_2Cu$

On the same samples discussed above, thermopower measurements have been conducted in addition to the determination of the electrical resistivity. They are shown in Fig. 4.3a. The step-like increase in the electrical resistivity caused by the Peierls transition goes along with a jump of the thermopower at the corresponding critical temperature $T_P$. It should be noted that the Seebeck coefficient is measured while heating the sample from 4 K to room temperature and accordingly, the transition temperatures correspond to the ones in the heating cycle of the resistivity measurements. The metallic part of the thermopower is magnified in Fig. 4.3b. All salts reveal negative Seebeck coefficients indicating electrons to be the majority charge carriers and electrical conduction to occur

mainly via bands formed by the LUMO of the DCNQI molecules. At RT, the Seebeck coefficient of $(\text{DCNQI-h}_8)_2\text{Cu}$ is about $S = -34\,\mu\text{V}\,\text{K}^{-1}$ with its absolute value decreasing upon cooling as expected for a metal. It can be fitted linearly with a constant offset $S_0$ between 200 K and 300 K:

$$S(T) = S_0 + \frac{dS}{dT} \cdot T \quad . \tag{4.3}$$

For salts undergoing a Peierls transition, the absolute values of the RT Seebeck coefficient $S_{RT}$ decrease in samples with higher transition temperature. In turn, the slope of the fit seems to increase. The data extracted from the fits are denoted in Tab. 4.2. The bandwidth $W$ was estimated from the slope with the help of Eq. 2.76, assuming an energy-independent relaxation time and a charge transfer ratio of $\delta = 2/3$.

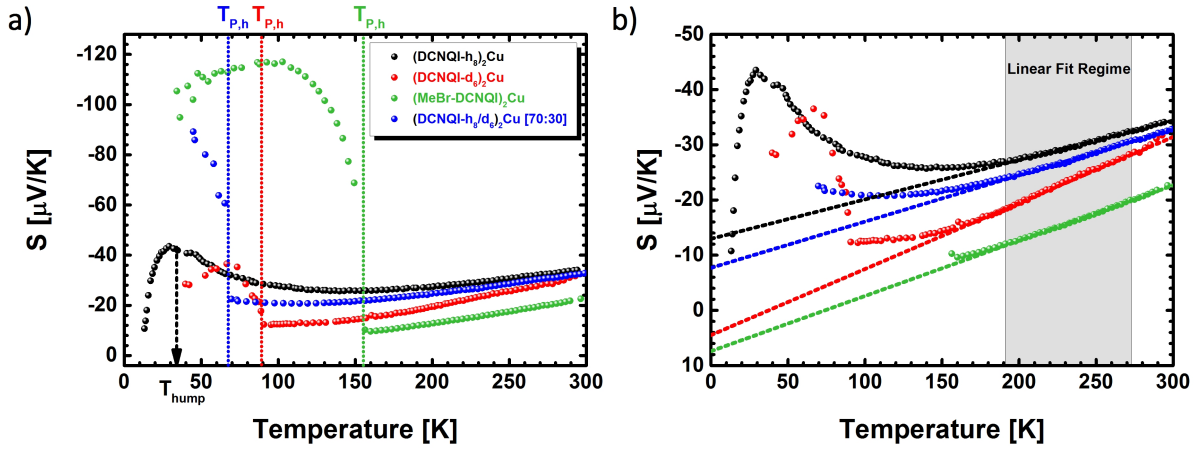


Figure 4.3: Thermopower measurement on the four $(\text{DCNQI})_2\text{Cu}$ salts. (a) The first-order Peierls transitions manifest in a jump of the Seebeck coefficient while the purely metallic $(\text{DCNQI-h}_8)_2\text{Cu}$ reveals an anomalous hump at about 35 K. (b) Magnifying the metallic regime, a linear temperature dependence of $S$, typical for metals, is observed. Slope and offset of the linear fits between 200 K and 300 K differ for the respective materials and are given in Tab. 4.2.

The calculated bandwidths of $(\text{DCNQI-h}_8)_2\text{Cu}$ and $(\text{DCNQI-d}_6)_2\text{Cu}$ differ by 80% and as such, are implausible due to the almost identical crystal and band structure of both materials (compare Ch. 2.3.1 and 2.3.2). The extracted bandwidths also deviate significantly from the value of 792 meV calculated by a tight-binding band structure approach [10]. Additionally, the observed offset is not predicted by the theory of simple metals and takes rather large values of even opposite sign for the respective materials. Accordingly, the simple band model description by Eq. 2.76 has to be revised for a consistent estimation of the Seebeck coefficient in the $(\text{DCNQI})_2\text{Cu}$ system. Some extensions on the model will be suggested in the following.

For the purely metallic $(\text{DCNQI-h}_8)_2\text{Cu}$ a hump at about $T_{hump} \approx 35\,\text{K}$ is observed,

| | $T_P$ [K] | $S_{RT}$ [$\frac{\mu V}{K}$] | $\frac{dS}{dT}$ [$\frac{nV}{K^2}$] | $S_0$ [$\frac{\mu V}{K}$] | W [meV] |
|---|---|---|---|---|---|
| $(DCNQI\text{-}h_8)_2Cu$ | - | -34.0 | -68.0±0.7 | -13.8±0.2 | 480±6 |
| $(DCNQI\text{-}h_8/d_6)_2Cu$ [70:30] | 54 | -32.7 | -83.8±0.8 | -7.7±0.2 | 390±4 |
| $(DCNQI\text{-}d_6)_2Cu$ | 83 | -31.3 | -124±2 | 5.5±0.3 | 260±4 |
| $(MeBr\text{-}DCNQI)_2Cu$ | 156 | -22.5 | -101±1 | 7.6±0.2 | 320±3 |

Table 4.2: Material parameters extracted from the linear fits of the Seebeck coefficient for four chemically different $(DCNQI)_2Cu$ salts as delineated in Fig. 4.3b.

in agreement with studies published in literature [85, 192]. It has been discussed in terms of a phonon-drag effect [85] as well as a hidden phase transition, i.e. in the presence of time-dependent fluctuations a Peierls insulating state occurrs in partial domains of the crystal [192]. The correlated hump in the resistivity measurement may favor the latter explanation. Yet, the apparent hidden phase transition would occur about 15 K above the corresponding peak in the Seebeck coefficient questioning this conclusion.

Rather, an additional non-diffusive phonon drag contribution to the thermopower, as discussed in Ch. 2.6.2, seems plausible and may also explain the different linear slopes observed in the thermopower above 200 K. The phonon drag effect is caused by phonons pushing charge carriers along a temperature gradient by virtue of phonon-electron scattering, giving rise to an additional contribution in the thermopower. According to Eq. 2.87, this effect also reduces the electrical resistivity and thus, the apparent hump in the resistivity at about 50 K may be due to the phonon drag coming into play at lower temperatures. This is in good agreement with the thermopower peaking 15 K below the hump in the resistivity. To model the thermopower over the entire temperature regime studied, Eqs. 2.77 and 2.86 may be combined to:

$$S = \underbrace{-\frac{2\pi^2 k_B^2 T}{3|e|W} \cdot \left[\frac{\cos\delta\pi/2}{(1-\cos^2\delta\pi/2)} + \frac{r}{\delta}\right]}_{S_{diff}} + \underbrace{\frac{\rho_{dens}}{nem_{mol}} \left(\frac{T_0}{T}\right)^{v} c_{mol}\left(\frac{\theta_{D/E}}{T}\right)}_{S_{drag}} \quad . \tag{4.4}$$

At small $T$, the temperature dependence of the phonon-drag thermopower $S_{drag}$ is determined by the molar specific heat $c_{mol}(\theta_{D/E}/T)$ of those phonon modes interacting efficiently with electrons. Depending on the dispersion of the involved phonon modes pushing electrons to the cold side of the sample, the specific heat can be modeled by a Debye (Eq. 2.48) or an Einstein model (Eq. 2.43) with $E = k_B\theta_{D/E}$ characterizing

the relevant energy scale of the modes. For higher $T$, the relative strength of phonon-electron scattering compared to other phonon-related scattering mechanisms limits its contribution to the thermopower. The temperature dependence of this scattering factor is phenomenologically captured by a power law $\beta = \left(\frac{T_0}{T}\right)^{\upsilon}$.

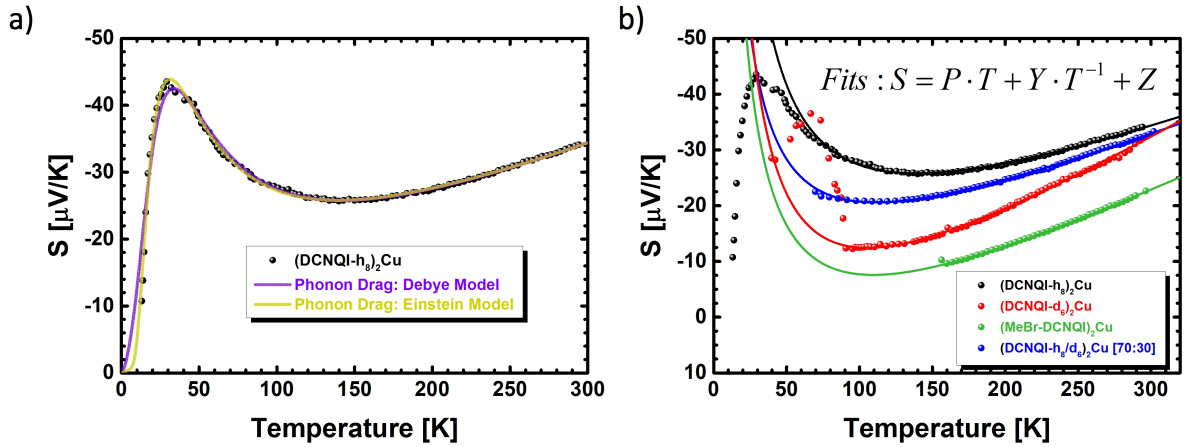


Figure 4.4: Phonon drag thermopower in (DCNQI)$_2$Cu. (a) The temperature-dependent Seebeck coefficient of (DCNQI-h$_8$)$_2$Cu can be accurately fitted by Eq. 4.4 assuming an Einstein or Debye model for the specific heat. (b) The metallic regime of all (DCNQI)$_2$Cu salts fitted to an equation including a diffusive ($\propto T$) and a phonon-drag contribution ($\propto T^{-1}$) as well as a constant offset.

For the diffusive part $S_{diff}$, Eq. 4.4 contains an energy-dependent relaxation time $\tau = c_0 E^r$. By reason of the one-dimensional band structure a value of $r = 0.5$ is assumed (compare Ch. 2.5.2). Fig. 4.4a depicts the thermopower of (DCNQI-h$_8$)$_2$Cu together with two fits by Eq. 4.4, one assuming a Debye and the other an Einstein model for the phonon mode dispersion. Both fits are able to describe the thermopower over the complete temperature regime while the Einstein model seems to capture the low-temperature data slightly better. It should be noted that no constant offset, as compared to the $S_0$ parameter in Eq. 4.3, had to be added to Eq. 4.4 in order to model the data for (DCNQI-h$_8$)$_2$Cu. The corresponding fit parameters are stated in Tab. 4.3.

| | W=4t [meV] | $T_0$ [K] | $\upsilon$ | $\theta_{D/E}$ [K] |
|---|---|---|---|---|
| Debye Model | 690±15 | 16.7±4.5 | 1.31±0.06 | 137±6 |
| Einstein Model | 710±7 | 13.7±1.0 | 1.18±0.02 | 85±1 |

Table 4.3: Parameters of the fits by Eq. 4.4 to the data of (DCNQI-h$_8$)$_2$Cu in Fig 4.3a.

The obtained bandwidth of about $W = 710\,\text{meV}$ for (DCNQI-h$_8$)$_2$Cu agrees significantly better with the value of 792 meV deduced from the tight binding band structure

calculation [67]. The relaxation time of the form $\tau(\epsilon) \propto \sqrt{\epsilon}$ corroborates the findings from the volume-corrected resistivity, i.e. that acoustic phonon scattering limits the charge carrier mobility at high $T$. The value of $\upsilon = 1.18$ is close to the expected value of 1 for phonon-phonon Umklapp scattering limiting the phonon drag at high temperature. Slightly higher $\upsilon$ values have also been observed in thermal conductivity measurements of various materials, also being limited by phonon-phonon Umklapp processes. It has been explained in terms of lattice anharmonicity as well as by four phonon scattering scattering events in addition to the ordinary three-phonon Umklapp process [92].

The Einstein temperature of $\theta_E = 85\,\mathrm{K}$ agrees with the Debye temperature of $\theta_D = 82\,\mathrm{K}$ [34] determined by low-temperature specific heat measurements and indicates that acoustic phonon modes with an upper energy of about $E = k_B\theta_E \approx 7\,\mathrm{meV}$ are predominantly in charge of the phonon-drag effect. It is surprising that, apparently, the Einstein model works better than the Debye one for these modes. Presumably the complex phonon spectrum in combination with the smaller dispersion and sound velocity in organic materials facilitates an Einstein description of acoustic phonon modes, at least far away from the very low temperature regime below 10 K. The additional influence of low-energy optical phonons, as depicted for the TTF-TCNQ phonon dispersion in Ch. 2.4.3, can furthermore promote an overall flat dispersion of the involved modes.

The Peierls transition prevents the other salts' thermopower from being modeled by Eq. 4.4. However, a simplified fit equation of the form

$$S = P \cdot T + Y \cdot T^{-1} + Z \tag{4.5}$$

was used to fit the data in the metallic regime of all investigated $(DCNQI)_2Cu$ salts. Here, the first term corresponds to the diffusive part $S_{diff}$ and the term scaling inversely with temperature models the high temperature side of the phonon drag phenomena in Eq. 4.4. In contrast to the previous phonon drag analysis of the thermopower in (DCNQI-$h_8$)$_2$Cu, an offset $Z$ had to be added again in order to model all measurements by the same equation, enabling a direct comparison of parameters. The fit results are listed in Tab. 4.4. The bandwidth was again calculated from the slope $P$ with the help of Eq. 4.4 assuming a charge transfer ratio of $\delta = 2/3$ as well as $r = 0.5$.

As to be expected, the bandwidths obtained for (DCNQI-$h_8$)$_2$Cu and (DCNQI-$h_8$/$d_6$)$_2$Cu [70:30] are almost similar and the constant $Z$ takes negligibly small values, in agreement with the fit results obtained by Eq. 4.4 for (DCNQI-$h_8$)$_2$Cu. In contrast, the apparent bandwidths of (DCNQI-$d_6$)$_2$Cu and (MeBr-DCNQI)$_2$Cu differ significantly in spite of the similar crystal and band structure compared to (DCNQI-$h_8$)$_2$Cu. This deviation can be resolved by considering the large positive offset $Z$. Apparently, a positive hole-like

| Material | P [$\frac{nV}{K^2}$] | Y [mV] | Z [$\frac{\mu V}{K}$] | W [meV] |
|---|---|---|---|---|
| (DCNQI-$h_8$)$_2$Cu | -99.7±1.1 | -1.93±0.02 | 1.98 ±0.35 | 690±8 |
| (DCNQI-$h_8$/$d_6$)$_2$Cu [70:30] | -103.7±0.7 | -1.28±0.02 | 2.47±0.25 | 670±5 |
| (DCNQI-$d_6$)$_2$Cu | -158.2±1.8 | -1.76±0.05 | 20.94±0.64 | 440±5 |
| (MeBr-DCNQI)$_2$Cu | -126.4±1.4 | -1.51±0.07 | 20.07±0.63 | 550±6 |

Table 4.4: Parameters of the fits by Eq. 4.5 to the data of (DCNQI)$_2$Cu in Fig 4.4b. The errors are estimated from the fit solely.

contribution to the thermopower appears in (DCNQI-$d_6$)$_2$Cu and (MeBr-DCNQI)$_2$Cu. The offset amounts to about $20\,\mu V\,K^{-1}$ for each of the two materials, but seems to be temperature-dependent itself causing the high-temperature slope of (DCNQI-$d_6$)$_2$Cu and (MeBr-DCNQI)$_2$Cu to differ from the other two salts. This leads to the apparent smaller bandwidth derived from a single band model without holes. The hole-contribution appears more prominent in salts with higher Peierls transition temperatures indicating an influence of the functional groups attached to the central quinone ring on the coordination of the DCNQI molecule around the Cu counter ions.

(DCNQI-$d_6$)$_2$Cu is electronically equivalent to (DCNQI-$h_8$)$_2$Cu and therefore, the hole contribution does not play a significant role at high temperatures, as evidenced by the similar absolute value of the RT Seebeck coefficient in the deuterated and undeuterated salt. On lowering the temperature, the subsequent change in the coordination angle $\alpha_{co}$ (compare Fig. 2.9e) causes the slope of the thermopower to become steeper in the deuterated salt as compared to (DCNQI-$h_8$)$_2$Cu because the hole contribution increases. In (MeBr-DCNQI)$_2$Cu the hole contribution already diminishes the Seebeck coefficient at RT by about $10\,\mu V\,K^{-1}$ (30%) and its contribution augments to the constant offset of $20\,\mu V\,K^{-1}$ at low T. Accordingly, the temperature slope has to be steeper as well compared to (DCNQI-$h_8$)$_2$Cu, but not as much as for (DCNQI-$d_6$)$_2$Cu. The resulting effective bandwidth therefore comes closer to that of 690 meV obtained for the undeuterated (DCNQI-$h_8$)$_2$Cu.

Independent de Haas-van Alphen measurements [77] evidence a 3D hole pocket around the Γ-point which has been theoretically explained by *ab-initio* calculations to originate from hybridized 3$d_{xy}$-$\pi$-orbitals [67]. Combined magnetoresistance and transient thermoelectric measurements also suggest a hole contribution gaining importance at low temperatures, being consistent with the results above [189]. In combination with band structure calculations, the concentration of holes at the Γ-point were found to be increased in

(DCNQI-$d_6$)$_2$Cu as compared to (DCNQI-$h_8$)$_2$Cu at low temperatures. The above thermopower measurements confirm the strong influence on the hole contribution to charge carrier transport by the functional groups attached to the quinone ring of DCNQI. The groups vary the coordination angle $\alpha_{co}$ of the DCNQI molecule around the copper ions and consequently, they influence the degree of $3d_{xy}$-$\pi$-hybridization, leading to a sensitive shift in the Fermi energy. The impact of this shift in Fermi energy on the Seebeck coefficient calculated by the Boltzmann theory is clarified in Fig. 4.5. According to the Boltzmann theory, the Seebeck coefficient is given by:

$$S = \mp\frac{1}{eT}\frac{\int g(\epsilon)\left[\vec{v}(\epsilon)\otimes\vec{v}(\epsilon)\right]\tau(\epsilon)[\epsilon - E_F]\frac{\partial f^0}{\partial \epsilon}d\epsilon}{\int g(\epsilon)\left[\vec{v}(\epsilon)\otimes\vec{v}(\epsilon)\right]\tau(\epsilon)\frac{\partial f^0}{\partial \epsilon}d\epsilon} \quad . \qquad \text{(2.74 revisited)}$$

The density of states $g(E)$ in the vicinity of the Fermi energy $E_F$, derived from *ab-initio* calculations of the band structure presented in Fig. 2.9a, is depicted in Fig. 4.5a (yellow curve) together with the material-independent argument $[\epsilon - E_F]\frac{\partial f^0}{\partial \epsilon}$ in the nominator of Eq. 2.74 (blue curve). Additionally, the energy dependency of the electron velocity $(\vec{v}(\epsilon)\otimes\vec{v}(\epsilon)) \propto (\epsilon - E_0)$ and of the scattering time $\tau(\epsilon) \propto \sqrt{\epsilon - E_0}$ are combined to $(\epsilon - E_0)^{3/2}$, as represented by the red curve, assuming the bottom of the energy band to be located at $E_0 = -0.25\,\text{eV}$ and neglecting their energy-independent prefactors. Multiplying the three curves with each other yields the integrand of the nominator in Eq. 2.74, neglecting energy-independent factors which cancel out in the calculation of the Seebeck coefficient, anyways. The integrand is delineated in Fig. 4.5b and the corresponding, mathematical area underneath the curve determines the sign of the Seebeck coefficient and scales its magnitude. To calculate the absolute thermopower, the integral needs to be normalized to the denominator of Eq. 2.74 (also neglecting energy-independent prefactors). Fig. 4.5b shows that the thermopower of (DCNQI)$_2$Cu must be smaller than zero according to the larger negative area above $E_F$.

The density of states is quite symmetric around $E_F$ and hence, the sign of the thermopower is mainly determined by the energy dependence of the electron velocity and scattering time, emphasizing the contribution from states above the Fermi energy. The local symmetry of $g(E)$ around $E_F = 0$, corresponding to the Fermi energy of (DCNQI-$h_8$)$_2$Cu at RT, is lifted upon slightly increasing the Fermi energy by 40 meV, as illustrated by the green curves in Fig. 4.5a-b. A shift of the Fermi energy by 40 meV roughly corresponds to an increase of charge transfer by $0.1e$ and hence, is of reasonable magnitude when compared to the charge transfer difference of about $0.03e$ between (MeBr-DCNQI)$_2$Cu and (DCNQI-$h_8$)$_2$Cu [82]. In this case, the density of states below the Fermi energy is higher than above, leading to a pronounced contribution of holes to the integral. In turn, the electron contribution is reduced. While the sign of the Seebeck coefficient remains negative

due to the energy dependence of the electron velocity and charge carrier scattering time, its absolute magnitude reduces upon increasing the Fermi energy. The opposite effect, a more pronounced electron contribution is anticipated for a decreased Fermi energy.

Assuming a temperature-dependent Fermi energy of the form

$$E_F = E_F(300\,\mathrm{K}) + \Delta E_F \cdot \left[1 - \frac{T}{300\,\mathrm{K}}\right] \quad , \tag{4.6}$$

the temperature-dependent Seebeck coefficients calculated by Eq. 2.74 are illustrated in Fig. 4.5c for different parameters $E_F(300\,\mathrm{K})$ and $\Delta E_F$. The shift is calculated relative to the Fermi energy of $E_F(h_8, 300\,\mathrm{K}) = 0$ for (DCNQI-h$_8$)$_2$Cu.

For $E_F = 0$ at RT, a Seebeck coefficient of about $-37\,\mu\mathrm{V\,K^{-1}}$ is evaluated, in good agreement with the experimental value of $S = -34\,\mu\mathrm{V\,K^{-1}}$ for the (DCNQI-h$_8$)$_2$Cu salt. The decrease in RT thermopower by about $10\,\mu\mathrm{V\,K^{-1}}$ observed in (MeBr-DCNQI)$_2$Cu can be explained by an effective increase of the Fermi energy to $E_F(300\,\mathrm{K}) = 20\,\mathrm{meV}$. The parameter $\Delta E_F$ scales the temperature dependence of $E_F$ in Eq. 4.6 being caused by the thermal contraction of the lattice which allows for a larger 3d$_{xy}$-$\pi$-hybridization upon cooling. This hybridization is expected to increase more significantly upon cooling in the deuterated salts as compared to (DCNQI-h$_8$)$_2$Cu, as proven by the occurrence of the Peierls transition in the former. Hence, the deuterated (DMe-DCNQI)$_2$Cu salts gradually advance the Fermi energy level of (MeBr-DCNQI)$_2$Cu upon cooling, thereby yielding different slopes in the Seebeck coefficient since the effect is more pronounced in (DCNQI-d$_6$)$_2$Cu than in (DCNQI-h$_8$/d$_6$)$_2$Cu [70:30]. Extrapolating the linear slopes above 200 K to zero, the presented model is also able to explain the different signs of the offsets for (DCNQI-h$_8$)$_2$Cu and (DCNQI-d$_6$)$_2$Cu at 0 K. Fig. 4.5c-d compare the calculated Seebeck coefficients with the experimental data. Neglecting the superimposed phonon drag effect in the experimental data, the diffusive thermopower, as anticipated by the linear fits in Fig. 4.5d, is qualitatively and quantitatively well explained by the above introduced model for the (DCNQI)$_2$Cu material system.

The influence of an increased Fermi level on the electronic structure is clarified in Fig. 4.5e. The Fermi level shift ascertains the hole character of the quasi-3D band at the $\Gamma$-point. The Fermi energy increases according to the order $\mathrm{E}_F[\mathrm{h_8}] < \mathrm{E}_F[\mathrm{d_6}] < \mathrm{E}_F[\mathrm{MeBr}]$. A Fermi level rise is also induced by a reduction of the sample temperature. The increase in $E_F$ goes along with an increased 3d$_{xy}$-$\pi$-hybridization and a larger filling of the quasi-1D electron band. The larger hybridization is also corroborated by XPS measurements conducted by Akaki *et al.* [82], indicating a larger Cu valence state of +1.32 in (MeBr-DCNQI)$_2$Cu as compared to +1.28 in (DCNQI-h$_8$)$_2$Cu. For a Cu valence state of +1.33 a commensurate Peierls metal-insulator transition is triggered on the DCNQI chain. In

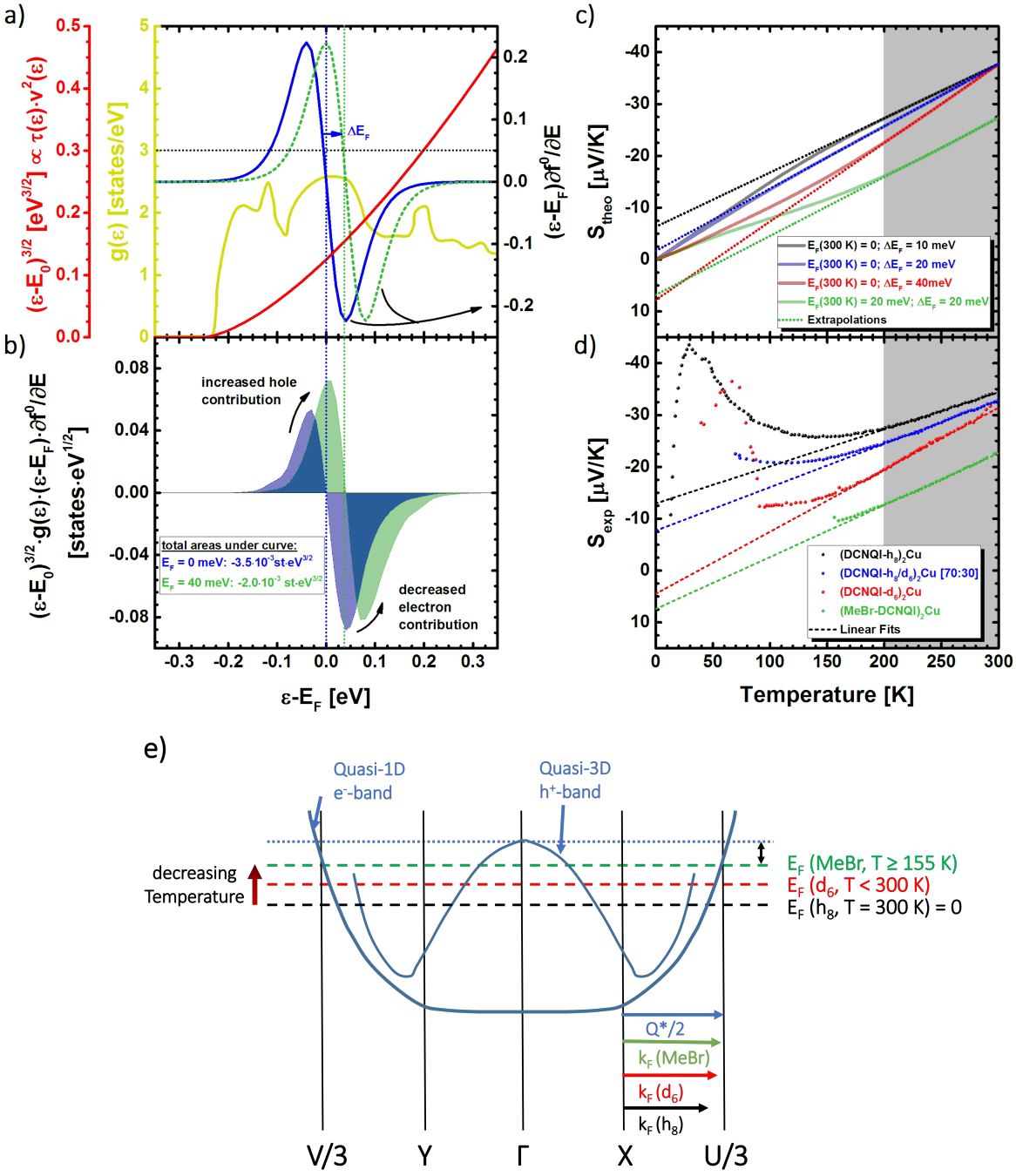


Figure 4.5: Boltzmann theory of the thermopower in $(DCNQI)_2Cu$. Multiplication of (a) the energy-dependent contributions by to the transport integral yields (b) the integrand of the nominator in Eq. 2.74, neglecting energy-independent prefactors. A shift in the Fermi energy lifts the local symmetry of g(E) and causes an increased hole contribution to the thermopower. Assuming a temperature-dependent shift of the Fermi energy, (c) the calculated Seebeck coefficients reproduce the linear diffusive contribution of (d) the experimental Seebeck coefficients very well. The gray shaded area marks the linear fit regime. (e) A schematic band model emphasizes how the commensurability condition $k_F = Q^*/2$ is only fulfilled for an upward-shifted Fermi energy relative to $(DCNQI\text{-}h_8)_2Cu$ at RT. This explains the occurrence of a CDW transition in $(MeBr\text{-}DCNQI)_2Cu$, being already close to this commensurability condition above its transition temperature $T_P = 155\,K$, in contrast to its absence in the whole temperature regime down to 4 K for $(DCNQI\text{-}h_8)_2Cu$. The Fermi level of $(DCNQI\text{-}d_6)_2Cu$ at RT is similar to that of $(DCNQI\text{-}h_8)_2Cu$ but shifts toward higher values for $T < 300\,K$.

this situation, the Fermi wave vector is increased to a value of $k_F = Q^*/2$ to fulfill the commensurability condition. This critical value is easily reached in (MeBr-DCNQI)$_2$Cu causing the CDW transition at a rather high temperature of $T_P = 155\,\mathrm{K}$. In contrast, the absence of a Peierls transition in (DCNQI-$h_8$)$_2$Cu indicates the Fermi wave vector to remain below this critical value in the whole temperature regime. For (DCNQI-$d_6$)$_2$Cu and (DCNQI-$h_8$/$d_6$)$_2$Cu [70:30] the transition occurs at intermediate temperatures. The XPS measurements were only able to verify a sudden valence change across the metal-insulator transition but not a temperature-dependent charge transfer preceding the occurrence of the phase transition. However, from the analysis of different (DCNQI)$_2$Cu compounds the coordination angle $\alpha_{co}$ was verified to depend on the copper valence state. Accordingly, owing to the temperature-dependent $\alpha_{co}$ [66, 71] the valence of Cu is expected to vary with temperature, too. In this sense, the temperature-dependent thermopower analysis conducted here is found to be more sensitive to the details of the electronic structure around the Fermi energy than the XPS measurements.

The outlined Fermi level shift may also explain the lower electrical conductivity $\sigma$ obtained for (MeBr-DCNQI)$_2$Cu as compared to (DCNQI-$h_8$)$_2$Cu because $E_F$ is moved away from the local maximum of the density of states. Yet, the absolute values of $\sigma$ will also sensitively depend on the purity and defect density of the crystal as well as the determined crystal cross section. Especially the MeBr-DCNQI molecule is harder to synthesize [193] and difficult to crystallize with copper [78] compared to DMe-DCNQI. The diffusive thermopower is less prone to these errors because it represents an intense quantity measured by a current-free technique.

### Thermopower in the Peierls Insulating State

Fig. 4.6 plots the thermopower of the three Peierl insulators against the inverse temperature. Complementary to the resistivity measurements in the previous section, the simple $S \propto T^{-1}$ law expected by Eq. 2.79 for a semiconductor is not obeyed over larger temperature regimes. In addition, the activation energies estimated from the linear parts are considerably lower as compared to the activation energies extracted from resistivity measurements. Furthermore, the absolute Seebeck coefficients differ significantly between the salts in spite of their common ground state. Tab. 4.5 compares the Seebeck coefficients at $T = 50\,\mathrm{K}$ of the different salts together with the activation energy $\Delta E_{act}$ derived from the conductivity measurement at this temperature in the previous section. Employing $\Delta E_{act}$ and an inferred scattering parameter of $r = 0.5$, the theoretical Seebeck coefficient $S_{theo}$ was calculated by Eq. 2.79 and is also cited.

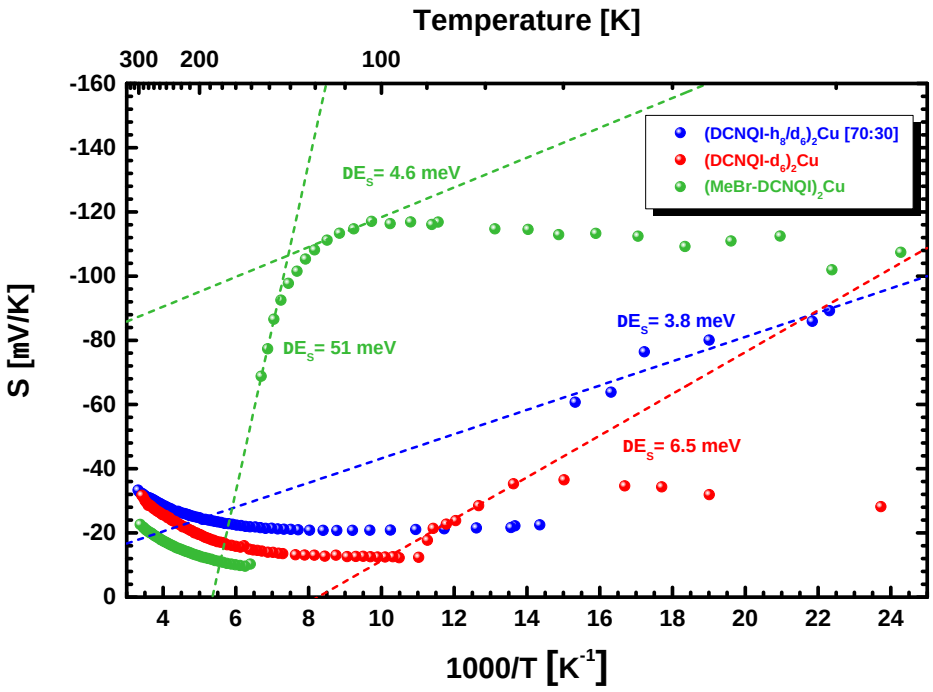


Figure 4.6: Seebeck coefficient in the Peierls insulating state. The thermopower is plotted against the inverse temperature for the three $(DCNQI)_2Cu$ salts undergoing a Peierls metal-insulator transition. A linear relation, as anticipated by the simple parabolic band model of Eq. 2.79, is not obtained over an appreciable temperature regime. Hence, the linear fits (dashed lines) are rather random and are only shown to compare the activation energy to the values estimated from the resistivity data.

Apparently, the case of a simple semiconductor with isotropic, parabolic bands and only one type of charge carrier does not apply in the Peierls insulating state of $(DCNQI)_2Cu$ salts. Moreover, Eq. 2.79 cannot explain the Seebeck coefficient going through a maximum for $(MeBr\text{-}DCNQI)_2Cu$ and $(DCNQI\text{-}d_6)_2Cu$. In addition, the large difference in the thermopower at 50 K between $(DCNQI\text{-}h_8/d_6)_2Cu$ [70:30] and $(DCNQI\text{-}d_6)_2Cu$ is somewhat surprising taking into account their equivalent electronic structure and the similar charge carrier activation energy obtained by the resistivity measurements.

The foregoing thermopower analysis of the metallic regime already suggested the presence of hole minority carriers gaining importance on lowering the temperature. The Seebeck coefficient will crucially depend on the relative density and mobility of electrons and holes, both of which may be temperature- and material-dependent. Because the 3D hole Fermi surface may not be completely removed by the Peierls transition, holes will reduce the absolute magnitude of the negative Seebeck coefficient in the insulating regime, too. In the metallic regime, the hole conduction was found to carry more weight for $(DCNQI\text{-}d_6)_2Cu$ compared to $(DCNQI\text{-}h_8/d_6)_2Cu$ [70:30] and accordingly, the Seebeck coefficient is more negative in the latter than in the former. The thermopower of $(MeBr\text{-}DCNQI)_2Cu$ should be even more drastically reduced by virtue of its larger hole contribution together with its lower charge carrier transport activation energy. However, the opposite is observed

| | $S_{exp}$ [$\frac{\mu V}{K}$] | $\Delta E_S$ [meV] | $\Delta E_{act}$ [meV] | $S_{theo}$ [$\frac{\mu V}{K}$] |
|---|---|---|---|---|
| (DCNQI-$h_8$/$d_6$)$_2$Cu [70:30] | -80 | $\approx 3.8$ | 43 | -601 |
| (DCNQI-$d_6$)$_2$Cu | -30 | $\leq 6.5$ | 43 | -601 |
| (MeBr-DCNQI)$_2$Cu | -108 | 4.6-51 | 24 | -221 |

Table 4.5: Experimental vs. theoretical Seebeck coefficients in the CDW state for the three investigated (DCNQI)$_2$Cu salts at 50 K. $S_{theo}$ is calculated by Eq. 2.79 assuming $r = 0.5$ and an activation energy $\Delta E_{act}$ as estimated from the temperature-dependent resistivity in the previous section. All values are taken at $T = 50$ K. The activation energies $\Delta E_S$, as deduced from the Seebeck coefficients in Fig. 4.6, do not compare well to $\Delta E_{act}$, except for (MeBr-DCNQI)$_2$Cu between 130 K and 155 K. Hence, the details of the band structure have to be taken into account and the simple parabolic band model does not apply.

and (MeBr-DCNQI)$_2$Cu yields a Seebeck coefficient of $-108\,\mu V\,K^{-1}$. This is due to the influence of the structural phase transition on the quasi-3D hole band. In the previous section it was concluded that the hole contribution sensitively depends on the coordination angle $\alpha_{co}$.

Literature XRD studies report a larger change in $\alpha_{co}$ from 126.3° to 128.5° across the phase transition in (DCNQI-$d_6$)$_2$Cu compared to an increase to only 128.0° in (MeBr-DCNQI)$_2$Cu [66]. The larger coordination angle in the insulating phase of (DCNQI-$d_6$)$_2$Cu therefore promotes a larger hole contribution as compared to the Peierls state in (MeBr-DCNQI)$_2$Cu. Upon cooling, the hole contribution also regains importance in (MeBr-DCNQI)$_2$Cu as the Seebeck coefficent passes through a negative maximum and becomes smaller in magnitude again. The effect is more pronounced in (DCl-DCNQI)$_2$Cu, the thermopower of which becomes positive at 100 K after undergoing a metal-insulator transition at 210 K and passing through a maximum at 160 K [85]. In (DCl-DCNQI)$_2$Cu the RT coordination angle is 127.1°, a value compellingly larger than the 124.8° [66] and 125.5° [71] measured for (DCNQI-$d_6$)$_2$Cu and (MeBr-DCNQI)$_2$Cu, respectively. This supports the idea of an additional hole contribution to the electrical conduction and thermopower also in the insulating regime.

Though having a lower hole contribution, Fig. 4.1a reveals the resistivity of (MeBr-DCNQI)$_2$Cu to be smaller by one order of magnitude compared to the other two salts in the insulating regime. This may indicate charge carriers generated by impurity doping to be of importance as well. More likely though, this is an additional evidence for the complex density of states in (DCNQI)$_2$Cu which allows thermopower and electrical conductivity to probe distinctively different states in the vicinity of the Fermi energy (see Ch. 2.5.1).

### 4.1.3 Alloyed $(DCNQI)_2Cu_xLi_{1-x}$

The electronic properties of the $(DCNQI)_2M$ system may not only be varied by the choice of functional groups attached to the quinone ring but also by the counterions used to form the crystals. $(DCNQI)_2Li$ has a very similar crystal structure compared to $(DCNQI)_2Cu$ (compare Ch. 2.3.1). However, the smaller lithium valency of +1 leads to quarter-filled metallic bands which are much more spatially anisotropic due to the lack of the 3d valence states in Li, prohibiting a 3d-$\pi$-hybridization as observed in $(DCNQI)_2Cu$. Hence, the system is characterized as quasi-1D organic metal. Due to the similar crystal structure of the copper and the lithium radical anion salts and their capability of forming mixed crystals across the entire concentration regime, the electronic properties can be varied continuously in alloyed $(DCNQI\text{-}h_8)_2Cu_xLi_{1-x}$ compounds (from now on tagged $(DCNQI)_2Cu_xLi_{1-x}$).

Crystals with varying composition have been grown and characterized. For each sample of nominal copper content $x_{nom}$, deduced from the net weights used in the crystal growth, the ratio of elemental copper and nitrogen (Cu/N) was determined by energy-dispersive X-ray spectroscopy in a scanning electron microscope (SEM-EDX). With four nitrogen atoms per DCNQI molecule, $(DCNQI)_2Cu$ crystals are assumed to reveal a value of Cu/N = 0.125. Experimentally, a higher ratio of $Cu/N = 0.168 \pm 0.002$ was determined for $x = 1$, probably due to a different stoichiometric ratio of elements at the crystal surface, redeposition of sputtered surface materials as well as inaccuracies in the scattering cross sections assumed by the evaluation software. Yet, the Cu/N ratio is found to decrease continuously with increasing lithium content. To determine the effective amount of copper $x_{eff}$ incorporated into each crystal, the linear relation

$$Cu/N = 0.168 \cdot x_{eff} \quad , \tag{4.7}$$

illustrated in Fig. 4.7a, was assumed. From the measurement of the Cu/N ratio for each nominal copper content $x_{nom}$, the $x_{eff}$ values were determined from the linear relation, as also depicted in Fig. 4.7a. It should be clarified that Fig. 4.7a is somewhat counter-intuitive because the abscissa $x_{eff} = x$ is the quantity deduced from the quantities Cu/N and $x_{nom}$ on the ordinate axes. Yet, the chosen graphic rendition allows for a direct comparison of electrical resistivity and Seebeck coefficient for the different stoichiometric contents at RT in Fig. 4.7b.

A continuous decrease in the RT electrical resistivity by one order of magnitude is obtained when going from lithium to copper-rich crystals. Simultaneously, the thermopower decreases in magnitude from about $-72\,\mu V\,K^{-1}$ to $-34\,\mu V\,K^{-1}$ at RT. The large decrement in the electrical resistivity cannot simply be ascribed to the change in the charge-

carrier density which only differs by a factor of 4/3. It is caused by the alternation of the electronic band structure which is understood from the lack of copper 3d states (compare Ch. 2.3.2). Thus, the associated large shift in the electrical conductivity underlines the significant share of 3d states in the high electrical conductivity of $(DCNQI)_2Cu$. The change in the electronic states due to doping has also been observed in the spin-lattice relaxation rate studied via nuclear magnetic resonance measurements [89]. Another aspect might be the larger electronic correlation in the 1D system, influencing the charge carrier scattering rate much stronger in $(DCNQI)_2Li$ due to its quarter-filled band structure. This will be discussed in more detail below when analyzing the Seebeck coefficient.

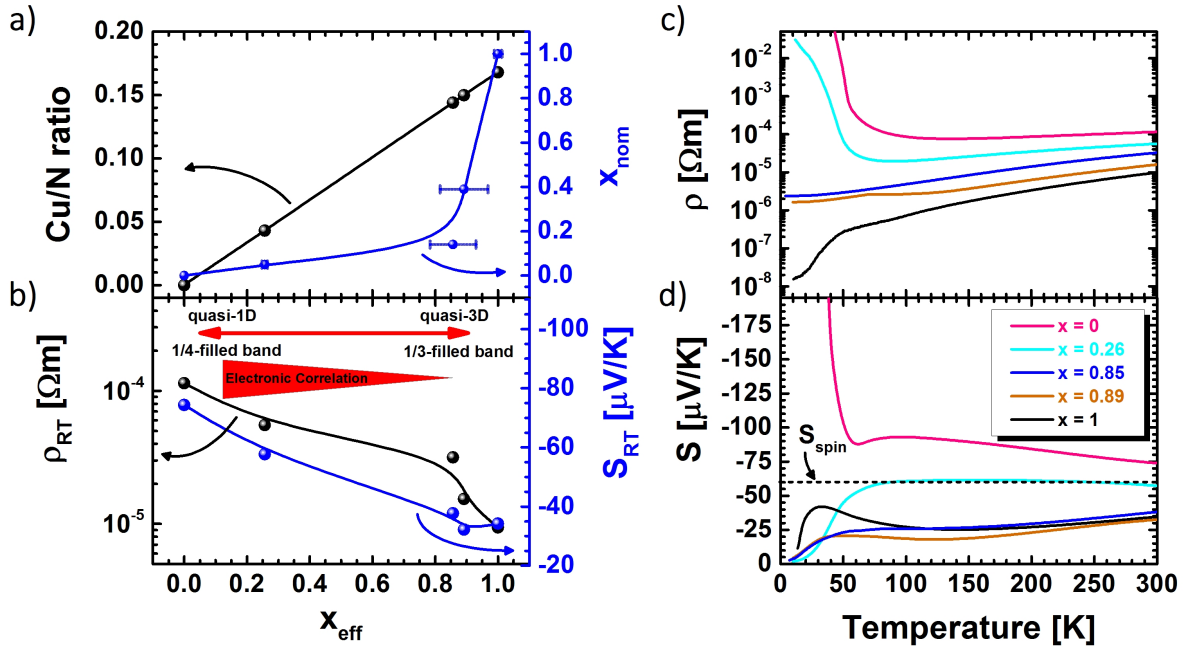


Figure 4.7: Electronic properties of alloyed $(DCNQI)_2Cu_xLi_{1-x}$ crystals. (a) The ratio of copper to nitrogen is expected to vary linearly with the effective copper concentration $x_{eff}$ in the $(DCNQI)_2Cu_xLi_{1-x}$ samples. Measuring Cu/N (black dots) for crystals of various nominal copper content $x_{nom}$ (inferred from the net weights used in the crystal growth procedure) by SEM-EDX allows to determine the effective copper content $x_{eff}$ by assuming a linear relation $Cu/N = 0.168 \cdot x_{eff}$. It should be noted that the abscissa values $x_{eff}$ have been determined for the varied ordinate quantity $x_{nom}$ in this graph. The SEM-EDX data was kindly provided by Stephan Braxmeier from the ZAE Bayern. (b) Change of the electrical resistivity and the Seebeck coefficient with copper content at RT. Temperature-dependent (c) electrical resistivity and (d) Seebeck coefficient of alloyed $(DCNQI)_2Cu_xLi_{1-x}$ crystals derived from interpolated measurements. The dashed line indicates the expected spin entropy $S_{spin} = -k_B/e \ln 2$ of interacting electrons in a quarter-filled band (compare Eq. 2.83).

The temperature-dependent electrical resistivity of various $(DCNQI)_2Cu_xLi_{1-x}$ single crystals is depicted in Fig. 4.7c. Both, $(DCNQI)_2Li$ and $(DCNQI)_2Cu$ are metallic at RT as indicated by the positive slope of the resistivity curve. While the copper-rich crystals with $x = 1$, $x = 0.89$ and $x = 0.85$ stay metallic down to cryogenic temperatures, $(DCNQI)_2Li$ is inherently unstable against a spin-Peierls transition at about $T_{sP} = 52\,K$

in agreement with values reported in literature [88, 89]. With increasing copper content the transition shifts to lower temperatures, due to the deviation from the optimum quarter band filling which favors the spin-Peierls transition. For copper contents above $x \approx 0.4$ the material remains metallic in the whole temperature regime between 4 K and 300 K [79]. In spite of their metallic behavior at RT, Coulomb correlations seems to be important in lithium rich samples as indicated by the almost constant Seebeck coefficient of about $S \approx -60\,\mu V\,K^{-1}$ in $(DCNQI)_2Cu_{0.26}Li_{0.74}$. This value corresponds to the spin entropy $S_{spin} = k_B/e \ln 2 = -59.6\,\mu V\,K^{-1}$ of a Mott-Hubbard metal in the presence of strong Coulomb repulsion, as given by Eq. 2.83 and indicated by the black dashed line in Fig. 4.7d. In this case, a charge transfer ratio of $\delta/2 = 1/2$ was assumed. Similar observations have been made for 1:2 organic charge transfer salts with the acceptor molecule TCNQ, also revealing a charge transfer of $\delta/2 = 1/2$ [194].

In the pure $(DCNQI)_2Li$ sample the thermopower is even higher. An increased finite temperature contribution to the thermopower in $(DCNQI)_2Li$ has been observed before, although not as pronounced as in this study [195]. In the metallic regime it goes through a maximum at $T_{max} = 95$ K and then continuously decreases with increasing temperature. As a consequence, one may anticipate a constant value of $S = -k_B/e \ln 2$ for $(DCNQI)_2Li$ far above room temperature as well. A contribution by orbital lattice site degeneracy in addition to the spin degrees of freedom has been suggested as explanation for the increased finite-temperature thermopower in the quarter-filled Coulomb correlated conductor $NaCo_2O_4$ [196]. According to this theory, the temperature of the maximum corresponds to an orbital energy splitting of only $k_B T_{max} = 8$ meV being negligible compared to the bandwidth of $W \approx 800$ meV in $(DCNQI)_2M$ salts. Hence, a contribution from orbital degeneracy might seem reasonable and is supported by the lack of degeneracy as soon as the copper content of the crystal reaches $x = 0.26$.

Some literature measurements on $(DCNQI)_2Li$ reveal semiconducting behavior already at room temperature [79]. This has been attributed to the formation of a $4k_F$-CDW at high temperatures [197] which in turn might also influence the Seebeck coefficient (compare Ch. 2.2.2). In this sample, the resistivity starts to increase below 100 K again, indicating the onset of a possible $4k_F$-CDW transition. This temperature is close to the maximum in the Seebeck coefficient and accordingly, the anomalous Seebeck coefficient of $(DCNQI)_2Li$ compared to $(DCNQI)_2Cu_{0.26}Li_{0.76}$ may rather be associated with the $4k_F$-CDW being absent in the latter. Fig. 4.8 plots the electrical resistivity and Seebeck coefficent of pure $(DCNQI)_2Li$ against the inverse temperature. Within the insulating spin-Peierls regime between temperatures of 35 K and 50 K, a similar activation energy of $\Delta E = 25$ meV is observed in both quantities, as determined by Eqs. 2.66 and 2.79. This is in sharp contrast to the copper salts where the 3d states seem to influence both quantities differently in

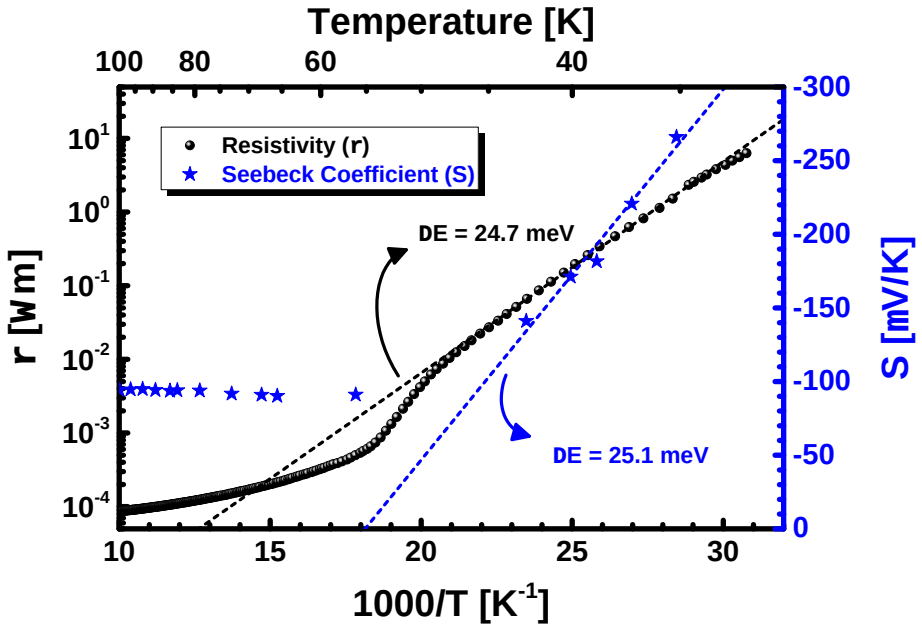


Figure 4.8: Electronic properties in the spin-Peierls state of $(DCNQI)_2Li$. The electrical resistivity and the Seebeck coefficient reveal the same thermally activated behavior in the spin-Peierls regime of $(DCNQI)_2Li$ with an activation energy of $\Delta E \approx 25\,\text{meV}$.

the CDW regime. The consistency of the activation energies in $(DCNQI)_2Li$ is therefore allegeable by the lack of copper 3d states, resulting in a more simple band structure as compared to $(DCNQI)_2Cu$. This again resembles an indirect hint to holes emerging from 3d copper states that significantly influence the transport properties of $(DCNQI)_2Cu$ in contrast to $(DCNQI)_2Li$.

### 4.1.4 Conclusions

Within this subchapter, the electrical transport properties of $(R_1,R_2\text{-DCNQI})_2M$ radical anion salts have been analyzed and discussed in detail. Depending on the functional groups $R_{1/2}$ attached to the quinone ring, a Peierls metal-insulator transition can be induced in $(DCNQI)_2Cu$. An unambiguous identification of the predominant charge carrier scattering mechanism is not possible by the resistivity measurements due to large thermal expansion effects of the underlying crystal lattice but an efficient interaction with acoustic or optical phonons is anticipated. The phonon drag effect is proposed to explain the anomalous low-temperature peak in the thermopower and the reduction of the low-temperature resistivity in $(DCNQI\text{-}h_8)_2Cu$. The thorough analysis of the resistivity and the thermopower as a function of temperature suggests an additional hole contribution to the charge carrier transport to emerge from the 3d copper states. It was demonstrated to crucially depend on the coordination angle of the DCNQI molecules around the central copper atom in the crystal, leading to a sensitive shift of the Fermi energy. In $(DCNQI)_2Li$ no indications

of hole-like charge carriers were found, substantiating the above findings. Its Seebeck coefficient is governed by the spin entropy of correlated electrons, as described by the Hubbard band model at quarter filling. Moreover, by analyzing (DMe-DCNQI)$_2$Cu$_x$Li$_{1-x}$ mixed crystals a continuous variation of the electronic properties from a quasi-1D organic metal with quarter band filling and appreciable electronic correlation to a quasi-3D organic conductor was possible. The RT electrical conductivity changed by more than one order of magnitude by virtue of this band structure manipulation. This approach will enable a more detailed analysis of the thermal transport and the thermoelectric properties of the material systems later in this thesis.

## 4.2 Nonlinear Conduction in the Peierls Insulating State of $(DCNQI)_2Cu$

As discussed in Ch. 2.5.3, nonlinear conduction phenomena have been observed in a variety of organic conductors and the electrothermal model proposed by Mori *et al.* has also been applied to the nonlinear conduction effects in halogensubstituted $(DCNQI)_2Cu$ radical anion salts [18]. The comparison of the simulated and measured nonlinear current-voltage characteristics of $(MeBr\text{-}DCNQI)_2Cu$ is shown in Fig. 4.9. In order to reproduce the experimental data, a specific heat of $C_e \approx 27\,\mathrm{J\,mol^{-1}\,K^{-1}}$ had to be assumed in Eq. 2.71. This value undermines the lattice specific heat by a factor of three to five and accordingly, it was attributed to the electronic nature of the observed nonlinearities. However, there are some doubts concerning this interpretation. First of all, the resistive switching occurs on a time-scale of $10^{-4}\,\mathrm{s}$ to $10^{-1}\,\mathrm{s}$ being by far too long compared to the electron-phonon relaxation times on the order of $10^{-14}\,\mathrm{s}$ observed in organic conductors [198]. This discrepancy rather points toward a thermal effect of the lattice. Moreover, charge carriers are, in principle, efficiently scattered by low-energy phonons in low-dimensional molecular metals as well as organic semiconductors [122, 128]. This is also corroborated by the above-mentioned results on the electrical resistivity and thermopower. Therefore, a small energy transfer rate $\alpha_e$ between the electronic subsystem and the lattice seems implausible and the current interpretation of the electrothermal model is highly doubtful.

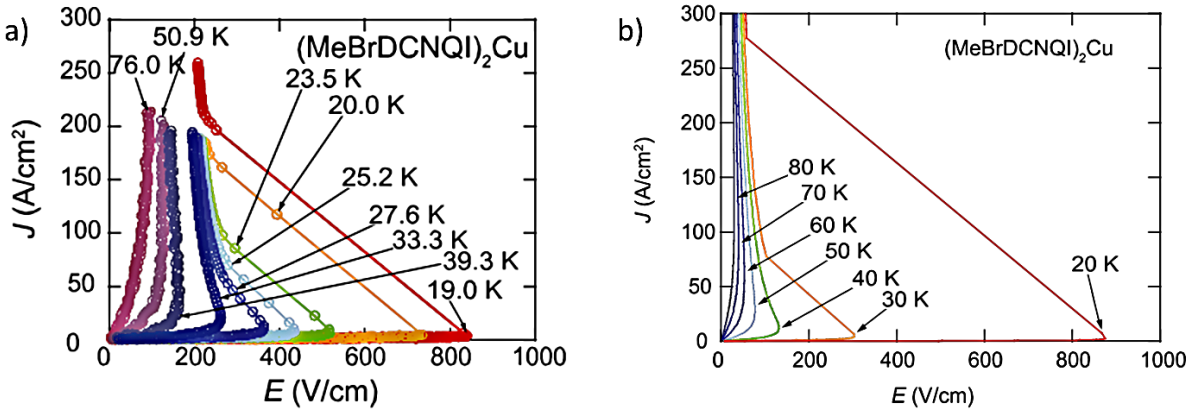


Figure 4.9: Literature data on nonlinear conduction in $(MeBr\text{-}DCNQI)_2Cu$. (a) Measured and (b) simulated two-probe current-voltage characteristics for $(MeBr\text{-}DCNQI)_2Cu$. The electrothermal model described by Eq. 2.71 is able to reproduce the observed nonlinearities and their temperature dependence semi-quantitatively assuming a specific heat of $C_e \approx 27\,\mathrm{J\,mol^{-1}\,K^{-1}}$. From: [18].

Nonetheless, the possibility to model nonlinear conduction effects for such a variety of different ground states proves the model by Mori to be a good starting point for further investigation. Deuterated $(DCNQI)_2Cu$ radical anion salts are expected to enable

a more detailed insight in the electrothermal model proposed by Mori *et al.* [143] and its microscopic ingredients. Their ground state appears sensitive to the change in energy when switching from the free electron gas in the metallic phase to localized electrons in the insulating phase [34], i.e. a gain in the kinetic energy or a delocalization of electrons by an applied electric field should be more likely to induce an insulator-metal transition compared to other low-dimensional metals (see Ch. 2.3.3). Therefore, a distinct non-equilibrium excitation of the electronic system by an applied electric field, as proposed by the electrothermal model, may be more likely in $(DCNQI)_2Cu$ as compared to other organic conductors.

Moreover, soliton-like charged domain wall pairs have been identified as relaxation channel by means of dielectric response measurements pointing toward collective electronic excitations being of importance in the semiconducting phase of $(DCNQI)_2Cu$ [199]. Finally, the availability of high-quality literature data [176, 34] on the temperature-dependent contributions of the electronic, acoustic and optical phonon excitations to the specific heat allows for an identification of the dominating microscopic mechanism causing nonlinear conduction by the effective specific heat in the electrothermal model.

The results presented in the following section were published in *Physical Review B* **92**, 155107 (2015) [177], to which the American Physical Society (APS) holds copyrights and from which the content below was mainly adapted.

### 4.2.1 Nonlinear Current-Voltage Characteristics

Fig. 4.10a shows the resistance of a $(DCNQI\text{-}d_6)_2Cu$ crystal contacted in two-probe geometry with silver paint (see inset). Care was taken to completely cover both ends of the sample with the conducting paste to ensure uniform current injection. In contrast to the four-probe measurement presented in Ch. 4.1.1, the two-probe resistance measurement only reveals a jump by two orders of magnitude at the Peierls transition temperature of $T_{P,c} = 85\,\mathrm{K}$, i.e. the contact resistance can be neglected in the Peierls insulating phase but dominates the conduction behavior in the metallic phase. Upon heating the phase transition occurs with a small hysteresis at $T_{P,h} = 89\,\mathrm{K}$ similar to the four-probe measurements presented in the subchapter above. In the metallic regime, the contact resistance revealed an activation energy of about 10 meV (fit not shown). Below $T_{P,c}$, the resistivity is thermally activated with a corresponding energy of about $\Delta E = (39 \pm 5)\,\mathrm{meV}$ between 35 K and 75 K in agreement with values obtained from four-probe measurements. The interpolated two-probe resistance from the heating cycle of the sample with cross-sectional area of $(0.03)^2$ mm$^2$ and length of 0.275 mm was used for all subsequent simulations in this section.

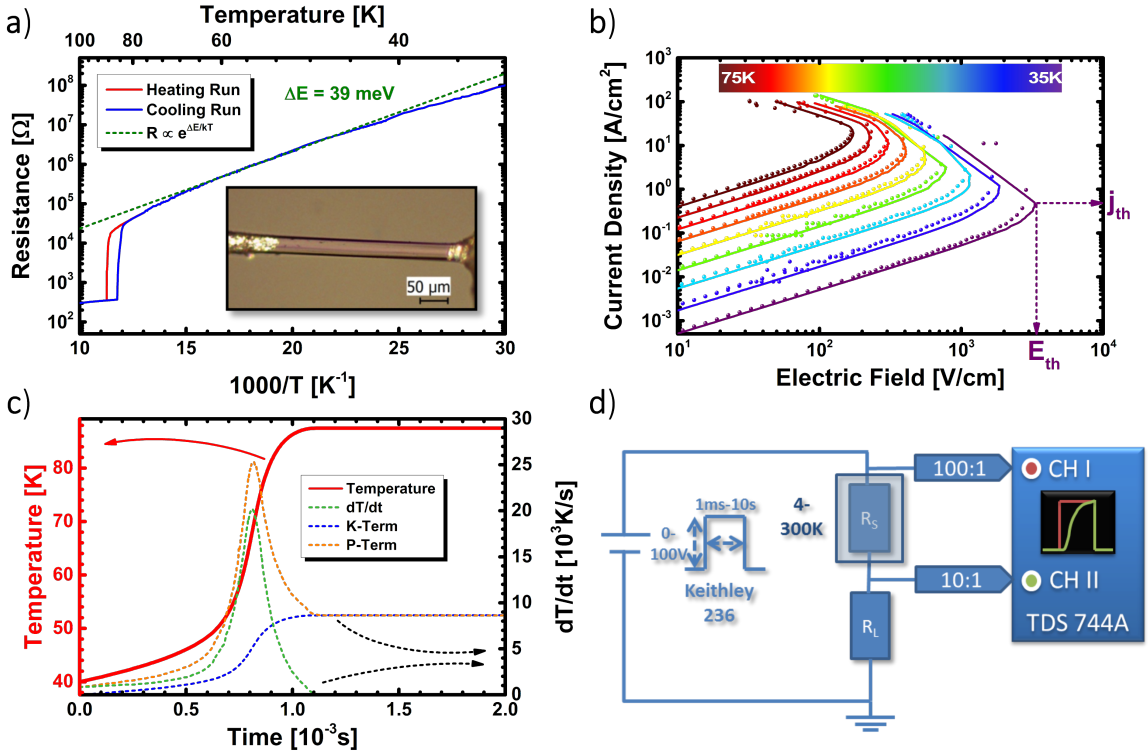


Figure 4.10: Nonlinear conduction in $(DCNQI\text{-}d_6)_2Cu$. (a) Two-probe sample resistance during cooling and heating run plotted logarithmically against the inverse temperature. The linear fit below the phase transition corresponds to an activation energy of $\Delta E \approx 39\,\mathrm{meV}$. The inset shows a microscope image of the sample. (b) Measured (dots) and simulated (solid lines) nonlinear current-voltage characteristics of $(DCNQI\text{-}d_6)_2Cu$ between 35 K and 75 K in steps of 5 K. (c) Simulated temperature transients after applying a voltage pulse of 87 V to the crystal at $T_0 = 40\,\mathrm{K}$. The respective transient P- and K-terms (Eq. 4.8) contributing to the temperature rise $\mathrm{d}T/\mathrm{d}t$ are also illustrated. (d) Setup used for the transient resistance experiments. Adapted from: [177], ©American Physical Society

Current-voltage characteristics were recorded with single voltage pulses of 40 ms length and $0.2 - 100\,\mathrm{V}$ amplitude at temperatures between 35 K and 75 K. Both, the applied voltage and measured current, were recorded with a Keithley 236 source measurement unit (SMU) and individual voltage pulses were separated by at least 0.5 s to ensure thermal relaxation in between each data point. A load resistor two orders of magnitude smaller than the low-field sample resistance was placed in series to the sample to avoid sample degradation as a result of high current flow after resistive switching. The voltage drop at the load resistor was subtracted from the measured voltage.

Fig. 4.10b delineates the nonlinear current-voltage characteristics in the CDW state of $(DCNQI\text{-}d_6)_2Cu$. Above a critical field $E_{th}$, negative differential resistivity similar to Fig. 4.9 is observed in the sample. The critical field decreases with increasing temperature while the associated critical current density $j_{th}$ exhibits the opposite behavior. To model the experimental data by the electrothermal model including any effect of the load resistor,

Eq. 2.71 was adjusted to the following form

$$\frac{dT}{dt} = \underbrace{\frac{m_{mol}\left\{\frac{U}{1+R_L/R_S(T)}\right\}^2}{\rho_{dens}\cdot V\cdot c_m(T)\cdot R_S(T)}}_{\text{P-term}} - \underbrace{\frac{m_{mol}\cdot\widetilde{\alpha}}{\rho_{dens}\cdot V\cdot c_m(T)}\{T-T_0\}}_{\text{K-term}} \quad . \tag{4.8}$$

with the sample volume $V$, the density $\rho_{dens} = 1.61\,\mathrm{g\,cm^{-1}}$ [66], the temperature-dependent molar specific heat $c_m(T)$ and the molar mass $m_{mol} = 444\,\mathrm{g\,mol^{-1}}$. $U$ is the voltage applied to the series of sample and load resistor ($R_S$ and $R_L$) and $\widetilde{\alpha}$ is the absolute energy transfer rate in $[\mathrm{W\,K^{-1}}]$ to the environment. From now on, the first term on the right hand side of Eq. 4.8 will be denoted as P-term and second one as K-term. Later, we also will allow the specific heat to become temperature-dependent.

As demonstrated by the solid lines in Fig. 4.10b, the data can be accurately modeled by numerical integration of Eq. 4.8 assuming $c_m = 55\,\mathrm{J\,mol^{-1}\,K^{-1}}$ and $\widetilde{\alpha} = 9\times10^{-5}\,\mathrm{W\,K^{-1}}$ to remain constant. The simulation is able to reproduce the current-voltage characteristics and the temperature dependence of threshold field $E_{th}$ and threshold current $j_{th}$. The reliability of the simulation can be understood by Fig. 4.10c where the transient temperature evolution after applying a voltage pulse of 87 V at $T_0 = 40\,\mathrm{K}$ is shown. In this case, after a short period of 1.1 ms a steady state ($dT/dt = 0$) is reached in the sample. This will be the case for most of the data points in the current-voltage characteristics which were recorded at a pulse width of 40 ms. With the steady state solution of Eq. 4.8 being independent of $c_m$, the final temperature and resistance value will be determined by the choice of $\widetilde{\alpha}$ as long as the value for $c_m$ remains moderate.

Fig. 4.10c also displays the separate contributions of the P- and the K-term to the transient temperature rise $dT/dt$. The P-term governs the behavior on short timescales until the K-term reacts on the temperature rise, leading to its steady state solution. It has to be noted that in the present description both terms still depend on $c_m$, i.e. until the steady state is reached, the dynamic solution depends on $c_m$ and $\widetilde{\alpha}$. The applied value of $c_m = 55\,\mathrm{J\,mol^{-1}\,K^{-1}}$ corresponds to the specific heat of (DCNQI-$d_6$)$_2$Cu at 30 K [176].

In order to gain detailed insights into the dependence of the resistive switching on microscopic contributions to the specific heat, shorter pulses are required or, even better, the complete transient evolution of the sample resistance has to be analyzed. This will be done in the following with the setup illustrated in Fig. 4.10d where the voltage applied by the Keithley 236 SMU is recorded transiently with a Tektronix TDS 744A oscilloscope. Recording the voltage drop at the load resistor $R_L$ enables a calculation of the transient current and sample voltage, from which the transient resistance $R_S(t)$ can be derived. Due to the high sample resistance in the Peierls insulating regime, a 100:1 passive probe

of high input resistance $R_{in} = 100\,\mathrm{M\Omega}$ was used to feed the applied voltage into the oscilloscope. For the voltage drop at the smaller load resistance a 10:1 passive probe with $R_{in} = 10\,\mathrm{M\Omega}$ was sufficient.

### 4.2.2 Dynamic Resistive Switching

#### Transient Analysis of Nonlinear Conduction

Exemplarily, the measured dynamic sample resistances at $T_0 = 40\,\mathrm{K}$ in response to voltage steps of $U = 56\,\mathrm{V}$ and $U = 97\,\mathrm{V}$ are displayed in Fig. 4.11a together with simulations employing fixed values of $c_m$ and $\widetilde{\alpha}$. Within the range of milliseconds, the resistance of the sample rapidly changes from a high-resistive to a low-resistive state. A kink can be seen in the resistivity data as well as in the simulations for high voltages applied. It is caused by the huge drop of the resistivity at the Peierls transition and marks the culmination of the transition temperature, i.e. the melting of the CDW. After switching, the steady-state values of measurement and simulation match for $\widetilde{\alpha} = (9 \pm 1) \times 10^{-5}\,\mathrm{W\,K^{-1}}$ in agreement with the steady-state analysis in Sec. 4.2.1. The dynamic behavior is only fairly reproduced by the simulation, especially for large temperature increments on intermediate time-scales. The deviation emanates from the inaccurate assumption of a temperature-independent specific heat of $c_m = 55\,\mathrm{J\,mol^{-1}\,K^{-1}}$. However, from the magnitude of $c_m$ it can be concluded that the nonlinear conduction in $(DCNQI\text{-}d_6)_2Cu$ is thermally driven, thus making it reasonable to treat the temperature parameter in the electrothermal model as the sample temperature.

For a direct determination of $c_m$ from the measurement data, an evaluation procedure known from the transient electrothermal method was refined [200]. Neglecting the K-term and assuming a constant heating power ($R_S = \mathrm{const}$), it is possible to extract the specific heat by linearly approximating Eq. 4.8 on short timescales to $\Delta T = (\text{P-term}) \cdot \Delta t$. This method has already been proven to work reasonably well in measuring the specific heat of rod-like samples, e.g. platinum wires, carbon fibres and carbon nanotubes [200, 201]. Yet, the temporal resolution has to be sufficient to neglect the K-term which often is problematic in samples of higher impedance. Therefore, the K-term is estimated for short timescales and small temperature steps by assuming a constant average temperature difference $\theta = T - T_0$ being half the temperature increase the transient linear fit extends to (compare Fig. 4.11b). Furthermore, utilizing a constant effective heating power by assuming $R_S(T) = R_{S,eff} = R_S(T_0 + \theta)$ reveals a simple analytic solution of Eq. 4.8

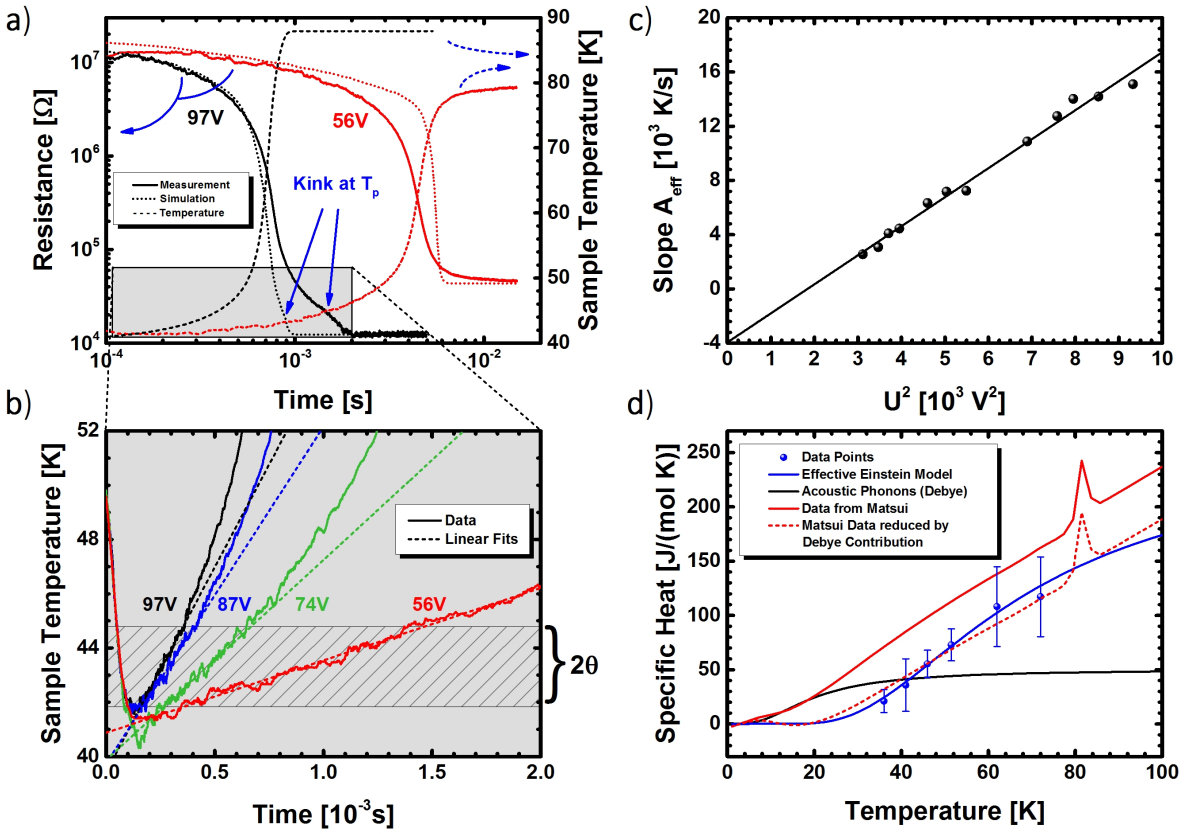


Figure 4.11: Transient analysis of nonlinear conduction in $(DCNQI\text{-}d_6)_2Cu$. (a) Dynamic resistance in response to voltage steps of 56 V and 97 V at 40 K together with the sample temperature (dashed line). Measurement (solid line) and simulation (dotted line) agree only fairly. For high voltages applied, a kink is observed in the measurement as well as in the simulations indicating the transition to the metallic state. (b) Magnification of the initial temperature increment which was linearly fitted for each voltage applied. The linear fit's slope $A_{eff}$ exhibits a (c) quadratic voltage dependence and enables an accurate determination of the (d) specific heat for each ambient temperature with the help of Eq. 4.10. The literature data measured by Matsui [176] and the expected acoustic phonon contribution are displayed for comparison. The data fits well to an effective Einstein model described by Eq. 4.12. Adapted from: [177], ©American Physical Society

$$\begin{aligned}\Delta T = & \left\{ \frac{U^2 \cdot m_{mol}[1+R_L/R_{S,eff}]^{-2}}{\rho_{dens} V c_m (T_0+\theta) R_{S,eff}} - \frac{m_{mol} \cdot \tilde{\alpha} \cdot \theta}{\rho_{dens} V c_m (T_0+\theta)} \right\} \cdot t \\ = & \quad \{B \cdot U^2 - C\} \cdot t = A_{eff} \cdot t \quad . \end{aligned} \tag{4.9}$$

From the voltage dependence of the slope $A_{eff} \propto U^2$ the specific heat of the system under study can be determined reliably as the K-Term only represents a voltage independent offset. In order to employ Eq. 4.9, the dynamic resistance needs to be converted into a transient sample temperature using the temperature-dependent resistance curve exposed in Fig. 4.10a. The resulting curves are exemplarily delineated in Fig. 4.11a as well. After zooming in, the voltage-dependent initial temperature rise is found to be lin-

ear on short time-scales (see Fig. 4.11b) as anticipated by Eq. 4.9. The striped area in Fig. 4.11b marks the fitting regime over the total temperature increase $2\theta$. The foreseen squared voltage-dependence of the linear fits' slope $A_{eff}$ is verified in Fig. 4.11c. Via Eq. 4.9 the molar specific heat can be extracted from the slope $B = \Delta A_{eff}/\Delta U^2$ by:

$$c_m = \frac{m_{mol}}{\rho_{dens} V B R_{S,eff}[1 + R_L/R_{S,eff}]^2} \quad . \tag{4.10}$$

In the determination of $c_m$ the average resistance of the sample $R_{S,eff} = R_S(T_0 + \theta)$ during the initial temperature rise $2\theta$ causes the largest uncertainty of about $\sigma_R = 1/2 \cdot (R_S[T_0 + 2\theta] - R_S[T_0])$. Eq. 4.9 also yields an estimate of $\widetilde{\alpha} = (7 \pm 4) \times 10^{-5}\,\mathrm{W\,K^{-1}}$ from the intercept C when fitting $A_{eff}(U^2)$ linearly at various sample temperatures. It is in good accordance with the value of $9 \times 10^{-5}\,\mathrm{W\,K^{-1}}$ derived from the data on long timescales above, especially considering the low sensitivity of the initial temperature rise on $\widetilde{\alpha}$.

The effective molar specific heat $c_m$ determined at various sample base temperatures is presented in Fig. 4.11d. The uncertainty bars originate from the errors of the effective resistance $R_{S,eff}$ and the slope B. Qualitatively, the temperature dependence and the magnitude of $c_m$ comply with the specific heat data of high accuracy reported by Matsui *et al.* [176]. Nevertheless, even including the conservatively estimated error, the measurement systematically undermines the published data by an almost constant offset of about $40\,\mathrm{J\,mol^{-1}\,K^{-1}}$. An inaccuracy in the optical determination of the sample volume is incapable to account for this large deviation. In general, the specific heat can be modeled by an additive contribution from acoustic and optical phonons as well as from mobile electrons:

$$c_m = C_{ac} + C_{opt} + C_{el} \quad . \tag{4.11}$$

The rather linear temperature dependence of the specific heat data with a slope of $(3.0 \pm 0.2)\,\mathrm{J\,mol^{-1}\,K^{-2}}$ (fit not shown) may be considered to originate from the electronic specific heat, given in Eq. 2.72 and being proportional to $T$. However, the electronic specific heat coefficient $\gamma = 0.025\,\mathrm{J\,mol^{-1}\,K^{-2}}$ [34] determined for metallic $(DCNQI)_2Cu$ is two orders of magnitude smaller and even more, should be negligible in the investigated insulating phase. As a result, the electronic effects, including other low-energy charge-carrying excitations [202], are disregarded in the further interpretation of the effective specific heat. In solids built up of molecules, each having three translational and three rotational degrees of freedom, the specific heat contribution by acoustic phonons amounts to twice the value predicted by the classical Debye model given in Eq. 2.48 for a monoatomic

lattice (compare Eq. 2.49 [119]). Assuming a Debye temperature of $\theta_D = 82\,\mathrm{K}$ [34], this contribution to the specific heat is depicted in Fig. 4.11d (black curve). According to the six degrees of freedom taken into account, the Debye specific heat originating from acoustic phonons approaches a high temperature limit of $6R \approx 50\,\mathrm{J\,mol^{-1}\,K^{-1}}$. While being of similar magnitude as the experimental data, acoustic phonons may only account for up to about $44\,\mathrm{J\,mol^{-1}\,K^{-1}}$, i.e. about half of the determined $c_m$ value, in the temperature regime investigated. More noticeably, the variation between 35 K and 75 K is quite small by means of the material's low Debye temperature. Considering the specific heat data to be systematically lower compared to literature, the saturated contribution of low-energy acoustic phonons to the specific heat does not seem to enable a transient heating of our sample by inelastic scattering of charge carriers.

Additional degrees of freedom are available by optical lattice phonons which may be characterized as external (intermolecular) or internal (intramolecular) vibrational modes. Considering $N = 22$ atoms per molecule, the phonon spectrum consists of $3N - 6 = 60$ internal modes and $6Z - 6 = 30$ external modes, $Z = 6$ denoting the number of molecular entities constituting the unit cell of (DCNQI-$d_6$)$_2$Cu single crystals [58]. Subtracting the calculated acoustic phonon part from the Matsui data, the estimated optical phonon contribution to the specific heat in (DCNQI-$d_6$)$_2$Cu agrees very well with the effective specific heat deduced from the transient resistance measurements. Because of their small dispersion, the contribution by internal and external optical phonon modes to the specific heat in molecular solids may be well described by a sum of independent Einstein oscillators (Eq. 2.43) [119]. As a consequence, the effective specific heat is well modeled by an effective Einstein model [203]

$$C_{opt} = N_E R \left(\frac{\theta_E}{T}\right)^2 \frac{e^{\theta_E/T}}{(e^{\theta_E/T} - 1)^2} \quad , \tag{4.12}$$

where $N_E$ is the number of oscillators with an effective frequency $\nu_E = k_B\theta_E/h$ of the involved phonon modes, $\theta_E$ denoting the Einstein temperature. Best fit results were obtained by modeling the data with an effective Einstein model solely, i.e. by neglecting the electronic ($C_{el}$) and acoustic phonon ($C_{ac}$) part of the specific heat and only taking into account internal and external optical phonon modes. The number of involved optical phonon modes amounts $N_E = 30 \pm 3$ and their average energy yields $\overline{E_{ph}} = 19\,\mathrm{meV}$ according to the effective Einstein temperature of $\theta_E = (211 \pm 9)\,\mathrm{K}$.

A Raman investigation on the optical phonon modes is illustrated in Fig. 4.12a, comparing the normalized Raman spectrum of (DCNQI-$d_6$)$_2$Cu to a measurement on pristine, crystalline DCNQI-$d_6$ powder. While low-frequency optical phonon modes are also present

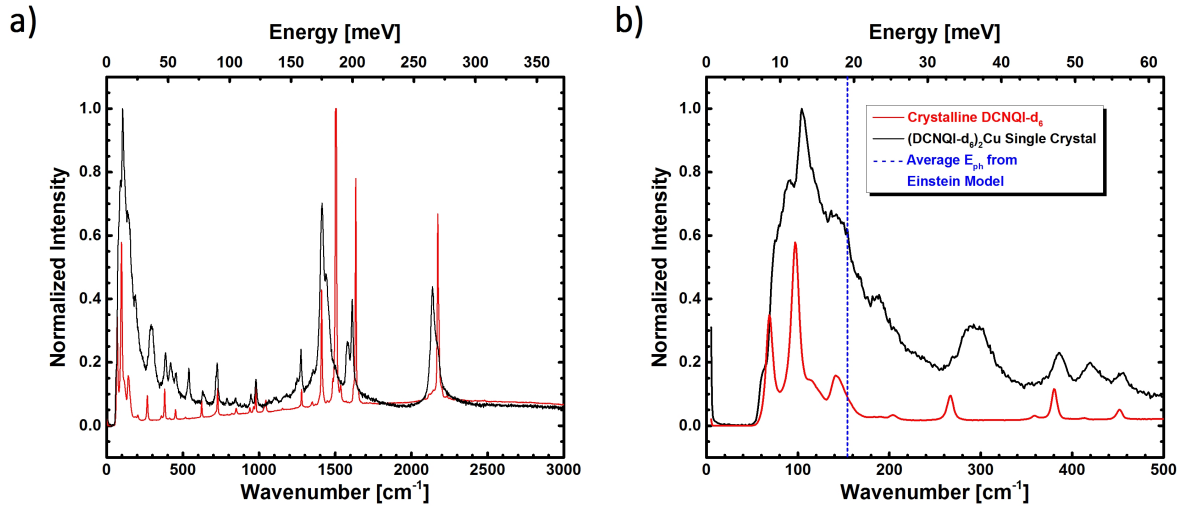


Figure 4.12: Raman investigation on optical phonon modes at RT. (a) Normalized Raman spectra of crystalline DCNQI-$d_6$ and its copper salt. (b) The same Raman spectra magnified at low frequencies reveal significant spectral weight in the vicinity of the estimated average phonon energy in the Einstein model, indicated by the dashed vertical line at 19 meV.

in the pristine powder due to its crystallinity, a clear shift of spectral weight from high frequency internal modes between 1000 $cm^{-1}$ and 2500 $cm^{-1}$ to low frequency internal optical phonon modes below 500 $cm^{-1}$ is observed when going from the neutral molecular to the radical ion salt single crystal. The magnified view on the low-frequency Raman spectrum in Fig. 4.12b reveals significant spectral weight in the vicinity of 19 meV in the Raman signal, corroborating the assumption of an Einstein model above. The effective number of involved phonons equals the number of possible external modes, but it is most likely that internal and mixed modes have their share as well [204]. The presence of low-frequency optical phonon modes in the pristine DCNQI-$d_6$ material might be indicative of this. Thus, it can be concluded that intra- and intermolecular optical modes drive the effective specific heat as derived from the electrothermal model in the investigated regime. The improved description of this parameter by an effective Einstein model facilitates a more accurate simulation of the complete dynamic resistance response which will be presented below.

### Simulated Dynamic Reponse

According to the temperature rise by several ten Kelvin within the sample in response to the large electric fields, the temperature dependence of $c_m$ should be taken into account in the simulation by Eq. 4.8. This is achieved by utilizing the effective Einstein model derived above. As a test, a latent heat contribution at the phase transition - similar to the peak in the Matsui data at 85 K in Fig. 4.11d - was added to the model, but found to be of

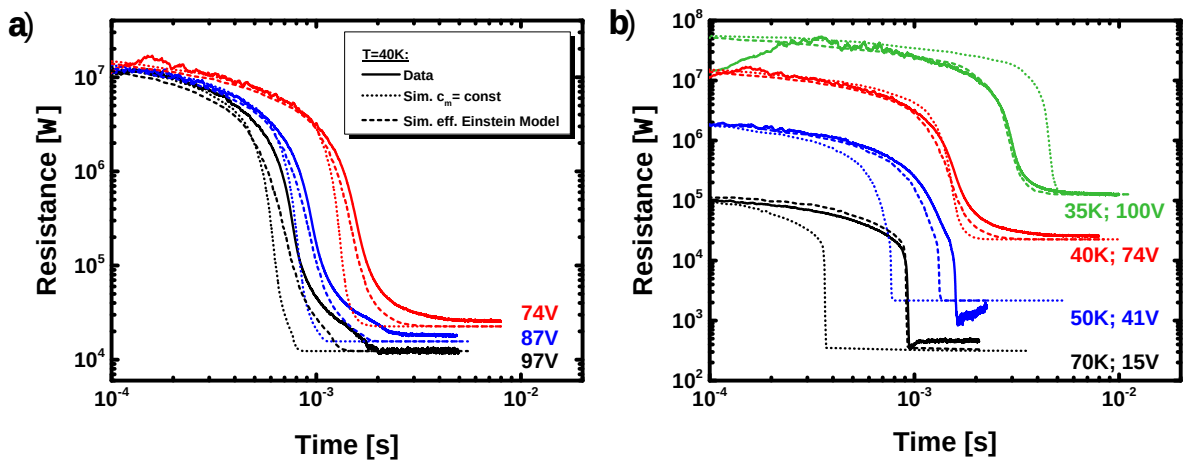


Figure 4.13: Measured and simulated dynamic nonlinear conduction in $(DCNQI\text{-}d_6)_2Cu$. Measurements (solid lines) and simulations are compared for (a) varying voltage pulses at $T_0 = 40\,K$ and (b) different ambient temperatures utilizing a constant specific heat of $c_m = 55$ J/(mole K) (dotted lines) and the effective Einstein model of the specific heat (dashed lines) as outlined in Sec 4.2.2. Adapted from: [177], ©American Physical Society

minor importance in the temperature regime under study. It will only affect the response at large temperature differences between sample and environment where the K-term of Eq. 4.8 already dominates.

Fig. 4.13a compares the transient resistance at $T_0 = 40\,K$ in response to voltage pulses of different magnitude to two simulations, one employing a constant specific heat of $c_m = 55\,J\,mol^{-1}\,K^{-1}$ (dotted line) and the other utilizing the temperature-dependent Einstein Model (dashed line). The simulated transients are evidently improved by explicitly including the temperature dependence of $c_m$ in the simulations. More strikingly, the transients at different ambient temperatures reveal superior conformity compared to the case of a constant specific heat (Fig. 4.13b). The small dip in the dynamic resistance after switching at temperatures above 50 K is caused experimentally by the current limiter of the pulsed voltage source, employed to prevent sample destruction and being without physical relevance here. The exceptional good agreement between simulations and measurements stress the validity of the methodical approach in the determination of the effective specific heat described before.

### 4.2.3 The Advanced Electrothermal Model

The difference in the effective specific heat as compared to literature data may be ascribed to the respective measurement principle utilized. First and foremost, instead of a steady-state heat flow into and out of the sample [176], the transient Joule heating of a sample at intermediate to large electric fields rather represents an out-of-equilibrium experimental condition. While the temperature distribution inside the sample is expected to be irrele-

vant on the short time scales used for the determination of $c_m$, an inhomogeneous current or field distribution inside the crystal might lead to an overestimation of the active cross section for charge transport in the present analysis. The possibility of an inhomogeneous high conduction state was already discussed by Mori and coworkers [143]. Flicker noise studies also reveal a pronounced noise level enhancement in organic charge transfer salts which was also ascribed to the presence of an inhomogeneous current flow [205, 206], backing the above perception. Moreover, the two-probe geometry with non-planar silver paint contacts, used to achieve the high fields necessary for the resistive switching, might facilitate an inhomogeneous field distribution accompanied by local fluctuations of the charge carrier density.

Nonetheless, the accuracy of the effective Einstein model explaining the effective specific heat solely based on optical phonon modes rather calls for an extension of the electrothermal model as shown in Fig. 4.14. The model explicitly considers the separation of the lattice system into an acoustic and optical phonon part.

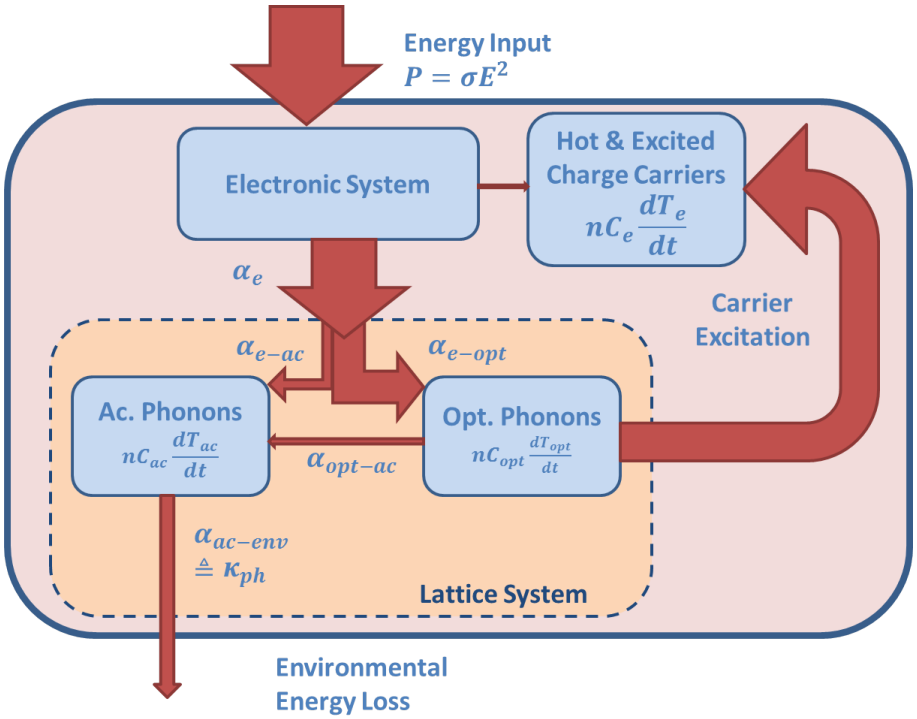


Figure 4.14: Scheme of the advanced electrothermal model. Depending on the preferred charge carrier scattering mechanism, the electrical energy can be deposited into the individual microscopic subsystems of the material. Inefficient electron-phonon scattering may lead to a direct excitation of charge carriers or hot electrons by the electric field. Efficient interaction with optical phonons causes a non-equilibrium population of optical phonon modes whose low group velocity inhibits a thermal relaxation to the environment. Hence, energy stored in the optical phonon system is available for excitation of additional charge carriers in contrast to the heat stored in acoustic phonons dissipating quickly out of the sample. The identification of the microscopic system being out of equilibrium is possible from the effective specific heat in the electrothermal model and allows for an understanding of the energy flows in the system. From: [177], ©American Physical Society

At the beginning, the energy provided by the electric field is fed into the electronic system. Depending on the electron scattering rate by acoustic and optical phonons ($\alpha_e = \alpha_{e-ac} + \alpha_{e-opt}$) this energy can be transferred to the lattice system. If $\alpha_e$ was small, hot carrier generation or direct population of excited electron states would constitute the preferred relaxation mechanisms of the energy supplied by the electric field. It would be indicated by a low electronic contribution $nC_e$ governing the observed effective specific heat. This case was originally discussed by Mori *et al.* when proposing the model and, in this case, the temperature $T = T_e$ is assumed to be a parameter describing the population of excited electronic states rather than resembling the crystal lattice temperature $T_L$ [143].

However, the identification of optical phonons ($nC_{opt}$) determining the effective specific heat provides evidence for an efficient interaction between charge-carrying excitations and optical phonons, ruling out a hot electron effect via direct field excitation. The relative strength of the electron scattering by acoustic and optical phonons moreover governs the preferred excitation of a distinct phonon subsystem. Yet, optical phonon modes barely contribute to thermal conduction due to their low group velocity, i.e. the continuous deposition of energy into the optical phonon system causes its population density to shift far off equilibrium and its temperature to decouple from the temperature of the acoustic phonon bath. This excess energy is available for quite a long time and enables the generation of additional charge carrier excitations, leading to a multiplication effect. The mechanism of nonlinear conduction originating from current-induced non-equilibrium optical phonon population has already been demonstrated in quasi-1D single-walled carbon nanotubes [207] as well as in 2D graphene [208]. The heat stored in acoustic phonons quickly dissipates out of the system. Hence, the measured $\widetilde{\alpha}$ characterizes the process limiting the energy transport out of the system. The activation energy of additional charge carriers can be estimated from the slope of the DC conductivity in Fig. 4.10, yielding an energy of about $\Delta E = (39 \pm 5)\,\mathrm{meV}$ slightly varying with temperature across the investigated regime and being smaller than the expected Peierls gap of $2\Delta \approx 79\,\mathrm{meV}$ as determined and discussed in Ch. 4.1.1. The activation energy related to the electronic transport is about twice as large as the average phonon energy of $\overline{E_{ph}} = 19\,\mathrm{meV}$ estimated by the Einstein model, for which reason two-phonon processes might be involved in the excitation of charge-carriers in the CDW state of $(DCNQI)_2Cu$.

An excited charge carrier needs to be accelerated by the electric field to an energy of about $\overline{E_{ph}} = 19\,\mathrm{meV}$ to scatter inelastically with these optical phonons. Taking an effective electron mass of $m_{eff} = 3.35 m_0$ [209] and an applied electric field of about $E \leq 3600\,\mathrm{V\,cm^{-1}}$, the required mobility of the charge carriers must be at least $\mu \geq (2\overline{E_{ph}}/m)^{-1/2} \cdot E^{-1} = 1200\,\mathrm{cm^2\,V^{-1}\,s^{-1}}$. This high value is considered to be not unrealistic taking into account the observed low-temperature Hall mobilities on the order

of $10^5\,cm^2\,V^{-1}\,s^{-1}$ for one-dimensional organic conductors such as $(TMTSF)_2PF_6$ [210]. From the low-temperature electrical conductivity $\sigma(50\,K) = 3.7 \times 10^4\,S\,cm^{-1}$ of $(DCNQI\text{-}h_8)_2Cu$ (compare Sec. 4.1.1), a mobility of about $\mu = 80\,cm^2\,V^{-1}\,s^{-1}$ may be anticipated in the metallic state of $(DCNQI)_2Cu$. It increases to $\mu = 1300\,cm^2\,V^{-1}\,s^{-1}$ below 20 K and is expected to be higher in the semiconducting regime by virtue of a smaller effective electron mass caused by the stronger band curvature at the Fermi energy. Furthermore, the saturated charge carrier velocity in the organic semiconductor naphthalene at cryogenic temperatures and high electric fields has also been related to optical phonon generation via inelastic charge-carrier scattering [128].

Alternatively, soliton-like charged domain walls might constitute another possibility for low-energy excitations of the electronic system, which have been proposed to explain the low-frequency dielectric response in the CDW state of $(DCNQI)_2Cu$ [199]. Soliton-like excitations are known to be of importance in the transport of commensurate CDW systems like polyacetylene [211] as well as of various organic charge transfer salts, e.g. $\alpha$-$(BEDT\text{-}TTF)_2I_3$ [16]. The charge carrier activation energy amounting to half the Peierls gap energy was also taken as indicator for soliton-like excitations in the previous section. The relative coupling strength of solitons to optical and acoustic phonon modes is characterized by a factor $\xi/a$, with $a$ denoting the lattice constant along the chain direction and $\xi$ the spatial extension of the soliton [212]. Therefore, a large spatial extension of the soliton with respect to the molecular lattice spacing might facilitate a preferred interaction with optical phonons, as indicated by the determined effective specific heat. While the fundamental conduction mechanisms cannot be explicitely resolved by the conducted electrothermal analysis, an efficient interaction between optical phonon modes and charge-carrying excitations seems to play a crucial role for the nonlinear conduction effects occurring in $(DCNQI)_2Cu$.

For the sake of completeness, the main heat loss mechanism to the environment can be estimated by analyzing the $\widetilde{\alpha}$ parameter. If the energy was transferred to the surroundings via convection or radiation from the crystal surface, the determined $\widetilde{\alpha} = 9 \times 10^{-5}\,W\,K^{-1}$ would yield a surface heat transfer coefficient of $h = \widetilde{\alpha}/A_S \approx 3000\,W\,m^{-2}\,K^{-1}$ assuming a surface area $A_S = 3 \times 10^{-4}\,cm^2$ of the sample. This heat transfer coefficient exceeds typical values for convection ($h_{conv} = 6-30\,W\,m^{-2}\,K^{-1}$ [213]) by far. The coefficient of radiative heat transfer can be estimated to $h_{rad} = \sigma_{SB}\cdot(T_1+T_0)(T_1^2+T_0^2) = 0.07\,W\,m^{-2}\,K^{-1}$ [213], $\sigma_{SB}$ being the Stefan Boltzmann constant, $T_1 = 90\,K$ the maximum crystal surface temperature and $T_0 = 35\,K$ the minimum ambient temperature. Because of its small magnitude it can also be neglected. The thermal conductivity $\kappa$ of the sample limits the conductive heat transfer to the contacts. It may be roughly estimated by $\kappa \leq \widetilde{\alpha}\cdot l/(8\cdot A_{cs})$, with $l$ denoting the length and $A_{cs}$ the cross-sectional area of the sample [214]. The ob-

tained value of $\kappa \leq 3.4\,\mathrm{W\,m^{-1}\,K^{-1}}$ agrees reasonably well with the thermal conductivity of about $1.5\,\mathrm{W\,m^{-1}\,K^{-1}}$ measured for $(DCNQI)_2Cu$ at 50 K [174]. Together with its assignment to acoustic phonons, the rather constant thermal conductivity between 30 K and 90 K confirms the interpretation of our temperature-independent $\widetilde{\alpha}$ value. Thus, the main energy loss mechanism in the crystal is the energy transfer to acoustic phonons which transport the heat to the contacts via thermal conduction as indicated in the model in Fig. 4.14. The energy exchange with acoustic phonons can be accomplished via charge carrier-phonon scattering ($\alpha_{e-ac}$) or scattering between optical and acoustic phonons ($\alpha_{opt-ac}$). Both mechanisms seem to be insufficient at high electric fields facilitating the observed nonlinear conduction effects.

### 4.2.4 Conclusions

The nonlinear conduction in $(DCNQI\text{-}d_6)_2Cu$ single crystals at high electric fields has been analyzed in terms of the electrothermal model proposed by Mori *et al.* [143] and discussed in Ch. 2.5.3. Compared to simulations of the current-voltage characteristics at fixed pulse width, applying the electrothermal description to the entire transient resistivity yields a more detailed insight into the microscopic energy exchange processes taking part inside the crystal. In contrast to the hot electron scenario proposed by Mori *et al.*, the simulations accurately reproduce the nonlinear conduction behavior by assuming only a current-induced, distinct, non-equilibrium excitation of optical phonon modes at a mean energy of about 19 meV. This pinpoints to an efficient scattering of charge carriers by optical phonons at high electric fields in this material class. By virtue of their small contribution to the thermal conductivity, the energy deposited into the optical phonon system remains within the crystal and thus, can generate additional charge carrying excitations, leading to a thermally induced multiplication effect. Energy transferred to the acoustic phonon system efficiently dissipates via heat conduction to the contacts. The involved optical phonon modes have an energy of around 19 meV being about half the activation energy of 39 meV inferred from the DC conductivity studies, and therefore, an excitation process including two phonons can be anticipated. Hence, the nonlinear conduction in $(DCNQI\text{-}d_6)_2Cu$ crucially depends on the charge carrier coupling strength to optical phonon modes relative to that of acoustic phonons. The interplay of low-energy optical phonon population, small transport activation energy, large mobility at low temperatures and strong coupling between optical phonons and charge carriers seems to provide the fundamental ingredient for the occurrence of nonlinear transport phenomena in this material class. These results bridge the gap between the phenomenological electrothermal model and the microscopic origin of nonlinear conduction in $(DCNQI)_2Cu$, and presumably also in other low-dimensional molecular conductors revealing different ground states.

## 4.3 Heat Conduction in $(DCNQI)_2M$

The extraction of thermal material properties from transient resistivity analysis at high electric fields facilitated an understanding of nonlinear conduction phenomena in the previous section. In this part of the thesis, the more sophisticated analysis of the thermal conductivity near equilibrium is presented by means of the $3\omega$ measurement technique delineated in Ch. 3.2. It enables an investigation of the Wiedemann-Franz law as well as an examination of the lattice thermal conductivity in the $(DCNQI)_2M$ system, both with unprecedented accuracy.

### 4.3.1 The Thermal Conductivity of $(DCNQI\text{-}h_8)_2Cu$

The temperature-dependent thermal conductivity of $(DCNQI\text{-}h_8)_2Cu$, as determined by the $3\omega$ method described in Ch. 3.2.4, is illustrated in Fig 4.15. At room temperature, the thermal conductivity attains a value of

$$\kappa_{RT} = (1.73 + 0.32/-0.10)\ \mathrm{W\,m^{-1}\,K^{-1}} \quad . \tag{4.13}$$

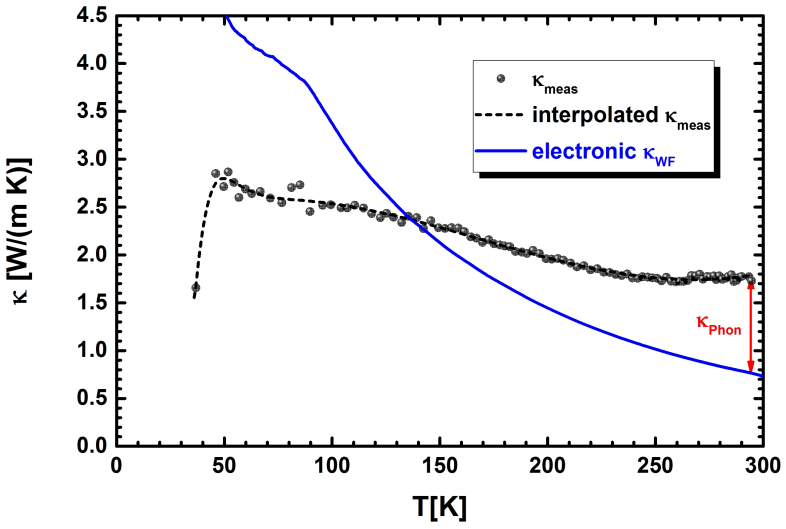


Figure 4.15: The thermal conductivity $\kappa_{meas}$ of $(DCNQI\text{-}h_8)_2Cu$ determined by the $3\omega$ method together with its interpolation. The expected electronic thermal conductivity $\kappa_{WF}$ according to the Wiedemann-Franz law described by Eq. 2.89 is also shown. For the electronic part, a temperature-independent standard Lorenz number of $L_0 = 2.44 \times 10^{-8}\,\mathrm{W\,\Omega\,K^{-2}}$ was assumed and the electrical conductivity data of the sample, as presented in Sec. 4.1.1, was taken into account.

According to the Wiedemann Franz (WF) law of Eq. 2.89, assuming a standard Lorenz number of $L_0 = 2.44 \times 10^{-8}\,\mathrm{W\,\Omega\,K^{-2}}$ and an electrical conductivity of $1070\,\mathrm{S\,cm^{-1}}$, the electronic contribution to heat conduction can be estimated to $\kappa_{WF} \approx 0.76\,\mathrm{W\,m^{-1}\,K^{-1}}$

at RT. As indicated by the red arrow in Fig. 4.15, the remainder of $\kappa_{RT} - \kappa_{WF} = 0.97\,\mathrm{W\,m^{-1}\,K^{-1}} = \kappa_{Phon}$ is ascribed to the heat carried by phonons. This value compares in magnitude to the lattice thermal conductivity data reported for crystalline organic semiconductors, such as naphthalene ($\kappa = 0.5\,\mathrm{W\,m^{-1}\,K^{-1}}$ [215]) or needle-like crystals of 6,13-bis(triisopropylsilylethynyl)pentacene ($\kappa = 1.6\,\mathrm{W\,m^{-1}\,K^{-1}}$ [216]).

Upon cooling the thermal conductivity of (DCNQI-$h_8$)$_2$Cu rises because both, the electronic and the lattice contribution are expected to increase. Yet, the steep increase of the electronic thermal conductivity anticipated by the WF law is not observed under the assumption of a temperature-independent Lorenz number $L_0$. Considering a rising amount of heat to be carried by phonons upon cooling as well, the WF law seems to overestimate the electronic contribution at low temperatures. Hence, a more detailed experimental investigation of the Wiedemann-Franz law in (DCNQI)$_2$Cu is presented in the following.

### 4.3.2 The Wiedemann-Franz Law in Organic Conductors

Organic conductors are known for their exceptional high electrical conductivity as well as their reduced dimensionality owing to the anisotropic electronic structure. Often denoted as *organic metals*, the question arises whether fundamental relationships like the Wiedemann-Franz law are as valid for this material class as for ordinary inorganic 3D metals, such as gold or copper. By means of their anisotropic electronic structure, low-dimensional conductors behaving as Luttinger liquids are expected to violate the WF law [47], as evidenced by increased Lorenz numbers which diverge in the zero temperature limit. This has been experimentally demonstrated for inorganic metals of reduced dimensionality, such as $Li_{0.9}Mo_6O_{17}$ [217]. On the other hand, the complex and diverse interaction mechanisms between electrons and phonons in organic conductors have been theoretically predicted to render reduced Lorenz numbers possible [49, 218]. Hence, a comprehensive investigation of the WF law appears to be mandatory for understanding the relation between thermal and electrical transport in low-dimensional organic conductors. Considering the potential application of this material class in thermoelectric generators, it is also of technological relevance.

(DCNQI)$_2$Cu serves as a model system and enables an investigation of the Wiedemann-Franz law by two methods: First of all, by attachment of different functional groups to the quinone ring of the DCNQI molecules, a first-order metal-insulator phase transition can be induced with a tunable critical temperature. Monitoring the change in the thermal conductivity concomitantly with the drop in electrical conductivity facilitates the determination of the Lorenz number at various transition temperatures. Secondly, the electrical conductivity can be varied by the lithium content in (DCNQI)$_2$Cu$_x$Li$_{1-x}$ crystals which are isostructural to the pure copper compound (compare Sec. 4.1.3). Thus, comparing

samples of different lithium concentration permits to discriminate between the electronic and the phononic contributions to thermal conduction. Performing simultaneous electrical and thermal conductivity studies on a single sample, as enabled by the newly designed measurement setup, is the essential requirement for obtaining the reliable data presented in the following.

### Phase Transition Analysis

The drastic change in the electrical conductivity at the Peierls transition should also be reflected in the thermal conductivity due to the reduced electronic contribution to thermal conduction, like anticipated by the Wiedemann-Franz law in Eq. 2.89. The correlated changes were investigated for $(MeBr\text{-}DCNQI)_2Cu$, $(DCNQI\text{-}d_6)_2Cu$ and $(DCNQI\text{-}h_8/d_6)_2Cu$ [70:30] undergoing Peierls transitions upon heating at 155 K, 90 K and 65 K, respectively. The different phase transition temperatures emerge from the influence of the functional groups on the coordination angle $\alpha_{co}$ and the consequential $3d_{xy}$-$\pi$-hybridization, as outlined in Ch. 2.3.3 as well as in the discussion on the electronic properties in Sec. 4.1. The reduction of the electrical and thermal conductivity in the vicinity of the phase transition is delineated in Fig. 4.16 for all three compounds. The phase transition affects both transport quantities as indicated by their first-order discontinuity.

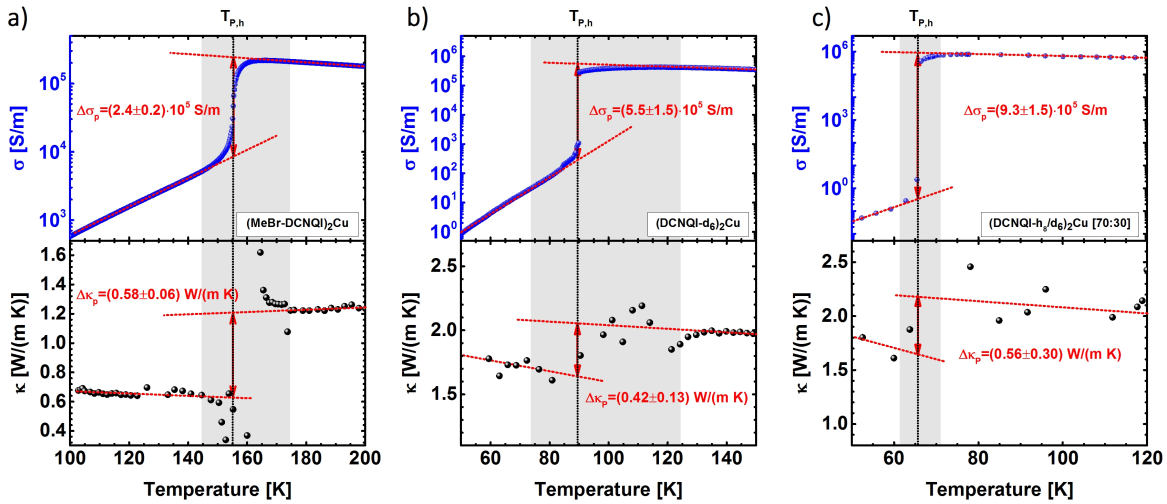


Figure 4.16: Wiedemann-Franz law in the vicinity of the Peierls transition. The change in electrical conductivity and thermal conductivity across the Peierls transition for (a) $(MeBr\text{-}DCNQI)_2Cu$, (b) $(DCNQI\text{-}d_6)_2Cu$ and (c) $(DCNQI\text{-}h_8/d_6)_2Cu$ [70:30]. Their respective extrapolations (dashed red lines) to $T_P$ (dotted vertical line) are also included. Due to the measurement uncertainty several extrapolations were made to estimate the error (not shown for the reason of clarity).

In close vicinity of the Peierls transition (shaded area) no meaningful determination of the thermal conductivity is possible as the temperature coefficient $\chi$ of the sample's

resistivity is needed to evaluate $\kappa$ from the measurement data (compare Eq. 3.18b). Since both, the electrical conductivity and its temperature coefficient are changing rapidly near the phase transition, the relative error of $\kappa$ in this temperature regime easily amounts to a few hundred percent and explains its noisy behavior within the shaded areas of Fig. 4.16. Nevertheless, a few Kelvin beneath and above the phase transition an accurate evaluation of $\kappa$ was possible. Extrapolating the measured $\kappa$ and $\sigma$ to the respective Peierls transition temperature $T_P$ from above and below, the Lorenz number can be determined from both changes $\Delta\sigma$ and $\Delta\kappa$

$$L = \frac{\Delta\kappa}{\Delta\sigma \cdot T_p} \quad . \tag{4.14}$$

The experimentally determined $\Delta\sigma$ and $\Delta\kappa$ together with the resulting Lorenz numbers for the three compounds at their transition temperatures are given in Tab. 4.6. The errors include the uncertainty of $\Delta\kappa$ and $\Delta\sigma$ as well as the error in $l$ by virtue of the distinct electrical and thermal lengths of the crystal, as discussed in Ch. 3.2.4. The uncertainty of the crystal cross section - usually one of the largest errors in the determination of transport properties on the small needle-like organic single crystals [219] - was not included as it introduces a similar inaccuracy in the thermal and electrical conductivity under the assumption of heat and electrical transport occurring in the same volume. For this reason, the approach presents the most accurate and coherent determination of the Lorenz number in organic conductors to date.

| | $T_P$ [K] | $\Delta\kappa$ [$\frac{\mathrm{W}}{\mathrm{m\,K}}$] | $\Delta\sigma$ [$10^5$ $\frac{\mathrm{S}}{\mathrm{m}}$] | L [$10^{-8}\,\mathrm{W\Omega/K^2}$] |
|---|---|---|---|---|
| (MeBr-DCNQI)$_2$Cu | 155 | $0.58 \pm 0.06$ | $2.40 \pm 0.20$ | $1.57 \pm 0.37$ |
| (DCNQI-d$_6$)$_2$Cu | 90 | $0.42 \pm 0.13$ | $5.5 \pm 1.5$ | $0.86 \pm 0.54$ |
| (DCNQI-h$_8$/d$_6$)$_2$Cu [70:30] | 65 | $0.56 \pm 0.30$ | $9.3 \pm 1.5$ | $0.92 \pm 0.69$ |

Table 4.6: Measured electrical and thermal conductivity drops at the Peierls transition of (MeBr-DCNQI)$_2$Cu, (DCNQI-d$_6$)$_2$Cu and (DCNQI-h$_8$/d$_6$)$_2$Cu [70:30]. From the correlated changes the Lorenz number was calculated.

As discussed in Sec. 2.7.1, the well-known form of the Wiedemann-Franz law with a temperature-independent Lorenz number is strictly valid only in the high and very low temperature limit by virtue of different relaxation processes of the electronic system upon electric field or thermal perturbations around and below the Debye temperature. This behavior is well reflected by the significantly smaller Lorenz numbers obtained for (DCNQI-h$_8$/d$_6$)$_2$Cu [70:30] and (DCNQI-d$_6$)$_2$Cu with Peierls transition temperatures

$T_P \lesssim \theta_D \approx 82\,\mathrm{K}$ [34]. Moreover, the high critical temperature of the metal-insulator transition in $(MeBr\text{-}DCNQI)_2Cu$ yields a unique opportunity to investigate the general applicability of the Wiedemann-Franz law in low-dimensional organic conductors at high temperatures $T > \theta_D$. Deviating by 36%, the determined Lorenz number does not agree within its error with the theoretically calculated value of $L_0 = 2.44 \times 10^{-8}\,\mathrm{W\,\Omega\,K^{-2}}$ for isotropic metals [121]. Hence, the data provides first evidence for a violation of the Wiedemann-Franz law in low-dimensional organic conductors. The reduction of the Lorenz number at phase transitions occurring below the Debye temperature furthermore indicates a pronounced violation of the Wiedemann-Franz law. Yet, especially for $(DCNQI\text{-}h_8/d_6)_2Cu$ [70:30] and $(DCNQI\text{-}d_6)_2Cu$ the error in the measured Lorenz numbers is quite large. In order to study the temperature dependence of $L$ more reliably, the approach by Li-alloying of $(DCNQI)_2Cu$ was chosen.

### Analysis of Alloyed $(DCNQI)_2Cu_xLi_{1-x}$ Crystals

To gain further insight into the WF law and the temperature-dependent Lorenz number in organic conductors, alloyed samples of $(DCNQI)_2Cu_xLi_{1-x}$ have been examined in which copper atoms in the crystal lattice are partially substituted by lithium according to the respective concentration $x$. The compound is isostructural and a similar lattice thermal conductivity as in pure $(DCNQI)_2Cu$ is anticipated. In turn, the variation of the electrical conductivity by up to one order of magnitude at RT upon alloying should be reflected in the electronic contribution to the thermal conductivity by virtue of the WF law, enabling the detailed investigation of the latter.

In Fig. 4.17a the temperature-dependent electrical and thermal conductivities of differently alloyed $(DCNQI)_2Cu_xLi_{1-x}$ single crystals are shown. Plotting the interpolated, measured thermal conductivity $\kappa$ of the different samples against their electrical conductivity $\sigma$ enables the determination of the Lorenz number $L$ at each ambient temperature $T$, according to the linear dependence:

$$\kappa = \kappa_{Phon} + \kappa_{el} = \kappa_{Phon} + L \cdot \sigma \cdot T \quad . \tag{4.15}$$

The lattice thermal conductivity $\kappa_{Phon}$ of $(DCNQI)_2Cu_xLi_{1-x}$ corresponds to the y-intercept of the fit with the ordinate. The $\kappa$-$\sigma$-graphs are illustrated in Fig. 4.17b at six selected temperatures between 50 K and 295 K. The six temperatures are indicated by dashed vertical lines in Fig. 4.17a as well. The upper error margin of each data point contains an estimated 5% measurement error in addition to the uncertainty in the thermal length of each sample, as discussed in Ch. 3.2.4. The relative error in the thermal length was less than 10% for all crystals. For the lower error limit, besides the 5% measurement error an uncertainty due to radiation losses according to Eq. 3.24 has been considered,

taking into account the sample dimensions of each individual crystal and assuming an emmissivity of $\epsilon = 0.6$. The radiation error can be neglected below about 200 K but it may become appreciable above for very thin specimen, e.g. in the $x = 0.85$ sample with a diameter of only $d \approx 10.7\,\mu\text{m}$.

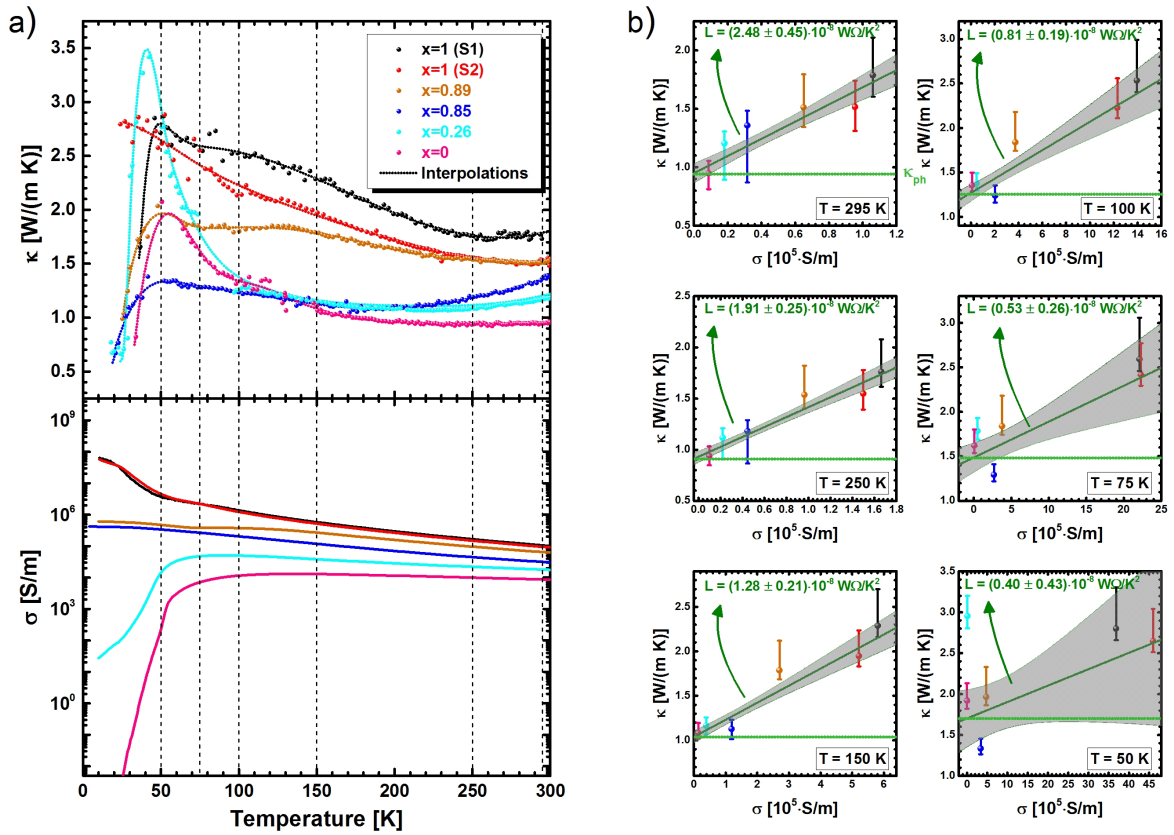


Figure 4.17: Correlated electrical and thermal conductivity measured in alloyed $(\text{DCNQI})_2\text{Cu}_x\text{Li}_{1-x}$ crystals. (a) Temperature-dependent electrical and thermal conductivity. (b) At six selected temperatures the relation between thermal and electrical conductivity together with linear fits are depicted. The gray-shaded areas mark the respective fit's confidence interval at one standard deviation. The lattice thermal conductivity $\kappa_{Phon}$ can be determined from the y-intercept of each fit with the ordinate while the slope enables a determination of the Lorenz number.

Fig. 4.17b demonstrates the linear $\kappa$-$\sigma$ dependence predicted by the WF law to be reasonably fulfilled at temperatures above 100 K. The shaded gray areas mark the one standard deviation confidence interval (68.2%) of each fit. At RT, the Lorenz number may be calculated to

$$L = (2.48 \pm 0.45) \times 10^{-8}\,\text{W}\,\Omega\,\text{K}^{-2} \tag{4.16}$$

which compares well to the standard Lorenz number $L_0 = 2.44 \times 10^{-8}\,\text{W}\,\Omega\,\text{K}^{-2}$ for a degenerate 3D-metal [121]. The appreciable error in the determined $L$ has to be valuated in the context of scarcity of $\kappa$ data, especially, in combination with electrical conductivity

data on the same sample. So far, very little thermal conductivity data has been reported for organic conductors at high temperature at all [220, 174, 175, 221, 219], none of which was correlated with electrical conductivity. To date, the present analysis is the most accurate examination of the WF law in low-dimensional organic metals and a relative error of 10-20% in the absolute value of $L$ is bearable. A comparison of experimental Lorenz numbers for different metals at RT is shown in Tab. 4.7 together with their respective Debye temperatures [96].

| | Cu | Ag | Au | W | $Li_{0.9}Mo_6O_{17}$ | $(DCNQI)_2Cu$ |
|---|---|---|---|---|---|---|
| $L$ $[10^{-8}\frac{W\Omega}{K^2}]$ | 2.23 | 2.31 | 2.35 | 3.04 | 18 [217] | $2.48 \pm 0.45$ |
| $\theta_D$ [K] | 343 | 225 | 165 | 400 | 400 [222] | 82 [34] |

Table 4.7: Comparison of $L$ obtained for $(DCNQI)_2Cu$ at RT with experimental Lorenz numbers of ordinary metals [96]. The respective Debye temperatures $\theta_D$ are also given. The value for the one-dimensional inorganic conductor $Li_{0.9}Mo_6O_{17}$ is highly increased compared to the other materials and resembles a prediction of the Tomonaga-Luttinger liquid theory [217].

In consideration of the assumptions and approximations made in calculating the theoretical $L_0$ of isotropic metals, a deviation in experimentally determined Lorenz numbers of about 10-15% is frequently observed in real materials, actually, also for inorganic metals for which the WF law is expected to hold. Taking the error of $L$ into account, the Wiedemann-Franz law can be taken as validated at RT. The few present studies on the electronic contribution to thermal conduction in organic conductors have been lacking the presented accuracy due to uncertainties in the sample cross section and were limited to low-temperature measurements where impurity scattering dominates [221]. This result confirms the mostly common relaxation mechanism for thermal and field perturbation at RT in $(DCNQI)_2Cu$.

Of minor importance seems to be the electronic correlation in the material. In contrast to Fermi liquid theory, a strong electron-electron interaction in the strictly one-dimensional Tomonaga-Luttinger liquid theory predicts a larger Lorenz number diverging in the zero temperature limit [223]. This behavior has been observed in the inorganic one-dimensional conductor $Li_{0.9}Mo_6O_{17}$ with a room temperature Lorenz number of $L = 18 \times 10^{-8}\,\mathrm{W\,\Omega\,K^{-2}}$ increasing by a factor of 5 upon cooling to 25 K [217]. Electronic correlation effects are also important in the $(DCNQI)_2Cu$ system as the CDW transition on the DCNQI molecules goes along with a Mott transition in the Cu 3d states at the Fermi energy which has been demonstrated by photoemission spectroscopy [224]. However, the 3d states are hybridized with the p$\pi$-states of the DCNQI LUMO resulting in a quasi-3D band structure. Thus, the absence of a Lorenz number enhancement

in $(DCNQI)_2Cu$ is eventually not surprising because it has been predicted by the strict one-dimensional Tomonaga-Luttinger model. Yet, the electronic dimensionality of organic conductors is sensitive to temperature, especially for the $(DCNQI)_2Cu$ material system. Hence, a temperature-dependent investigation of the WF law appears to be necessary to take into account the relevant thermal effects.

Upon lowering the temperature the Lorenz number decreases. On the other hand the error is significantly larger at $T = 75\,\mathrm{K}$ compared to RT and a linear relationship between $\kappa$ and $\sigma$ seems questionable at $T = 50\,\mathrm{K}$. Therefore, prior to analyzing the temperature dependence of $L$ in detail, it is crucial to investigate the statistical significance of the above analysis. Deduced from the linear fits between 36 K and 300 K, Fig. 4.18a depicts the Pearson $r$, a correlation coefficient characterizing the linearity between the two quantities [225]:

$$r = \frac{Cov(\kappa, \sigma)}{\sqrt{Var(\kappa) \cdot Var(\sigma)}} \quad . \tag{4.17}$$

Here, $Var(x)$ denotes the variance of the respective quantity $x$ and $Cov(x, y)$ the covariance between two quantitites $x$ and $y$. The Pearson $r$ amounts to 1 for a perfectly linear relationship with positive slope and yields $-1$ for a negative linear correlation. A zero value indicates no correlation at all. For a linear fit through six data points, values above 0.81 indicate a positive linear correlation with 95 % significance. This confidence level, as marked by the horizontal, dashed, black line in Fig. 4.18a, is clearly met above 80 K. Moreover, an analysis of variance (ANOVA) was performed to test the data against a null hypothesis, i.e. whether a constant value might describe the data as good as a linear fit. The resulting p-value defines the probability of a constant model with vanishing slope to be applicable. Usually, a value below 5%, as indicated by the horizontal, dashed, purple line in Fig. 4.18a, allows to reject the null hypothesis. Again, this confidence level is achieved above 80 K where probability of correctly describing the set of experimental data by a constant model is less than 5 %. Both analyses point out the validity of modelling the experimental data by a linear fit at temperatures higher than 80 K while a constant fit might be as good for lower temperatures. Hence, the extraction of the temperature-dependent Lorenz number from the fits is feasible in the high temperature regime.

The temperature dependence of the normalized Lorenz number $L/L_0$ is illustrated in Fig. 4.18b. The fit error is marked as gray shaded area in the graph. In accordance with the above statistical analyses, the relative error below 80 K strongly increases, as evidenced by the increased absolute error in Fig. 4.18b going along with smaller absolute

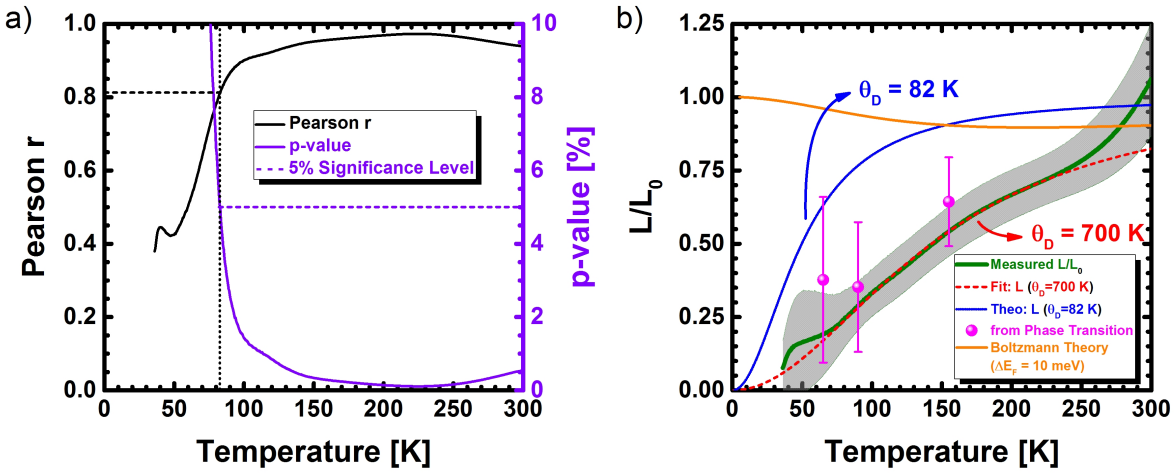


Figure 4.18: Temperature-dependent Lorenz number in $(DCNQI)_2Cu_xLi_{1-x}$. (a) The statistical fit analysis reveals the liability of the linear fits shown in Fig. 4.17b. Above 80 K, the Pearson linear correlation coefficient $r$ surpasses its 95% significance value (dashed black line). By an analysis of variance (ANOVA), the null hypothesis of a constant value data representation can be rejected attaining only 5 % significance above this temperature as well (dashed purple line). (b) The normalized Lorenz number $L/L_0$ shows an appreciable temperature dependence in the investigated regime. A fit by Eq. 2.93 to the data between 80 K and 220 K yields an anomalously high Debye temperature of $\theta_D = 700$ K (dashed red curve). A theoretical model assuming the literature Debye temperature of $\theta_D = 82$ K [34] (blue curve) is in striking contrast to the observed Lorenz number, even considering the error interval as marked by the gray shaded area. The Lorenz numbers evaluated at the Peierls transition of three $(DCNQI)_2Cu$ compounds are also delineated by the pink data points.

values of $L$. In spite of the perceptible error even above 80 K, it is evident that the Lorenz number reduces below its standard value $L_0$ upon decreasing temperature. The Lorenz numbers determined by the phase transition analysis above are also depicted in Fig. 4.18b and corroborate the data obtained for the Li-alloyed samples.

The experimental data suggests different relaxation times for thermal and electric field perturbations of the Fermi distribution of electrons in $(DCNQI)_2Cu$ below RT. Following the discussion in Ch. 2.7.1, a discrimination between the relaxation times is necessary below the Debye temperature because thermal perturbations may relax via small angle scattering events of long wavelength phonons while large angle scattering needs to take place for the electric field relaxation. The latter is most easily accomplished by Umklapp scattering events requiring phonons of high energy and wave vector to be excited. Eq. 2.93 takes the different relaxation mechanisms into account in the calculation of the Lorenz number and the blue solid curve represents the temperature-dependent Lorenz ratio as anticipated for a Debye temperature of $\theta_{D,Lit} = 82$ K [34]. Clearly, the calculated behavior does not resemble the experimental data (green curve). Yet, Eq. 2.93 may be fitted to the data between 80 K and 220 K assuming a Debye temperature of $\theta_{D,Fit} = 700$ K (red dashed curve) being one order of magnitude larger than the literature value. This anomalous high value demands some discussion.

First of all, the standard model for the Lorenz number assumes a Fermi sphere, representing a 3D electronic structure that certainly does not reflect the flat Fermi surface characteristics of the low-dimensional DCNQI radical anion salts. Secondly, it assumes dominant scattering of electrons by acoustic phonons whose energy is characterized by the Debye temperature. Yet, electrons might also interact inelastically with optical phonon modes of higher energy, as implied by the deduced high Debye temperature of $\theta_{D,Fit} = 700\,\mathrm{K}$. This value corresponds to a Debye energy of $k_B\theta_{D,Fit} = 60\,\mathrm{meV}$ but an efficient interaction with charge carriers is unlikely due to the low occupation density of optical phonon modes of such high energy. Even the high-field nonlinear conduction experiments performed in Ch. 4.2 indicated inelastic scattering by optical phonons having a much lower energy of only 19 meV. Consequently, this interpretation is disregarded.

Thirdly, the large temperature dependence of $L/L_0$ may not only be caused by different relaxation times but also by probing different electronic states in the electrical and the thermal conductivity. According to the Boltzmann theory discussed in Ch. 2.5.1, the heat is carried by charge carriers at higher energetic distances to the Fermi level compared to the charges responsible for electrical conduction. The same effect has already been taken into consideration for explaining the distinct values of the Seebeck coefficient in the $(DCNQI)_2Cu$ salts, as discussed in Sec. 4.1.2. The $K_2$ transport integral of Eq. 2.55c, used to calculate the thermal conductivity, probes states of even further distance to the Fermi surface as compared to the thermopower. The position of the maxima of the material-independent integrand of $K_2$ (see Fig. 2.15) depends on the temperature as well. Therefore, the temperature-dependent Lorenz number may be caused by subsequently probing different energy states in the electrical and thermal conductivity measurements when lowering the temperature. In line with the calculation of the Seebeck coefficient in Sec. 4.1.2, the Lorenz number can be evaluated according to Eqs. 2.55a-c and 2.53:

$$L = \frac{1}{T^2}\frac{\int g(\epsilon)\vec{v}^{\,2}(\epsilon)\tau(\epsilon)[\epsilon - E_F]^2\frac{\partial f^0}{\partial \epsilon}d\epsilon}{\int g(\epsilon)\vec{v}^{\,2}(\epsilon)\tau(\epsilon)\frac{\partial f^0}{\partial \epsilon}d\epsilon} \quad . \tag{4.18}$$

Assuming a temperature-dependent shift of the Fermi energy with $\Delta E_F = 10\,\mathrm{meV/K}$, as defined by Eq. 4.6 in Sec. 4.1.2 when analyzing the thermopower in $(DCNQI\text{-}h_8)_2Cu$, the deduced Lorenz number is depicted in Fig. 4.18b as orange curve. In contrast to the Seebeck coefficient, the temperature-dependent Fermi energy is not able to explain the observed behavior of the electronic thermal conductivity. Already in the discussion of the electrical properties in Sec. 4.1, the difficulty in analyzing temperature- and pressure-dependent charge transport quantities in organic conductors has been emphasized. The contribution by 3D holes to the transport properties of $(DCNQI)_2Cu$ as well as their absence in $(DCNQI)_2Li$ has been evidenced. Accordingly, both materials are expected

to reveal distinct band structures and should yield different Lorenz numbers, i.e. each $(DMe\text{-}DCNQI)_2Cu_xLi_{1-x}$ sample has a distinct Lorenz number L(x,T) depending on the composition $x$ and temperature $T$. This would also explain the very coarse linear relationships illustrated in Fig. 4.17b. However, a variation of the temperature-dependent Fermi energy as well as the calculation of $L$ for $(DCNQI)_2Li$ revealed similar results to the above calculation. As a consequence, the simple Boltzmann theory taking into account the energetic states probed by electrical and thermal conductivity cannot explain the temperature dependence of the Lorenz number. More elaborate DFT calculations of the band structure based on the distinct, temperature-dependent electronic structures of $(DCNQI)_2Cu$ and $(DCNQI)_2Li$, respectively, as well as on their degree of electronic correlation are currently under way. They could shed further light on this issue by resolving more details of the electronic band structure of the mixed single crystals.

More likely than the above scenarios, the electronic dimensionality causes the deviation from the classical Wiedemann-Franz law. The very large thermal conductivity in the Li-rich samples at low temperatures may be understood in this context because $(DCNQI)_2Li$ reveals a more pronounced one-dimensional Fermi surface compared to $(DCNQI)_2Cu$. The one-dimensionality may precipitate in increased Lorenz numbers diverging in the zero temperature limit, as expected for a one-dimensional Luttinger liquid [47]. The increased Lorenz numbers for the low-conductivity samples lead to an underestimation upon their determination by the $\kappa$-$\sigma$-analysis presented above and thus, resolve the continuous reduction of $L$ toward lower temperatures. Yet, the deviation from the classical WF law was also confirmed by the phase transition analysis of the $(DCNQI)_2Cu$ salts. Hence, another effect seems to be of importance. The additional ingredients being relevant for a complete understanding of the WF law in the $(DMe\text{-}DCNQI)_2Cu_xLi_{1-x}$ material system might be the degree of electronic correlation and the nature of the scattering mechanism which can differ for $(DCNQI)_2Li$ and $(DCNQI)_2Cu$.

### 4.3.3 Lattice Thermal Conductivity

In addition to the investigation of the WF law, the above analysis also allows for an evaluation of the lattice thermal conductivity in $(DCNQI)_2Cu_xLi_{1-x}$, as determined by the intercept of the linear fits with the ordinate in Fig. 4.17b. Its temperature dependence is plotted against the inverse temperature in Fig. 4.19a. Between 80 K and 200 K a linear fit represents the data well and verifies the $\kappa \propto T^{-1}$ behavior expected for phonon-phonon Umklapp scattering limiting the heat transport across the lattice above the Debye temperature (compare Ch. 2.7.2). To discuss the deviations at $T > 200$ K as well as the low-temperature characteristics, the linear temperature graph in Fig. 4.19b depicts the

same data as Fig. 4.19a. While the linear fits of the $\kappa$-$\sigma$-relation below 80 K are prone to errors with respect to their slope, the y-intercept, i.e. the phonon contribution to thermal conduction, may be regarded as a good average on samples of different structural order. The above ANOVA analysis also indicated the validity of a constant value representation due to the decreasing Lorenz number which would still provide a suitable determination of the phonon thermal conductivity. Accordingly, the lattice thermal conductivity data depicted in Fig. 4.19 is interpreted within its confidence interval marked by the gray shaded areas.

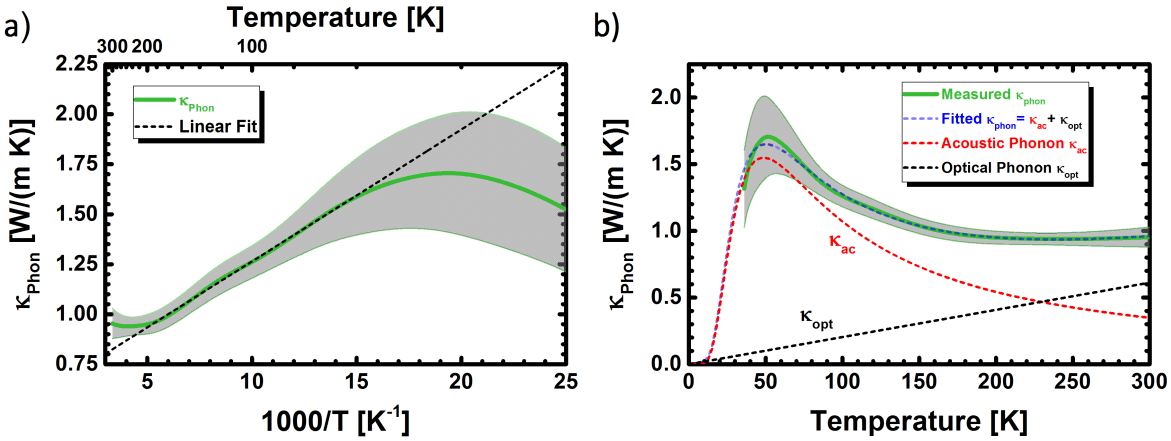


Figure 4.19: Lattice thermal conductivity $\kappa_{Phon}$ in $(DCNQI)_2Cu_xLi_{1-x}$. Gray shaded areas mark the confidence interval of $\kappa_{Phon}$. (a) Plotting $\kappa_{Phon}$ against the inverse temperature, the linear relation expected from phonon-phonon Umklapp scattering is verified between 80 K and 200 K. (b) The full temperature dependence of $\kappa_{Phon}$ can be modeled by combining acoustic and optical phonon contributions.

A few things become obvious when analyzing the temperature dependence of $\kappa_{Phon}$ in Fig. 4.19b. Firstly, on the high temperature side the thermal conductivity saturates and even slightly increases with temperature instead of obeying the neat $T^{-1}$ law predicted by Umklapp scattering of acoustic phonons. Furthermore, in the low-temperature region a maximum at around $T_{max} \approx 50$ K occurs, i.e. at a temperature being close to the peak in the Seebeck coefficient which was discussed in terms of a phonon drag effect. Phonon drag, like lattice thermal conductivity, increases sharply with $T$ in the cryogenic regime following the heat capacity of acoustic phonons. After going through a maximum at some fraction of the Debye temperature, it decreases upon increasing temperature due to phonon-phonon Umklapp scattering placing restrictions on the relative momentum transfer to electrons. Because the same physical quantities are expected to limit the heat conduction by acoustic lattice phonons, a temperature dependence similar to that in the phonon drag description by Eq. 4.4 was applied to the lattice thermal conductivity:

$$\kappa_{ac} = \frac{3N_A k_B v_s^2 \rho_{dens}}{m_{mol}} \left(\frac{\Omega}{T}\right)^{v} \left(\frac{\theta_E}{T}\right)^2 \frac{e^{\theta_E/T}}{(e^{\theta_E/T}-1)^2} \quad . \tag{4.19}$$

Here, $\tau_U = \left(\frac{\Omega}{T}\right)^{\upsilon}$ is the phonon-phonon Umklapp scattering time. As proven beneficial for the description of the phonon drag, an Einstein model was employed for the heat capacity, in which the Einstein temperature $\theta_E$ characterizes the mean energy $E_{ac} = k_B\theta_E$ of the acoustic phonon modes. Modeling the experimental data solely by Eq. 4.19 (not shown) did not facilitate decent fit results, especially on the high temperature side. Also adding a constant to Eq. 4.19 only marginally improved the accuracy. Instead, a good agreement with the experimental data was found assuming an additional contribution to thermal conduction by optical phonons of the form:

$$\kappa_{opt} = K_{opt} \cdot T \quad . \tag{4.20}$$

The temperature dependence was chosen to reflect the almost linear increase in the lattice heat capacity above 30 K in $(DCNQI)_2Cu$ due to an increasing number of optical phonon modes becoming populated with temperature [176]. Fig. 4.19 demonstrates the sum $\kappa_{Phon} = \kappa_{ac} + \kappa_{opt}$ of both contributions to reflect the experimental data perfectly within its errors. The individual contributions of acoustic and optical phonons are also drawn separately and the fit parameters are given in Tab. 4.8. It is evident that optical phonons account for up to $0.6\,\mathrm{W\,m^{-1}\,K^{-1}}$ of the lattice thermal conductivity at RT being almost twice as large as the heat carried by acoustic phonons. At high temperatures, the phonon mean free path $l_{ph} = v_g\tau_{ph}$ becomes small and remains almost constant [92]. When it reaches the length scale of the lattice spacing, the phonon concept is expected to break down, similar to the minimum thermal conductivity of an amorphous solid discussed in Ch. 2.7.3. The condition is more easily fulfilled for optical phonon modes by virtue of their small group velocity $v_g$ [92]. The dispersion of optical phonon modes has been comprehensively characterized in the organic semiconductor naphthalene [116], as shown in Fig. 2.13a of Ch. 2.4.3. The dispersion was employed to estimate a reasonable group velocity of $v_g \leq 500\,\mathrm{m\,s^{-1}}$ for optical phonons, yielding a characteristic temperature above which the phonon theory breaks down for the optical modes [155]:

$$T_0^{opt} = \frac{hv_g}{k_B c} \leq 62\,\mathrm{K} \quad . \tag{4.21}$$

Here, $c = 3.8811\,\text{Å}$ marks the lattice constant along the heat transport direction. Accordingly, the thermal conduction by optical phonons is mostly incoherent in the investigated temperature regime. In this situation, a constant mean free path for each optical phonon mode is expected and correspondingly, the total heat carried by optical phonons scales with the number of thermally excited optical phonon modes being almost linear in temperature. Hence, the linear term assumed by Eq. 4.20 becomes justified.

From the Debye temperature of $\theta_D = 82\,\mathrm{K}$ [34], the group velocity of acoustic phonons

(i.e. the sound velocity) can be estimated to $v_S = 2130\,\mathrm{m\,s^{-1}}$ yielding $T_0^{ac} = 260\,\mathrm{K}$. This sound velocity compares well to the value of $v_S = 1800 - 3000\,\mathrm{m\,s^{-1}}$ in TTF-TCNQ which was determined by neutron scattering experiments [103, 104]. Hence, for the acoustic modes the phonon description remains valid almost up to RT and, as a consequence, the dominant thermal conduction mechanism changes from coherent lattice heat transport by plane-wave acoustic phonons to incoherent hopping transport by optical phonons at some intermediate temperature. In general, an incoherent phonon heat conduction with concomitant coherent charge transport is a good prerequisite to create an efficient thermoelectric material, but the large number of low-frequency optical phonon modes in $(DCNQI)_2Cu$ still facilitates an appreciable heat to be carried by the lattice as a whole. Accordingly, the total lattice thermal conductivity at RT

$$\kappa_{lat}(RT) = (0.95 \pm 0.06)\,\mathrm{W\,m^{-1}\,K^{-1}} \tag{4.22}$$

significantly undermines values of $1.7\,\mathrm{W\,m^{-1}\,K^{-1}}$ [226] determined for $Bi_2Te_3$, representing the best reference thermoelectric material at RT to date. Yet, it does not compare to the low values usually obtained in complex crystal structures, e.g. in the thermolectric Zintl compounds with $\kappa_{lat} = 0.45\,\mathrm{W\,m^{-1}\,K^{-1}}$ [51] or the experimental values of $\kappa_{lat} = 0.5\,\mathrm{W\,m^{-1}\,K^{-1}}$ for the organic semiconductor naphthalene [215]. Hence, the lattice thermal conductivity still takes surprisingly high values by virtue of the large optical phonon contribution.

| Parameter | $\Omega$ $[10^{-9}\,\mathrm{K\,s^{1/\upsilon}}]$ | $\upsilon$ | $\theta_E$ [K] | $K_{opt}$ $[10^{-3}\,\frac{\mathrm{W}}{\mathrm{m}}]$ |
|---|---|---|---|---|
| Value | 6.77 | 1.14 | 134 | 2.04 |

Table 4.8: Parameters for the fits of $\kappa_{Phon}$ in Fig 4.19b to the experimental data.

The temperature coefficient $\upsilon = 1.14$ takes a similar value as in the fit of the phonon drag effect (compare $\upsilon_{drag} = 1.18$ in Ch. 4.1.2), indicating a similar process limiting both quantities. A value of $\upsilon = 1$ is theoretically expected for phonon-phonon Umklapp scattering but a slightly larger temperature dependence is commonly observed in thermal conductivity measurements. It has been explained by thermal expansion of the lattice as well as by higher-order phonon interaction processes (four-phonon processes) [92]. Fig. 4.20 delineates the phonon-phonon Umklapp scattering rate $\tau_U^{-1}$ as calculated by Eq. 4.19 from the fit parameters in Tab. 4.8. The scattering factor $\beta \approx \tau_{ph-e}^{-1}/(\tau_{ph-e}^{-1}+\tau_U^{-1})$ in Eq. 4.4 quantifies the relative strength of phonon-electron to phonon-phonon Umklapp scattering and was separately determined in the fit of the phonon drag thermopower in Ch. 4.1.2. Employing $\tau_U$ from above, the phonon-electron scattering rate $\tau_{ph-e}^{-1}$ may be resolved as

well. This is illustrated in Fig. 4.20, too. It decreases with increasing temperature and provides the reason for the low temperatures at which phonon drag is observed.

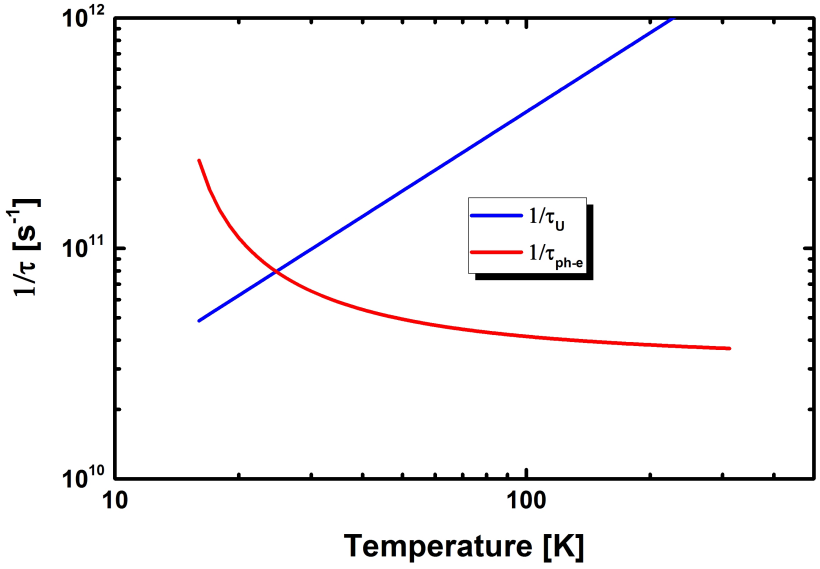


Figure 4.20: Phonon scattering rates in $(DCNQI)_2M$. The phonon-phonon Umklapp scattering rate $\tau_U^{-1}$ was determined from the fit of the lattice thermal conductivity in Fig. 4.19b. In combination with the analysis of the thermopower it also enabled a calculation of the phonon-electron scattering rate $\tau_{ph-e}^{-1}$ which is higher than the Umklapp rate at low temperature allowing for the phonon drag effect.

The Einstein temperature of $\theta_E = 134\,\mathrm{K}$ is somewhat higher compared to the phonon drag analysis ($\theta_E = 85\,\mathrm{K}$) and relative to the literature values on the Debye temperature obtained from specific heat measurements ($\theta_D = 82\,\mathrm{K}$ [34]). Yet, as the fit parameter $\theta_E$ is sensitive to the sizable error of $\kappa_{Phon}$ in the temperature regime below 80 K, its similar magnitude indicates the same phonon modes to be involved. Hence, strong evidence is presented that both, the heat conduction by acoustic phonons as well as the phonon drag thermopower are limited by the same phonon-phonon Umklapp process of acoustic phonon modes. This also indirectly proves the phonon drag to precipitate the anomalous low-temperature maximum in the Seebeck coefficient.

### 4.3.4 Conclusions

For the first time, a consistent examination of the Wiedemann-Franz law for an organic conductor above the Debye temperature $\theta_D$ has been achieved. The resulting Lorenz number takes similar values as obtained for inorganic metals at RT but decreases when the temperature is lowered, already far above $\theta_D$. Hence, the Wiedemann-Franz law in its common form for 3D metals is invalid for $(DCNQI)_2Cu$ over a wide temperature range and seems to depend crucially on the complex electronic structure of organic conductors and their degree of electronic correlations. The analysis of the lattice thermal conductivity

revealed a similar heat transport behavior as observed in the thermopower at low temperature, indicating both processes to be limited by phonon-phonon Umklapp scattering of acoustic phonons. With rising temperature, the contribution of optical phonons to lattice thermal conduction increases and indicates a transition from a coherent to an incoherent phonon transport.

## 4.4 Thermodynamic Investigation on the Phase Transition in $(DCNQI)_2Cu$

In Ch. 2.3.3, the phenomenological thermodynamic model by Nishio *et al.* [34] was discussed. It explains the phase diagram of the $(DCNQI)_2Cu$ copper system in terms of a competition between spin and charge degrees of freedom contributing to the entropy in the insulating and the metallic ground state, respectively. However, to quantitatively explain the phase diagram and the latent heat measurements, a third non-electronic contribution was proposed to come into play. A separate investigation of the individual contributions to the entropy in the respective ground states is presented here. While the total entropy difference is estimated by the quantitative analysis of the latent heat at the first-order phase transitions of $(MeBr\text{-}DCNQI)_2Cu$, $(DCNQI\text{-}d_6)_2Cu$ and $(DCNQI\text{-}h_8/d_6)_2Cu$ [70:30], the neat electronic contribution may be determined from the temperature-dependent thermopower.

### 4.4.1 Entropy Change from Latent Heat

It was already pointed out that a detailed evaluation of the thermal properties in the close vicinity of the phase transition is barely possible by the $3\omega$ method due to the large uncertainty in the temperature coefficient $\chi$ of the resistance. Nonetheless, it is worthwhile to take a look at the thermal response time $\tau \propto c_{mol}/\kappa$ (as defined in Eq. 3.12), which can be directly extracted from the measurement data without the necessity to input additional quantities, such as $R$, $\chi$ or $I_0$.

As illustrated in Fig. 4.21 for $(MeBr\text{-}DCNQI)_2Cu$, $\tau$ reduces across the phase transition at $T_P = 155\,\mathrm{K}$ from about 4 s at 140 K to 2 s at 170 K. Here, $T_P$ corresponds to the phase transition temperature in the heating run. The faster thermal response above $T_P$ is mainly caused by the additional electronic contribution to $\kappa$. This interpretation is in line with the thermal conductivity drop across the transition presented in the previous section. However, just at the phase transition a drastic slow down in the thermal response of the system is observed, as evidenced by the increase of $\tau$ from 4 s up to 8 s. This rise of $\tau$ can only be caused by an increased heat capacity or decreased $\kappa$ which shall be discussed in more detail in the following.

Below $T_P$, $\kappa$ is mainly due to lattice thermal conduction because the electrical conductivity is small in this temperature regime. Approaching $T_P$ from the low-temperature side, the electrical contribution is expected to gain importance, thus increasing the overall thermal conductivity. Additionally, more exotic low-energy excitations, such as solitons or moving charged domain walls [199], might allow for an additional heat conduction channel

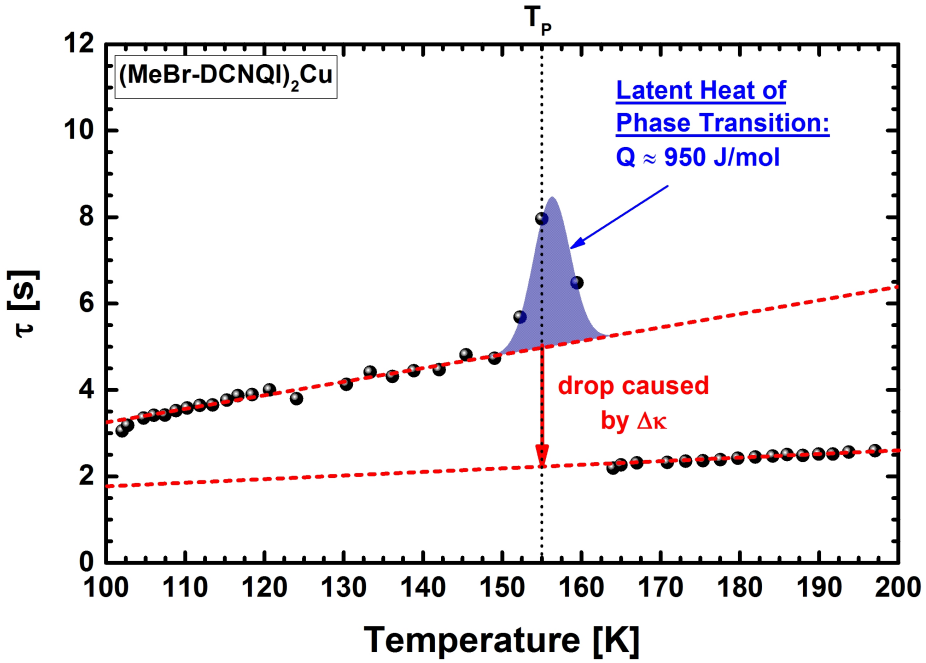


Figure 4.21: Measured thermal response time $\tau$ across the Peierls transition in (MeBr-DCNQI)$_2$Cu. The increase in $\kappa$ leads to a reduced $\tau$ above the phase transition temperature $T_P$. The latent heat at the phase transition, indicated by the blue area, causes a slow down of the thermal response.

close to the phase transition. All these effects would decrease the thermal response time in contrast to the experimental observation. Neglecting changes in the population density of phonons at this stage, the only possible effect leading to a diminution of $\kappa$ close to the phase transition might be a shortened phonon mean free path promoting a smaller lattice thermal conductivity.

In proximity to $T_P$, both metallic and insulating domains are known to coexist in (DCNQI)$_2$Cu. This has been evidenced by a correlated ESR, AC susceptibility and electrical conductivity study [182]. Due to the lattice distortion in the insulating phase, the crystal structure differs slightly as compared to the metallic state. The alternating insulating and metallic domains impinge on the long-range periodicity of the crystal and hence, reduce the phonon mean free path. This principle, i.e. the preparation of an artificial superlattice structure by means of an alternating layer growth, has also been applied to reduce the lattice thermal conductivity in $Bi_2Te_3$ by a factor of 2.2 [44]. Yet, these values have been achieved with superlattice structures on the order of 1 nm. The sizes of insulating and metallic domains in (DCNQI)$_2$Cu are expected to be at least several lattice constants in order to establish an energetically favorable long-range trimerization of the lattice. Additionally, the change in the lattice constants and the lattice symmetry is so small across the phase transition that the crystal symmetry of the trimerized lattice has never been completely resolved [66]. Consequently, this interpretation is disregarded.

More likely, the increase in $\tau$ may be ascribed to the latent heat at the phase transition due to the change in the electronic and lattice degrees of freedom. A similar peak has already been observed in previous heat capacity measurements close to the phase transition in deuterated $(DCNQI\text{-}d_x)_2Cu$ [176] and also for other organic conductors [227]. With the help of Eq. 3.16, the molar latent heat of the phase transition can be estimated from the experimental data by:

$$Q_{lat} = \int \Delta c_{mol} \cdot dT = \frac{10 m_{mol} \kappa}{4\pi L^2 \rho_{dens}} \int \Delta\tau \cdot dT \tag{4.23}$$

Here, the integral corresponds to the blue shaded area in Fig. 4.21 characterizing the increase in $\tau$ at $T_P$. It has been determined by fitting a Gaussian peak on top of the linear slope. Assuming a thermal conductivity of $\kappa = (0.63 \pm 0.05)\,\mathrm{W\,m^{-1}\,K^{-1}}$ extrapolated from beneath the phase transition, the latent heat can be calculated to

$$Q_{lat} = (1.69 \pm 0.38)\,\mathrm{J\,g^{-1}} \equiv (950 \pm 216)\,\mathrm{J\,mol^{-1}}. \tag{4.24}$$

The error includes the uncertainty in the determination of the area $\int \Delta\tau \cdot dT$ due to small number of data points in the vicinity of the phase transition. The slow-down of the relaxation time emphasizes the anomalous first-order character of the Peierls transition in $(DCNQI)_2Cu$. The classical Peierls theory predicts a second-order metal-insulator transition for which no latent heat should be observed. The latent heat at the first-order metal-insulator transition in $\alpha$-$(BEDT\text{-}TTF)_2I_3$ was determined to $Q_{lat} \geq 0.32\,\mathrm{J\,g^{-1}} \equiv 368\,\mathrm{J\,mol^{-1}}$ being of similar magnitude [227]. From the latent heat one can calculate the entropy change when going from the insulating to the metallic state [34]:

$$\Delta\Sigma = \frac{Q_{lat}}{T_P} = (10.8 \pm 2.5)\,\mathrm{mJ\,g^{-1}\,K^{-1}} \equiv (6.1 \pm 1.4)\,\mathrm{J\,mol^{-1}\,K^{-1}} \quad . \tag{4.25}$$

The latent heat was also extracted from the thermal response time of $(DCNQI\text{-}h_8/d_6)_2Cu$ [70:30] and $(DCNQI\text{-}d_6)_2Cu$ as depicted in Fig. 4.22. Here, the effect is not as pronounced as before and the number of data points is very limited, i.e. quite large experimental errors have to be expected. The extracted quantities are given in Tab. 4.9.

Plotting the estimated change in entropy across the phase transition $\Delta\Sigma$ against the transition temperature $T_P$, a linear relation similar to that obtained by Nishio *et al.* [34] can be deduced, both being depicted in Fig. 4.23. From the linear slope an effective $\gamma^* = (65.8 \pm 8.7)\,\mathrm{mJ\,mol^{-1}\,K^{-2}}$ can be extracted. The large error bars indicate that an accurate determination of $\gamma^*$ is hardly possible from the data. Nishio *et al.* have also analyzed the latent heat by means of high-accuracy specific heat measurements for various degrees of deuteration in $(DCNQI\text{-}d_x)_2Cu$ undergoing the Peierls transition at different temperatures

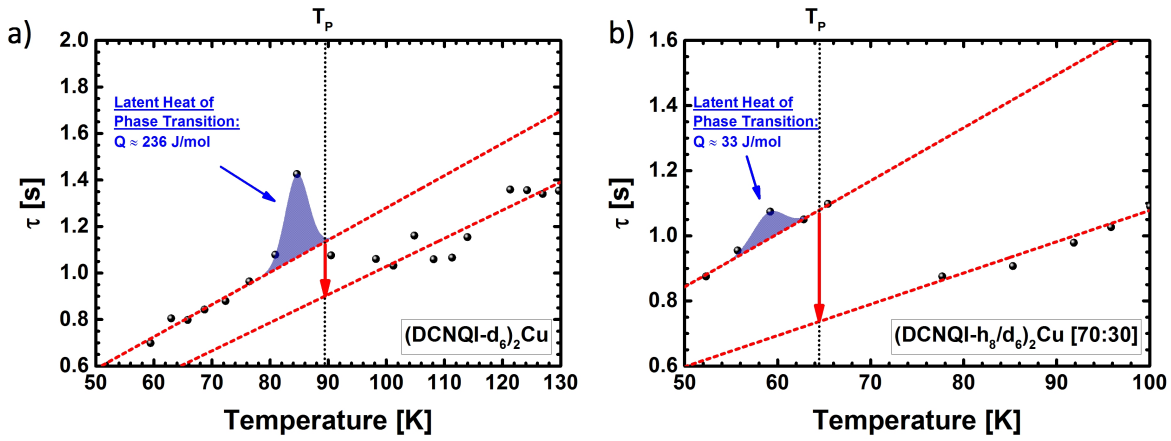


Figure 4.22: Determination of the latent heat for (a) (DCNQI-$h_8/d_6$)$_2$Cu [70:30] and (b) (DCNQI-$d_6$)$_2$Cu with the same procedure as described for (MeBr-DCNQI)$_2$Cu.

| | $T_P$ [K] | $\kappa$ [$\frac{\mathrm{W}}{\mathrm{m\,K}}$] | $\int \Delta\tau \cdot dT$ [K·s] | $Q_{lat}$ [$\frac{\mathrm{J}}{\mathrm{mol}}$] | $\Delta\Sigma$ [$\frac{\mathrm{J}}{\mathrm{mol\,K}}$] |
|---|---|---|---|---|---|
| (MeBr-DCNQI)$_2$Cu | 155 | $0.63 \pm 0.05$ | $20.2 \pm 3.0$ | $950 \pm 216$ | $6.1 \pm 1.4$ |
| (DCNQI-$d_6$)$_2$Cu | 90 | $1.63 \pm 0.05$ | $1.80 \pm 0.45$ | $236 \pm 73$ | $2.62 \pm 0.84$ |
| (DCNQI-$h_8/d_6$)$_2$Cu | 65 | $1.8 \pm 0.1$ | $0.34 \pm 0.17$ | $33 \pm 30$ | $0.50 \pm 0.3$ |

Table 4.9: Latent heat and entropy change determined from the thermal response time in the vicinity of the Peierls transition of several (DCNQI)$_2$Cu compounds with different phase transition temperatures $T_P$.

$T_P$ [34]. As discussed in Ch. 2.3.3, they found a linear relationship $\Delta\Sigma = -S_I + \gamma^*_{Lit} \cdot T_P$ for the entropy change across the phase transition. $S_I$ denotes the spin entropy of localized Cu 3d electrons below the Peierls transition by virtue of the accompanying electronic Mott transition on the copper chains.

It should be noted that a negative offset of similar magnitude might also be explained by a configurational lattice entropy difference of $\Delta\Sigma = -k_B N_A \ln 3 = -9.3\,\mathrm{J\,mol^{-1}\,K^{-1}}$ due to the tripling of the unit cell in the insulating Peierls regime. A negative offset of $S_I \approx -(3.7 \pm 0.6)\,\mathrm{J\,mol^{-1}\,K^{-1}}$ can also be seen in the presented data but an unambiguous distinction between the configurational lattice and the spin degrees of freedom is not possible as it does not agree with either of the expected values within its error. However, the additional low-temperature specific heat data on the antiferromagnetic phase transition at 6 K in (DCNQI)$_2$Cu reported by Nishio *et al.* rather suggests the offset of $S_I = 1.8\,\mathrm{J\,mol^{-1}\,K^{-1}}$ to originate from the spin degrees of freedom. Their more reliably determined $\gamma^*_{Lit} = 40\,\mathrm{mJ\,mol^{-1}\,K^{-2}}$ is larger than the expected Sommerfeld constant of $\gamma_{el} = 25\,\mathrm{mJ\,mol^{-1}\,K^{-2}}$ obtained from low-temperature measurements on the specific heat

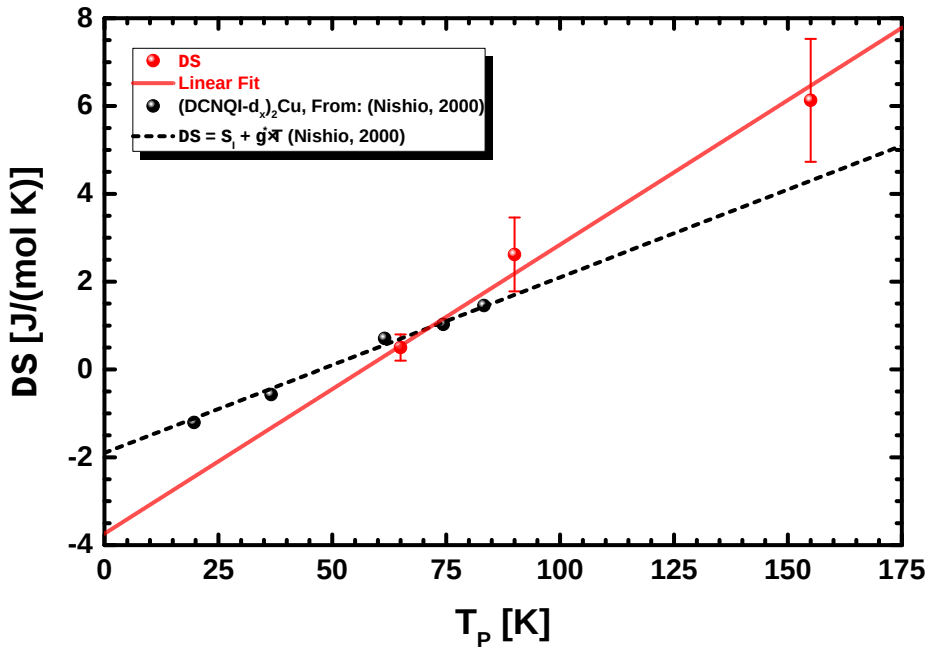


Figure 4.23: Entropy change at different phase transition temperatures. A roughly linear temperature dependence of $\Delta\Sigma$ is obtained. In spite of the large error due to the low data point density and the assumptions made on $\kappa$, the data is comparable to the linear relation published by Nishio *et al.* [34].

of $(DMe\text{-}DCNQI)_2Cu$. The Sommerfeld constant relates the electronic entropy in the metallic state linearly to the temperature. It was argued that an additional contribution $\gamma_{lat}$ from the lattice increases the effective $\gamma^* = \gamma_{el} + \gamma_{lat}$. Thus, the determined higher $\gamma^*$ of this study corroborates these findings. It should be pointed out that, in spite of the large uncertainty in $\gamma^*$ and in $S_I$, the magnitude of both quantities are closer to the values of $\gamma^* = 95\,\mathrm{mJ\,mol^{-1}\,K^{-2}}$ and $S_I = -3.5\,\mathrm{J\,mol^{-1}\,K^{-1}}$ determined by fitting the thermodynamic model of Eq. 2.35 to the phase diagram of $(DCNQI)_2Cu$ in Ch. 2.3.3.

The lattice degrees of freedom have also been proposed to explain the thermodynamics of the first-order metal-insulator transition in $VO_2$ (Vanadiumdioxide) [228]. Similarly to $(DCNQI)_2Cu$, the phase transition has been discussed in terms of an electronic Mott transition as well as a Peierls-driven lattice instability, i.e. both, the electronic and the phonon degrees of freedom drive the phase transition. In addition, the reported large entropy increase of $12.5\,\mathrm{J\,mol^{-1}\,K^{-1}}$ across the phase transition [228] amounts to a multiple of the value expected for the electronic contribution as well. Recently, a thorough experimental and theoretical determination of the phonon density of states in $VO_2$ revealed that lattice degrees of freedom account for up to two thirds of the entropy increase across the insulator-to-metal transition [84]. This has been explained by a pronounced, anharmonic lattice potential in the metallic state. The population density of low-energy phonons changes across the phase transition, leading to a significant contribution of vi-

brational entropy to the latent heat. Their amplitude scales with temperature due to the anharmonicity of the interatomic potential. By the shallow lattice potential in van-der-Waals bound organic crystals, anharmonic effects can be expected to play a key role in the thermodynamic description of the $(DCNQI)_2Cu$ phase diagram as well.

### 4.4.2 Determination of the Electronic Entropy

The above analysis of the entropy change across the Peierls transition considered two separate contributions, one from the lattice and one from the charge carriers. However, the interpretation relies on the electronic specific heat coefficient $\gamma_{el} = 25\,\mathrm{mJ\,mol^{-1}\,K^{-2}}$ measured at significantly lower temperatures than the phase transition temperatures at which $\gamma^*$ was determined. Furthermore, it was determined only for samples being metallic at very low temperature, such as undeuterated $(DCNQI\text{-}h_8)_2Cu$ [34]. In alloyed $(MeBr_x\text{-}DMe_{1-x}\text{-}DCNQI)_2Cu$ crystals a significant change in the electronic specific heat was observed upon alloying [229]. Hence, a determination of the mere electronic specific heat coefficient for each individual material at high temperatures is required to validate the proposed thermodynamic model.

Because both, electrons and phonons contribute to the specific heat, a direct separation of the two fractions is not a priori possible from the latent heat analysis. Yet, the analysis of the Seebeck coefficient might yield further evidence for the above interpretation of the entropy change. In Eq. 2.11b the Seebeck coefficient was defined as the heat carried per charge carrier. Utilizing the electronic specific heat per carrier given by Eq. 2.72, a Seebeck coefficient linear in temperature is anticipated

$$S_{el} = \frac{q}{e \cdot T} = \frac{c_{el} \cdot T}{e \cdot T} = \underbrace{\frac{\gamma_{el} \cdot \rho_{dens}}{e \cdot m_{mol} \cdot n}}_{P} \cdot T \quad , \tag{4.26}$$

$n$ being the charge carrier density, $m_{mol}$ the molar specific heat and $\rho_{dens}$ the density of the material. Thus, from the linear temperature coefficient $P$ of the thermopower in Eqs. 4.5 and 4.26, the electronic specific heat coefficient $\gamma_{el}$ can be obtained. The metallic charge carrier density $n_{met} = 2.94 \cdot 10^{21}\ \mathrm{cm^{-3}}$ is determined by the charge transfer to the DCNQI molecule and the crystal structure. The Seebeck coefficients measured for $(MeBr\text{-}DCNQI)_2Cu$, $(DCNQI\text{-}d_6)_2Cu$ and $(DCNQI\text{-}h_8/d_6)_2Cu$ [70:30] have been presented in Sec. 4.1.2 and are illustrated in Fig. 4.4b. Thus, the respective electronic specific heat coefficients $\gamma_{el}$ can be calculated by Eq. 4.26 from the fit parameters in Tab. 4.4 and are stated in Tab. 4.10.

All values of $\gamma_{el}$ determined in this way are substantially lower than both, $\gamma^* = (65.8 \pm 8.7)\,\mathrm{mJ\,mol^{-1}\,K^{-2}}$ obtained from the previous latent heat analysis and $\gamma^*_{Lit} =$

| | $P$ [$10^{-8}$ V K$^{-2}$] | $\gamma_{el}$ [mJ mol$^{-1}$ K$^{-2}$] |
|---|---|---|
| $(MeBr\text{-}DCNQI)_2Cu$ | -12.64 | 15.5 |
| $(DCNQI\text{-}d_6)_2Cu$ | -15.82 | 19.7 |
| $(DCNQI\text{-}h_8/d_6)_2Cu$ [70:30] | -10.37 | 12.7 |

Table 4.10: Electronic specific heat coefficients $\gamma_{el}$ determined from the linear term in Eq. 4.5 fitted to the temperature-dependent Seebeck coefficient in the metallic regime (compare Fig. 4.4b).

40 mJ mol$^{-1}$ K$^{-2}$ reported by Nishio *et al.* [34]. On the other hand, they are close to the Sommerfeld constant of 25 mJ mol$^{-1}$ K$^{-2}$, i.e. to the value of the electronic specific heat. The presented $\gamma_{el}$ data has been determined from the high-temperature side of the phase transition supplementing the values of $\gamma_{el,Lit}$ = 22-25 mJ mol$^{-1}$ K$^{-2}$ which were determined by low-temperature specific heat measurements on samples retaining their metallicity down to cryogenic temperatures [34]. Hence, this approach independently verifies the model of an electronic and phononic entropy change driving the phase transition.

### 4.4.3 Conclusions

In this section the change of entropy across the metal-insulator transition in $(DCNQI)_2Cu$ has been discussed. A detailed analysis of the latent heat at the first-order Peierls transition of three $(DCNQI)_2Cu$ compounds revealed an entropy change across the phase transition being large compared to the value expected from the neat electronic system. By separately determining the electronic specific heat coefficient from the Seebeck coefficient, it was possible to separate the electronic contribution from the overall entropy variation across the phase transition. The significantly lower electronic part implies an entropy contribution from other non-electronic degrees of freedom, such as the lattice. Hence, these results do not only provide further evidence for the metal-insulator transition being driven by electronic and lattice degrees of freedom in $(DCNQI)_2Cu$, as proposed by Nishio *et al.* [34], but also prove its applicability to an extended temperature regime beyond the Debye temperature of 82 K. This emphasizes the robustness of the phase transition toward higher temperatures. By the application of high (chemical or external) pressures, the phase transition can be shifted toward technologically relevant temperatures near RT [78]. The above results verify the underlying physics to remain the same. In this context, the $(DCNQI)_2Cu$ material system might gain technological relevance upon utilizing the external stimulation of the phase transition, e.g. by light or electrical pulses, in future devices, such as ultrafast optical switches or infrared sensors [12].

## 4.5 Thermoelectric Potential of $(DCNQI)_2Cu$

As outlined in Ch. 2.1.4, organic thermoelectrics based on conducting polymers have been of considerable scientific interest recently. In spite of their appreciable thermoelectric performance, the inherent disorder in polymers places restrictions on the charge carrier mobility and conductivity achievable, especially in real working devices operating over larger length scales on the order of mm. On the basis of the transport coefficients consistently determined for the $(DCNQI)_2Cu$ material system in the previous subchapters, the alternative class of low-dimensional molecular metals is evaluated with respect to its thermoelectric performance in this final part of the thesis. $(DCNQI)_2Cu$ combines the advantage of chemical variety and low-temperature processibility of conducting polymers with a high charge carrier mobility of about $2.3\,cm^2\,V^{-1}\,s^{-1}$ and a reduced electronic dimensionality. In addition, its low specific weight together with its thermodynamic stability is a good prerequisite for portable device manufacturing with long-term usage. Also, the large number of atoms per unit cell puts them on a list with other complex thermoelectric crystals, such as skutterudites and Zintl compounds, permitting large figure of merits in principle. In comparison to polymers the availability of both, high-performance p- and n-type organic conductors facilitates the construction of all-organic thermoelectric devices.

### 4.5.1 Thermoelectric Power Factor and Figure of Merit

In Fig. 4.24a the temperature-dependent transport quantities $\sigma$, $\kappa$ and $S$ interpolated from the measurement data presented in the previous subchapters are illustrated for $(DCNQI\text{-}h_8)_2Cu$. The derived power factor and figure of merit are shown in Fig. 4.24b.

$(DCNQI\text{-}h_8)_2Cu$ reveals a RT power factor of $PF(295\,K) = 110\,\mu W\,K^{-2}\,m^{-1}$ being of similar magnitude as values obtained for the conducting polymers PEDOT:Tos ($324\,\mu W\,K^{-2}\,m^{-1}$ [54]) and PEDOT:PSS ($469\,\mu W\,K^{-2}\,m^{-1}$ [33]). The figure of merit reaches a decent value of $zT = 0.02$ at RT, exceeding values of ordinary pure metals by about two orders of magnitude. For example, copper's thermoelectric figure of merit only amounts to $zT = 1.1 \times 10^{-4}$ at RT, assuming an electrical conductivity of $\sigma = 6 \times 10^7\,S\,m^{-1}$ [230], a thermal conductivity of $\kappa = 380\,W\,m^{-1}\,K^{-1}$ [230] and a Seebeck coefficient of $S = 1.6\,\mu V\,K^{-1}$ [164]. $(DCNQI\text{-}h_8)_2Cu$'s thermoelectric figure of merit falls short by an order of magnitude compared to conducting polymers by reason of the higher thermal conductivity. Values of $zT = 0.11$ [54] and $zT = 0.42$ [33] have been reported for PEDOT:Tos and PEDOT:PSS, respectively. The determined $\kappa = 1.73\,W\,m^{-1}\,K^{-1}$ is larger by about a factor of ten compared to the thermal conductivity of $\kappa_{pol} = 0.24\,W\,m^{-1}\,K^{-1}$

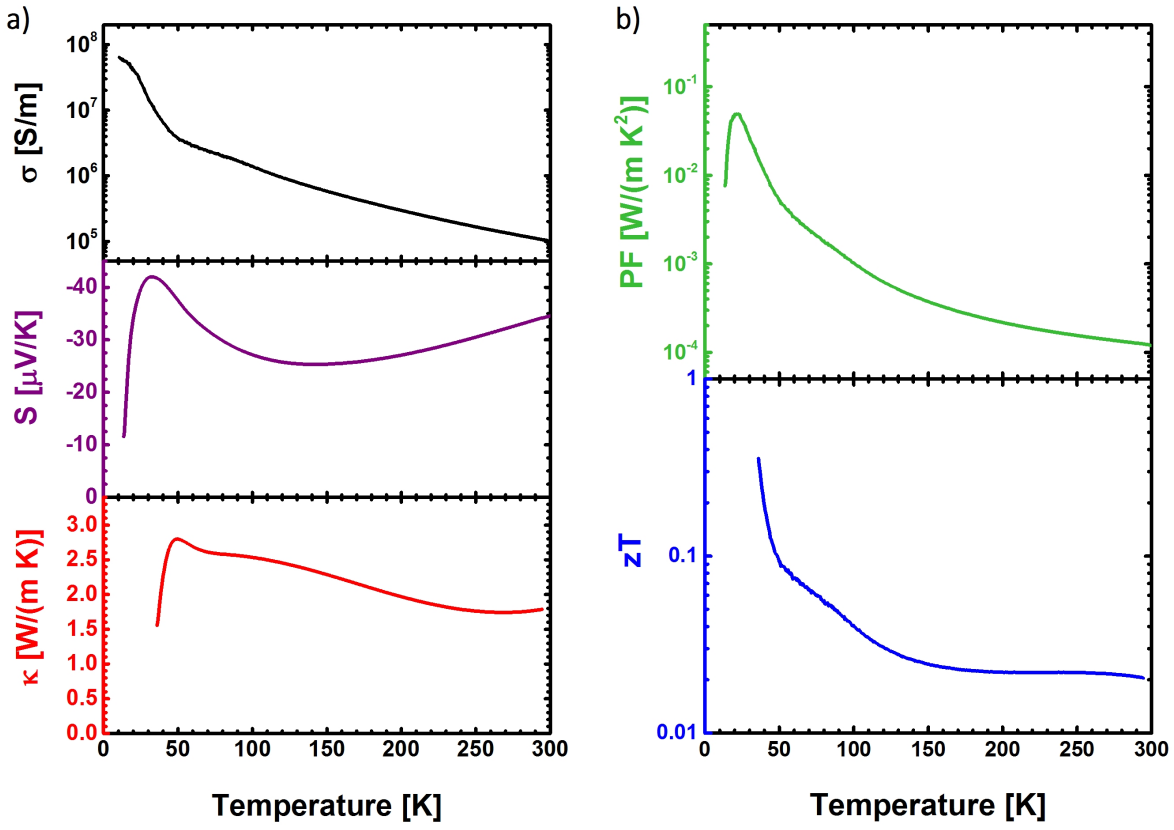


Figure 4.24: Thermoelectric properties of $(DCNQI\text{-}h_8)_2Cu$. (a) The electrical and thermal conductivity ($\sigma$ and $\kappa$) together with the Seebeck coefficient $S$, interpolated from the measurement data of the previous sections, result in (b) the temperature-dependent power factor $PF$ and thermoelectric figure of merit $zT$.

measured for PEDOT:PSS [33]. Yet, attention has to be paid when analyzing claimed zT values of polymers since their thermal conduction is usually measured along the out-of-plane direction of the film, i.e. along the normal of the substrate, while the electrical conductivity is measured in the plane of the layer. A recent more consistent study on suspended samples of PEDOT:PSS revealed in-plane thermal conductivity values of up to $\kappa_{pol} = 1.8\,\mathrm{W\,m^{-1}\,K^{-1}}$ [53]. Also, at RT only values of $zT \leq 0.005$ were obtained in this study. Electrical conductivity was also found to be very anisotropic and reduced by almost two orders of magnitude in the out-of-plane compared to the in-plane direction [231]. Reliable measurements on the figure of merit for chemical variations of the organic polymer PEDOT reach values between $0.01 \leq zT \leq 0.11$ [54]. According to this data, a competitive thermoelectric performance in comparison to conducting polymers can be ascribed to the low-dimensional organic conductor $(DCNQI\text{-}h_8)_2Cu$ at RT. Even more important, $(DCNQI\text{-}h_8)_2Cu$ is one of the best n-type organic thermoelectric materials [32, 232].

While not reaching the thermoelectric performance of $Bi_2Te_3$ yet, the latter representing the best RT thermoelectric material with $zT \gtrsim 1$ (compare Ch. 2.1.4) to date, the full

potential of (DCNQI-$h_8$)$_2$Cu becomes clear when looking at the temperature-dependent power factor and figure of merit. Above 100 K, both quantities remain rather constant enabling a wide applicable temperature regime for device operation. At temperatures below 100 K, a steep increase in the power factor is observed enabling power factors of $PF(30\,\mathrm{K}) \approx 50\,\mathrm{mW\,K^{-2}\,m^{-1}}$ which exceeds RT values by more than two orders of magnitude. Moreover, the power factor outperforms the values of nanstructured $YbAgCu_4$, marking the best thermoelectric material in this temperature regime to date, by a factor of 5 [233]. The high power factor in (DCNQI-$h_8$)$_2$Cu originates from the proposed phonon drag effect in the thermopower together with the anomalously high temperature dependence of the electrical conductivity. High mobilities are attainable in organic conductors at low temperature by freezing out the large number of phonon modes and thus their scattering with charge carriers, facilitating the large power factor. The additional breakdown of the WF law at low temperature empowers a figure of merit clearly exceeding values of $zT(< 40\,\mathrm{K}) \geq 0.15$ which surpass the highest value of $zT(42\,\mathrm{K}) = 0.11$ reported for $YbAgCu_4$ in the temperature regime below 77 K [233]. Hence, low-dimensional organic conductors represent an alternative class of thermoelectric materials for cryogenic applications, e.g. for Peltier cooling below the liquid nitrogen temperature of 77 K.

Low-weight cryocoolers of high reliability are also needed for space applications [234, 235]. Large temperature gradients of several hundred degrees can occur between the sun-faced and the eclipsed side of spacecrafts, the latter only experiencing heat transfer by radiation to the cosmic background at 3 K. This requires a highly efficient thermal management inside satellites at cryogenic temperatures [236]. Moreover, infrared sensors are used in space telescopes for mapping the cosmic background radiation in space telescopes or attached to satellites' surface for earth observation purposes [236]. These sensors need to be cooled or thermally stabilized for minimized noise levels. In spite of their appreciable cooling power, thermoelectric coolers have been of limited use so far due to their rather high operating temperatures [237]. Hence, new materials with decent low-temperature $zT$ values, like (DCNQI-$h_8$)$_2$Cu, might lead to further innovation in this field. The maximum temperature difference achievable by a Peltier cooler is given by [37]:

$$\Delta T = \frac{1}{2} z T_0^2 \tag{4.27}$$

Implying $T_0 = 35\,\mathrm{K}$ and $zT_0 = 0.15$ one obtains $\Delta T = 2.65\,\mathrm{K}$ for (DCNQI-$h_8$)$_2$Cu, a temperature range suitable for thermal stabilization of detectors. Thus, an eligible potential for thermoelectric applications can be anticipated for (DCNQI)$_2$Cu and other low-dimensional organic conductors.

### 4.5.2 The Effect of Li-Alloying

Virtually all thermoelectric materials are low-bandgap semiconductors or semimetals. The previous section demonstrated the outstanding thermoelectric potential of organic metals in the cryogenic temperature regime which was achieved by a stoichiometric single crystal without further optimization of the band filling. A tuned charge-carrier density via doping plays a key role in obtaining high power factors and thermoelectric figures of merit in semiconductors. In contrast, metals usually do not offer a wide range of control over the charge carrier density which is determined by the number of valence electrons of the atoms constituting the solid. Some control can be gained via alloying which on the downside will also create a significant amount of disorder, at least at high concentrations, and thereby, will reduce the mobility of charge carriers.

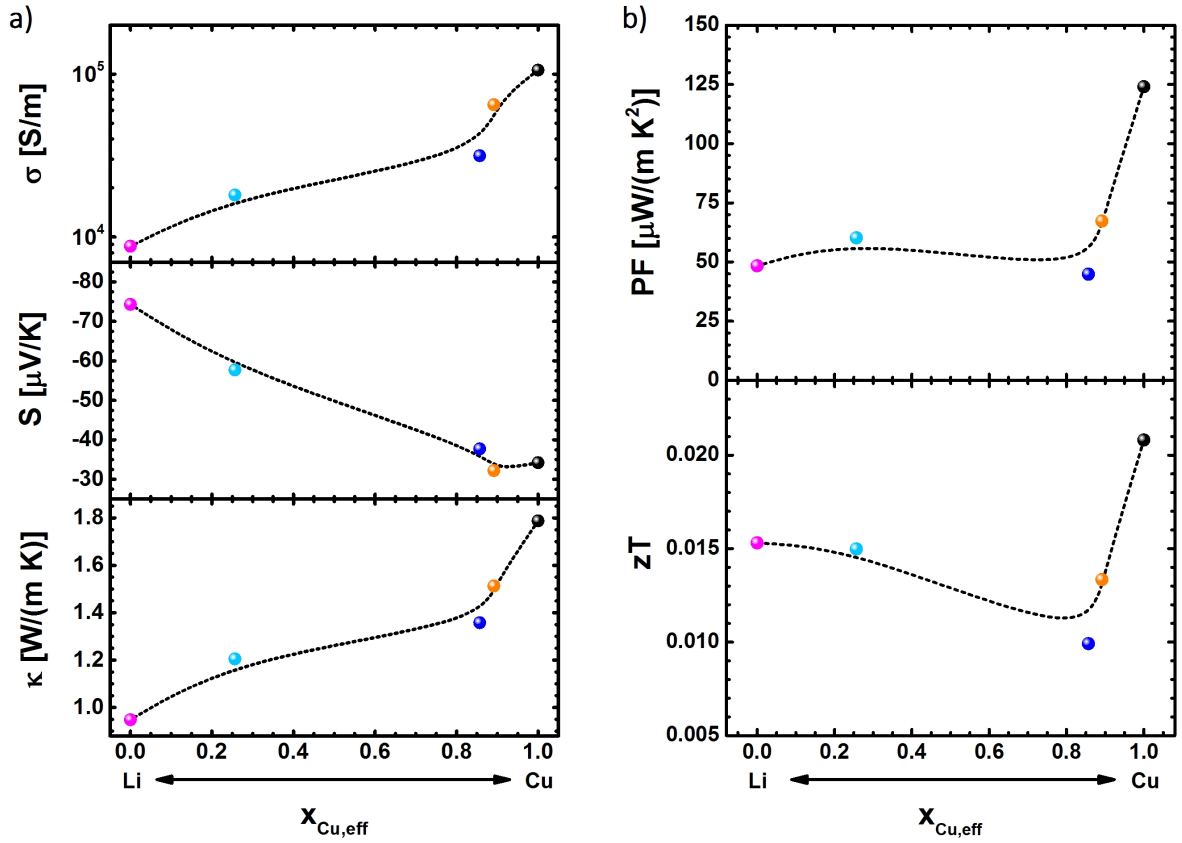


Figure 4.25: Thermoelectric properties of alloyed $(DMe\text{-}DCNQI)_2Cu_xLi_{1-x}$ crystals at RT. (a) Dependence of thermoelectric transport quantities $\sigma$, $S$ and $\kappa$ on the copper content at RT. (b) The derived thermoelectric power factor and figure of merit is also shown.

Organic metals may overcome these limitations. Conduction in quasi-1D radical ion salts usually takes place via states of energy bands formed by the LUMO (HOMO) of the acceptor (donor) molecule. The filling of these energy bands is governed by the charge

transfer process between the molecule and the counterion crystallizing in a separated stack from the molecules, the latter finally constituting the transport band. Thus, manipulations on the counterion may affect the charge carrier density while only minor influence on the orbital overlap, and hence the charge carrier mobility, in the molecular stack is expected. In the $(DCNQI)_2Cu_xLi_{1-x}$ system such a substitutional tuning is possible by alloying copper and lithium counterions because $(DCNQI)_2Cu$ and $(DCNQI)_2Li$ reveal similar crystal structures. This facilitates a continuous change of the band filling from 1/3 in $(DCNQI)_2Cu$ to 1/4 $(DCNQI)_2Li$. A reduction of overall band filling has been theoretically predicted to enhance the thermoelectric performance of the p-type organic conductor $TTT_2I_3$, exhibiting a quarter-filled one-dimensional band structure [126] (compare Ch. 2.5.2). Fig. 4.25 illustrates the thermoelectric properties of $(DMe\text{-}DCNQI)_2Cu_xLi_{1-x}$ at RT depending on the copper content.

While the reduction of the copper content increases the Seebeck coefficient $S$ and decreases the thermal conductivity $\kappa$, the diminution of electrical conductivity $\sigma$ by one order of magnitude impedes an improvement of the thermoelectric performance. This large drop in electrical conduction cannot solely be explained by the change in charge carrier density but points toward a variation in the scattering mechanism and its related length scale or in the electronic band structure. Hence, a slight distortion of the lattice when substituting Cu by Li might still occur. More importantly though, in $(DCNQI)_2Li$ electronic correlations are expected to gain impact by virtue of the quarter band filling and probably, reduce the charge-carrier mobility. Apparently, as shown in Sec. 4.1, the 3d copper hole states lacking in $(DCNQI)_2Li$ contribute more significantly to electrical transport in $(DCNQI)_2Cu$ than expected. As a result, neat $(DCNQI)_2Cu$ is the superior thermoelectric material at RT.

From the interpolated temperature-dependent experimental data on the transport properties, as shown in Fig. 4.26a, the power factor and the thermoelectric figure of merit have been evaluated. Fig. 4.26b discloses that $(DCNQI)_2Cu$ retains its superior thermoelectric performance over all alloyed systems under study in the entire temperature regime investigated, although the Li-rich $(DCNQI)_2Cu_xLi_{1-x}$ alloys ($x = 0$ and $x = 0.26$) come close to its $zT$ values between 150 K and 200 K. While this approach failed to improve the performance of this specific material combination, the continuous variation of thermoelectric properties by chemical doping has been demonstrated as a proof-of-concept and thus, might pave the way for the optimization of other organic conductors, such as $TTT_2I_3$.

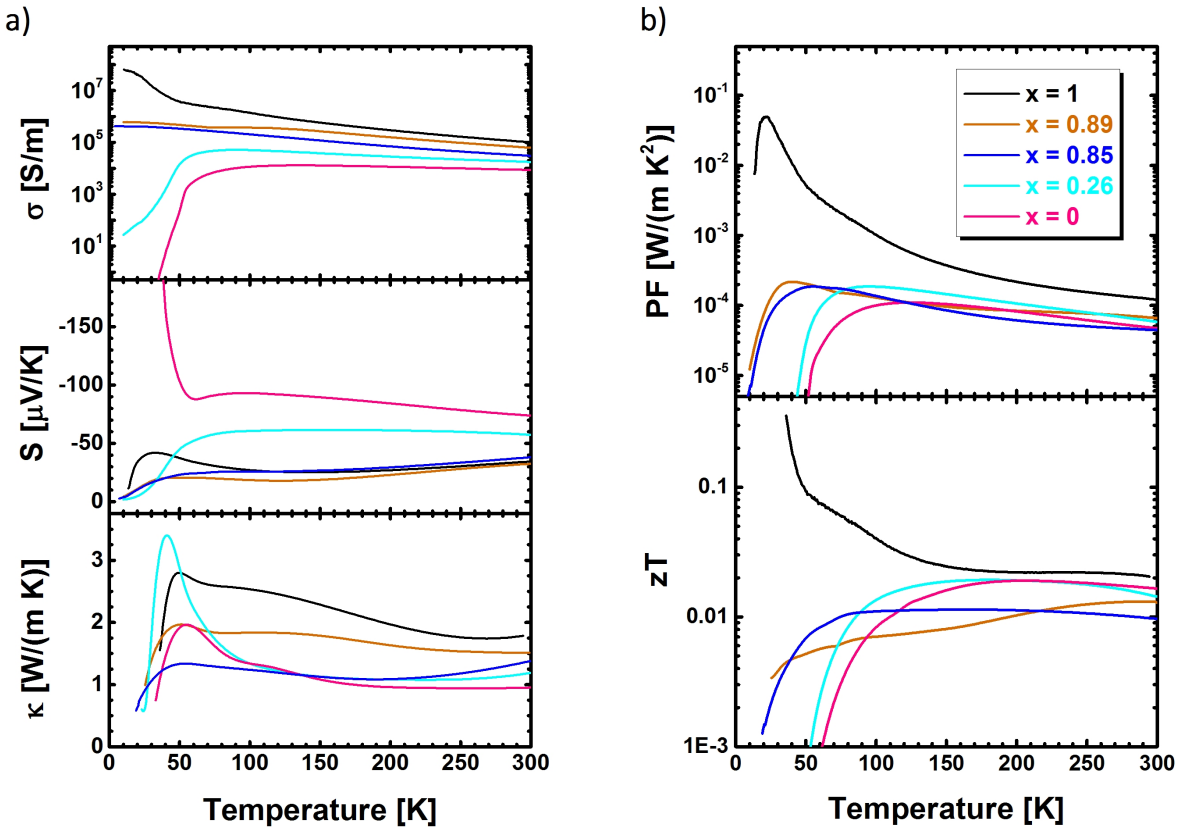


Figure 4.26: Temperature-dependent thermoelectric properties of alloyed $(DME\text{-}DCNQI)_2Cu_xLi_{1-x}$ crystals. (a) Dependence of thermoelectric transport quantities $\sigma$, $S$ and $\kappa$ on temperature (b) together with the derived thermoelectric power factor and figure of merit for various copper contents $x$.

### 4.5.3 Thermoelectric Properties across the CDW-Transition

Another promising aspect considering the thermoelectric potential of quasi-1D organic conductors is their reduced electronic dimensionality offering a manifold of different ground states. As extensively discussed in previous chapters, $(R_1,R_2\text{-}DCNQI)_2Cu$ salts undergo a Peierls metal-insulator transition depending on the functional groups $R_1$ and $R_2$ attached to the quinone ring. In $(MeBr\text{-}DCNQI)_2Cu$, the CDW transition occurs at a relatively high temperature of $T_P = 155\,K$ where the electrical conductivity drops by more than one order of magnitude. Fig. 4.27a depicts the interpolated transport properties of $(MeBr\text{-}DCNQI)_2Cu$ in the vicinity of the phase transition. In the shaded area, no meaningful determination of $\kappa$ was possible and the curve represents a simple spline interpolation between the data from below to above the phase transition. Also the Seebeck coefficient changes rapidly in this temperature regime and is prone to error. However, it is evident that the large drop in the electrical conductivity is accompanied by a significant increase in the Seebeck coefficient and a reduction of the thermal conductivity.

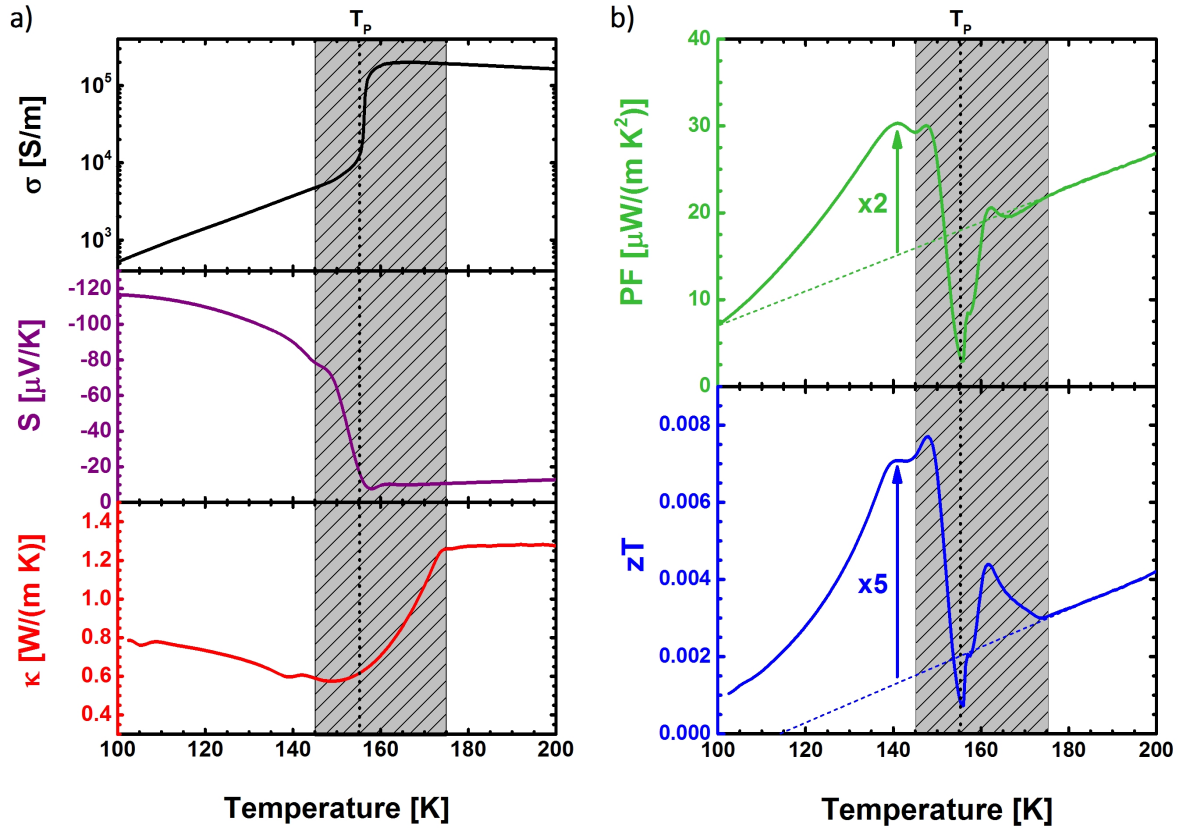


Figure 4.27: Thermoelectric properties in the vicinity of a Peierls transition. (a) Transport properties, (b) power factor and figure of merit in the vicinity of the CDW transition in (MeBr-DCNQI)$_2$Cu at $T_P = 155\,\mathrm{K}$.

Fig. 4.27b shows the evaluated thermoelectric power factor and figure of merit across the phase transition. Again, the shaded area is to be neglected for a detailed quantification of these properties. Furthermore, the inferior thermoelectric performance compared to (DCNQI-h$_8$)$_2$Cu shall be of minor importance as it is partly due to a slightly more impure MeBr-DCNQI starting material used in the crystal growth procedure [193]. The interesting aspect is the doubling of the power factor just below the phase transition compared to the value extrapolated from the metallic regime. The additional reduction of $\kappa$ boosts the $zT$ value even by a factor of five at 140 K. Hence, the exotic ground states observed in low-dimensional organic conductors provide additional means to improve the thermoelectric efficiency if occurring at sufficiently high temperature.

### 4.5.4 All-Organic Thermoelectric Generator

A distinct advantage of low-dimensional molecular metals over conducting polymers is the availability of n- and p-type conductors achieving comparable thermoelectric performance. This enables the fabrication of all-organic thermoelectric generators, a prototype of which

is displayed in Fig. 4.28a. It consists of a single junction made-up of $(DCNQI\text{-}h_8)_2Cu$ as n-type and $TTT_2I_3$ as p-type leg. The crystals were glued together by conducting graphite at the hot junction which was thermally connected to a heating block utilizing a copper wire. The temperature gradient across the copper wire was measured by means of an alumel-copper-alumel differential thermocouple to calculate the heat input and to estimate the efficiency. The opposite ends of the crystals were thermally anchored to a heat reservoir consisting of an alumina block and electrically contacted to measure the current-voltage characteristics for a given temperature gradient from which the power output curves are calculated.

The $(DCNQI\text{-}h_8)_2Cu$ crystals have been thoroughly characterized in this thesis providing a power factor of $PF = 110\,\mu W\,m^{-1}\,K^{-2}$ and a thermoelectric figure of merit of $zT = 0.02$. The dimensions of the n-type leg were 2 mm x 0.035 mm x 0.035 mm ($l$ x $w$ x $h$). The p-type $TTT_2I_3$ single crystals were grown and characterized by Alexander Steeger and details of its material properties will be presented in his forthcoming PhD thesis. The dimensions of the p-type leg were 1.75 mm x 0.12 mm x 0.009 mm ($l$ x $w$ x $h$). A $TTT_2I_3$ crystal from the same growth batch exhibited an electrical hole conductivity of $\sigma = 2.1 \times 10^5\,S\,m^{-1}$ and a Seebeck coefficient of $S = +42\,\mu V\,K^{-1}$ at RT, resulting in a power factor of $PF = 387\,\mu W\,m^{-1}\,K^{-2}$. The measured thermal conductivity of $\kappa = 3.7\,W\,m^{-1}\,K^{-1}$ yields a figure of merit amounting to $zT = 0.03$ at RT. This value is similar to $(DCNQI\text{-}h_8)_2Cu$ and leads to a combined thermoelectric figure of merit of about $zT_{comb} = 0.026$ according to Eq. 2.19.

Fig. 4.28b delineates the power output characteristics measured at various temperature differences between the two heating blocks. The output power is increasing with applied temperature gradient and a maximum value of 125 nW was measured for a single junction at a temperature difference of 92 K. It is intuitive to analyze the specific power output, i.e. the output power normalized on the cross section of both crystals which constitute the active area of the thermoelectic device. A high specific power output (per area) is crucial in the application of thermoelectric generators for waste heat recovery. It was shown that the costs-per-watt are largely determined by the power factor and the specific areal power output of thermoelectric generators [238]. Accordingly, a smaller $zT$ may even be tolerated in materials of low production costs revealing larger areal power outputs. Here, a value of $5\,mW\,cm^{-2}$ is reached. For comparison, thermoelectric devices built of conducting polymers reach specific power outputs of about $3\,\mu W\,cm^{-2}$ at $\Delta T = 30\,K$ being three orders of magnitude smaller [32]. Thus, the thermoelectric characteristics measured across macroscopic sample distances within this thesis may be more directly translated to thermoelectric devices in comparison to conducting polymers. In the latter, the thin films of only a few hundred nanometer thickness are unable to maintain an

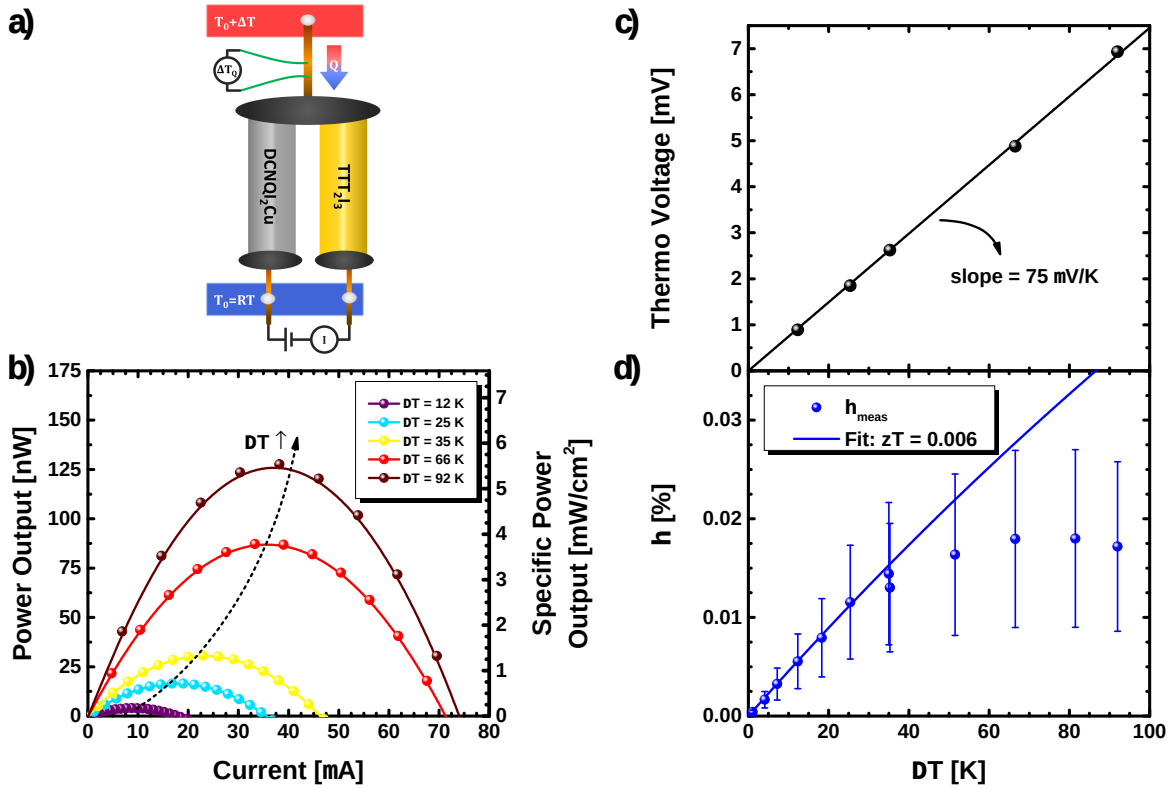


Figure 4.28: All-organic thermoelectric generator. (a) Scheme of the thermoelectric generator consisting of the organic conductors $TTT_2I_3$ and $(DCNQI\text{-}h_8)_2Cu$ as p- and n-type leg, respectively. (b) RT power output characteristic at various temperature differences applied. (c) The thermo voltage under open circuit conditions scales linearly with temperature gradient and the slope of 75 µV K$^{-1}$ corresponds to the added Seebeck coefficients of $(DCNQI)_2Cu$ and $TTT_2I_3$. (d) Measured efficiency for different temperature gradients at RT.

appreciable temperature gradient in thermoelectric generators. In the present device the thermo voltage measured under open circuit conditions at various temperature differences, as depicted in Fig. 4.28c, corresponds to the subtracted Seebeck coefficients

$$S = S_{TTT} - S_{DCNQI} \approx 76\,\mu\mathrm{V\,K^{-1}} \tag{4.28}$$

of $(DCNQI)_2Cu$ and $TTT_2I_3$. Hence, the thermal gradient drops mainly across the crystals rather than interfaces.

In Fig. 4.28d the conversion efficiency of the thermoelectric generator is plotted against the applied temperature difference. The efficiency of the generator increases with temperature gradient and saturates above $\Delta T \approx 60\,\mathrm{K}$ at about $\eta \approx 0.02\%$. This is due to a degredation of the organic thermoelectric generator above $\Delta T = 30\,\mathrm{K}$ which proved to be irreversible and also manifested itself in the slope of the measured current-voltage characteristics. The efficiency data below $\Delta T = 20\,\mathrm{K}$ was fitted to Eq. 2.17 yielding $zT \approx 0.006$. Though not reaching the theoretical combined figure of merit $zT_{comb} = 0.026$ yet, it is

of almost similar magnitude. The deviation is ascribed to an overall contact resistance which so far has been optimized to $R \approx 23\,\Omega$. For the manufacturing of efficient organic thermoelectric devices a distinct contact engineering, similar to the work done on organic transistors and light-emitting diodes [239], will be crucial in the future.

### 4.5.5 Conclusions

In this final part of the thesis, the thermoelectric application potential of the low-dimensional organic conductor $(DCNQI)_2Cu$ has been evaluated with respect to its power factor and its thermoelectric figure of merit. At RT, both quantities attain values comparable to conducting polymers which have recently gained interest in the thermoelectric community. Furthermore, $(DCNQI)_2Cu$ was demonstrated to be one of the best organic materials with respect to the n-type thermoelectric performance.

At cryogenic temperatures below 40 K, the thermoelectric figure of merit exceeds $zT \geq 0.15$ due to the anomalously high power factor of $PF(30\,\mathrm{K}) \approx 50\,\mathrm{mW\,K^{-2}\,m^{-1}}$. These unprecendented key figures even outperform the best inorganic thermoelectric material in this temperature regime. Different routes for further optimization of the thermoelectric performance have been outlined. A control over the metallic electron density has been achieved within a limited range via manipulation of the charge transfer between the neighboring molecular and counterion stacks in the crystal. Moreover, in $(MeBr\text{-}DCNQI)_2Cu$ the Peierls transition occurring at 155 K was found to double the power factor and to increase the $zT$ value by a factor of five. Finally, a prototypical all-organic thermoelectric generator was built by combining the n-type $(DCNQI)_2Cu$ conductor with the quasi-1D molecular metal $TTT_2I_3$ offering p-type conductivity. Its specific power output reached values of $5\,\mathrm{mW\,cm^{-2}}$ which, at least to my knowledge, is unattained in organic thermoelectric generators so far.

# Chapter 5

# Summary

This thesis aimed at the coherent investigation of the electrical and thermal transport properties of the low-dimensional organic conductor $(DCNQI)_2M$ (DCNQI: dicyanoquinonediimine; M: metallic counterion). These radical anion salts present a promising, new material class for thermoelectric applications and hence, a consistent characterization of the key parameters is required to evaluate and to optimize their performance. For this purpose, a novel experimental measurement setup enabling the determination of the electrical conductivity, the Seebeck coefficient and the thermal conductivity on a single crystalline specimen has been designed and implemented in this work. Here, the most important key results obtained in the course of my thesis are summarized.

**Electrothermal Characterization of Charge and Heat Transport**

The presented, new methodological approach builds upon the experimental setup developed by Chaikin and Kwak [163]. It enables the determination of the electrical conductivity and the Seebeck coefficient on fragile, rod-like organic single crystals of small diameter by their attachment to free-standing wires connected to two independent heat sources. This method was extended by an electrothermal technique on the basis of the self-heating $3\omega$ method to measure the thermal conductivity as well as the specific heat of the sample in the same contact arrangement [169, 166]. The thermal boundary conditions have been verified by finite-element simulations and the setup has been thoroughly characterized by a reference sample made of stainless steel. An overall measurement uncertainty of less than 10 % has been achieved for the thermal conductivity. The results are reproducible upon thermal cycling in contrast to the temperature-dependent, experimental data available on the thermal conductivity of organic conductors, hitherto [175, 174, 240]. Furthermore, the approach facilitated a correlated investigation of electrical and thermal transport properties, independently of the error introduced by the cross section of the sample. As such, the experimental setup established in this thesis allows for a systematic study of thermal transport properties of organic conductors with unprecedented accuracy.

### Electronic Properties of ($R_1$,$R_2$-DCNQI)$_2$M

The measured Seebeck coefficients and electrical resistivities reflect the low-dimensional electronic structure of DCNQI radical anion salts to a large extend. ($R_1$,$R_2$-DCNQI)$_2$Cu crystals are metallic at room temperature (RT) revealing electrical conductivities as high as $\sigma_{RT} = 1070\,\mathrm{S\,cm^{-1}}$ and a negative Seebeck coefficient of $S_{RT} = -34\,\mu\mathrm{V\,K^{-1}}$. As such, it represents the organic conducting material of highest n-type conductivity to-date. Depending on the functional groups attached to the DCNQI molecule, the Fermi surface may become unstable against the formation of a charge-density-wave (CDW) along with a periodic lattice distortion upon cooling. This transition is of first order as evidenced by the correlated discontinuous increases of the electrical resistivity and of the Seebeck coefficient. The electrical resistivity reveals an anomalously large temperature dependence following $\rho(T) = \rho_0 + A \cdot T^{2.3}$ which to some extent is caused by the large thermal contraction along the crystallographic axis of preferred electrical transport. Yet, hole-like charge carriers emerging from the quasi-3D electronic structure of (DCNQI)$_2$Cu have been demonstrated to gain importance at low temperatures as well and may partly account for the large temperature dependence of the resistivity, too. The Seebeck coefficient shows an anomalously large peak at about 35 K which can be explained by a phonon drag effect limited by phonon-phonon Umklapp scattering at high temperatures.
The increasing hole contribution to charge carrier conduction has been shown to emerge from a shift of the Fermi energy by an increased $3d_{xy}$-$\pi$-hybridization, sensitively depending on the tetrahedral coordination of the DCNQI molecules around the central copper atom in the crystal. This is in sharp contrast to the reference measurements done on (DCNQI)$_2$Li radical anion salts. Here, the hole contribution is absent due to the lack of 3d valence electrons in lithium, leading to a rather pure quasi-1D band structure. In this material electronic correlations come into play by virtue of the materials quarter band filling, as evidenced by the occurrence of a spin-Peierls transition as well as an almost temperature-independent Seebeck coefficient of about 59 to 80 $\mu\mathrm{V\,K^{-1}}$ for (DMe-DCNQI)$_2$Cu$_x$Li$_{1-x}$ salts with $x \leq 0.26$. In crystalline (DMe-DCNQI)$_2$Cu$_x$Li$_{1-x}$ alloys the electrical conductivity may be controlled over one order of magnitude while keeping the crystal structure conserved. Therefore, it facilitates to contrast the thermoelectric transport properties of an anisotropic, quasi-3D organic conductor with a quasi-1D organic metal revealing electronic correlations.

### Nonlinear Conduction in the Peierls Insulating State of (DCNQI)$_2$Cu

The deuterated (DCNQI-$d_6$)$_2$Cu radical anion salt exhibits a CDW insulating ground state below $T_P = 82\,\mathrm{K}$ which is accompanied by a Mott transition along the copper chain of the lattice. Like many other low-dimensional organic conductors of other ground states, it

reveals nonlinear conduction characteristics below the phase transition temperature. The electrothermal model was proposed by Mori *et al.* to explain the universal occurrence of nonlinear conduction in materials of quite distinct ground states [143]. Its key parameter is the effective specific heat. By reason of its magnitude, it is commonly identified as electronic specific heat and therefore, the nonlinear conduction effects are believed to originate from correlated electronic states, such as solitons or CDWs. In this work, the temperature dependence of the effective specific heat has been determined for the first time by a transient analysis of the nonlinear resistivity at high electric fields. As a result, the effective specific heat has been clearly attributed to the phonon system and hence, the nonlinear conductivity is thermally driven. A non-equilibrium population of distinct optical phonon modes at an energy of about 19 meV is deduced which amounts to about half of the charge carrier activation energy in this temperature regime. Therefore, the universal nonlinear conduction in $(DCNQI)_2Cu$ is demonstrated to be caused by efficient interaction of charge carriers with optical phonons which provide an energy reservoir for additional charge carrier excitation. This advanced electrothermal model is expected to be valid also for other low-dimensional organic conductors, explaining the universal nonlinear conduction effects by the efficient interaction of charge carriers with low-energy optical phonon modes inherent to this material class. The results of this section have been published in *Physical Review B* **92**, 155107 (2015) [177].

### Heat Conduction in $(DCNQI)_2M$

The novel measurement setup brought to operation within this thesis enabled a thorough investigation of the thermal transport properties in the $(DCNQI)_2M$ system. The thermal conductivity of $(DCNQI\text{-}h_8)_2Cu$ at RT was determined to $\kappa = 1.73\,\mathrm{W\,m^{-1}\,K^{-1}}$. By reducing of the copper content in isostructural, crystalline $(DMe\text{-}DCNQI)_2Cu_xLi_{1-x}$ alloys, the electrical conductivity has been lowered by one order of magnitude and the correlated changes in the thermal conductivity allowed for a verification of the Wiedemann-Franz (WF) law at RT. A room temperature Lorenz number of $L = (2.48 \pm 0.45) \times 10^{-8}\,\mathrm{W\,\Omega\,K^{-2}}$ was obtained in agreement with the standard Lorenz number $L_0 = 2.44 \times 10^{-8}\,\mathrm{W\,\Omega\,K^{-2}}$ for 3D bulk metals. This value appears to be significantly reduced upon cooling below RT, even far above the Debye temperature of $\theta_D \approx 82\,\mathrm{K}$, below which a breakdown of the WF law is caused by different relaxation times in response to thermal and to electric field perturbations. While the violation of the WF law may be partly ascribed to a composition-dependent Lorenz number caused by the different dimensionality of $(DCNQI)_2Li$ versus $(DCNQI)_2Cu$, a similar temperature dependence of $L$ was extracted from the reduction of the thermal conductivity accompanying the sudden increase in the electrical resistivity across the CDW transition of three ($R_1$,$R_2$-

DCNQI)$_2$Cu compounds. Therefore, the WF law in its conventional form seems to be violated far above the Debye temperature in low-dimensional organic conductors and a more elaborate theoretical approach to take into account the distinct band structure and degree of electronic correlation is needed. The presented combination of electrical and thermal conductivity data, measured on the same specimen in the same geometry, presents the most accurate investigation of the Wiedemann-Franz law for low-dimensional organic conductors, to date. It also enabled an investigation of the lattice thermal conductivity in the (DCNQI)$_2$M system. The heat carried by acoustic phonons is limited by phonon-phonon Umklapp scattering above 50 K, similar to the phonon drag effect observed in the thermopower. However, the heat carried by optical phonons rises almost linearly with temperature and accounts for up to two-thirds of the lattice heat capacity at RT. In this sense, a transition from coherent heat conduction by acoustic phonons to incoherent optical phonon transport can be anticipated at some intermediate temperature.

**Thermodynamic Investigation on the Phase Transition in (DCNQI)$_2$Cu**

The change of thermal properties across the CDW phase transition in (DCNQI)$_2$Cu also provides the means to study the thermodynamic model of the phase diagram proposed by Nishio *et al.* [34]. They explained the phase diagram by the competing spin, charge and lattice degrees of freedom, causing an entropy difference between the insulating and the metallic ground state of (DCNQI)$_2$Cu. Similar to their approach, this entropy difference was deduced from the latent heat in the vicinity of the phase transition, obeying a linear temperature dependence of $\Delta\Sigma = -S_I + \gamma^* \cdot T_P$ . The obtained value for $\gamma^* \approx 66\,\mathrm{mJ\,mol^{-1}\,K^{-1}}$ is large compared to the electronic specific heat coefficient determining the electronic contribution to entropy. This suggests a second, non-electronic contribution to the entropy in the metallic state, presumably by the lattice. This interpretation was corroborated by determining the pure electronic part of the entropy in the metallic state from the thermopower measurements to $\gamma_{el} \approx 13 - 20\,\mathrm{mJ\,mol^{-1}\,K^{-2}}$ in various (DCNQI)$_2$Cu compounds. Therefore, the independent determination of the electronic entropy substantiates the conclusions drawn by Nishio *et al.* [34]. By virtue of the large Peierls transition temperature of $T_P = 155\,\mathrm{K}$ for (MeBr-DCNQI)$_2$Cu, the presented data extends the validity of the thermodynamic model for above the Debye temperature. Hence, even upon chemically tuning the DCNQI molecule to allow for higher CDW transition temperatures, the underlying physics remain the same.

**Thermoelectric Potential of (DCNQI)$_2$Cu**

The above mentioned experimental data enabled the first consistent evaluation of the thermoelectric performance of (DCNQI)$_2$Cu. The RT power factor of $110\,\mu\mathrm{W\,K^{-2}\,m^{-1}}$ is

comparable to values obtained on PEDOT-based thermoelectric polymers [54]. The RT figure of merit amounts to $zT = 0.02$ which falls short by a factor of ten compared to the best values of $zT = 0.42$ claimed for conducting polymers [33]. It originates from the larger thermal conductivity in the organic crystals of about $1.73\,\mathrm{W\,m^{-1}\,K^{-1}}$ in $(DCNQI)_2Cu$. Yet, more elaborate studies on the anisotropy of the thermal conductivity in PEDOT polymers assume their figure of merit to be $zT = 0.15$ at most, recently [54]. Therefore, $(DCNQI)_2Cu$ can be regarded as thermoelectric material of similar performance to polymer-based ones. Moreover, it represents one of the best organic n-type thermoelectric materials to date and as such, may also become important in hybrid thermoelectrics in combination with conducting polymers [32, 232].

Upon cooling below room temperature, $(DCNQI)_2Cu$ reveals its full potential attaining power factors of $50\,\mathrm{mW\,K^{-2}\,m^{-1}}$ and exceeding values of $zT > 0.15$ below 40 K. These values represent the best thermoelectric performance in this low-temperature regime for organic as well as inorganic compounds and thus, low-dimensional organic conductors might pave the way toward new applications in cryogenic thermoelectrics. Further improvements may be expected from optimizing the charge carrier concentration by taking control over the CT process via the counterion stack of the crystal lattice. The concept has also been demonstrated in this work. Moreover, the thermoelectric performance in the vicinity of the CDW transition in $(MeBr\text{-}DCNQI)_2Cu$ was found to be increased by a factor of 5. Accordingly, the diversity of electronic ground states accessible in organic conductors provides scope for further improvements. Finally, the prototype of an all-organic thermoelectric generator has been built in combination with the p-type organic metal $TTT_2I_3$. While it only converts about 0.02% of the provided heat into electrical energy, the specific power output per active area attains values of up to $5\,\mathrm{mW\,cm^{-2}}$. This power output, defining the cost-limiting factor in the recovery of waste heat [238], is three orders of magnitude larger than in conducting polymer devices and as such, unrivaled in organic thermoelectrics [32]. While the thermoelectric key parameters of $(DCNQI)_2Cu$ still lack behind conventional thermoelectrics made of e.g. $Bi_2Te_3$, the promising performance together with its potential for improvements make this novel material class an interesting candidate for further exploration. Particularly, the low-cost and energy-efficient synthesis routes of organic materials highlight their relevance for technological applications. The results on the thermoelectric performance of $(DCNQI)_2Cu$ and $TTT_2I_3$ are going to be published in *Advanced Materials* (2017, accepted) soon.

# Kapitel 6

# Zusammenfassung

Ziel der vorliegenden Arbeit war die umfassende Untersuchung der elektrischen und thermischen Transportgrößen von quasi-eindimensionalen, leitfähigen Radikalanionensalzen basierend auf dem Dicyanochinondiimin-Molekül (DCNQI). Diese kristallinen $(DCNQI)_2M$ (M: Metallion) Verbindungen stellen eine vielversprechende, neuartige Materialklasse für thermoelektrische Anwendungen dar, weshalb eine konsistente Charakterisierung der thermoelektrischen Kenngrößen von großem wissenschaftlichen Interesse ist. Dafür wurde in dieser Arbeit ein neuer experimenteller Aufbau entwickelt und in Betrieb genommen, der die Messung der elektrischen und thermischen Leitfähigkeit sowie des Seebeck-Koeffizienten an einer einzigen Kristallprobe ermöglicht. Die sich daraus ergebenden, zentralen Ergebnisse dieser Dissertation werden im Folgenden kurz zusammengefasst.

**Elektrothermische Charakterisierung des Ladungs- und Wärmetransports**

Die experimentelle Charakterisierung der thermoelektrischen Kenngrößen in organischen Metallen basiert auf einem Messaufbau, der von Chaikin und Kwak zur Messung des Seebeck-Koeffizienten sowie der elektrischen Leitfähigkeit nadelförmiger Einkristalle vorgeschlagen wurde [163]. Zur Vermeidung thermisch induzierter mechanischer Spannungen werden die dünnen, fragilen Proben an freistehenden Drähten in Vierpunkt-Geometrie kontaktiert und zur Bestimmung der Thermokraft an ihren jeweils gegenüberliegenden Seiten an ein Wärmereservoir gekoppelt. Dieser Ansatz wurde durch die elektrothermische Bestimmung der Wärmeleitfähigkeit mittels der $3\omega$ Methode erweitert. Hierbei wird der Kristall mittels eines periodischen, elektrischen Stroms geheizt und die Temperaturoszillation innerhalb der Probe anhand des Spannungsabfalls gemessen, woraus die Wärmeleitfähigkeit ermittelt werden kann [169, 166]. Die Einhaltung der für die Analyse erforderlichen thermischen Randbedingungen wurde anhand von Finite-Elemente-Simulationen verifiziert. Der Messaufbau wurde eingehend an einer nadelförmigen Referenzprobe aus Edelstahl kalibriert und für die bestimmte Wärmeleitfähigkeit konnte eine Messunsicherheit von weniger als 10% verlässlich bestätigt werden. Der Aufbau erlaubt zudem eine Messung der temperaturabhängigen Wärmeleitfähigkeit in organischen Metallen, wobei besonders die im Vergleich zu Literaturdaten hohe Reproduzierbarkeit der Messergebnisse

bei wiederholtem Abkühlen und Aufheizen der Probe hervorzuheben ist [175, 174, 240]. Außerdem wird durch die Messung an einer einzigen Probe mit definierten Dimensionen eine bisher unerreichte Genauigkeit in der Korrelation von elektronischen und thermischen Transportgrößen ermöglicht.

### Elektronische Eigenschaften von ($R_1$,$R_2$-DCNQI)$_2$M-Kristallen

Die gemessenen Seebeck-Koeffizienten und elektrischen Leitfähigkeiten bilden die niederdimensionale, elektronische Bandstruktur von DCNQI Radikalanionensalzen ab. ($R_1$,$R_2$-DCNQI)$_2$Cu Kristalle zeigen bei Raumtemperatur (RT) metallisches Verhalten mit einer elektrischen Leitfähigkeit von bis zu $\sigma_{RT} = 1070\,\mathrm{S\,cm^{-1}}$ und einer negativen Thermokraft von $S_{RT} = -34\,\mu\mathrm{V\,K^{-1}}$. Sie sind damit bis heute das organische Material mit der höchsten Elektronenleitfähigkeit. Je nach funktioneller Gruppe, die am DCNQI Molekül gebunden ist, kann die Fermi-Fläche bei Abkühlung instabil gegenüber der Ausbildung einer Ladungsdichtewelle werden. Diese geht mit einer periodischen Verzerrung des Kristallgitters sowie einem Metall-Isolator Phasenübergang, auch Peierls-Übergang genannt, einher. Die unstetige Erhöhung des elektrischen Widerstands sowie des Seebeck-Koeffizienten zeigt, dass es sich dabei um einen Phasenübergang erster Ordnung handelt.

Im metallischen Bereich weist der spezifische Wiederstand eine ausgeprägte Temperaturabhängigkeit der Form $\rho(T) = \rho_0 + A \cdot T^{2.3}$ auf, welche sich zum Teil auf die starke thermisch induzierte Kontraktion des Kristallgitter zurückführen lässt, jedoch auch auf einen zusätzlichen Leitungsbeitrag durch Löcher aufgrund der komplexen quasi-dreidimensionalen Bandstruktur von (DCNQI)$_2$Cu hindeutet. Die erhöhte Thermokraft bei tiefen Temperaturen von 35 K konnte mit einem Phonon-Drag Modell erklärt werden, dessen Beitrag bei höheren Temperaturen durch Phonon-Phonon Umklappstreuung begrenzt wird.

Ein mit sinkender Temperatur erhöhter Beitrag der Lochleitung konnte durch eine Verschiebung der Fermi-Energie in Abhängigkeit der quasi-tetraedischen Anordnung der DCNQI Moleküle um das zentrale Kupferatom innerhalb der Kristallstruktur und der daraus resultierenden Beeinflussung der $3d_{xy}$-$\pi$-Hybridisierung zwischen den Kupfer- und den LUMO-Orbitalen des Moleküls erklärt werden. Letztere ist abhängig von der Temperatur sowie den funktionellen Gruppen am DCNQI Molekül. In Referenzmessungen an nahezu strukturgleichen (DCNQI)$_2$Li Kristallen war diese starke Abhängigkeit aufgrund der nicht besetzen 3d-Orbitale in Lithium nicht vorhanden, was auf eine deutlich eindimensionalere, elektronische Struktur dieses Materials schließen lässt. Aufgrund dieser Eindimensionalität sowie des bis zu einem Viertel gefüllten Leitungsbandes spielt in dieser Verbindung wiederum die elektronische Korrelation der Ladungsträger eine deutlich größere Rolle. Diese zeigt sich beispielsweise im Auftreten eines Spin-Peierls-Übergangs

sowie in einem nahezu temperaturunabhängigen Seebeck-Koeffizienten oberhalb von 70 K. In isostrukturellen, kristallinen $(DCNQI)_2Cu_xLi_{1-x}$ Mischkristallen kann daher nicht nur die Leitfähigkeit über eine Größenordnung hinweg manipuliert, sondern ebenfalls die Dimensionalität der Bandstruktur sowie die elektronische Korrelation der Ladungsträger kontrolliert eingestellt und damit deren Einfluss auf die thermoelektrischen Kenngrößen untersucht werden.

**Nichtlineare Leitfähigkeitseffekte im Peierls-Grundzustand von $(DCNQI)_2Cu$**

Die deuterierten $(DCNQI\text{-}d_6)_2Cu$ Radikalanionensalze bilden unterhalb von $T_P = 82\,K$ eine Ladungsdichtewelle aus, welche mit einem Mott-Übergang der auf den Kupferatomen lokalisierten Ladungsträger einhergeht. Wie viele andere niederdimensionale, organische Leiter zeigt das Material unterhalb des Phasenübergangs ab einer gewissen Feldstärke nichtlineare, elektrische Leitfähigkeitseffekte. Das universelle Auftreten einer nichtlinearen Leitfähigkeit in organischen Materialien mit unterschiedlichen Grundzuständen wurde von Mori *et al.* mittels eines elektrothermischen Modells erklärt [143]. Die charakteristische Größe des Modells ist die effektive spezifische Wärme, deren Werte Aufschluss über die mikroskopischen Ursachen der nichtlinearen Leitfähigkeit liefern können. Aufgrund ihrer geringen Größe wird dem nichtlinearen Transportverhalten meist ein elektronischer Ursprung zugewiesen, z.B. die korrelierten, elektronischen Zustände wie Ladungsdichtewellen oder Solitonen in diesen Materialien. Das Temperaturverhalten der effektiven spezifischen Wärme wurde bisher zur eindeutigen Identifizierung ihres mikroskopischen Ursprungs jedoch nicht bestimmt. In dieser Arbeit konnte die Temperaturabhängigkeit dieser charakteristischen Größe zum ersten Mal durch eine transiente Analyse des nichtlinearen Transports bei hohen elektrischen Feldstärken ermittelt werden. Hierdurch konnte sie eindeutig einem phononischen und somit thermischen Ursprung in Form einer Nichtgleichgewichts-Population von optischen Phononenmoden mit Energien von etwa 19 meV zugeordnet werden. Dies entspricht der halben Aktivierungsenergie von Ladungsträgern im Peierls-isolierenden Zustand von $(DCNQI\text{-}d_6)_2Cu$. Das Auftreten der nichtlinearen Leitfähigkeit wird daher durch eine starke Wechselwirkung von Ladungsträgern mit diesen optischen Phononen bei hohen Feldstärken verursacht, welche ein Wärmereservoir für die Anregung zusätzlicher Ladungsträger bilden. Dieses erweiterte elektrothermische Modell kann möglicherweise auch die Universalität der nichtlinearen Transportphänomene in organischen Materialien mit unterschiedlichen Grundzuständen durch die Wechselwirkung von Ladungsträgern mit spezifischen, niederenergetischen optischen Phononen erklären. Die Ergebnisse zur nichtlinearen Leitfähigkeit in $(DCNQI)_2Cu$ wurden in *Physical Review B* **92**, 155107 (2015) publiziert [177].

### Wärmeleitung in $(DCNQI)_2M$

Der neu etablierte Messaufbau ermöglichte eine grundlegende Untersuchung der Wärmeleitfähigkeit in der $(DCNQI)_2M$ Materialklasse, wobei für $(DCNQI\text{-}h_8)_2Cu$ ein Raumtemperaturwert von $\kappa_{RT} = 1.73\,W\,m^{-1}\,K^{-1}$ ermittelt werden konnte. Durch eine Variation des Kupferanteils in $(DMe\text{-}DCNQI)_2Cu_xLi_{1-x}$ Mischkristallen konnte die elektrische Leitfähigkeit über eine Größenordnung variiert und die korrelierten Änderungen der Wärmeleitfähigkeit studiert werden. Dies erlaubte eine Bestätigung des Wiedemann-Franz (WF) Gesetzes bei RT mit einer Lorenzzahl von $L = (2.48 \pm 0.45) \times 10^{-8}\,W\,\Omega\,K^{-2}$, welche im Rahmen des Fehlers der nach dem Sommerfeld-Modell erwarteten Lorenzzahl von $L_0 = 2.44 \times 10^{-8}\,W\,\Omega\,K^{-2}$ für dreidimensionale Metalle entspricht. Unterhalb von RT ist das Wiedemann-Franz Gesetz in seiner etablierten Form jedoch nicht mehr erfüllt und unterschiedliche Relaxationszeiten für thermische und elektrische Störungen der elektronischen Fermi-Verteilung treten bereits weit oberhalb der Debye Temperatur von $\theta_D \approx 82\,K$ auf. Zudem scheint die Lorenzzahl auch von der detaillierten Bandstruktur der $(DMe\text{-}DCNQI)_2Cu_xLi_{1-x}$ Mischkristalle abhängig zu sein, deren Dimensionalität sich mit dem Kupferanteil ändert. Jedoch wurde ein Verstoß gegen das WF Gesetz unterhalb von RT auch an den Phasenübergängen von quasi-dreidimensionalen $(R_1,R_2\text{-}DCNQI)_2Cu$ Kristallen nachgewiesen. Hier wurden die korrelierten Sprünge der elektrischen und der thermischen Leitfähigkeit über den Metall-Isolator-Übergang verfolgt, um daraus die Lorenzzahl zu bestimmen. Daher ist das Wiedemann-Franz Gesetz in den hier untersuchten niederdimensionalen, organischen Metallen in seiner gewöhnlichen Form nicht erfüllt. Dies verlangt nach einer genaueren theoretischen Beschreibung, welche beispielsweise die Effekte der elektronischen Korrelation auf die Ladungsträgerstreuung sowie die Bandstruktur mit einbezieht.

Es ist hervorzuheben, dass die hier präsentierte Untersuchung der elektrischen und thermischen Leitfähigkeit die detailliertesten und zuverlässigsten Daten zum WF Gesetz in organischen Metallen liefert. Die Messergebnisse erlaubten zudem eine Separation der beiden phononischen Beiträge zur Wärmeleitung im $(DCNQI)_2M$ Materialsystem. Die von akustischen Phononen transportierte Wärme steigt mit sinkender Temperatur und wird oberhalb der Debye Temperatur durch die Phonon-Phonon Umklappstreuung limitiert, ähnlich wie der Phonon-Drag Beitrag zur Thermokraft. An der Wärmeleitung des Kristallgitters sind jedoch auch optische Phononen beteiligt, deren Anteil etwa linear mit der Temperatur ansteigt und bei RT etwa zwei Drittel der Wärme transportiert. Dies kann als Übergang von einem vorwiegend kohärenten Wärmetransport durch akustische Phononen zu einem inkohärenten Hüpftransport durch optische Phononen bei endlichen Temperaturen gedeutet werden.

### Thermodynamische Untersuchungen des Phasenübergangs in $(DCNQI)_2Cu$

Die Analyse der thermischen Eigenschaften erlaubt ebenfalls eine thermodynamische Untersuchung des Phasendiagramms, in Analogie zu der Studie von Nishio *et al.* [34], in der das Auftreten des Metall-Isolator Übergangs durch die Spin- und Ladungsfreiheitsgrade des elektronischen Systems sowie einer zusätzlichen Gitterentropie erklärt wurde. Diesem experimentellen Ansatz folgend wurde die Entropiedifferenz zwischen dem isolierenden und metallischen Zustand aus der latenten Wärme am Phasenübergang für drei repräsentative $(DCNQI)_2Cu$ Salze bestimmt.

Dabei weist die Entropiedifferenz zwischen metallischer und isolierender Phase eine lineare Abhängigkeit gemäß $\Delta\Sigma = -S_I + \gamma^* \cdot T_P$ von der Phasenübergangstemperatur $T_P$ auf. Die Proportionalitätskonstante $\gamma^* \approx 66\,\mathrm{mJ\,mol^{-1}\,K^{-1}}$ ist deutlich größer als die Sommerfeld-Konstante der spezifischen Wärme und deutet auf einen weiteren, nicht-elektronischen Beitrag zur Entropieänderung am Peierls-Phasenübergang in den $(DCNQI)_2Cu$ Kristallen hin, welcher vermutlich auf das Gitter zurückzuführen ist. Diese Schlussfolgerung wurde durch eine Abschätzung des rein elektronischen Beitrags zur Entropie im metallischen Grundzustand auf $\gamma_{el} \approx 13 - 20\,\mathrm{mJ\,mol^{-1}\,K^{-2}}$, d.h. $\gamma_{el} < \gamma^*$, untermauert, welcher aus dem Seebeck-Koeffizienten für die drei $(DCNQI)_2Cu$ Salze bestimmt wurde. Die in dieser Arbeit gezeigte korrelierte Untersuchung der Entropiedifferenz der Grundzustände und des elektronischen Entropieanteils der metallischen Phase bestätigt daher die thermodynamische Betrachtung des Phasenübergangs basierend auf den Gitter-, Spin- und Ladungsfreiheitsgraden nach Nishio *et al.* [34]. Außerdem konnte die Gültigkeit des thermodynamischen Modells durch die Analyse des Phasenübergangs von $(MeBr\text{-}DCNQI)_2Cu$ bei $T_P = 155\,\mathrm{K}$ auf Temperaturen oberhalb der Debye Temperatur von $(DCNQI)_2Cu$ erweitert werden. Die physikalischen Ursachen des Phasenübergangs bleiben daher auch bei hohen Temperaturen gleich, sodass eine hydrostatische oder chemische Verschiebung der Phasenübergangstemperaturen in einen technologisch nutzbaren Bereich möglich erscheint. Dies könnte sich beispielsweise für ultraschnelle Fotodetektoren als nützlich erweisen.

### Thermoelektrisches Anwendungspotential von $(DCNQI)_2Cu$

Die in dieser Arbeit gewonnenen, experimentellen Daten erlauben zum ersten Mal eine konsistente Evaluierung der thermoelektrischen Kenngrößen von $(DCNQI)_2Cu$ Radikalanionensalzen. Ein thermoelektrischer Leistungsfaktor von $110\,\mathrm{\mu W\,K^{-2}\,m^{-1}}$ konnte bei RT nachgewiesen werden, welcher vergleichbar mit den zur Zeit besten organischen Thermoelektrika basierend auf dem lochleitenden Polymer PEDOT ist [33]. Die thermoelektrische Gütezahl erreicht bei RT einen Wert von $zT = 0.02$, welcher aufgrund der höheren Wärmeleitfähigkeit von $1.73\,\mathrm{W\,m^{-1}\,K^{-1}}$ in $(DCNQI)_2Cu$ etwa eine Größenordnung

schlechter ist als die höchste, publizierte Gütezahl für PEDOT:PSS [33]. Literaturwerte für leitfähige Polymere sind jedoch häufig aufgrund der Anisotropie der Transportgrößen überschätzt, wenn die thermoelektrischen Kenngrößen nicht in einer einheitlichen Probenrichtung gemessen werden [54]. Daher kann die thermoelektrische Leistungsfähigkeit von $(DCNQI)_2Cu$ zumindest als vergleichbar betrachtet werden. Hinzu kommt, dass $(DCNQI)_2Cu$ eines der besten organischen Thermoelektrika mit negativen Majoritätsladungsträgern ist und deshalb für thermoelektrische Hybridgeneratoren in Kombination mit lochleitenden Polymeren Bedeutung besitzt [32, 232]. Unterhalb von Raumtemperatur zeigen $(DCNQI)_2Cu$ Kristalle ihr großes thermoelektrisches Anwendungspotential mit Leistungsfaktoren von bis zu $50\,\mathrm{mW\,K^{-2}\,m^{-1}}$ und Gütezahlen größer als $zT > 0.15$ unterhalb von 40 K. Nach aktuellem Kenntnisstand stellen diese Werte einen Rekord im Niedrigtemperaturbereich dar, sodass niederdimensionale organische Metalle hier neue thermoelektrische Anwendungsfelder bei kryogenen Temperaturen erschließen könnten. Eine weitere Optimierung der thermoelektrischen Kenngrößen sollte durch gezielte Einstellung der Ladungsträgerdichte erreicht werden können, beispielsweise durch die Kontrolle des Ladungstransfers von den Gegenionen auf das organische Molekül. Die Gültigkeit dieses Konzepts wurde in der vorliegenden Arbeit ebenfalls demonstriert. Zusätzlich konnte eine Verfünffachung der thermoelektrischen Gütezahl in der Nähe des Peierls-Phasenübergangs von $(MeBr\text{-}DCNQI)_2Cu$ gezeigt werden. Die diversen elektronischen Grundzustände in organischen Metallen stellen daher einen weiteren Ansatz zur Verbesserung der thermoelektrischen Leistungsfähigkeit dieser Materialklasse dar.

Abschließend wurde ein Prototyp eines organischen, thermoelektrischen Generators aus einer Kombination von elektronenleitendem, einkristallinen $(DCNQI)_2Cu$ und dem niederdimensionalen, lochleitenden, organischen Metall $TTT_2I_3$ hergestellt. Obwohl der aktuelle, nicht-optimierte Generator nur 0.02% der eingespeisten Wärme in elektrische Energie umwandeln konnte, erreichte seine auf die aktive Fläche normierte Leistung bereits Werte von $5\,\mathrm{mW\,cm^{-2}}$. Diese übertreffen die Kenndaten vergleichbarer thermoelektrischer Generatoren basierend auf leitfähigen Polymeren um drei Größenordnungen [32], wobei zu beachten ist, dass dieser Parameter einen großen Teil der Kosten in der thermoelektrischen Abwärmenutzung bestimmt [238]. Trotz der noch nicht erreichten Leistungsmerkmale von konventionellen thermoelektrischen Generatoren basierend auf $Bi_2Te_3$ verdeutlichen die Ergebnisse für $(DCNQI)_2Cu$ dennoch das hohe Potential organischer Metalle für die thermoelektrische Materialforschung, besonders unter Berücksichtigung der kostengünstigen und weniger energieintensiven Herstellung dieser Materialien in Hinblick auf technologische Anwendungen. Die Ergebnisse zur thermoelektrischen Leistungsfähigkeit von $(DCNQI)_2Cu$ und $TTT_2I_3$ werden in naher Zukunft in *Advanced Materials* (2017, akzeptiert) veröffentlicht.

# Bibliography


[1] J. Bardeen, L. Cooper, and J. Schrieffer. Microscopic theory of superconductivity. *Physical Review*, 106(1):162–164, April 1957.

[2] W. Little. Possibility of synthesizing an organic superconductor. *Physical Review*, 134(6A):A1416–A1424, June 1964.

[3] L. Coleman, M. Cohen, D. Sandman, F. Yamagishi, A. Garito, and A. Heeger. Superconducting fluctuations and the peierls instability in an organic solid. *Solid State Communications*, 12(11):1125–1132, June 1973.

[4] P. Grant, R. Greene, G. Wrighton, and G. Castro. Temperature dependence of the near-infrared optical properties of tetrathiofulvalinium tetracyanoquinodimethane (TTF-TCNQ). *Physical Review Letters*, 31(21):1311–1314, November 1973.

[5] R. Peierls. *More Surprises in Theoretical Physics*. Princeton University Press, Princeton, 1991.

[6] D. Jérome and H. Schulz. Organic conductors and superconductors. *Advances in Physics*, 31(4):299–490, July 1982.

[7] N. Toyota, M. Lang, and J. Müller. *Low-dimensional molecular metals*. Springer-Verlag Berlin Heidelberg, Berlin, 2007.

[8] A. Aumüller and S. Hünig. One-step entry to N-Cyanimines and to N,N'-Dicyanoquinonediimines, a novel class of electron-acceptors. *Angewandte Chemie International*, 23(6):447–448, June 1984.

[9] A. Aumüller, P. Erk, G. Klebe, S. Hünig, J. U. von Schütz, and H. P. Werner. A radical anion salt of 2,5-Dimethyl-N,N'-Dicyanoquinonediimine with extremely high electrical conductivity. *Angewandte Chemie International Edition in English*, 25(8):740–741, August 1986.

[10] R. Kato, S. Aonuma, and H. Sawa. Selectively deuterated molecular conductor (DMe-DCNQI)$_2$Cu - phase diagram and dimensionality. *Synthetic Metals*, 70(1-3):1071–1074, March 1995.

[11] J.-P. Farges, editor. *Organic Conductors: Fundamentals and Applications*. Marcel, New York, 1994.

[12] F. O. Karutz, J. U. von Schütz, H. Wachtel, and H. C. Wolf. Optically reversed peierls transition in crystals of Cu(Dicyanoquinonediimine)$_2$. *Physical Review Letters*, 81(1):140–143, July 1998.

[13] Y. Tokura, H. Okamoto, T. Koda, T. Mitani, and G. Saito. Nonlinear electric transport and switching phenomenon in the mixed-stack charge-transfer crystal tetrathiafulvalene-p-chloranil. *Physical Review B*, 38(3):2215–2219, July 1988.

[14] R. Rommel, B. Hartmann, J. Brandenburg, J. A. Schlueter, and J. Müller. Nonlinear electronic transport in the anomalous metallic state of quasi-2D organic superconductors $\kappa$-(BEDT-TTF)$_2$X. *Physica Status Solidi (B)*, 250(3):568–574, March 2013.

[15] T. Inada, I. Terasaki, H. Mori, and T. Mori. Giant nonlinear conduction from inhomogeneous charge order in rapidly cooled $\theta$-(BEDT-TTF)$_2$RbZn(SCN)$_4$. *Physical Review B*, 79(16):165102, April 2009.

[16] T. Ivek, B. Korin-Hamzić, O. Milat, S. Tomić, C. Clauss, N. Drichko, D. Schweitzer, and M. Dressel. Collective excitations in the charge-ordered phase of $\alpha$-(BEDT-TTF)$_2$I$_3$. *Physical Review Letters*, 104(20):206406, May 2010.

[17] R. Kumai, Y. Okimoto, and Y. Tokura. Current-induced insulator-metal transition and pattern formation in an organic charge-transfer complex. *Science*, 284(5420):1645–1647, June 1999.

[18] H. Wakita, T. Ozawa, Y. Bando, and T. Mori. Nonlinear conductivity in dicyanoquinonediimine complexes. *Journal of the Physical Society of Japan*, 79(9):094703, August 2010.

[19] F. Sawano, I. Terasaki, H. Mori, T. Mori, M. Watanabe, N. Ikeda, Y. Nogami, and Y. Noda. An organic thyristor. *Nature*, 437(7058):522–4, September 2005.

[20] T. Mori and T. Kawamoto. Organic conductors - from fundamentals to nonlinear conductivity. *Annual Reports Section C (Physical Chemistry)*, 103:134, March 2007.

[21] R. Weitz, A. Walter, R. Engl, R. Sezi, and C. Dehm. New charge-transfer salts for reversible resistive memory switching. *Nano Letters*, 6(12):2810–2813, November 2006.

[22] H. M. Yamamoto, Y. Kawasugi, H. Ito, T. Fukunaga, T. Suzuki, K. Tsukagoshi, and R. Kato. Conduction properties of micro-crystals of 2,5-dimethyl-N,N'-dicyanoquinonediimine metal (metal=Ag, Cu) complexes on $SiO_2$/Si substrates. *Solid State Sciences*, 10(12):1757–1761, December 2008.

[23] A. Casian, Z. Dashevsky, H. Scherrer, V. Dusciac, and R. Dusciac. A possibility to realize a high thermoelectric figure of merit in quasi-one-dimensional organic crystals. In *Proceedings ICT'03. 22nd International Conference on Thermoelectrics (IEEE Cat. No.03TH8726)*, pages 330–335. IEEE, August 2003.

[24] J. Wüsten and K. Potje-Kamloth. Organic thermogenerators for energy autarkic systems on flexible substrates. *Journal of Physics D: Applied Physics*, 41(13):135113, July 2008.

[25] A. Casian and I. Sanduleac. Thermoelectric properties of tetrathiotetracene iodide crystals: Modeling and experiment. *Journal of Electronic Materials*, 43(10):3740–3745, October 2014.

[26] L. E. Bell. Cooling, heating, generating power, and recovering waste heat with thermoelectric systems. *Science*, 321(5895):1457–1461, September 2008.

[27] C. Forman, I. K. Muritala, R. Pardemann, and B. Meyer. Estimating the global waste heat potential. *Renewable and Sustainable Energy Reviews*, 57:1568–1579, May 2016.

[28] S. LeBlanc, S. K. Yee, M. L. Scullin, C. Dames, and K. E. Goodson. Material and manufacturing cost considerations for thermoelectrics. *Renewable and Sustainable Energy Reviews*, 32:313–327, April 2014.

[29] O. Bubnova, Z. U. Khan, A. Malti, S. Braun, M. Fahlman, M. Berggren, and X. Crispin. Optimization of the thermoelectric figure of merit in the conducting polymer poly(3,4-ethylenedioxythiophene). *Nature Materials*, 10(6):429–33, June 2011.

[30] O. Bubnova, Z. U. Khan, H. Wang, S. Braun, D. R. Evans, M. Fabretto, P. Hojati-Talemi, D. Dagnelund, J.-B. Arlin, Y. H. Geerts, S. Desbief, D. W. Breiby, J. W. Andreasen, R. Lazzaroni, W. M. Chen, I. Zozoulenko, M. Fahlman, P. J. Murphy, M. Berggren, and X. Crispin. Semi-metallic polymers. *Nature Materials*, 13(2):190–4, February 2014.

[31] C. Cho, K. L. Wallace, P. Tzeng, J.-H. Hsu, C. Yu, and J. C. Grunlan. Outstanding low temperature thermoelectric power factor from completely organic thin films enabled by multidimensional conjugated nanomaterials. *Advanced Energy Materials*, 6(7):1502168, January 2016.

[32] Y. Sun, P. Sheng, C. Di, F. Jiao, W. Xu, D. Qiu, and D. Zhu. Organic thermoelectric materials and devices based on p- and n-type poly(metal 1,1,2,2-ethenetetrathiolate)s. *Advanced Materials*, 24(7):932–937, February 2012.

[33] G.-H. Kim, L. Shao, K. Zhang, and K. P. Pipe. Engineered doping of organic semiconductors for enhanced thermoelectric efficiency. *Nature Materials*, 12(8):719–23, August 2013.

[34] Y. Nishio, M. Tamura, K. Kajita, S. Aonuma, H. Sawa, R. Kato, and H. Kobayashi. Thermodynamical study of $(DMe\text{-}DCNQI)_2Cu$ system - mechanism of reentrant metal-insulator transition. *Journal of the Physical Society Japan*, 69(5):1414–1422, 2000.

[35] T. J. Seebeck. Ueber die magnetische Polarisation der Metalle und Erze durch Temperaturdifferenz. *Annalen der Physik*, 82(3):253–286, 1826.

[36] J. Peltier. Nouvelles expériences sur la caloricité des courants électriques. *Annales de Chimie et de Physique*, 56:371–386, 1834.

[37] H. Goldsmid. *Introduction to Thermoelectricity*, volume 121 of *Springer Series in Material Science*. Springer Verlag Berlin Heidelberg, 2nd edition, 2010.

[38] W. Thomson. On a mechanical theory of thermo-electric currents. *Proceedings of the Royal Society of Edinburgh*, 3:91–98, January 1851.

[39] K. Behnia. *Fundamentals of Thermoelectricity*. Oxford University Press, Oxford, 2015.

[40] H. B. Callen. The application of Onsager's reciprocal relations to thermoelectric, thermomagnetic, and galvanomagnetic effects. *Physical Review*, 73(11):1349–1358, June 1948.

[41] P. M. Chaikin. An introduction to thermopower for those who might want to use it to study organic conductors and superconductors. In *Organic Superconductivity*, pages 101–115. Springer Science+Business Media, New York, 1990.

[42] G. J. Snyder and E. S. Toberer. Complex thermoelectric materials. *Nature Materials*, 7(2):105–114, February 2008.

[43] A. Shakouri. Recent developments in semiconductor thermoelectric physics and materials. *Annual Review of Materials Research*, 41(1):399–431, August 2011.

[44] R. Venkatasubramanian, E. Siivola, T. Colpitts, and B. O'Quinn. Thin-film thermoelectric devices with high room-temperature figures of merit. *Nature*, 413(6856):597–602, October 2001.

[45] B. Poudel, Q. Hao, Y. Ma, Y. Lan, A. Minnich, B. Yu, X. Yan, D. Wang, A. Muto, D. Vashaee, X. Chen, J. Liu, M. S. Dresselhaus, G. Chen, and Z. Ren. High-thermoelectric performance of nanostructured bismuth antimony telluride bulk alloys. *Science*, 320(5876):634–8, May 2008.

[46] L. Hicks and M. Dresselhaus. Thermoelectric figure of merit of a one-dimensional conductor. *Physical Review B*, 47(24):16631–16634, June 1993.

[47] A. Garg, D. Rasch, E. Shimshoni, and A. Rosch. Large violation of the Wiedemann-Franz law in Luttinger liquids. *Physical Review Letters*, 103(9):096402, August 2009.

[48] N. Stojanovic, D. H. S. Maithripala, J. M. Berg, and M. Holtz. Thermal conductivity in metallic nanostructures at high temperature: Electrons, phonons, and the Wiedemann-Franz law. *Physical Review B*, 82(7):075418, August 2010.

[49] A. Casian. Violation of the Wiedemann-Franz law in quasi-one-dimensional organic crystals. *Physical Review B*, 81(15):155415, April 2010.

[50] J. Vavro, M. C. Llaguno, J. E. Fischer, S. Ramesh, R. K. Saini, L. M. Ericson, V. A. Davis, R. H. Hauge, M. Pasquali, and R. E. Smalley. Thermoelectric power of p-doped single-wall carbon nanotubes and the role of phonon drag. *Physical Review Letters*, 90(6):065503, February 2003.

[51] S. M. Kauzlarich, S. R. Brown, and G. J. Snyder. Zintl phases for thermoelectric devices. *Dalton Transactions*, (21):2099–107, June 2007.

[52] X. Shi, J. Yang, L. Wu, J. R. Salvador, C. Zhang, W. L. Villaire, D. Haddad, J. Yang, Y. Zhu, and Q. Li. Band structure engineering and thermoelectric properties of charge-compensated filled skutterudites. *Scientific Reports*, 5:14641, October 2015.

[53] A. Weathers, Z. U. Khan, R. Brooke, D. Evans, M. T. Pettes, J. W. Andreasen, X. Crispin, and L. Shi. Significant electronic thermal transport in the conducting polymer poly(3,4-ethylenedioxythiophene). *Advanced Materials*, 27(12):2101–2106, March 2015.

[54] Z. U. Khan, J. Edberg, M. M. Hamedi, R. Gabrielsson, H. Granberg, L. Wågberg, I. Engquist, M. Berggren, and X. Crispin. Thermoelectric polymers and their elastic aerogels. *Advanced Materials*, 28(22):4556–4562, June 2016.

[55] G. Grüner. *Density Waves in Solids*. Perseus Publishing, Cambridge, Massachusetts, 2000.

[56] R. Peierls. *Quantum Theory of Solids*. Oxford University Press, New York, 1955.

[57] G. Grüner. The dynamics of charge-density waves. *Reviews of Modern Physics*, 60(4):1129–1181, October 1988.

[58] M. Schwoerer and H. C. Wolf. *Organic Molecular Solids*. Wiley-VCH, Weinheim, 2007.

[59] S. Kagoshima, H. Nagasawa, and T. Sambongi. *One-Dimensional Conductors*, volume 72 of *Springer Series in Solid-State Sciences*. Springer Verlag Berlin Heidelberg, 1988.

[60] J. H. de Boer and E. J. Verwey. Semi-conductors with partially and with completely filled 3d-lattice bands. *Proceedings of the Physical Society*, 49(4S):59, August 1937.

[61] N. F. Mott and R. Peierls. Discussion of the paper by de Boer and Verwey. *Proceedings of the Physical Society*, 49(4S):72–73, August 1937.

[62] J. Hubbard. Electron correlations in narrow energy bands. *Proceedings of the Royal Society A: Mathematical, Physical and Engineering Sciences*, 276(1365):238–257, November 1963.

[63] H. Seo, C. Hotta, and H. Fukuyama. Toward systematic understanding of diversity of electronic properties in low-dimensional molecular solids. *Chemical Reviews*, 104(11):5005–5036, October 2004.

[64] B. Hilti and C. W. Mayer. Electrical properties of the organic metallic compound bis (tetrathiotetracene)-triiodide, $(TTT)_2I_3$. *Helvetica Chimica Acta*, 61(1):501–511, January 1978.

[65] F. Hüwe. Growth and characterization of radical anion salt single crystals. Master's thesis, Julius-Maximilian-University Würzburg, 2012.

[66] K. Sinzger, S. Hünig, M. Jopp, D. Bauer, W. Bietsch, J. U. von Schütz, H. C. Wolf, R. K. Kremer, and T. Metzenthin. The organic metal $(Me_2\text{-}DCNQI)_2Cu$: Dramatic changes in solid-state properties and crystal structure due to secondary deuterium effects. *Journal of the American Chemical Society*, 115(17):7696–7705, August 1993.

[67] T. Miyazaki and K. Terakura. First-principles theoretical study of metallic states of DCNQI-(Cu,Ag,Li) systems. *Physical Review B*, 54(15):10452–10464, October 1996.

[68] A. Kobayashi, R. Kato, H. Kobayashi, T. Mori, and H. Inokuchi. The organic $\pi$-electron metal system with interaction through mixed-valence metal cation: Electronic and structural properties of radical salts of dicyano-quinodiimine, (DMe-DCNQI)$_2$Cu and (MeCl-DCNQI)$_2$Cu. *Solid State Communications*, 64(1):45–51, October 1987.

[69] J. Sugar and A. Musgrove. Energy levels of copper, Cu I through Cu XXIX. *Journal of Physical and Chemical Reference Data*, 19(3):527, May 1990.

[70] P. Erk, H. Meixner, T. Metzenthin, S. Hünig, U. Langohr, J. U. von Schütz, H.-P. Werner, H. C. Wolf, R. Burkert, H. W. Helberg, and G. Schaumburg. A guidance for stable metallic conductivity in copper salts of N,N'-dicyanobenzoquinonediimines (DCNQIs). *Advanced Materials*, 3(6):311–315, June 1991.

[71] R. Kato, H. Kobayashi, and A. Kobayashi. Crystal and electronic structures of conductive anion-radical salts, (2,5-$R_1R_2$-DCNQI)$_2$Cu (DCNQI = N,N'-dicyanoquinonediimine; $R_1$, $R_2$ = $CH_3$, $CH_3O$, Cl, Br). *Journal of the American Chemical Society*, 111(14):5224–5232, July 1989.

[72] S. Hünig and P. Erk. DCNQIs - new electron acceptors for charge-transfer complexes and highly conducting radical anion salts. *Advanced Materials*, 3(5):225–236, May 1991.

[73] C. G. Garton. Charge transfer from metal to dielectric by contact potential. *Journal of Physics D: Applied Physics*, 7(13):1814–1823, September 1974.

[74] W. Brütting, editor. *Physics of Organic Semiconductors*. Wiley-VCH, Weinheim, 2005.

[75] A. J. Heeger, S. Kivelson, J. R. Schrieffer, and W. P. Su. Solitons in conducting polymers. *Reviews of Modern Physics*, 60(3):781–850, July 1988.

[76] H. Kobayashi, A. Miyamoto, R. Kato, F. Sakai, A. Kobayashi, Y. Yamakita, Y. Furukawa, M. Tasumi, and T. Watanabe. Mixed valency of Cu, electron-mass enhancement, and three-dimensional arrangement of magnetic sites in the organic conductors ($R_1$, $R_2$-N,N'-dicyanoquinonediimine)$_2$Cu (where $R_1$, $R_2$ = $CH_3$, $CH_3O$,Cl,Br). *Physical Review B*, 47(7):3500–3510, February 1993.

[77] S. Uji, T. Terashima, H. Aoki, J. Brooks, R. Kato, H. Sawa, S. Aonuma, M. Tamura, and M. Kinoshita. Coexistence of one- and three-dimensional fermi surfaces and heavy cyclotron mass in the molecular conductor (DMe-DCNQI)$_2$Cu. *Physical Review B*, 50(21):15597–15601, December 1994.

[78] R. Kato. Conductive copper salts of 2,5-Disubstituted N,N'-Dicyanobenzoquinonediimines (DCNQIs): Structural and physical properties. *Bulletin of the Chemical Society of Japan*, 73(3):515–534, 2000.

[79] T. Yamamoto, H. Tajima, J.-I. Yamaura, S. Aonuma, and R. Kato. Reflectance spectra and electrical resistivity of $(Me_2\text{-DCNQI})_2Li_{1-x}Cu_x$. *Journal of the Physical Society of Japan*, 68(4):1384–1391, 1999.

[80] M. Tamura, H. Sawa, S. Aonuma, R. Kato, M. Kinoshita, and H. Kobayashi. Weak ferromagnetism and magnetic anisotropy in cu salt of fully deuterated DMe-DCNQI, $(DMe\text{-}DCNQI\text{-}d_8)_2Cu$. *Journal of the Physical Society of Japan*, 62(5):1470–1473, 1993.

[81] D. Gómez, J. U. von Schütz, H. C. Wolf, and S. Hünig. Tunable phase transitions in conductive $Cu(2,5\text{-Dimethyl-Dicyanoquinonediimine})_2$ radical ion salts. *Journal de Physique I*, 6(12):1655–1671, 1996.

[82] O. Akaki, A. Chainani, T. Takahashi, Y. Kashimura, and R. Kato. Temperature-dependent core-level x-ray photoemission spectroscopy of the organic conductors $(MeCl\text{-}DCNQI)_2Cu$, $(MeBr\text{-}DCNQI)_2Cu$, and $(DI\text{-}DCNQI)_2Cu$. *Physical Review B*, 57(19):11846–11849, May 1998.

[83] H. Kobayashi, R. Kato, A. Kobayashi, T. Mori, and H. Inokuchi. The first molecular metals with ordered spin structures, $R_2R_2\text{-}DCNQI_2Cu$ ($R_1$, $R_2$ = $CH_3$, $CH_3O$, Cl, Br) with Jahn-Teller distortion, CDW instability and antiferromagnetic spin ordering. *Solid State Communications*, 65(11):1351–1354, March 1988.

[84] J. D. Budai, J. Hong, M. E. Manley, E. D. Specht, C. W. Li, J. Z. Tischler, D. L. Abernathy, A. H. Said, B. M. Leu, L. A. Boatner, R. J. Mcqueeney, and O. Delaire. Metallization of vanadium dioxide driven by large phonon entropy. *Nature*, 515(7528):535–539, November 2014.

[85] T. Mori, H. Inokuchi, A. Kobayashi, R. Kato, and H. Kobayashi. Electrical conductivity, thermoelectric power, and ESR of a new family of molecular conductors, dicyanoquinonediimine-metal $[(DCNQI)_2M]$ compounds. *Physical Review B*, 38(9):5913, September 1988.

[86] S. Mazumdar and A. Bloch. Systematic trends in short-range coulomb effects among nearly one-dimensional organic conductors. *Physical Review Letters*, 50(3):207–211, January 1983.

[87] R. Moret, P. Erk, S. Hünig, and J. U. von Schütz. X-ray scattering evidence for dimerization ($4k_F$) and spin-peierls distortion ($2k_F$) in silver salts of dicyanoquinodiimine (2,5 MR-DCNQI)$_2$Ag (R = $CH_3$, Cl or Br, M = $CH_3$). *Journal de Physique*, 49(11):1925–1931, November 1988.

[88] Y. Nakazawa, A. Sato, M. Seki, K. Saito, K.-i. Hiraki, T. Takahashi, K. Kanoda, and M. Sorai. Spin-peierls transition of the quasi-one-dimensional electronic system (DMe-DCNQI)$_2$M (M=Li,Ag) probed by heat capacity. *Physical Review B*, 68(8):1–8, August 2003.

[89] K.-I. Hiraki and K. Kanoda. Ground states of DCNQI-metal complexes, ($R_1$, $R_2$-DCNQI)$_2$M; ($R_1$, $R_2$ = $CH_3$, I, M = Ag, Cu, $Li_{1x}Cu_x$). *Molecular Crystals and Liquid Crystals Science and Technology. Section A*, 285(1):157–162, July 1996.

[90] M. Hiraoka, H. Sakamoto, K. Mizoguchi, T. Kato, and R. Kato. Charge transport in the insulating state of (DMe-DCNQI)$_2$Li above $T_{SP}$: A possible fractional charge soliton conduction with $\pm 12e$. *Physical Review Letters*, 91(5):056604, August 2003.

[91] T. Yamamoto, H. Tajima, R. Kato, M. Uruichi, and K. Yakushi. Raman spectra of (Me$_2$-DCNQI)$_2$Cu$_x$Li$_{1-x}$ ($0 \leq x \leq 1$): The evidence for charge separation at room temperature in a one-dimensional conductor having a quarter-filled band. *Journal of the Physical Society of Japan*, 71(8):1956–1964, August 2002.

[92] G. P. Srivastava. *The Physics of Phonons*. Taylor & Francis, New York, 1990.

[93] J. J. Quinn and K. Yi. *Solid State Physics: Principles and Modern Applications*, chapter Ch. 2: Lattice Vibrations, pages 37–78. Springer Verlag Berlin Heidelberg, 2009.

[94] V. P. Tolstoy, I. V. Chernyshova, and V. A. Skryshevsky. *Handbook of infrared spectroscopy of ultrathin films*. Wiley Interscience, New York, 2003.

[95] Y. B. Band. *Light and matter: electromagnetism, optics, spectroscopy and lasers*. John Wiley, Chichester, 2006.

[96] C. Kittel. *Introduction to Solid State Physics*. John Wiley and Sons, New York, 8th edition, 2005.

[97] A. Einstein. Die Plancksche Theorie der Strahlung und die Theorie der spezifischen Wärme. *Annalen der Physik*, 327(1):180–190, 1906.

[98] P. Debye. Zur Theorie der spezifischen Wärmen. *Annalen der Physik*, 344(14):789–839, 1912.

[99] A. Pertsin and A. Kitaigorodsky. *The Atom-Atom Potential Method*, volume 43 of *Springer Series in Chemical Physics*. Springer Verlag Berlin Heidelberg, 1987.

[100] P. D. Desai. Thermodynamic properties of iron and silicon. *Journal of Physical and Chemical Reference Data*, 15(3):967, 1986.

[101] T. Wei, S. Etemad, A. Garito, and A. Heeger. Low temperature specific heat of (TTF)(TCNQ). *Physics Letters A*, 45(4):269–270, October 1973.

[102] J. J. Hall. Electronic effects in the elastic constants of n-type silicon. *Physical Review*, 161(3):756–761, September 1967.

[103] T. Tiedje, R. Haering, M. Jericho, W. Roger, and A. Simpson. Temperature dependence of sound velocities in TTF-TCNQ. *Solid State Communications*, 23(10):713–718, September 1977.

[104] H. A. Mook and C. R. Watson. Neutron inelastic scattering study of tetrathiafulvalene tetracyanoquinodimethane (TTF-TCNQ). *Physical Review Letters*, 36(14):801–803, April 1976.

[105] R. A. Craven, M. B. Salamon, G. DePasquali, R. M. Herman, G. Stucky, and A. Schultz. Specific heat of tetrathiofulvalinium-tetracyanoquinodimethane (TTF-TCNQ) in the vicinity of the metal-insulator transition. *Physical Review Letters*, 32(14):769–772, April 1974.

[106] R. Newnham. *Properties of Materials: Anisotropy, Symmetry, Structure*. Oxford University Press, Oxford, 2005.

[107] A. Filhol, G. Bravic, J. Gaultier, D. Chasseau, and C. Vettier. Room- and high-pressure neutron structure determination of tetrathiafulvalene-7,7,8,8-tetracyano-p-quinodimethane (TTF-TCNQ). Thermal expansion and isothermal compressibility. *Acta Crystallographica B*, 37(6):1225–1235, June 1981.

[108] V. K. Jindal and J. Kalus. Calculation of thermal expansion and phonon frequency shift in deuterated naphthalene. *Physica Status Solidi (b)*, 133(1):89–99, January 1986.

[109] C. de Kruif and H. Govers. Enthalpies of sublimation and vapor pressures of 2,2-bis-1,3-dithiole (TTF), 7,7,8,8-tetracyanoquinodimethane (TCNQ), and TTF-TCNQ (1:1). *The Journal of Chemical Physics*, 73(1):553, July 1980.

[110] B. Schatschneider, J.-J. Liang, A. M. Reilly, N. Marom, G.-X. Zhang, and A. Tkatchenko. Electrodynamic response and stability of molecular crystals. *Physical Review B*, 87(6):060104, February 2013.

[111] S. M. Sze and K. K. Ng. *Physics of Semiconductor Devices*. Wiley-Interscience, New York, 3rd edition, 2007.

[112] M. Pope and C. E. Swenberg. *Electronic Processes in Organic Crystals and Polymers*. Oxford University Press, New York, 2nd edition, 1999.

[113] G. C. Pimentel and A. L. McClellan. The infrared spectra of naphthalene crystals, vapor, and solutions. *The Journal of Chemical Physics*, 20(2):270–277, February 1952.

[114] E. R. Lippincott and E. J. O'Reilly. Vibrational spectra and assignment of naphthalene and naphthalene-$d_8$. *The Journal of Chemical Physics*, 23(2):238–244, February 1955.

[115] R. Zallen and E. Conwell. The effect of temperature on libron frequencies in molecular crystals: Implications for TTF-TCNQ. *Solid State Communications*, 31(8):557–561, August 1979.

[116] I. Natkanieq, I. Natkanieq, L. Bokhenkovt, L. Bokhenkovt, J. Kalusfi, J. Kalusfi, U. Schmelzers, U. Schmelzers, E. F. Shekat, and E. F. Shekat. Phonon dispersion in d$_8$-naphthalene crystal at 6 k. *Journal of Physics C: Solid State Physics*, 13(23):4265–83, 1980.

[117] M. Holt, Z. Wu, H. Hong, P. Zschack, P. Jemian, J. Tischler, H. Chen, and T.-C. Chiang. Determination of phonon dispersions from x-ray transmission scattering: The example of silicon. *Physical Review Letters*, 83(16):3317–3319, October 1999.

[118] P. Flubacher, A. J. Leadbetter, and J. A. Morrison. The heat capacity of pure silicon and germanium and properties of their vibrational frequency spectra. *Philosophical Magazine*, 4(39):273–294, March 1959.

[119] N. Sallamie and J. Shaw. Heat capacity prediction for polynuclear aromatic solids using vibration spectra. *Fluid Phase Equilibria*, 237(1-2):100–110, October 2005.

[120] R. Pan, M. Nair, and B. Wunderlich. On the $C_p$ to $C_v$ conversion of solid linear macromolecules II. *Journal of Thermal Analysis and Calorimetry*, 35(3):955–966, May 1989.

[121] T. Tritt, editor. *Thermal Conductivity: Theory, Troperties, and Applications*. Kluver Academic/Plenum Publishers, New York, 2004.

[122] E. M. Conwell. *Semiconductors and Semimetals: Highly Conducting Quasi-One-Dimensional Organic Crystals*. Academic Press. Inc, San Diego, 1988.

[123] A. Matthiessen. Ueber die elektrische Leitungsfähigkeit der Legirungen. *Annalen der Physik*, 186(6):190–221, 1860.

[124] H. Gutfreund and M. Weger. Temperature dependence of the metallic conductivity of tetrathiafulvalene-tetracyanoquinodimethane (TTF-TCNQ). *Physical Review B*, 16(4):1753–1755, August 1977.

[125] W. Brütting, P. H. Nguyen, W. Rieß, and G. Paasch. dc-conduction mechanism and peierls gap in organic and inorganic charge-density-wave conductors. *Physical Review B*, 51(15):9533–9543, April 1995.

[126] A. Casian, V. Dusciac, and I. Coropceanu. Huge carrier mobilities expected in quasi-one-dimensional organic crystals. *Physical Review B*, 66(16):165404, October 2002.

[127] M. Kaveh and N. Wiser. Electron-electron scattering in conducting materials. *Advances in Physics*, 33(4):257–372, January 1984.

[128] N. Karl. Charge carrier transport in organic semiconductors. *Synthetic Metals*, 133-134:649–657, March 2003.

[129] L. Landau. The theory of a fermi liquid. *Soviet Physics JETP Letters*, 3(6):920, January 1957.

[130] J. S. Chappell, A. N. Bloch, W. Bryden, M. Maxfield, T. Poehler, and D. Cowan. Degree of charge transfer in organic conductors by infrared absorption spectroscopy. *Journal of the American Chemical Society*, 103(9):2442–2443, May 1981.

[131] E. M. Conwell. Mobility in tetrathiafulvalene-tetracyanoquinodimethane (TTF-TCNQ). *Physical Review Letters*, 39(12):777–780, September 1977.

[132] J. R. Cooper. Comments on the metallic conductivity of tetrathiafulvalenium-tetracyanoquinodimethanide (TTF-TCNQ). *Physical Review B*, 19(4):2404–2408, February 1979.

[133] R. Friend, M. Miljak, D. Jérome, D. Decker, and D. Debray. Linear temperature dependence of the constant volume resistivity of TTF-TCNQ. *Journal de Physique Lettres*, 39(9):134–138, January 1978.

[134] J. Voit. A brief introduction to Luttinger liquids. *AIP Conference Proceedings*, 544(1):309–318, October 2001.

[135] M. Dressel. Spin-charge separation in quasi one-dimensional organic conductors. *Die Naturwissenschaften*, 90(8):337–344, August 2003.

[136] J. Moser, M. Gabay, P. Auban-Senzier, D. Jérome, K. Bechgaard, and J. Fabre. Transverse transport in organic conductors: possible evidence for a Luttinger liquid. *The European Physical Journal B*, 1(1):39–46, January 1998.

[137] T. Giamarchi. Theoretical framework for quasi-one dimensional systems. *ChemInform*, 36(5), February 2005.

[138] K. Tamura, T. Ozawa, Y. Bando, T. Kawamoto, and T. Mori. Voltage oscillation associated with nonlinear conductivity in the organic conductor $\alpha$-(BEDT-TTF)$_2$I$_3$. *Journal of Applied Physics*, 107(10):103716, May 2010.

[139] T. Ivek, I. Kovačević, M. Pinterić, B. Korin-Hamzić, S. Tomić, T. Knoblauch, D. Schweitzer, and M. Dressel. Cooperative dynamics in charge-ordered state of $\alpha$-(BEDT-TTF)$_2$I$_3$. *Physical Review B*, 86(24):245125, December 2012.

[140] Y. Iwasa, T. Koda, S. Koshihara, Y. Tokura, N. Iwasawa, and G. Saito. Intrinsic negative-resistance effect in mixed-stack charge-transfer crystals. *Physical Review B*, 39(14):10441–10444, May 1989.

[141] K. Okamoto, T. Tanaka, W. Fujita, K. Awaga, and T. Inabe. Charge ordering and nonlinear electrical transport in quasi-one-dimensional organic chains with strong electrostatic interchain interactions. *Physical Review B*, 76(7):075328, August 2007.

[142] T. Mori, Y. Bando, T. Kawamoto, I. Terasaki, K. Takimiya, and T. Otsubo. Giant nonlinear conductivity and spontaneous current oscillation in an incommensurate organic superconductor. *Physical Review Letters*, 100(3):037001, January 2008.

[143] T. Mori, T. Ozawa, Y. Bando, T. Kawamoto, S. Niizeki, H. Mori, and I. Terasaki. Nonlinear dynamics of conduction electrons in organic conductors. *Physical Review B*, 79(11):115108, March 2009.

[144] S. Hunklinger. *Festkörperphysik*. Oldenbourg Wissenschaftsverlag GmbH, München, January 2009.

[145] G. R. Stewart. Heavy-fermion systems. *Reviews of Modern Physics*, 56(4):755–787, October 1984.

[146] S. Uji, T. Terashima, H. Aoki, R. Kato, H. Sawa, S. Aonuma, M. Tamura, and M. Kinoshita. Fermi surface and absence of additional mass enhancement near the insulating phase in (DMe-DCNQI)$_2$Cu. *Solid State Communications*, 93(3):203–207, January 1995.

[147] A. C. Jacko, J. O. Fjaerestad, and B. J. Powell. A unified explanation of the Kadowaki-Woods ratio in strongly correlated metals. *Nature Physics*, 5:422–425, April 2009.

[148] P. M. Chaikin, R. L. Greene, S. Etemad, and E. Engler. Thermopower of an isostructural series of organic conductors. *Physical Review B*, 13(4):1627–1632, February 1976.

[149] D. MacDonald. *Thermoelectricity: An Introduction to the Principles*. John Wiley and Sons, New York, 1962.

[150] R. L. Powell, H. M. Roder, and W. J. Hall. Low-temperature transport properties of copper and its dilute alloys: Pure copper, annealed and cold-drawn. *Physical Review*, 115(2):314–323, July 1959.

[151] G. D. Mahan and J. O. Sofo. The best thermoelectric. *Proceedings of the National Academy of Sciences*, 93(15):7436–7439, July 1996.

[152] T. E. Humphrey and H. Linke. Reversible thermoelectric nanomaterials. *Physical Review Letters*, 94(9):096601, March 2005.

[153] J. Callaway. Model for lattice thermal conductivity at low temperatures. *Physical Review*, 113(4):1046, February 1959.

[154] V. Narayanamurti and R. O. Pohl. Tunneling states of defects in solids. *Reviews of Modern Physics*, 42(2):201–236, April 1970.

[155] C. Kittel. Interpretation of the thermal conductivity of glasses. *Physical Review*, 75(6):972–974, March 1949.

[156] A. J. Minnich. Thermal transport: Naturally glassy crystals. *Nature Nanotechnology*, 8(6):392–393, June 2013.

[157] D. Cahill and R. Pohl. Lattice vibrations and heat transport in crystals and glasses. *Annual Review of Physical Chemistry*, 39:93–121, October 1988.

[158] M. Cohen, L. Coleman, A. Garito, and A. Heeger. Electrical conductivity of tetrathiofulvalinium tetracyanoquinodimethan (TTF)(TCNQ). *Physical Review B*, 10(4):1298, August 1974.

[159] C. Kloc, T. Siegrist, and J. Pflaum. Growth of single-crystal organic semiconductors. In G. Dhanaraj, K. Byrappa, V. Prasad, and M. Dudley, editors, *Springer Handbook of Crystal Growth*, pages 845–867. Springer Verlag Berlin Heidelberg, 2010.

[160] Y. Kawasugi, H. M. Yamamoto, M. Hosoda, N. Tajima, T. Fukunaga, K. Tsukagoshi, and R. Kato. Strain-induced superconductor/insulator transition and field effect in a thin single crystal of molecular conductor. *Applied Physics Letters*, 92(24):243508, June 2008.

[161] H. M. Yamamoto, H. Ito, K. Shigeto, K. Tsukagoshi, and R. Kato. Direct formation of micro-/nanocrystalline 2,5-dimethyl-N,N'-dicyanoquinonediimine complexes on $SiO_2$/Si substrates and multiprobe measurement of conduction properties. *Journal of the American Chemical Society*, 128(3):700–701, January 2006.

[162] H. M. Yamamoto, M. Nakano, M. Suda, Y. Iwasa, M. Kawasaki, and R. Kato. A strained organic field-effect transistor with a gate-tunable superconducting channel. *Nature Communications*, 4:2379, August 2013.

[163] P. M. Chaikin and J. F. Kwak. Apparatus for thermopower measurements on organic conductors. *Review of Scientific Instruments*, 46(2):218, February 1975.

[164] F. J. Blatt and R. H. Kropschotf. Thermoelectric power of dilute copper alloys. *Physical Review*, 118(2):480–489, April 1960.

[165] D. G. Cahill. Thermal conductivity measurement from 30 to 750 K: The $3\omega$ method. *Review of Scientific Instruments*, 61(2):802–808, February 1990.

[166] C. Dames and G. Chen. $1\omega$, $2\omega$, and $3\omega$ methods for measurements of thermal properties. *Review of Scientific Instruments*, 76(12):1–14, December 2005.

[167] J. G. Kimling. *Transport phenomena in thermoelectric and ferromagnetic nanostructures*. PhD thesis, Universität Hamburg, 2013.

[168] C. Dames. Measuring the thermal conductivity of thin films : 3 omega and related electrothermal methods. *Annual Review of Heat Transfer*, 16:7–49, 2013.

[169] L. Lu, W. Yi, and D. L. Zhang. $3\omega$ method for specific heat and thermal conductivity measurements. *Review of Scientific Instruments*, 72(7):2996–3003, June 2001.

[170] B. Hamdou, J. Kimling, and A. Dorn. Thermoelectric characterization of bismuth telluride nanowires, synthesized via catalytic growth and post-annealing. *Advanced Materials*, 25(2):239–244, January 2013.

[171] L. R. Holland. Physical properties of titanium. III. The specific heat. *Journal of Applied Physics*, 34(8):2350–2357, August 1963.

[172] D. Mann. LNG materials and fluids. Technical report, National Bureau of Standards, Cryogenics Division, 1977.

[173] K. Torizuka, H. Tajima, Y. Kawamura, H. Sawa, and T. Yamamoto. Thermal transport of organic molecular crystals (DMe-DCNQI)$_2$Li$_{(1-x)}$Cu$_x$ and observation of their super-lattice structure by means of synchrotron radiation X-ray. *Journal of Physics and Chemistry of Solids*, 66(89):1575 – 1578, August 2005.

[174] K. Torizuka, H. Tajima, and T. Yamamoto. Thermal conductivity of (DMe-DCNQI)$_2$Li$_{(1-x)}$Cu$_x$ (x = 1 and 0.75): Anomalous temperature hysteresis depending on Cu concentration. *Journal of the Physical Society of Japan*, 75(7):074604, August 2006.

[175] M.-Y. Choi, P. Chaikin, and R. Greene. Thermal conductivity of bis-tetramethyltetraselenafulvalene perchlorate [(TMTSF)$_2$ClO$_4$]. *Physical Review B*, 34(11):7727–7732, December 1986.

[176] A. Matsui, Y. Takaoka, Y. Nishio, R. Kato, and K. Kajita. Thermal study of DCNQI-Cu using a high accuracy specific heat measurement system. *Journal of Physics: Conference Series*, 150(4):42120, 2009.

[177] F. Huewe, A. Steeger, I. Bauer, S. Doerrich, P. Strohriegl, and J. Pflaum. Energy exchange between phononic and electronic subsystems governing the nonlinear conduction in DCNQI$_2$Cu. *Physical Review B*, 92(15):155107, October 2015.

[178] J. Fraxedas. *Molecular Organic Materials*. Cambridge University Press, Cambridge, 2006.

[179] M. N. Gueye, A. Carella, N. Massonnet, E. Yvenou, S. Brenet, J. Faure-Vincent, S. Pouget, F. Rieutord, H. Okuno, A. Benayad, R. Demadrille, and J.-P. Simonato. Structure and dopant engineering in pedot thin films: Practical tools for a dramatic conductivity enhancement. *Chemistry of Materials*, 28(10):3462–3468, May 2016.

[180] W. Warta, R. Stehle, and N. Karl. Ultrapure, high mobility organic photoconductors. *Applied Physics A*, 36(3):163–170, March 1985.

[181] S. Hünig. N, N'-dicyanoquinone diimines (DCNQIs): unique acceptors for conducting materials. *Journal of Materials Chemistry*, 5(10):1469–1479, 1995.

[182] D. Bauer, J. U. von Schütz, H. C. Wolf, S. Hünig, K. Sinzger, and R. K. Kremer. Alloyed deuterated copper-DCNQI salts: Phase transitions and reentry of conductivity, giant hysteresis effects, and coexistence of metallic and semiconducting modes. *Advanced Materials*, 5(11):829–834, November 1993.

[183] T. Vuletić, M. Pinterić, M. Lončarić, S. Tomić, and J. von Schütz. Non-ohmic electrical transport in the Peierls-Mott state of deuterated copper-DCNQI systems. *Synthetic Metals*, 120(1-3):1001–1002, March 2001.

[184] H. P. Werner, J. U. von Schütz, and H. C. Wolf. Radical anion salts of N, N'-dicyanoquinonediimine (DCNQI): Conductivity and magnetic properties. *Solid state Communications*, 65(8):809–813, February 1988.

[185] Y. Nogami, S. Hayashi, T. Date, K. Oshima, K. Hiraki, and K. Kanoda. High pressure structures of organic low dimensional conductor DCNQI compounds. *The Review of High Pressure Science and Technology*, 7:404–406, August 1998.

[186] S. Tomić, D. Jérome, A. Aumüller, P. Erk, S. Hünig, and J. U. von Schütz. Pressure-induced metal-to-insulator phase transitions in the organic conductor (2,5 DM-DCNQI)$_2$Cu. *(EPL) Europhysics Letters*, 5(6):553, March 1988.

[187] R. Burkert, H. W. Helberg, and J. U. von Schütz. Longitudinal and transverse conductivity in (2,5-Me$_2$-DCNQI)$_2$Cu fibres. *Synthetic Metals*, 56(1):2519–2524, March 1993.

[188] H. Hild, J. U. von Schütz, and H. Wachtel. Effect of tensile stress on the phase transition in Cu(2,5-dimethyl-N,N-dicyanoquinonediimine)$_2$ - correlation of crystal length and conductivity. *Solid State Communications*, 101(8):563–567, February 1997.

[189] M. Sasaki, S. Tanaka, H. Negishi, M. Inoue, and R. Kato. Static and dynamic transport studies of molecular conductors (DMe-DCNQI)$_2$Cu. *Journal of the Physics Society Japan*, 67(5):1693–1703, May 1998.

[190] J. Bardeen. Macroscopic quantum tunneling in quasi one-dimensional metals. II. Theory. *Physical Review Letters*, 55(9):1010–1013, August 1985.

[191] J. L. Bredas and G. B. Street. Polarons, bipolarons, and solitons in conducting polymers. *Accounts of Chemical Research*, 18(10):309–315, October 1985.

[192] D. Bauer, B. Maier, D. Schweitzer, and J. U. von Schütz. Thermopower of deuterated and alloyed Cu-DCNQI-crystals - Evidences for a quite normal reentry of the conductivity. *Synthetic Metals*, 71(1-3):1887–1888, April 1995.

[193] I. Bauer. University of bayreuth. Private Communication, 2015.

[194] G. Beni, J. Kwak, and P. Chaikin. Thermoelectric power, coulomb correlation and charge transfer in TCNQ salts. *Solid State Communications*, 17(12):1549–1551, December 1975.

[195] T. Yamamoto, H. Tajima, R. Kato, M. Uruichi, and K. Yakushi. Thermoelectric power and Raman spectra of $(Me_2DCNQI)_2Cu_xLi_{1-x}$. *Synthetic Metals*, 133:291–292, March 2003.

[196] W. Koshibae and S. Maekawa. Effects of spin and orbital degeneracy on the thermopower of strongly correlated systems. *Physical Review Letters*, 87(23):236603, November 2001.

[197] H. Tajima, T. Yamamoto, J. Yamaura, S. Aonuma, and R. Kato. The study of $4k_F$ CDW in a one-dimensional system, $(DMe\text{-}DCNQI)_2Li_{1-x}Cu_x$. *Synthetic Metals*, 103(1):2193–2194, June 1999.

[198] P. H. P. Nguyen, G. Paasch, W. Brütting, and W. Riess. Analysis of the dc conductivity of the quasi-one-dimensional charge-density-wave conductor $(fluoranthene)_2X$. *Physical Review B*, 49(8):5172–5181, February 1994.

[199] M. Pinterić, T. Vuletić, M. Lončarić, S. Tomić, and J. U. von Schütz. Low frequency dielectric spectroscopy of the peierls-mott insulating state in the deuterated copper-DCNQI systems. *The European Physical Journal B*, 16(3):487–493, August 2000.

[200] J. Guo, X. Wang, and T. Wang. Thermal characterization of microscale conductive and nonconductive wires using transient electrothermal technique. *Journal of Applied Physics*, 101(6):063537, March 2007.

[201] C. Xing, T. Munro, C. Jensen, and H. Ban. Analysis of the electrothermal technique for thermal property characterization of thin fibers. *Measurement Science and Technology*, 24(10):105603, August 2013.

[202] J. C. Lasjaunias, K. Biljaković, and P. Monceau. Time-dependent specific heat below 1 K in the spin-density-wave state of $(TMTSF)_2PF_6$. *Physical Review B*, 53(12):7699–7703, March 1996.

[203] T. Wei, P. S. Kalyanaraman, K. D. Singer, and A. F. Garito. Low-temperature specific heats of tetrathiafulvalene-tetracyanoquinodimethane (TTF-TCNQ) and its derivatives. *Physical Review B*, 20(12):5090–5093, December 1979.

[204] D. D. Dlott. Optical phonon dynamics in molecular crystals. *Annual Review of Physical Chemistry*, 37:157–187, October 1986.

[205] L. A. Galchenkov, S. N. Ivanov, I. I. Pyataikin, V. P. Chernov, and P. Monceau. 1/f noise in conducting langmuir-blodgett films. *Physical Review B*, 57(20):13220–13226, May 1998.

[206] J. Müller, J. Brandenburg, and J. A. Schlueter. 1/f noise in the quasi-two-dimensional organic conductor $\kappa$-(BEDT-TTF)$_2$Cu[N(CN)$_2$]Cl. *Physical Review B*, 79(21):214521, June 2009.

[207] E. Pop, D. Mann, J. Cao, Q. Wang, K. Goodson, and H. Dai. Negative differential conductance and hot phonons in suspended nanotube molecular wires. *Physical Review Letters*, 95(15):155505, October 2005.

[208] S. Berciaud, M. Y. Han, K. F. Mak, L. E. Brus, P. Kim, and T. F. Heinz. Electron and optical phonon temperatures in electrically biased graphene. *Physical Review Letters*, 104(22):227401, June 2010.

[209] S. Hill, P. S. Sandhu, M. E. J. Boonman, J. A. A. J. Perenboom, A. Wittlin, S. Uji, J. S. Brooks, R. Kato, H. Sawa, and S. Aonuma. Magnetoelectrodynamics of a three-dimensional organic conductor: Observation of cyclotron resonance in d$_2$[1,1;0]-(DMe-DCNQI)$_2$Cu. *Physical Review B*, 54(19):13536–13541, November 1996.

[210] P. M. Chaikin, P. Haen, E. M. Engler, and R. L. Greene. Magnetoresistance and Hall effect in tetramethyl-tetraselenafulvalene-phosphorus hexafloride [(TMTSF)$_2$PF$_6$]. *Physical Review B*, 24(12):7155–7161, December 1981.

[211] W. P. Su and J. R. Schrieffer. Soliton dynamics in polyacetylene. *Proceedings of the National Academy of Sciences*, 77(10):5626–5629, October 1980.

[212] K. Maki. Soliton diffusion in polyacetylene. I. Optical phonons. *Physical Review B*, 26(4):2181–2186, August 1982.

[213] F. Kreith, R. Manglik, and M. Bohn. *Principles of Heat Transfer*. Cengage Learning, Stanford, 7th edition, 2011.

[214] J. W. Brill, C. P. Tzou, G. Verma, and N. P. Ong. Thermal conductivity of NbSe$_3$. *Solid State Communications*, 39(2):233–237, July 1981.

[215] R. Ross, P. Andersson, and G. Bäckström. Thermal conductivity and heat capacity of benzene, naphthalene and anthracene under pressure. *Molecular Physics*, 38(2):527–533, August 1979.

[216] H. Zhang, Y. Yao, M. M. Payne, J. E. Anthony, and J. W. Brill. Thermal diffusivities of functionalized pentacene semiconductors. *Applied Physics Letters*, 105(7):073302, August 2014.

[217] N. Wakeham, A. F. Bangura, X. Xu, J.-F. Mercure, M. Greenblatt, and N. E. Hussey. Gross violation of the Wiedemann-Franz law in a quasi-one-dimensional conductor. *Nature Communications*, 2:396, July 2011.

[218] M. Kaveh, H. Gutfreund, and M. Weger. Thermal conductivity of tetrathiafulvalenium-tetracyanoquinodimethanide (TTF-TCNQ). *Physical Review B*, 20(2):543–549, July 1979.

[219] S. Belin, K. Behnia, and A. Deluzet. Heat conduction in $\kappa$-(BEDT-TTF)$_2$Cu(NCS)$_2$. *Physical Review Letters*, 81(21):4728–4731, November 1998.

[220] K. Torizuka, H. Tajima, and T. Yamamoto. Thermal conductivity of (DMe-DCNQI)$_2$Li$_{1-x}$Cu$_x$ ($0 \leq x \leq 0.14$): Phonon propagation and the spin-peierls lattice distortion. *Physical Review B*, 71(19):193101, May 2005.

[221] S. Belin and K. Behnia. Thermal conductivity of superconducting (TMTSF)$_2$ClO$_4$: Evidence for a nodeless gap. *Physical Review Letters*, 79(11):2125–2128, September 1997.

[222] M. Boujida, C. Escribe-Filippini, J. Marcus, and C. Schlenker. Superconducting properties of the low dimensional lithium molybdenum purple bronze Li$_{0.9}$Mo$_6$O$_{17}$. *Physica C: Superconductivity*, 153-155:465–466, June 1988.

[223] C. L. Kane and M. P. Fisher. Thermal transport in a Luttinger liquid. *Physical Review Letters*, 76(17):3192–3195, April 1996.

[224] T. Takahashi, T. Yokoya, A. Chainani, H. Kumigashira, O. Akaki, and R. Kato. Cooperative effects of electron correlation and charge ordering on the metal-insulator transition in quasi-one-dimensional deuterated (DMe-DCNQI)$_2$Cu. *Physical Review B*, 53(4):1790–1794, January 1996.

[225] D. LeBlanc. *Statistics: Concepts and Applications for Science*, volume 2. Jones and Bartlett Learning, Sudbury, Massachusetts, 2004.

[226] J. Fleurial, L. Gailliard, R. Triboulet, H. Scherrer, and S. Scherrer. Thermal properties of high quality single crystals of bismuth telluride - Part I: Experimental characterization. *Journal of Physics and Chemistry of Solids*, 49(10):1237–1247, 1988.

[227] N. Fortune, K. Murata, M. Ishibashi, M. Tokumoto, N. Kinoshita, and H. Anzai. Calorimetric observation of the metal-insulator phase transition in $\alpha$-(BEDT-TTF)$_2$I$_3$. *Solid State Communications*, 79(3):265–269, July 1991.

[228] C. N. Berglund and H. J. Guggenheim. Electronic properties of $VO_2$ near the semiconductor-metal transition. *Physical Review*, 185(3):1022–1033, September 1969.

[229] Y. Nishio, K. Kajita, W. Sasaki, R. Kato, A. Kobayashi, and H. Kobayashi. Thermal and magnetic properties in organic metals (DMe-DCNQI)$_2$Cu, (DMeO-DCNQI)$_2$Cu and (DMe$_{1-x}$MeBr$_x$-DCNQI)$_2$Cu: Enhancement of density of states. *Solid State Communications*, 81(6):473 – 476, February 1992.

[230] E. A. Brandes and G. Brook, editors. *Smithells Metals Reference Book*. Butterworth-Heinemann, Oxford, 7th edition, 1992.

[231] Q. Wei, M. Mukaida, K. Kirihara, Y. Naitoh, and T. Ishida. Recent progress on PEDOT-based thermoelectric materials. *Materials*, 8(2):732–750, February 2015.

[232] K. Shi, F. Zhang, C.-A. Di, T.-W. Yan, Y. Zou, X. Zhou, D. Zhu, J.-Y. Wang, and J. Pei. Toward high performance n-type thermoelectric materials by rational modification of BDPPV backbones. *Journal of the American Chemical Society*, 137(22):6979–6982, June 2015.

[233] M. Koirala, H. Wang, M. Pokharel, Y. Lan, C. Guo, C. Opeil, and Z. Ren. Nanostructured $YbAgCu_4$ for potentially cryogenic thermoelectric cooling. *Nano Letters*, 14(9):5016–20, September 2014.

[234] R. Ross. Requirements for long-life mechanical cryocoolers for space application. *Cryogenics*, 30(3):233–238, March 1990.

[235] G. Walker. *Cryocoolers: Part 2: Applications*. Plenum Press, New York, 1983.

[236] A. K. Maini and V. Agrawal. *Satellite Technology: Principles and Applications*. John Wiley and Sons, Chichester, 2nd edition, 2011.

[237] R. J. Moss and S. B. Gabriel. A critical review of space-cooling techniques. *Advances in Space Research*, 17(1):119–122, 1996.

[238] D. M. Rowe and G. Min. Evaluation of thermoelectric modules for power generation. *Journal of Power Sources*, 73(2):193–198, June 1998.

[239] S. Lee, D. Khim, Y. Xu, J. Kim, W. Park, and D. Kim. Simultaneous improvement of hole and electron injection in organic field-effect transistors by conjugated polymer-wrapped carbon nanotube interlayers. *Scientific Reports*, 5:10407, May 2015.

[240] T. Lorenz, M. Hofmann, M. Grüninger, A. Freimuth, G. S. Uhrig, M. Dumm, and M. Dressel. Evidence for spin-charge separation in quasi-one-dimensional organic conductors. *Nature*, 418:614–617, August 2002.

# List of Figures

# List of Tables

# Acknowledgements

I want to thank all people who made this work possible. First of all, I am grateful to my parents and my family for their moral and financial support throughout my education. My friends encouraged me to keep a stiff upper lip in every situation I felt stuck, too. Thanks to all of you! Of course another person has to be mentioned. Dear Juliane, with your even-tempered nature and your affection you always managed to smooth the ups and downs between excitement and depression in science. Thank you for enduring my moods.

Moreover, I would like to express my gratitude to Professor Jens Pflaum for giving me the opportunity to this work. The financial support by the DFG, the DAAD and the EU is gratefully acknowledged, too. I also would like to thank Professor Vladimir Dyakonov, André Thiem-Riebe and the whole EP VI, Roland Ebert and Cornelius Ziga from the cryogenic workshop, as well as all the guys from the mechanical and the electrical workshops for providing the necessary infrastructure. The same applies for Stephan Braxmeier from the ZAE for performing the SEM measurements. I was very happy to work with my external project partners Professor Markus Schwoerer, Professor Peter Strohriegl, Irene Bauer, Nicolas Erasmus, Bart Smit, Professor Simon Woodward and Steffen Dörrich. Thank you for the scientific support in all respects. In particular, I am indebted to Professor Heinrich Schwoerer for giving me the opportunity to work in his laser laboratory in Stellenbosch for almost half a year. Both from a personal and professional viewpoint, it was an unforgettable, positive experience which I do not want to miss in my life.

Special thanks go to the whole *AG Pflaum* for the academic support and even more, for the great time we had inside and outside the lab. The tabletop football skills will (hopefully) remain, independently of physics and science. Even more, we shared a lot of great moments which I will surely keep in mind and heart. Verena, I really enjoyed sharing the office with you, keep going on the short remaining distance without me. There is one more person I need to set apart from the others: My dear friend Axel! Without you none of this would have ended well. I will miss to work by your side as scientist, singer, bartender or purifier.